

# INDEX

|  |           |
|--|-----------|
| <b>INDEX</b> .....   | <b>1</b>  |
| <b>RESUME</b> .....  | <b>3</b>  |
| <b>1 FOREWORD</b> .....  | <b>13</b> |
| <b>2 TASK: TERRESTRIAL PLANETS' ATMOSPHERES</b> .....                    | <b>17</b> |
| 2.1 VENUS .....  | 18        |
| 2.1.1 <i>The Atmosphere of Venus</i> .....                               | 23        |
| 2.1.2 <i>The Sulphuric Acid Clouds of Venus</i> .....                    | 26        |
| 2.1.3 <i>Winds on Venus</i> .....  | 29        |
| 2.2 MARS .....   | 32        |
| 2.2.1 <i>The Martian atmosphere: gaseous components</i> .....            | 33        |
| 2.2.2 <i>Dust</i> .....  | 39        |
| 2.2.3 <i>Main phenomena of Martian atmosphere</i> .....                  | 41        |
| <b>3 TOOLS: SPECTROMETERS AND INFRARED SPECTROSCOPY</b> .....            | <b>47</b> |
| 3.1 THE INSTRUMENT: VIRTIS - VEX .....                                   | 49        |
| 3.1.1 <i>Venus Express mission</i> .....                                 | 49        |
| 3.1.2 <i>The Visible and Infrared Thermal Imaging Spectrometer</i> ..... | 49        |
| 3.1.3 <i>VIRTIS technical specifications</i> .....                       | 55        |
| 3.2 THE INSTRUMENT: PFS - MEX .....                                      | 57        |
| 3.2.1 <i>The Planetary Fourier Spectrometer experiment (PFS)</i> .....   | 57        |
| 3.2.2 <i>General instrumental set-up</i> .....                           | 57        |
| 3.2.3 <i>Examples of PFS Martian spectra</i> .....                       | 62        |
| 3.3 IR SPECTRA OF A PLANETARY ATMOSPHERE .....                           | 66        |
| 3.3.1 <i>Basic definitions</i> .....                                     | 66        |
| 3.3.2 <i>Effects of surface</i> .....                                    | 68        |
| 3.3.3 <i>Microscopic effects of gases</i> .....                          | 71        |
| 3.3.4 <i>Microscopic effects of aerosols</i> .....                       | 75        |
| 3.3.5 <i>Macroscopic description</i> .....                               | 76        |
| 3.3.6 <i>Total field</i> .....   | 81        |
| <b>4 GENERAL RETRIEVAL METHOD</b> .....                                  | <b>85</b> |
| 4.1 INTRODUCTION .....   | 85        |
| 4.2 FORWARD MODEL: RESOLUTION OF RT EQUATION .....                       | 86        |

|          |   |            |
|----------|---|------------|
| 4.2.1    | <i>Radiative transfer without scattering</i> .....  | 93         |
| 4.2.2    | <i>Radiative transfer with multiple scattering</i> .....  | 96         |
| <b>5</b> | <b>RESULTS FOR VENUS</b> .....  | <b>99</b>  |
| 5.1      | VENUS SPECTRA COMPUTATION TO MODEL VIRTIS-M DATA .....  | 100        |
| 5.1.1    | <i>Models for night side spectra in the region 3.5 – 5.0 <math>\mu\text{m}</math></i> .....                     | 101        |
| 5.1.2    | <i>Test: comparison of CO<sub>2</sub> spectroscopic databases</i> .....   | 102        |
| 5.1.3    | <i>Choice of the monochromatic grid</i> .....   | 104        |
| 5.1.4    | <i>Test of different CO<sub>2</sub> line cutoff</i> .....   | 106        |
| 5.1.5    | <i>Test of different radiative transfer options for the treatment of scattering</i><br>107                      |            |
| 5.1.6    | <i>Validation of a fast direct RT method for the retrieval of the atmospheric<br/>temperature profile</i> ..... | 108        |
| 5.2      | TASK: SEARCH FOR WATER IN VENUS ATMOSPHERE.....   | 111        |
| 5.2.1    | <i>Water from VIRTIS M data</i> .....   | 112        |
| 5.2.2    | <i>Water from VIRTIS H data</i> .....   | 115        |
| 5.2.3    | <i>Atmospheric model</i> .....  | 123        |
| 5.2.4    | <i>Retrieval method</i> .....   | 126        |
| 5.2.5    | <i>Results for the cloud tops altitude</i> .....  | 134        |
| 5.2.6    | <i>Results for water abundance</i> .....  | 140        |
| 5.2.7    | <i>Inverse Method</i> .....   | 146        |
| <b>6</b> | <b>RESULTS FOR MARS</b> .....   | <b>153</b> |
| 6.1      | CARBON MONOXIDE ABUNDANCE (CO) IN MARTIAN ATMOSPHERE.....   | 154        |
| 6.1.1    | <i>Retrieval method and Atmospheric model</i> .....   | 156        |
| 6.1.2    | <i>Data</i> .....   | 160        |
| 6.1.3    | <i>Error evaluation</i> .....   | 160        |
| 6.1.4    | <i>Results</i> .....  | 163        |
| 6.1.5    | <i>Discussion</i> .....   | 169        |
| 6.2      | CO <sub>2</sub> ISOTOPES RETRIEVAL IN MARTIAN ATMOSPHERE.....   | 171        |
| 6.2.1    | <i>Data</i> .....   | 172        |
| 6.2.2    | <i>Retrieval method and Atmospheric model</i> .....   | 173        |
| 6.2.3    | <i>Results on isotopic abundances</i> .....   | 175        |
| 6.2.4    | <i>Discussion</i> .....   | 190        |
| <b>7</b> | <b>CONCLUSIONS</b> .....  | <b>193</b> |
| <b>8</b> | <b>REFERENCES</b> .....   | <b>199</b> |

## Resume

This work presents part of the efforts which I carried out in the Interplanetary Space Physics Institute (IFSI) and in the Cosmic Physics and Space Astrophysics Institute (IASF) of the Italian National Institute for Astrophysics (INAF) in the analysis of the data from the *Planetary Fourier Spectrometer* (PFS) experiment, included in the scientific payload of the ESA *Mars Express* (MEX) mission to Mars and the *Visual and Infrared Thermal Imaging Spectrometer* (VIRTIS) experiment, included in the ESA *Venus Express* (VEX) mission to Venus.

Information obtained from the study of terrestrial planets are fundamental for the understanding of Earth past and future climate evolution, since other terrestrial planets represent in some sense a possible stage – or alternative path - of the Earth's history.

The study of our closest neighbors, Mars and Venus, gives important information also in the search for planets belonging to other planetary systems - which is one of the mayor current interest of the scientific community - in order to provide a paradigm about planets orbiting around other stars, and which may possibly host life.

Mars and Venus pertain to the planets with a “CO<sub>2</sub> dominated” atmosphere and since they experiment different atmospheric conditions they provide an unique chance to obtain complete information on this atmospheric type at different evolutionary stages (in Chapter 2 a brief description of the two planet atmospheres is presented).

In particular, using the data acquired by the two ESA spacecraft we investigated the atmospheric composition of the two planets in order to give a contribute to the understanding of the main properties of Mars and Venus, since the composition of the atmosphere on global and regional scales influences the planetary climate and the evolution and the retrieved

information can therefore be used to trace the atmospheric circulation, give constraints to the atmospheric stability and its long term evolution.

Efforts have focused on topics still affected by large uncertainties in our understanding of atmospheric constituents other than carbon dioxide, in order to provide also firm constraints for future studies on atmospheric aeronomy and interaction with surface phenomena such as volcanism and related outgassing.

Namely, for this task we had the first chance to perform an *intensive* study of *water vapor* on *Venus* (previous studies regarded just limited local time or locations in the planet), since the role of water as a trace constituent is key to illuminating the present-day Venus atmospheric energy balance, particularly with respect to the global cloud layers which permanently envelop the planet.

On *Mars* we investigated the *stable isotope record* contained within *carbon and oxygen (CO<sub>2</sub> isotopes)*, to provide important constraints regarding the origin of the planet and its relationship to the Earth. Stable oxygen isotopes are particularly useful in the study of Mars because oxygen is abundantly present in both the Martian atmosphere and lithosphere, in particular in the main atmospheric constituent, carbon dioxide. We also investigated *carbon monoxide (CO) on Mars*, since it represents the main product of the CO<sub>2</sub> photolysis and therefore is directly related to the problem of the stability of the Martian CO<sub>2</sub> atmosphere.

*Infrared spectroscopy* and *present-day high resolution spectrometers* have demonstrated to be one of the most *powerful remote sensing tools* in the context of planetary observation, for atmospheric as well as for surface studies: they give together a remote access to most of the important information carried by the radiation which directly interacted with the planet.

Spectroscopic signatures of gaseous atmospheric components can be found over the whole range of the electromagnetic spectrum; nevertheless the important property of the infrared spectral range ( $\lambda = [1-100] \mu\text{m}$ ) is to

cover the main roto-vibrational bands of several molecules being present in planetary atmospheres, so that at the present time, most of our knowledge regarding planetary atmospheric composition and structure has been achieved by remote sensing spectroscopy.

Since the IR radiation emerging from a planetary atmosphere it is described from the Radiative Transfer equation, we presented (Chapter 3) some basic principles of the theory of radiative Transfer in the appropriate form for planetary atmospheres.

Once we have available the infrared spectra of Mars and Venus acquired by PFS and VIRTIS, we need to produce models which properly describe (simulate) what the instrument measures, in order to retrieve from the spectra the required quantities, namely composition.

Many factors contribute to the formation of a spectrum emerging from a planet: the chemical and physical state of the surface, the atmospheric composition and thermal structure, the aerosols content and their nature, the observational and illumination geometry (emission, incidence and phase angles) and also the instrumental properties as the response function and resolution, since our measured spectrum consist actually in the convolution of the radiance with the instrumental function.

We need to take into account all these factors when working to model the atmospheres and the radiance spectra emerging from it.

We have illustrated (in chapter 4) methods and models we used and built with the aim of computing synthetic spectra, which are essential for comparison with the data produced from the instruments and which occupied an essential and demanding part of this study.

We have described the *analytic techniques* for the resolution of the radiative transfer equation, discussing not only the basic background but also the practical choices made to solve the various physical equations; the main mathematical equations required for the retrieval of atmospheric state observed by the instruments were also introduced.

Afterwards we presented the specific methods and results for Venus (chapter 5), including a description of the first approach we had on

modelling the Venus atmosphere due to the importance the methodology development had in this work for the achievements of our tasks; we described then the specific task in the investigation of this planet, i.e.: the water content and its variation in the mesosphere, just above the thick Venusian clouds of sulphuric acid. After showing the atmospheric model developed to solve the RT equation, we explained the retrieval methods which we implemented to analyse the atmospheric quantities.

This last topic has been very interesting and instructive since I had to completely create the code which was used for the automatic and extensive retrieval and analysis of the Venusian cloud top altitude (to determine the correct atmospheric pressure and optical path) simultaneously to the retrieval of the water vapour above the clouds, with all this performed on individual spectra and for all the available data. Results obtained with this method were then interpreted, validated and a formal inverse method to quantify the errors was implemented too.

We have described (chapter 6) both the methods and results obtained for Mars, with the task of investigating the CO<sub>2</sub> isotopomers ratio in the atmosphere and the content of carbon monoxide, important tracers of atmospheric physical and dynamical phenomena.

This last part describes more briefly the model developed to simulate the Martian spectrum and the methods to retrieve the physical quantities - since the retrieval procedure are similar (despite the model changes completely) to the ones used to study Venus atmosphere - to quickly arrive to the presentation of the results.

## Results

The ***water vapor abundance*** in the *mesosphere of Venus* has been already measured in a number of ground-based and spaceborn experiments. Various experiments gave approximately the same values from several ppm to a bit more than 10 ppm. An intriguing exception was the strong local enhancement up to  $10^2$  ppm soon after the subsolar point in the equatorial region observed by the Pioneer Venus OIR (Schoefield et al., 1982; Irwin et al., 1997; Koukouli et al., 2005). Thus our present study had two main goals: to measure the water vapor abundance at the cloud tops with high spatial resolution, and to search for the wet spots observed by the Pioneer Venus. As a byproduct we measured the cloud top altitude.

The Venus Express and VIRTIS observation strategy was particularly favorable for measurements at low latitudes around noon. Here the water vapor abundance near cloud top level at  $2.5 \mu\text{m}$  was found to be  $6 \pm 2$  ppm. Our best horizontal spatial resolution was about 10 km on the cloud “surface”, giving for the first time the chance with our high spatial resolution to measure local variations.

Pixel-to pixel variations were within 20% and do not exceed random measurement error. Thus we did not observe any anomalously wet regions reported by the Pioneer Venus OIR experiment team. To be precise we have to note that the cloud top region in the far IR is located lower by several kilometers than that at  $2.5 \mu\text{m}$ , and therefore we were sensitive to a higher level of atmosphere. The level of maximum sensitivity to the variations of water vapor is equal to 68 km, the corresponding cloud top altitude at  $1.5 \mu\text{m}$  being equal to  $75 \pm 1$  km.

We observed an increase of water vapor abundance up to 20 ppm near both morning and evening terminator. However, the result is highly sensitive to the absolute precision of the continuum level calibration, since

in this region the intensity of outgoing radiation is low due to high incidence solar angle. With the instrumental uncertainties related to the removal of the dark current and absolute calibration of the VIRTIS-H spectra, a systematic bias is possible. Thus this result needs additional confirmation.

The future attempts should be devoted to the improvements of spectral and radiometric calibration of the VIRTIS-H & M instruments to get rid of the possible systematic biases related to calibration uncertainties and to increase the data amount suitable for studies of minor species. A next step would be a complex high spatial resolution study of water vapor abundance and its correlation with cloud properties, UV absorber, and abundances of other minor species.

Results show a **CO mixing ratio** with an average value of about *800 ppm* from a first analyzed dataset observations acquired in a latitude range of approximately  $(- 60) \div (+ 60)$  degrees and in a solar longitude range which encompass the summer and the beginning of autumn in the northern hemisphere, therefore winter in the southern one (Ls range:  $90^\circ - 200^\circ$ ). Higher average values of about *900 ppm* are found in the second dataset which comprises observations at the end of winter and beginning of spring in the north hemisphere (Ls range:  $330^\circ - 95^\circ$ ).

Since the two datasets differ in the atmospheric model (used temperature-pressure profile), absolute values of CO atmospheric content may depend on the model. For this reason besides reporting both results of absolute CO content values, which anyway are comparable within the computed errors, we particularly stress the observed variability and trends.

From the analysis of carbon monoxide in Martian atmosphere it appears a variability of the CO content at different atmospheric conditions (25 % for a first dataset, 35% for a second), however not so strong in percentage as resulted from other studies (e.g. Billebaud et al. – 1998, which attributed to the range of CO variability values from 0 to 100%).

We have found an independence of the mixing ratio from planet altimetry in agreement with a uniform mixing ratio along the atmospheric column.

In fact the eddy diffusion coefficient is  $K \approx 10^6 \text{ cm}^2 \text{ s}^{-1}$  in Mars' troposphere [Korablev et al., 1993], and the vertical mixing time  $H^2/K$  is two weeks ( $H$  is the scale height). Being this mixing time much shorter than CO lifetime, carbon monoxide should be vertically well mixed.

Our results confirm this observation; we however stress that we did not yet study observations in proximity of great volcanoes, where mixing ratio could possibly vary in case of founding outgassing processes. Due to the PFS high spatial resolution, as soon as calibration over high elevated Martian features will be improved, the study of carbon monoxide over a higher altitude range will give further clarifications on previous results indicating altitude's dependence (Rosenqvist et al., 1992)

We observe an absence of strong diurnal CO variability in agreements with models predicting the CO lifetime to be equal to 6 years, assessing for diurnal variations a very low range.

The however observed low variations with local time suggest a weak enhance on midday, where the Sun is high and the photolysis rate is more efficient.

There is an evident correlation with the Sun incidence angle. From both analyzed dataset we can observe a decrease of CO mixing ratio increasing the incidence angle.

This trend may be correlated with the energy present in the atmosphere depending on solar illumination, which could enhance CO production when the incident solar beams density is higher (small angles).

The main observed correlation is however with latitudes closer to the subsolar point in a given season. Mars Express satellite elliptical and not Sun synchronous orbits, bring to a not unimportant bias for observations in Ls (season), Latitude and Local Time, which can affect the dataset and consequently the interpretation of the variability.

Due to the mentioned bias we can mainly attribute the CO variations with incidence angle to the latitudinal dependence on the subsolar point. The observed trend of mixing ratio versus Latitude presents a maximum around latitudes in which the Sun rays meet the surface with the minimum angle in the considered season. We can observe a maximum at

low latitudes in the southern hemisphere winter, which could be correlated with CO<sub>2</sub> decreasing due to intense condensation of CO<sub>2</sub> on the south polar cap.

In this case, the actual CO column density does not vary, but what changes is the mixing ratio which is related to the total atmosphere (almost totally made of CO<sub>2</sub> in Martian case). In fact condensation and sublimation of CO<sub>2</sub> result in enhancement and depletion, respectively, in the mixing ratios of incondensable species like CO.

**Summarizing** results on carbon monoxide, we find an increase in the Southern winter and at the latitudes of subsolar point where solar flux is higher and therefore CO<sub>2</sub> photolysis is more efficient. In general seasonal features are more pronounced at equatorial latitudes and meridian profiles of the mixing ratio (for individual orbits) present seasonal shift of the maximum versus the sub solar point. We find an enhancement also at low incidence angles and at midday local time.

Results on **CO<sub>2</sub> isotopes** consisted primarily in the identification of all the CO<sub>2</sub> isotopes in PFS data (LWC), with an instrumental spectral resolution never available before.

The retrieved abundances of the main isotopes outside the center of the main CO<sub>2</sub> absorption band at 667 cm<sup>-1</sup> (LWC) resulted to be close to terrestrial values and are reported and are presented in Table 1 in the form of isotopic ratios.

| Isotopic ratio                         |
|--|
| $^{12}\text{C}/^{13}\text{C} = 82.4$   |
| $^{16}\text{O}/^{18}\text{O} = 479.5$  |
| $^{16}\text{O}/^{17}\text{O} = 2437.9$ |

**Table 1. Results expressed as isotopic ratios.**

In these observations there are some differences between the observed abundance of 628 isotope (the most important CO<sub>2</sub> isotopomer - together

with the 627- which gives indication of the CO<sub>2</sub> oxygen isotope's content) at different wavelengths: at 576 cm<sup>-1</sup> is similar to the terrestrial value, while in the bottom of the band (663 cm<sup>-1</sup>) it is found to be a little higher. From the last spectral range even the 627 isotope seems to have much higher abundance than terrestrial value.

The retrieved abundance of 628 in the SWC (the band at 2614 cm<sup>-1</sup>) is about 0.8 times the terrestrial value. In general, the quantity retrieved from this spectral range pertains to the atmospheric mass of the first scale height of the atmosphere.

For this reason, a realistic interpretation of the results of this study can be a variability of mixing ratio of the oxygen isotopes with the altitude. We pass from a lower value obtained in the first layers of the atmosphere (from SWC), less than terrestrial value, to values similar to the terrestrial one from the ranges of the band in LWC pertaining an altitude around 20-30 Km, to higher values in the center of the band which probes an altitude around 30-50 Km. This decreasing trend with altitude could be explained by the escape of lighter isotopes from the top of the atmosphere, with enrichment of the heavier ones going closer to the surface. Anyway some further considerations should be developed.

The column CO<sub>2</sub> abundance in the Martian atmosphere is  $2 \times 10^{23}$  cm<sup>-2</sup>, the column photolysis rate is  $10^{12}$  cm<sup>-2</sup> s<sup>-1</sup>. Their ratio is the mean CO<sub>2</sub> lifetime relative to chemical processes which is 6000 years. Local lifetimes may be shorter or longer; for example, the CO<sub>2</sub> lifetime is 30 years at 80 km. Mixing time is  $H^2/K$  where H is the scale height and K is eddy diffusion. Mixing time varies from two weeks in the lower atmosphere to 15 hours at 80 km. Mixing time is very much shorter than the chemical lifetime of CO<sub>2</sub>; therefore all CO<sub>2</sub> isotopes should be well mixed in the atmosphere and the CO<sub>2</sub> isotope ratios do not depend on height up to a homopause at 120-135 km where the diffusive separation begins.

The 628 abundances obtained in this study from various bands are  $1.01 \pm 0.40$ ,  $1.20 \pm 0.50$ ,  $1.10 \pm 0.46$ , and  $0.8 \pm 0.20$ . The uncertainty intervals for all values are well overlapping, and we can calculate a weighted-mean value which is equal to  $0.91 \pm 0.18$ .

The weighted-mean abundances of the other isotopes are  $1.10 \pm 0.35$  for 636 and  $1.21 \pm 0.63$  for 627. The abundance of 627 is equal to square root of 628 for mass-dependent fractionation, that is,  $0.95 \pm 0.42$ . The abundance of 638 is equal to product of 636 and 628, that is,  $1.00 \pm 0.38$ . The former agrees with the measured value within their uncertainties, the latter perfectly fits the measured value.

For the above reasons, without further information, we can conclude that retrieval of CO<sub>2</sub> isotopic abundance performed from the short and long wavelength channel of PFS spectrometer suggest results close to “terrestrial one” with a weighted-mean value which is equal to  $0.91 \pm 0.18$ .

# **1 Foreword**

This work presents part of the efforts which I carried out in the Interplanetary Space Physics Institute (IFSI) and in the Cosmic Physics and Space Astrophysics Institute (IASF) of the Italian National Institute for Astrophysics (INAF) in the analysis of the data from the *Planetary Fourier Spectrometer* (PFS) experiment, included in the scientific payload of the ESA *Mars Express* (MEX) mission to Mars and the *Visual and Infrared Thermal Imaging Spectrometer* (VIRTIS) experiment, included in the ESA *Venus Express* (VEX) mission to Venus.

Information obtained from the study of terrestrial planets are fundamental for the understanding of Earth past and future climate evolution, since other terrestrial planets represent in some sense a possible stage – or alternative path - of the Earth's history.

The study of our closest neighbors, Mars and Venus, also gives important information for the search for planets in other planetary systems - which is one of the mayor current interest of the scientific community - in order to provide a paradigm about planets orbiting around other stars, and which may possibly host life.

Mars and Venus pertain to the planets with a “CO<sub>2</sub> dominated” atmosphere and since they experiment different atmospheric conditions they provide an unique chance to obtain complete information on this atmospheric type at different evolutionary stages (in Chapter 2 a brief description of the two planet atmospheres is presented).

In particular, using the data acquired by the two ESA spacecraft we investigated the atmospheric composition of the two planets in order to give a contribute to the understanding of the main properties of Mars and Venus, since the composition of the atmosphere on global and regional scales influences the planetary climate and the evolution and the retrieved

information can therefore be used to trace the atmospheric circulation, give constraints to the atmospheric stability and its long term evolution.

Efforts have focused on topics still affected by large uncertainties in our understanding of atmospheric constituents other than carbon dioxide, in order to provide also firm constraints for future studies on atmospheric aeronomy and interaction with surface phenomena such as volcanism and related outgassing.

Namely, for this task we had the first chance to perform an *intensive* study of *water vapor* on *Venus* (previous studies regarded just limited local time or locations in the planet), since the role of water as a trace constituent is key to illuminating the present-day Venus atmospheric energy balance, particularly with respect to the global cloud layers which permanently envelop the planet.

On *Mars* we investigated the *stable isotope record* contained within *carbon and oxygen (CO<sub>2</sub> isotopes)*, to provide important constraints regarding the origin of the planet and its relationship to the Earth. Stable oxygen isotopes are particularly useful in the study of Mars because oxygen is abundantly present in both the Martian atmosphere and lithosphere, in particular in the main atmospheric constituent, carbon dioxide. We also investigated *carbon monoxide (CO) on Mars*, since it represents the main product of the CO<sub>2</sub> photolysis and therefore is directly related to the problem of the stability of the Martian CO<sub>2</sub> atmosphere.

*Infrared spectroscopy* and *present-day high resolution spectrometers* have demonstrated to be one of the most *powerful remote sensing tools* in the context of planetary observation, for atmospheric as well as for surface studies: they give together a remote access to most of the important information carried by the radiation which directly interacted with the planet.

Spectroscopic signatures of gaseous atmospheric components can be found over the whole range of the electromagnetic spectrum; nevertheless the important property of the infrared spectral range ( $\lambda = [1-100] \mu\text{m}$ ) is to

cover the main roto-vibrational bands of several molecules being present in planetary atmospheres, so that at the present time, most of our knowledge regarding planetary atmospheric composition and structure has been achieved by remote sensing spectroscopy.

Since the IR radiation emerging from a planetary atmosphere it is described from the Radiative Transfer equation, we presented (Chapter 3) some basic principles of the theory of radiative Transfer in the appropriate form for planetary atmospheres.

Once we have available the infrared spectra of Mars and Venus acquired by PFS and VIRTIS, we need to produce models which properly describe (simulate) what the instrument measures, in order to retrieve from the spectra the required quantities, namely composition.

Many factors contribute to the formation of a spectrum emerging from a planet: the chemical and physical state of the surface, the atmospheric composition and thermal structure, the aerosols content and their nature, the observational and illumination's geometry (emission, incidence and phase angles) and also the instrument's properties as the response function and resolution, since our measured spectrum consist actually in the convolution of the radiance with the instrumental function.

We need to take into account all these factors when working to model the atmospheres and the radiance spectra emerging from it.

We have illustrated (in chapter 4) methods and models we used and built with the aim of computing synthetic spectra, which are essential for comparison with the data produced from the instruments and which occupied an essential and demanding part of this study.

We have described the *analytic techniques* for the resolution of the radiative transfer equation, discussing not only the basic background but also the practical choices made to solve the various physical equations; the main mathematical equations required for the retrieval of atmospheric state observed by the instruments were also introduced.

Afterwards we presented the specific methods and results for Venus (chapter 5), including a description of the first approach we had on

modelling the Venus atmosphere due to the importance the methodology development had in this work for the achievements of our tasks; we described then the specific task in the investigation of this planet, i.e.: the water content and its variation in the mesosphere, just above the thick Venusian clouds of sulphuric acid. After showing the atmospheric model developed to solve the RT equation, we explained the retrieval methods which we implemented to analyse the atmospheric quantities.

This last topic has been very interesting and instructive since I had to completely create the code which was used for the automatic and extensive retrieval and analysis of the Venusian cloud top altitude (to determine the correct atmospheric pressure and optical path) simultaneously to the retrieval of the water vapour above the clouds, with all this performed on individual spectra and for all the available data. Results obtained with this method were then interpreted, validated and a formal inverse method to quantify the errors was implemented too.

We described (chapter 6) both the methods and results obtained for Mars, with the task of investigating the CO<sub>2</sub> isotopomers ratio in the atmosphere and the content of carbon monoxide, important tracers of atmospheric physical and dynamical phenomena.

This last part describes more briefly the model developed to simulate the Martian spectrum and the methods to retrieve the physical quantities - since the retrieval procedure are similar (despite the model changes completely) to the ones used to study Venus atmosphere - to quickly arrive to the presentation of the results.

## **2 Task: terrestrial planets' atmospheres**

The bodies of the Solar System gradually formed and reached their current state as we observe today. These bodies started their evolution in different initial conditions in terms of composition and mass, solar distance and other parameters. Therefore it is important to follow and compare the evolutionary path of these individual objects.

Information obtained from the study of terrestrial planets are fundamental for the understanding of Earth past and future climate evolution, since other terrestrial planets represent in some sense a possible stage – or alternative path - of the Earth's history.

The study of our closest neighbors, Mars and Venus, also gives important information for the search for planets in other planetary systems - which is one of the mayor current interest of the scientific community - in order to provide a paradigm about planets orbiting around other stars, and which may possibly host life.

For example, observations of the cloud-covered “sister planet” Venus become more and more important since Venus's evolution and geology are very similar to Earth's; and a deeper understanding of Venus's geophysical and atmospheric characteristics could help us in the quest for earth-like planets. Also Venus's notorious “runaway greenhouse effect” may offer lessons for limiting our potentially interference with our own planet's climate, to ensure a long term perspective for life on Earth. Eventually, the study of planets as Venus and Mars can aid our understanding of terrestrial and extra-solar planet evolution, surface and interior processes, atmospheric circulation, chemistry, and aeronomy.

In the following paragraphs a short introduction to Venus and Mars is given, discussing the major basic facts about the two planets, their general characteristics and their atmosphere. Extensive information can be found in *Venus, 1983*, *Venus II, 1997* and *Mars, 1993*.

## **2.1 Venus**

Venus is Earth's closest neighbor, the second planet from the Sun. Considered Earth's twin for many decades, Venus must have followed a very different evolutionary path since it exhibits almost no Earth-like characteristic other than a similar mass and radius. Its small rotation axis obliquity and orbital eccentricity ensures that no seasons affect its rocky surface where the temperatures rise to 500°C with a pressure 90 times the Earth's one. Venus atmosphere is composed almost solely of carbon dioxide and is enshrouded by sulphuric acid clouds that contribute greatly to the runaway greenhouse effect responsible for the high temperatures on its surface. These clouds also do not allow a direct view of the surface in the visible domain and actually - until the first UV telescope started looking at the planet - the complicated patterns created by the cloud motions were thought to belong to the planetary surface.

Venus belongs to the family of terrestrial planets, alongside Earth, Mars and Mercury. Known since ancient times due to its brilliant color, brightness and unusual appearances in the sky, Venus is a planet similar to the Earth in mass and radius but has no moon and no magnetic field shielding it from cosmic rays and solar winds. Venus' obliquity is only 2.6°, compared to ~24° of the Earth and Mars and orbits in the prograde direction about the Sun in a nearly circular orbit every 224.7 earth days. Its rotation relative to the stars, the sidereal motion, is retrograde every 243.01 earth days. If the Sun could be seen from the surface of the planet, it would make roughly one complete circuit of the Venusian sky in half a Venus year. Hence, the length of the Venus day, also known as the solar day, is 116.75 Earth days.

Since Venus is closer to the Sun than the Earth, the planet shows phases when viewed with a telescope: sometimes it appears as a crescent, others half-illuminated and others nearly full. Galileo Galilei's (1564-1642) astounding observation of this phenomenon in late 1610 was the first

irrevocable piece of important evidence in favor of Copernicus's heliocentric theory of the solar system. As an inferior planet Venus revolves around the Sun faster than the Earth; and as the two planets are moving in the same direction around the Sun, Venus appears for a few months in the early morning, some hours before sunrise, then disappears only to be seen as a bright moon-like object emerging after sunset for a further few months before disappearing again.

The main orbital and solid body characteristics of Venus and Earth are given in Table 2 for easy comparison, while in Table 3 the Venusian observational parameters are presented.

Venus was explored by a fleet of American and Soviet spacecraft starting with Mariner 2 in 1962, the first successful spacecraft to fly-by Venus, up to the Magellan orbiter in 1990, which produced global detailed maps of Venus' surface using radar mapping, altimetry and radiometry techniques with a resolution of ~100 m. In between, more than twenty missions have explored Venus, including the Soviet Venera 7 in 1970 which was the first spacecraft to land on another planet, Venera 9 in 1975 which returned the first photographs of the surface and the American Pioneer Venus Orbiter in 1978 which carried several atmospheric environment experiments and four entry probes. Magellan's observations further revealed that the surface of Venus is mostly covered by volcanic materials. Volcanic surface features, such as vast lava plains, fields of small lava domes and large volcanoes are common. A color-coded composite of these observations is shown in Figure 1. The planetary elevation is calculated over the mean radius of the planet; 6050 km. Venus has two major continents, Aphrodite Terra and Ishtar Terra, which occupy only a few percent of the total surface area. Aphrodite Terra, seen in Figure 1, is a long, narrow area which stretches over 150° in longitude and contains a few peaks higher than 8 km. Ishtar Terra contains the highest elevation region, Maxwell Montes, around 65°K which rises to altitudes of 10.5 km above mean planetary radius. The remainder of the surface of Venus is covered mostly by volcanic materials.

|  | Venus   | Earth     | (Venus/Earth) |
|--|---------|-----------|---------------|
| <i>Bulk parameters</i>                         |         |           |               |
| Mass (10 <sup>24</sup> kg)                     | 4.8685  | 5.9736    | 0.815         |
| Volume (10 <sup>10</sup> km <sup>3</sup> )     | 92.843  | 108.321   | 0.857         |
| Equatorial radius (km)                         | 6051.8  | 6378.1    | 0.949         |
| Polar radius (km)                              | 6051.8  | 6356.8    | 0.952         |
| Volumetric mean radius (km)                    | 6051.8  | 6371.0    | 0.950         |
| Ellipticity (polar flattening)                 | 0.000   | 0.00335   | 0.0           |
| Mean density (kg/m <sup>3</sup> )              | 5243    | 5515      | 0.951         |
| Surface gravity at equator (m/s <sup>2</sup> ) | 8.87    | 9.80      | 0.905         |
| Escape velocity (km/s)                         | 10.36   | 11.19     | 0.926         |
| Bond albedo                                    | 0.76    | 0.30      | 2.53          |
| Visual geometric albedo                        | 0.65    | 0.367     | 1.77          |
| Solar irradiance (W/m <sup>2</sup> )           | 2613.9  | 1367.6    | 1.911         |
| Equivalent blackbody temperature (K)           | 231.7   | 254.3     | 0.911         |
| Topographic range (km)                         | 15      | 20        | 0.750         |
| <i>Orbital parameters</i>                      |         |           |               |
| Semi major axis (10 <sup>6</sup> km)           | 108.21  | 149.60    | 0.723         |
| Sidereal orbit period (days)                   | 224.701 | 365.256   | 0.615         |
| Tropical orbit period (days)                   | 224.695 | 365.242   | 0.615         |
| Perihelion (10 <sup>6</sup> km)                | 107.48  | 147.09    | 0.731         |
| Aphelion (10 <sup>6</sup> km)                  | 108.94  | 152.10    | 0.716         |
| Synodic period (days)                          | 583.92  | —         | —             |
| Mean orbital velocity (km/s)                   | 35.02   | 29.78     | 1.176         |
| Max. orbital velocity(km/s)                    | 35.26   | 30.29     | 1.164         |
| Min. orbital velocity (km/s)                   | 34.79   | 29.29     | 1.188         |
| Orbit inclination (deg.)                       | 3.39    | 0.00      | —             |
| Orbit eccentricity                             | 0.0067  | 0.0167    | 0.401         |
| Sidereal rotation period (h)                   | 5832.   | 5 23.9345 | 243.686       |
| Length of day (h)                              | 2802.0  | 24.0000   | 116.750       |
| Obliquity (deg.)                               | 177.36  | 23.45     | (0.113)       |

**Table 2. Venus/Earth comparison (after Williams, 2005)**

|   |       |
|---|-------|
| <i>Distance from Earth</i>                                |       |
| Minimum (106 km)  | 38.2  |
| Maximum (106 km)  | 261.0 |
| Apparent diameter from Earth                              |       |
| Maximum (seconds of arc)                                  | 66.0  |
| Minimum (seconds of arc)                                  | 9.7   |
| <i>Mean values at inferior conjunction<br/>with Earth</i> |       |
| Distance from Earth (106 km)                              | 41.44 |
| Apparent diameter (seconds of arc)                        | 60.2  |

**Table 3. Observational parameters.**

Although Venus has a dense atmosphere, the surface shows no evidence of substantial wind erosion, and there has been only slight evidence of limited wind transport of dust.

On Venus we cannot find evidence of plate tectonics (trenches, ridges), as the absence of water in the surface, which evaporated and went lost with the increase of greenhouse effect, did not help the subduction of the crust; this on the contrary induced an increase of heat which produced diffuse volcanism. Moreover on the Venus surface there is no clear distinction between basaltic (ocean) crust from continental granitic crations, as observed on our planet. The absence of craters on Venus is an indication of a young surface, which is dated no more than 1 Gy.



**Figure 1. Color-coded topographic map of Venus from Magellan radar observations. Aphrodite Terra appears as the bright feature along the equator with an area the size of South America (NASA).**

### **2.1.1 The Atmosphere of Venus**

On June 6, 1761, at the University Observatory of Saint Petersburg, Russia, Mikhail Lomonosov (1711 -1765) observed a transit of Venus: a rare passage of the planet directly in front of the Sun. He was able to get a fairly good measurement of Venus' diameter and found that it was very similar to the Earth's. But the edge of Venus' disk, instead of appearing sharp, as he had expected, was fuzzy and indistinct, and a grey halo surrounded the planet. He had discovered the atmosphere of Venus and in his own words, he had found evidence of “an atmosphere equal to, if not greater, than that which envelops our Earthly sphere”.

The current atmospheric composition of Venus is dominated by CO<sub>2</sub> (96.5%), with a few percent of N<sub>2</sub> (3.5%) and a number of trace gases like H<sub>2</sub>O, CO and SO<sub>2</sub> in the parts per million scale. This composition resembles the atmosphere of Mars which is also made of CO<sub>2</sub> and N<sub>2</sub> and is instead very different from the terrestrial atmosphere where N<sub>2</sub> and O<sub>2</sub> play the leading part. The composition of the Venus' atmospheres is tabulated in Table 4.

The high surface temperature of Venus (750 K) is significantly above its effective temperature, that is, the equilibrium temperature expected from its heliocentric distance. Indeed, the surface and the lower atmosphere of Venus have been heated by a runaway greenhouse effect, mostly to be ascribed to the large amounts of gaseous CO<sub>2</sub> and H<sub>2</sub>O which were most likely present in the primordial atmosphere and, in lesser part, to its cloud coverage.

|  |                         |
|--|-------------------------|
| <u>Atmosphere</u>  |                         |
| Surface pressure   | 92 bar                  |
| Surface density  | 65 kg/m <sup>3</sup>    |
| Scale height   | 15.9km                  |
| Total mass of atmosphere   | 4.8_10 <sup>20</sup> kg |
| Average temperature  | 737K (464 1C)           |
| Diurnal temperature range  | 0                       |
| Wind speeds  | 0.3–1.0 m/s (surface)   |
| Mean molecular weight  | 43.45 g/mol             |
| <u>Atmospheric composition</u><br><u>(near surface, by volume)</u> |                         |
| Major Carbon dioxide (CO <sub>2</sub> )                            | 96.5%                   |
| Nitrogen (N <sub>2</sub> )   | 3.5%                    |
| Minor (ppm) Sulphur dioxide (SO <sub>2</sub> )                     | 150                     |
| Argon (Ar)   | 70                      |
| Water (H <sub>2</sub> O)   | 20                      |
| Carbon monoxide (CO)   | 17                      |
| Helium (He)  | 12                      |
| Neon (Ne)  | 7                       |

**Table 4. Atmospheric properties and composition**

Venus is covered by a thick cloud deck of sulfuric acid H<sub>2</sub>SO<sub>4</sub>, at an altitude of 40–70 km, which prevents the visible observation of the surface (see paragraph 2.1.2).

The atmosphere of Venus may be divided into three natural regions, a troposphere (surface to 60 km), a mesosphere (60 to 90 km) and a thermosphere (above 90 km). On Earth we find a troposphere (surface to 12 km), a stratosphere (12 to 45 km), mesosphere (45 to 85 km) and, as on Venus, a thermosphere (above 85 km). Vertical profiles of temperatures on Venus and Earth as a function of pressure at 30° latitude, as measured by the Pioneer Venus OIR and Nimbus 7 spacecraft respectively, are presented in Figure 2 on the left. Throughout the troposphere and mesosphere the temperature decreases with height, from around 740 K to 100 K on Venus and from 280 K to 210 K on Earth. No

temperature inversions can be seen since UV absorbing ozone that cause the Earth's stratosphere do not exist in the Venus' CO<sub>2</sub> dominated atmosphere. On Venus' dayside the temperature above 85-90 km rises to an exospheric value of around 300 K due to solar EUV absorption and therefore behaves like the thermosphere on Earth, where temperatures rise from ~ 180 K to ~ 1000 K. The nightside upper atmosphere on Venus differs from that on Earth because Venus' slow rotation period causes solar heating to be absent for far too long to maintain the high temperatures found on the dayside. Night side temperatures on Venus' thermosphere above 85-90 km in fact do not rise above 100 K, justifying the name of "cryosphere" ("sphere of cold" in Greek). The Venus temperature structure above the clouds and the thermosphere/cryosphere region is shown in Figure 2 on the right, as observed by three Pioneer probes and Venera 11 and 12.

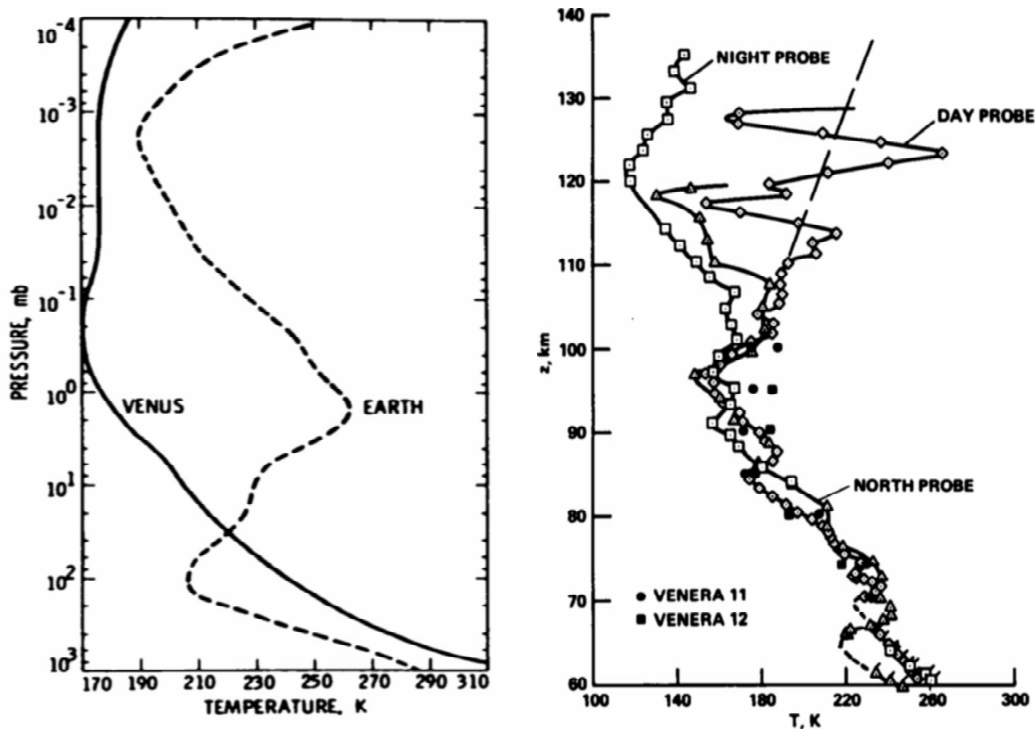


Figure 2. Left. Vertical profiles of temperature vs. pressure at 30°N latitude, as measured on Venus by PV OIR and on Earth by Nimbus 7. Adapted from Houghton et al. (1984). Right. Temperatures above the main cloud regions derived from three Pioneer probes and Venera 11 and 12. Adapted from Seiff (1983).

Due to its slow rotation rate and its obliquity, the troposphere of Venus is almost isothermal in equatorial and middle latitudes. Near the poles of Venus, starting at 60° N, a long-lived dramatic instability occurs, known as the “polar collar” (or cold collar), which takes the form of a ribbon of very cold air about 10 km deep and 1000 km in radius, centered on the pole and situated at about 64 km of altitude. Inside the polar collar temperatures are about 40 K cooler than outside the feature. Poleward of the inner region of the collar lies at about 65 km the "polar dipole", a feature consisting of two well-defined warm regions circulating rapidly around the pole with a period of 2.7 days.

### **2.1.2 The Sulphuric Acid Clouds of Venus**

On the global scale, Venus’ climate is strongly driven by the most powerful greenhouse effect found in the Solar System. The greenhouse agents sustaining it are water vapour, carbon dioxide and sulphuric acid aerosols.

Surrounding the planet completely and all the time, sulphuric acid clouds have played a key role in the evolution of the planet and its atmosphere. Venus is covered by one global cloud layer whose main constituent is the strong aqueous solution of sulphuric acid, H<sub>2</sub>SO<sub>4</sub> (75 %), which is formed from the photochemical combination of H<sub>2</sub>O and SO<sub>2</sub> near the cloud tops<sup>1</sup>. The cloud layer is very opaque at visible and infrared wavelengths and reflects back ~80 % of the incoming solar radiation, about 10% is absorbed by the atmosphere and only 10% manages to get through it. Only the ~2.5 % of the original sunlight reaches the surface and it appears with an orange color as the blue and violet colors have been

---

<sup>1</sup> For the subsequent part of the thesis the aqueous sulphuric acid solution the Venus clouds are made of will be referred to as the “H<sub>2</sub>SO<sub>4</sub> cloud” for simplicity.

absorbed by the clouds. However, the thermal radiation emitted at infrared wavelengths by the surface gets trapped by the same atmosphere. The result is a 500 °C difference between the surface and cloud-top temperatures.

The main cloud layer of Venus spans from 50 km altitude to an upper boundary near 65 km, with haze layers expanding down to 30 km and upwards to 70 km. Earth-based polarimetry experiments (Hansen and Honevier, 1974) showed that the cloud particles are spherical droplets, with an effective radius of  $\sim 1 \mu\text{m}$ . In these studies the unity cloud optical thickness was found to occur at a pressure of 50 mbars ( $\sim 68 \text{ km}$ ) around  $1 \mu\text{m}$  wavelengths.

Mie scattering theory (Hansen and Travis, 1974) was used to model the optical properties of the Venus cloud. From the precise limits of the observed refractive index, it was confirmed that it is composed of concentrated sulphuric acid droplets containing between 75 % and 90 % of  $\text{H}_2\text{SO}_4$ . The yellow colour of the clouds is attributed to sulphur, whereas it has lately been postulated that the unknown UV-blue absorber that has puzzled scientists since the Pioneer Venus times is disulphur monoxide,  $\text{S}_2\text{O}$  (Na and Esposito. 1997).

Further to their omnipresence, the Venus clouds are orders of magnitude thicker than the terrestrial or Martian ones, blocking the view of the surface to all but radio wavelengths. Water plays a role cloud compositions in all three planets, being the major constituent in Earth's atmosphere, a minor constituent in Mars' atmosphere and locked in the sulphuric acid droplets that mainly compose Venus' clouds. The main production process is chemistry for Venus'  $\text{H}_2\text{SO}_4$  clouds and condensation for Earth's and Mars'  $\text{H}_2\text{O}$  clouds. The variability of Venus' clouds is insignificant and incomparable to the daily variability of the Earth's clouds and the yearly variability of Mars' clouds.

A scheme of Venus's atmosphere is shown in Figure 3.

In terms of a detailed vertical structure of the Venus cloud system, the Cloud Particle Size Spectrometer (LCPS) on board the Pioneer Venus Sounder probe has provided excellent in situ measurements.

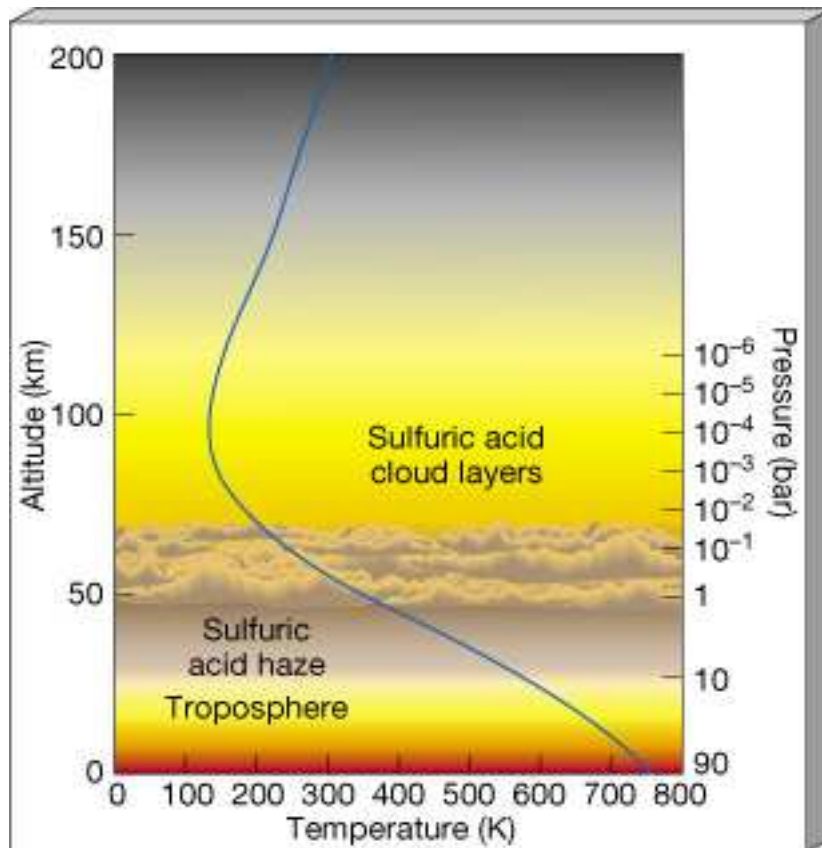


**Figure 3.** The probable structure of Venus's atmosphere showing the main cloud layer and also how temperature (blue line) varies with height. The temperature scale is in K (kelvins) where 273 K = 0°C. [Graphic: NASA].

The actual amount of cloud droplets in the atmosphere is given by the mass loading of the atmosphere: the first 30 km are composed of clear CO<sub>2</sub> air, with the thin haze extending upwards until the altitude where the temperature drops to ~400 K and pressures of ~ 1 bar and the atmosphere is able to sustain H<sub>2</sub>SO<sub>4</sub> droplets. Then, between 44 and 48 km of altitude, a four orders of magnitude increase in the density of the cloud defines the beginning of the main cloud deck which extends upwards to 65 km altitude. Above that altitude, another haze layer spans a further 10 km. Vertical mixing from regions below the main cloud layer enriches it with sulphur dioxide and water. At the region of the cloud top a thin, but highly active photochemically layer exists and is the main production region of the sulphuric acid droplets.

### 2.1.3 Winds on Venus

Unlike the Earth's lower atmosphere, which is mainly driven from bottom boundary by absorption of sunlight at the surface, Venus' atmospheric circulation is largely driven from above by the absorption of sunlight within and above the upper cloud layer. The cloud cover has an important influence on the atmospheric circulation by controlling the amount and distribution of solar energy absorption (Schubert, 1980).

One of the least explained phenomena of atmospheric circulation on Venus is its zonal retrograde super-rotation; the entire atmosphere, above the lowest scale height, extending upwards to >90-100 km, participates in the global super-rotation which was first observed in Earth-based ultraviolet pictures of the planet. The large-scale albedo feature known as the "dark horizontal Y" , visible in Figure 5, was observed to re-appear approximately every 4 Earth days, indicating a zonal rotation of the cloud level atmosphere with equatorial wind speeds of about  $110 \text{ m s}^{-1}$ , which is considerably faster than the rotation speed of the planet at the equator of  $2 \text{ m s}^{-1}$ . This super-rotation is known to occur in the atmospheres of only two solid body planets of our solar system, Venus and Saturn's largest moon, Titan. In the case of Venus the super-rotation is thought to reach the lower thermosphere, up to an altitude of around 100 km. At the cloud altitudes the wind speed and characteristics have been inferred from feature tracking in ultraviolet images of Mariner 10, Venera 9, Pioneer Venus and others. Above the clouds, in the absence of diagnostic features, analysis of Doppler shifts of selected molecular lines has provided further wind information. In Figure 4, averaged retrograde zonal wind velocities are shown as measured by experiments on board the Mariner 10 and Pioneer Venus satellites. The wind is maximum over the equator with speeds of  $\sim 100 \text{ m s}^{-1}$  and drops off evenly towards the poles. The solid curve represents the predicted zonal wind calculated for solid body retrograde rotation.

At the present date, the only large scale model describing the circulation of Venus' atmosphere is the Venus Thermosphere General Circulation Model (VTGCM) (Bougher et al., 1988). Further modeling is being prohibited by the inability to identify a suitable physical mechanism that explains the cloud-top super-rotation.

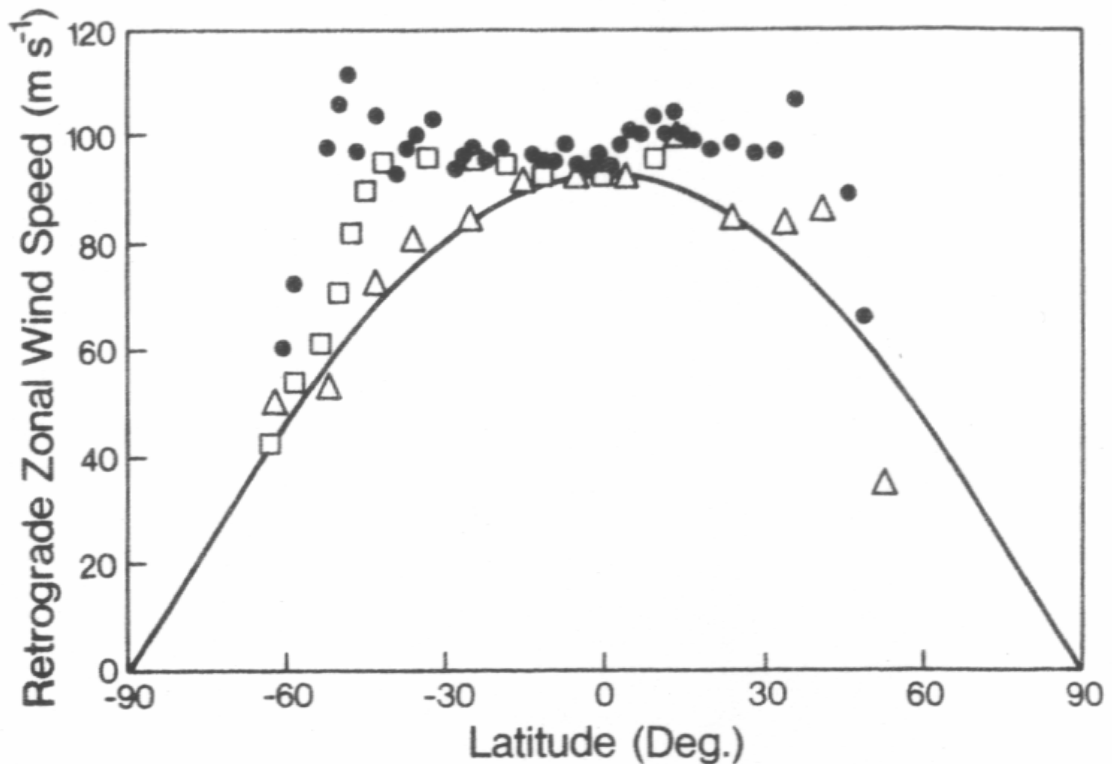


Figure 4. Longitudinally averaged retrograde zonal wind velocities vs latitude, inferred from tracking of small-scale cloud features from ultraviolet images of Venus. Triangles, Pioneer Venus, by Rossow et al. (1980); circles, Mariner 10, by Limaye and Suomi (1981); squares, Mariner 10, by Travis (1978). The solid curve is the zonal wind velocity calculated for solid body retrograde rotation with equatorial speed of  $92.4 \text{ m s}^{-1}$ . Adapted from Schubert (1980).



**Figure 5. Pioneer Venus image of the planet.**

## **2.2 Mars**

In the last years Mars has been the target of most of the planetary missions. The huge amount of data collected by the spacecrafts has displayed a rich and diverse geological history, as well as many unsolved puzzles about the evolution of the planet and its present condition.

Although Mars is smaller than Earth (its radius is just a little over half of Earth's) it hosts a variety of impressive features: roughly along the equator there is Valles Marineris, a fault in the Martian crust 4000 km long (about a fifth of the distance around the whole of Mars), up to 600 km wide and 7 km deep; there is the Hellas Basin in the southern hemisphere, which is an enormous impact crater, 2300 km in diameter and more than 9 km deep; there is the highest volcano in the solar system, Olympus Mons which stands at 26 km above the surrounding plain; moreover Olympus Mons lies at the western edge of another impressive feature, the Tharsis region, which is a 10 km high, 4000 km wide bulge in the Martian surface. But probably the most intriguing issue about this planet is related to the role of water on its surface and the connected implications. Several of geomorphologic features (evidence of catastrophic floods, network of channels, layered rocks) let suppose that in the Martian past history water should have been stable on the planet surface. This implies that Mars was warmer and with a denser atmosphere in the past compared to the present conditions, making reasonable the exciting hypothesis that life could have developed in such kind of environment. At the moment the values of temperature and pressure at the surface are well below the triple point of H<sub>2</sub>O, making impossible to have stable liquid water on the ground. Anyway the hypothesis that somewhere on the planet (under the surface or near some hydrothermal sources, if any) life could have developed and still withstands, is not completely ruled out.

Other important characteristics of Mars are the presence of two polar caps that act as cold trap for CO<sub>2</sub> and H<sub>2</sub>O, their seasonal regression and condensation, a high (and highly variable) content of thin dust spread all over the planet that gives rise to several atmospheric phenomena such as dust storms (also at planetary global scale) and dust devils. Water vapor and water ice clouds are also present in the atmosphere.

The following pages provide a very short outline of our present knowledge of Mars, limited to the subjects more directly interested by IR spectroscopy investigation. An excellent review and historical introduction can be found in the volume *Mars* (edited by Kieffer et al., 1992) and reference therein. More recent results are mentioned explicitly along the text.

### **2.2.1 The Martian atmosphere: gaseous components**

Table 5 lists the gases composing the Martian atmosphere, as measured by space probes.

The atmosphere is very thin: a reference, annual averaged, value for surface pressure can be set at 6 mbar. This value is extremely variable, due not only to the great topographic differences observed on the surface, but also because the temperature, during polar night, may fall below the condensation temperature of CO<sub>2</sub>, determining the frosting of a significant fraction of atmosphere's mass. This annual bimodal cycle was well observed by Viking landers (Figure 6).

The study of isotopic and elemental ratios has demonstrated that Mars experienced a substantial erosion of its primitive atmosphere, formed after the end of *T Tauri* phase of Sun's life cycle. Different values have been proposed for the surface pressure of early Mars, but the orders of magnitude agree around one bar. Erosion affected mainly the carbon dioxide component, impact by meteoroids and thermal escape

representing the leading phenomena. Several authors pointed out the role of carbon inclusion in carbonates in a water-rich environment. Up to now, anyway, carbonates have not been detected on Mars and therefore this effect, even if present, should be of minor importance.

| Constituent                           | Volume mixing ratio |
|---------------------------------------|---------------------|
| CO <sub>2</sub>                       | 0.9532              |
| N <sub>2</sub>                        | 0.027               |
| Noble gases (mainly <sup>40</sup> Ar) | 0.016               |
| O <sub>2</sub>                        | 0.0013              |
| CO                                    | 0.0007              |
| H <sub>2</sub> O                      | 0.0003*             |
| O <sub>3</sub>                        | 0.2-0.04 ppm*       |

**Table 5. Average composition of Martian atmosphere. Confirmed constituents only. \*:average value, variable in time and space.**

CO and O<sub>2</sub> are both derived from CO<sub>2</sub>. The thinness of the atmosphere and the (apparent) lack of a substantial ozonosphere allows to UV Solar photons to penetrate until the surface.

The photo-dissociation



occurs therefore in the whole height of the atmosphere. The inverse reaction has a very low probability. In very simple conditions therefore, an enrichment of CO and O<sub>2</sub> would be therefore expected.

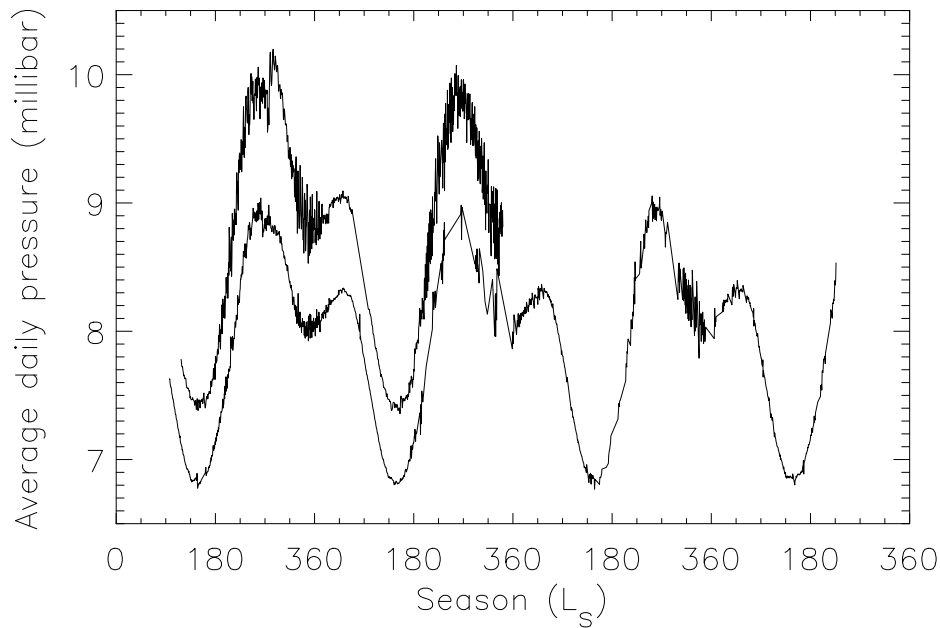


**Figure 6. Average daily pressure observed by Viking landers.  $L_s$  is the aerocentric longitude of the Sun, being 0 at the Northern spring equinox. This parameter is usually adopted to define the season. Upper curve: Viking lander 2; lower curve: Viking lander 1. Data from Tillman, J. E., 1989, PDS web site.**

Predicted values exceed several order of magnitude the observed concentrations, demonstrating the existence of more complex mechanisms. Some catalytic cycles involving hydrogen have been proposed and, at this time, represent the more promising solution to the problem (see Atreya & Gu, 1995, for review). These reactions invoke also the production of quite exotic species such as  $H_2O_2$  and some radicals, but observative constraints in this sense are, at the moment, very sparse and basically limited to Earth observation. The situation is further complicated by reaction speed considerations related to the altitude. For CO and  $O_2$ , as well as for the other atmospheric components but  $CO_2$ , the vertical mixing ratio profile remains almost unknown.

The role of water on Mars is the topic of much literature, probably exceeding any other subject in planetary sciences.  $H_2O$  vapor presents a concentration very variable in space and time. Seasonal trends have been observed by MAWD and confirmed recently by TES instrument on MGS

(Smith M. D. et al., 2003a, Figure 7). Water vapor shows a maximum concentration during the retreat of the north polar cap, when an important fraction of H<sub>2</sub>O, trapped as ice during winter, is sublimated in the atmosphere; another minor maximum is observed during southern spring.

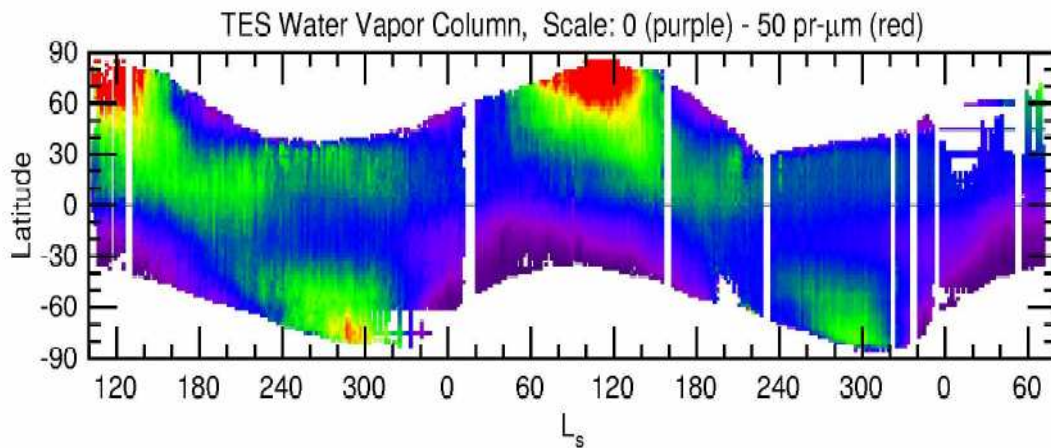


**Figure 7. Annual behavior of water vapor in the Martian atmosphere, as observed by TES instrument (from Smith M.D. et al., 2003a)**

Soil plays a complex role as a water source/sink. External layers are important, due to their possibly hygroscopic character, on a seasonal as well as on a daily basis. Here, single water molecules are bounded by electric forces to polar sites of mineral crystals. Temperature of the soil drives the balance between released and captured molecules. Moreover, deep underground (i.e. some meters below surface) may possibly host the greatest planet water reservoir in form of permafrost, i.e.: water in a crystalline form dispersed in a matrix of mineral grains. Evidence of this sense is represented by rampart craters (Figure 8) as well as by observations of GRS experiment on Mars Odyssey (Boynton et al., 2002). Further details are being provided from MARSIS and SHARAD radar observations on Mars Express and Mars Reconnaissance Orbiter, but, at this time it is hard to quantify the total mass involved in these formations. Water vapor mixing ratio as a function of altitude shall be influenced deeply by these interactions with the surface, but, unfortunately, very

limited data is available up to now (Titov, 2002). Needless to say, the vertical distribution of water vapor is a particularly important subject because of the high number of atmospheric chemical reactions having H<sub>2</sub>O as a key player. Sky brightness observed at the Pathfinder site seems to point toward a layer (with a thickness in the order of 1-3 km) with uniform mixing ratio close to the surface, overlaid by an almost dry atmosphere (Titov et al., 1999). Behavior of water vapor with height is constrained further by the observed distribution of ice clouds on Mars. The altitudes of these structures demonstrate how the vertical distribution of trace components of the atmosphere is influenced deeply by the great scale dynamic of the atmosphere (Rodin, 2002).

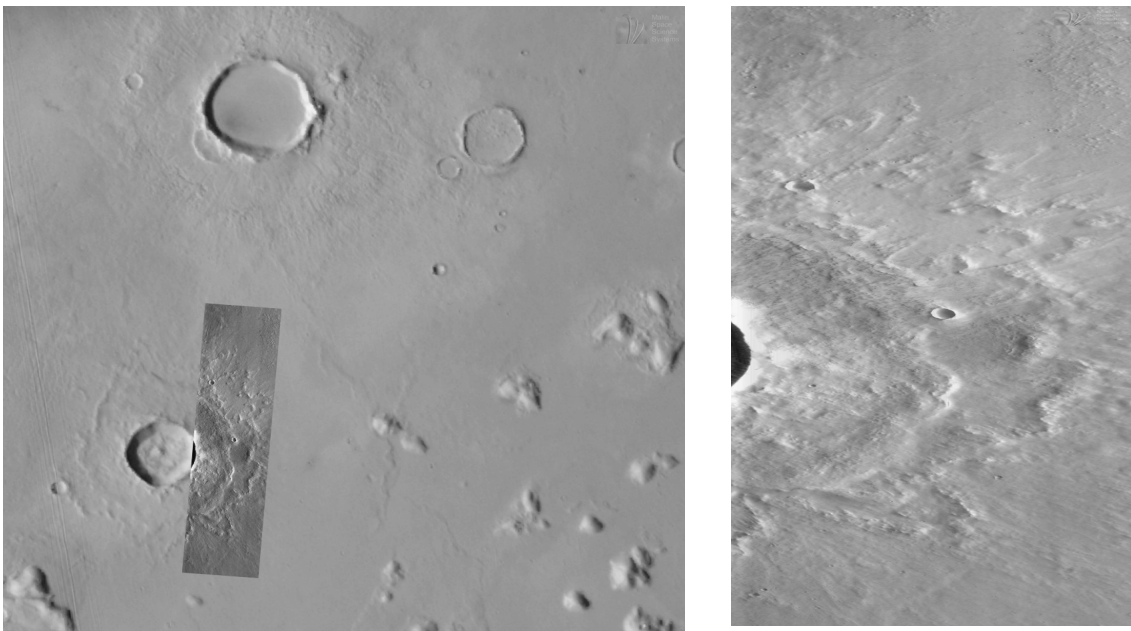


**Figure 8. An example of rampart crater. Lobes at the rims of these structures are interpreted as evidences of the flow of a water-rich mud after the impact. The permafrost ice would have been liquefied by the heat released during the impact, giving to the ejecta mechanical characteristics very different from those of dry materials. (Images from MOC press release, August 13<sup>th</sup>,1998).**

Liquid water cannot exist in stable form in today's thin atmosphere. Several structures observed by spacecraft cameras on the surface demonstrated the existence of an ancient climatic regime very different

from the present one. Among them, channels systems and gullies appear particularly impressive (Figure 9). The dating of these structures in the context of Martian history is still a matter of debate, as well as the role of liquid water in the geochemical evolution of Martian surface (Hamilton et al., 2003, Wyatt & McSween, 2003). Ozone was detected by spacecraft UV observations in early '70. Other measurements are available from Earth's and HST observatories, as well as from the limited dataset of AUGUSTE experiment on Phobos 2 (Blamont & Chassefière, 1993). They are however too sparse to provide a clear picture of the temporal and spatial behaviors of this gas. Ozone is formed by photo - dissociation of O<sub>2</sub>, and subsequent combination with another O<sub>2</sub> molecule.



The process is inhibited by the presence of water vapor, which subtracts atomic oxygen, possibly in the context of the CO<sub>2</sub>-forming cycles. The anti-correlation between O<sub>3</sub> and H<sub>2</sub>O was confirmed by spacecraft observations. The uncertainties about vertical distribution of atmospheric components do not allow ruling out an atmosphere of alternate water-rich and ozone-rich layers.

Other identified gas constituents have a minor importance. We mention only a nitrogen cycle, foreseen by models, but still without experimental evidence and little impact on global aeronomy of the planet.

For other gases, only upper limits have been fixed, mainly on the basis of IRIS data. Future experiments, namely PFS, will focus their attention on the detection of the species involved in the CO<sub>2</sub> cycle and other minor species of possible organic origin (CH<sub>4</sub> and other hydrocarbons).

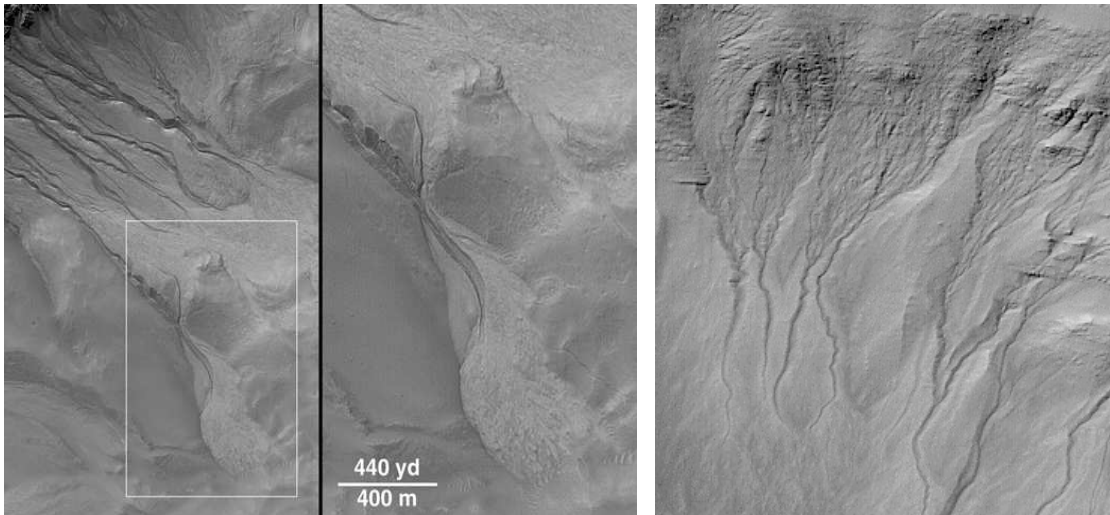


**Figure 9. Channels systems (a.) and gullies (b.) have been invoked as proofs of the existence, in the past, of an environment able to sustain a complete water cycle on Mars. (Images from MOC press releases, June 22<sup>nd</sup>, 2000 and August, 8<sup>th</sup>, 2002)**

### **2.2.2 Dust**

Besides gases and water ice clouds, Martian atmosphere contains also an amount of mineral dust. Its presence results in several interesting phenomena. Among them, dust devils (columns of dust, with a diameter in the order of several meters and over 6 km high, raised from the surface by whirlpools, Cantor & Edgett, 2002), diffuse haze, and the impressive dust storms, that may hide wide areas of the surface from visual observations for several days.

The dust concentration in the atmosphere is extremely variable, and the observations of Viking landers have demonstrated that it can never be considered negligible. The optical thickness of the atmosphere decreases of only one order of magnitude from the peak of the greatest storm to the quietest periods (from 0.5 to 5, considering the visual region). Consequently, even if surface features can be observed in detail, great

care must be used in the analysis spectroscopic data, deformed in surface reflectivity features details as well as in the phase functions.

The first clues on dust composition come from early IRIS observation, acquired during the greatest dust storm ever recorded on Mars. The shape of thermal IR spectra is consistent with a silicate material, with moderate-high silica content. Moreover, dust must include some fraction of a magnetic material, as demonstrated by simple experiments on Pathfinder lander (Gunnlaugsson, 2000), probably represented by some form of iron oxide, as suggested by visual colorimetric studies. A more precise definition of dust composition has been attempted by several authors indicating montmorillonite + basalt, palagonite (Clancy et al., 1995) and a mixture of different materials, where albite (a member of feldspar group) represents the main constituent (Grassi & Formisano, 2000). None of these models are, at the date, able to reproduce correctly the observed spectra in all their details. Research in this field is still severely limited by the restricted availability of complex refractive indices of different geological materials.

Dust grains have a diameter in the order of micrometer, being therefore much smaller than usual Earth sand. The size distribution is anyway another point of discussion. Most recent results by Montmessin et al., 2002, point toward a bimodal function, indicating perhaps a variety of different phenomena at the origin of the aerosol. Analysis of temperature fields retrieved from IRIS data by Conrath et al. (1975) suggests a constant size distribution with height, despite the expected gravity-driven settling. The Clancy et al. 2002 study of a limited TES set of phase angle measurements claims, on the contrary, the actual occurrence of this phenomenon.

This picture of great uncertainty is completed by the considerations about the vertical distribution of dust. A general consensus grew around the Conrath et al., (1975) model, very similar to an exponential distribution. This measure is anyway a very indirect one. Sparse results by Phobos 2 (Chassefière et al., 1995) were not able to provide a better understanding.

Aerosol are known to be one of the key factors in the energy balance of the planet, and every aspect mentioned above, far from being a mere speculative interest, potentially has a great impact on their thermal properties, and, consequently, on our capability to model atmospheric phenomena. We shall also keep in mind that any study of spectral data aiming to retrieve surface or atmospheric properties, have the dust optical properties and size distribution as mandatory inputs. We will see that PFS does not represent an exception.

### **2.2.3 Main phenomena of Martian atmosphere**

The study of Martian atmosphere's dynamics is a subject of particular interest, due to the strong similarities with Earth. Moreover, due to very close values of the length of the day and inclination of rotation axes on the orbital planes, the two environments are characterized by similar boundary conditions. Being, for several aspects, a more simplified system, Mars study can provide very useful insights in the physics of air masses, that may possibly give us new perspectives and tools for the understanding of our own home planet.

Presently at least five global circulation models (Bridger, 2003) are available, being able to reproduce with reasonable accuracy the phenomena (temperature fields, winds, long-scale waves, pressure variations at the surface) observed by space instruments. This correspondence ensures us that main drive mechanisms of atmosphere dynamic have been considered in their relative importance. All these models anyway still present some weak points, where a parameterization of some complex process becomes needed. This means that the user is required to provide some input because the code is not able to foresee the situation by its own; very often these inputs are of key importance, as expected in an essential chaotic system such as an atmosphere. Examples

are represented by the dust load (which vary considerably in different years) very variable considering different years, the chemical evolution of gas species and the condensation processes, treated only in their basic aspects. All these points give a sense in still pursuing the collection of experimental data by space probes.

The seasonal condensation of CO<sub>2</sub> at the poles is, by far, the most important phenomenon on Mars. The process involves about the 30% of the total atmospheric mass. Detailed energy description of polar caps environment requires very complex modeling, including thermal properties of surface and aerosols, which are still affected by great uncertainties. While CO<sub>2</sub> ice features have been unambiguously detected on TES spectra of southern pole (Kieffer et al., 2000), the mode of condensation is still unclear, due to lack of measurements in the polar night (visual and near IR are of course ruled out, while the thermal IR signal is very low). Some indications exist of direct condensation at the surface as well as of the existence of CO<sub>2</sub> clouds (Titus et al., 2001) but the relative importance of the two processes is still unclear. The condensation of CO<sub>2</sub> determines strong atmospheric depression during the polar winter, as detected by Mars Odyssey during its aerobraking phase (Withers et al., 2001). The atmosphere may become locally enriched of minor species, and due to the absence of UV flux, the chemical environment should become extremely complex.

The sublimation phase during spring is characterized by strong winds blowing toward low latitudes. Very often, they raise dust at the edge of the polar caps, determining regional dust storm. During summer, the north polar cap reaches a temperature higher than the triple point of CO<sub>2</sub>, demonstrating that this component has completely sublimed from surface. The residual cap is then formed mainly of H<sub>2</sub>O ice and buried CO<sub>2</sub> ice. This process has not been observed in such a complete manner in the southern hemisphere, where the temperature remains lower than sublimation temperature of CO<sub>2</sub> due to eccentricity of Martian orbit. The asymmetry in seasonal cycles has long term effects: features in the southern cap such as pits and cracks, observed by MOC camera, seems to

become much and much deeper with years, instead of presenting an annual cycle (Malin & Cantor, 2003), indicating probably a secular change in the Martian climate.

Mars atmosphere is interested further by a great scale Hadley cell circulation. This phenomenon creates, especially during equinox periods, a global convective cell. Air is warmed at the equator by the very hot surface. Buoyancy forces carry it high in the atmosphere, while the gap is filled by cooler air from lower latitudes. The expected thermal structure has been confirmed by TES air temperature retrievals (Smith M. D., et al., 2003b). The air flux associated to convection origins of a series of other phenomena. The Coriolis force produces baroclin waves at mid- latitudes, spectacularly traced by dust veils and ice clouds. Diurnal cycle, inducing a modulation on the heat flux on the atmosphere, produces the so-called thermal waves, strictly associated to surface pressure variations measured on diurnal basis. Air motions at very local scale are poorly constrained by experimental data. Limited wind measures at lander sites are available but they do not provide information about the vertical mixing of the atmosphere, a key factor in determining the vertical distribution of constituents and the settling modes of dust.

Temperature profiles of Martian atmosphere have been measured by entry probes, radio occultation experiments and, with much lower spatial resolution but wider time coverage, by inversion of thermal IR data (Smith M. D. et al., 2003b). Temperature profiles demonstrated to be extremely variable. The Martian air is very dry compared to Earth, and therefore does not benefit of the thermal buffer effects by water vapor<sup>2</sup> that keep the temperature on our planet relatively constant. Variations in temperature of several tenths of Kelvin are observed during daytime in the lowest levels, where air temperature is more coupled with surface one. The latter is basically directly driven by incoming Sun flux (Figure 10 shows some typical values).

---

<sup>2</sup> These effects are related mainly to the storage/release of energy during phase change gas – liquid and vice versa.

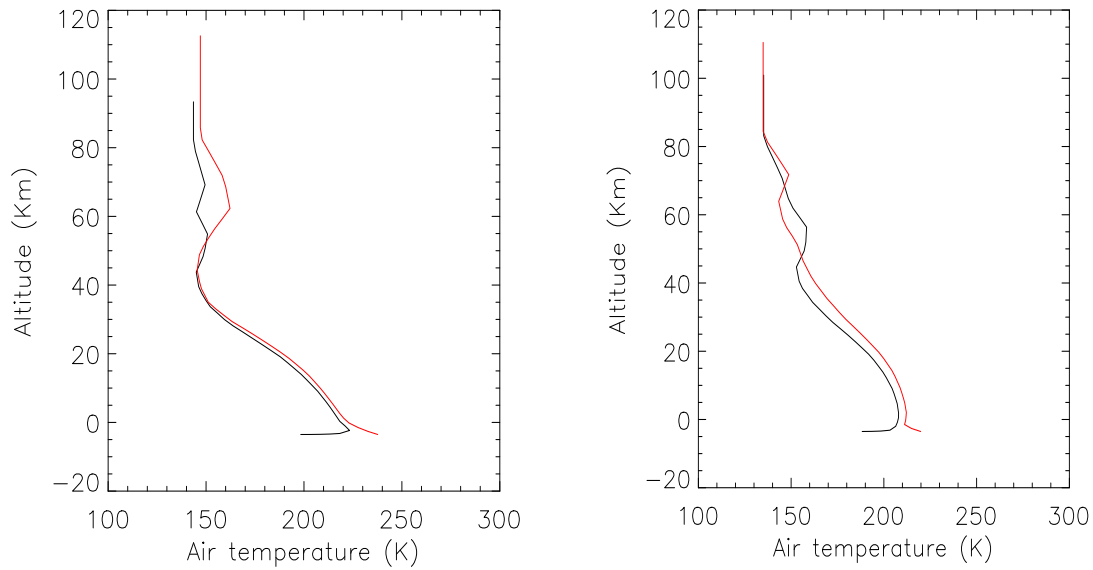


**Figure 10.** Typical temperature profiles of the Martian atmosphere, as expected from European Martian Climate Database v3.1 (<http://www-mars.lmd.jussieu.fr/>). a.: Latitude  $40^{\circ}\text{N}$ ,  $L_s = 105^{\circ}$  (Northern summer). Black: 3 AM, red: 3 PM. b.: Same conditions, but for  $L_s = 15^{\circ}$  (Northern spring). Viking dust scenario adopted.

Upper levels are less affected by daily cycle, being that the direct absorption of the Sun's visible light by atmospheric gases is extremely limited. The picture is strongly complicated by suspended dust grains. Aerosols are efficient absorbers of visible light. The energy from the Sun raises the temperature of grains, which are in thermal equilibrium with surrounding gas molecules. On the other hand, the Sun's flux at the surface is reduced and the soil temperature tends to decrease during dusty periods. These modifications of thermal structure of the atmosphere induce the anomalous pressure variations well seen in Figure 10. Mars does not have any substantial ozonosphere, therefore thermal inversions in the middle atmosphere are much reduced compared to Earth's stratosphere. Temperature decreases almost monotonically until non-LTE conditions become possible (Lopez-Puertas & Lopez-Valverde, 1995) and, at even higher altitudes, substantial variations of the atmosphere's

composition occur due to the interaction with space environment. Models are able to reproduce observed profiles in a wide range of situation (Forget et al., 2003), but several discrepancies still exist, especially in very cold conditions.

The origins of dust storms are still matter of debate. They occur mainly during southern summer, close to the sub-solar latitude. The season and location point toward a key role of surface heating in determining instability of the atmosphere. Local events, such as dust devils, had been often invoked as the triggering mechanism for dust storms, but no statistical correlation was found between their number and occurrence of extended events (Malin & Cantor, 2003). Great storms seem, on the contrary, to originate from diffuse dust haze and to develop suddenly and quickly, from several separate sources. This fact suggests the existence of some positive feedbacks in dust rising phenomena. One of the best global observations, due to MOC pictures (Malin & Cantor, 2003), shows a front able to expand in few days from southern intermediate latitudes to the other hemisphere, before to get a comparable longitude coverage. The study of the evolution of a storm of similar magnitude in the past (Fenton et al., 1997) showed other peculiar phenomena also during settling phase, such as different decay times in different regions. The intensities of the storms vary considerably and only a few become real global ones. Usually they remain regional events of limited size, which show anyway considerable inter-annual variability. Very often, theoretical models have still to include dust load as a parameter, being unable to model dust rise mechanisms. Some attempts have been made to model the storm spread and dust settling processes in the context of global circulation models (Newmann C. E. et al., 2003), but results are still preliminary.

The study of the occurrence of water ice clouds is even more complex. These structures are easily identified by their spectral signatures in IRIS Mariner 9 and TES spectra. They form a compact, optically thick, cloud deck (polar hood) during northern spring, in correspondence of the main water vapor enrichment on annual basis; a corresponding southern hood of smaller extension exists as well (Smith M. D. et al, 2003a). Another

preferential location is represented by the tops of great volcanic domes, where orographic winds raise quickly the air upward, determining the condensation of water. Clouds close to volcanic domes have an integrated content of water in the order of 0.5 pr  $\mu\text{m}^3$ . Beside morning fogs, a faint equatorial belt ( $\sim 2$  pr  $\mu\text{m}$ ) has been detected (Newmann G. A. et al., 2003 and Smith et al. 2003) during aphelion periods. This structure may play a key role in the Martian water cycle, with a non negligible mass flux toward northern latitude. Moreover, it presents at least two kinds of spectrally distinct cloud types (Clancy & Wolff, 2003), probably related to different grain size and condensation processes. The altitude of clouds is often very high, suggesting a key role for the Hadley circulation in the distribution of the minor components of the atmosphere. MGS and HST observed a cloud occurrence much greater than the one expected from Viking studies, suggesting, once again, a secular trend in Martian climate. The first attempt to produce a general modeling including condensation microphysics was presented only in very recent time (Rodin et al., 2002). The processes involved are intrinsically very complicated (e.g.: condensation on dust grain of unknown properties) while observations are presently too sparse at to allow a satisfactory determination of involved parameters.

---

<sup>3</sup> Precipitable  $\mu\text{m}$  are units to measure the column-integrated amount of water in an atmosphere.  $1 \mu\text{m}$  precipitable =  $10^{-4} \text{ g/cm}^2 = 3,35 \times 10^{18} \text{ molecules/cm}^2$ .

### **3 Tools: spectrometers and infrared spectroscopy**

Until fifty years ago our knowledge of planetary atmospheres consisted almost entirely of telescopic observations and intelligent guesses based on what scientists already knew about Earth's atmosphere. This situation began to change in the early 1960s when Soviet and American space scientists launched space probes designed to study the inner planets first and later the outer ones. The most successful of the early flights were the NASA's Mariner 2, which flew past Venus in December 1962; its Mariner 4, which flew past Mars in July 1965; and the Soviet Union's Venera 3 space probe, which landed on Venus on March 1, 1966.

With these missions and their payload instruments the science introduced other ways to get information from planets using remote sensing techniques.

At the present time, most of our knowledge regarding planetary atmospheric composition and structure has been achieved by *remote sensing spectroscopy*.

It is a powerful tool for investigating the atmospheres and surfaces of solar-system planets. Spectroscopic signatures of gaseous atmospheric components can be found over the whole range of the electromagnetic spectrum. In the UV, visible, and near-IR range (typically, wavelength below 4  $\mu\text{m}$ ) the planetary spectrum corresponds to the reflected solar blackbody, peaking at 0.5  $\mu\text{m}$ , over which planetary absorption features can be observed. These signatures allow us to determine the nature and the column density (the number of molecules integrated along the line of sight) of the different atmospheric constituents, the clouds, the aerosol particles and the characteristics of the surface, if any.

At longer wavelengths, the planetary spectrum corresponds to its thermal emission; its maximum depends upon the effective temperature of the planet and it can give information on surface and atmospheric temperature profile.

**Infrared** spectroscopic techniques therefore are extremely powerful for a number of observational objectives for "understanding" planetary atmospheres: the infrared spectral range ( $\lambda = [1-100] \mu\text{m}$ ) covers the main roto-vibrational bands of several molecules being present in planetary atmospheres. Namely, key species for chemical cycles such as  $\text{CO}_2$ ,  $\text{H}_2\text{O}$  and  $\text{CO}$  strongly interact with the radiation field in the IR domain. The same spectral region hosts distinctive signatures of aerosols, a ubiquitous presence in planets with substantial atmospheres. Consequently, despite the technical difficulties related to its implementation, IR spectroscopy has represented the choice investigation tool for the remote sensing of planetary environments since the beginning of space exploration.

In the next paragraphs we will shortly illustrate the physical concepts behind these investigations as the general properties of spectroscopy and IR radiation emerging from a planetary atmosphere. Then we will outline the basic principles of the theory of radiative Transfer, presenting some radiometric quantities and defining the general form of the radiative transfer equation appropriate for planetary atmospheres.

Before the general description of infrared spectroscopy as a technique to get information from a planet and in particular from its atmosphere, we will describe two actual tools which permit to acquire spectra of respectively Mars and Venus, the instruments PFS-MEX and VIRTIS-VEX. The *Planetary Fourier Spectrometer (PFS)* and the *Visible and Infrared Thermal Imaging Spectrometer (VIRTIS)* onboard the missions orbiting around the two planets provide the data which then we study using the principle of spectroscopy and *Radiative Transfer* of radiation through the atmosphere.

### **3.1 The instrument: VIRTIS - VEX**

#### **3.1.1 Venus Express mission**

Venus Express is the first ESA mission to Venus. The spacecraft was successfully launched from the Baikonur Cosmodrome on 9 November 2005 on a Soyuz-Fregat rocket and entered in the orbit of Venus in April 2006.

The name Venus Express comes from the short time available to define, prepare and launch the mission. It took less than three years from the approval to the launch of the mission. To do this, ESA re-used the same design as the Mars Express mission and the same industrial teams which worked on that mission.

With respect to previous missions to Venus, the scientific instrumentation on board Venus Express is enormously improved, allowing studying in great detail the atmosphere of Venus, to understand its complex dynamics and its tight relationship with the surface and with the planetary space environment around it.

#### **3.1.2 The Visible and Infrared Thermal Imaging Spectrometer**

VIRTIS (Visible and Infrared Thermal Imaging Spectrometer) is a complex instrument initially developed for remote sensing study of comet Wirtanen on the Rosetta mission (Coradini et al., 1998), at wavelengths between 0.3 and 5  $\mu\text{m}$ .

It is a sophisticated imaging spectrometer that combines three data channels in one compact instrument:

- a mapping channel (-M) which provides images at multiple wavelengths in the band 0.25-5  $\mu\text{m}$ . It comprises two channels which are committed to spectral mapping and are housed in the

Mapper (-M) optical subsystem. One frame records a spectral image, and the second image dimension is obtained through a scanning mirror. One channel is devoted to acquire infrared radiation in the range 1-5  $\mu\text{m}$  while the other observes the visible radiance from 0.25 to 1  $\mu\text{m}$ ;

- a high-resolution channel (-H) devoted solely to spectroscopy, providing high resolution spectra in the wavelength range 2-5  $\mu\text{m}$  and housed in the High resolution (-H) optical subsystem.

The focal planes, with CCD and infrared detectors achieve high sensitivity for low intensity sources. Due to the high flexibility of the operational modes of VIRTIS, these performances are also ideally adapted for the study of Venus atmosphere, both on night and day sides. VIRTIS is therefore aimed to provide a 4-dimensional study of Venus atmosphere (2D imaging + spectral dimension + temporal variations), the spectral variations permitting a sounding at different levels of the atmosphere, from the ground up to the thermosphere. The infrared capability of VIRTIS is especially well fitted to the thermal sounding of the night side atmosphere which gives a tomography of the atmosphere down to the surface; much information may also be retrieved from dayside observations and in the visible range.

In Figure 11 a simple graphic representation of the output data is given. VIRTIS-M obtains images of the planet at chosen spectral channels as the one shown in Figure 12.

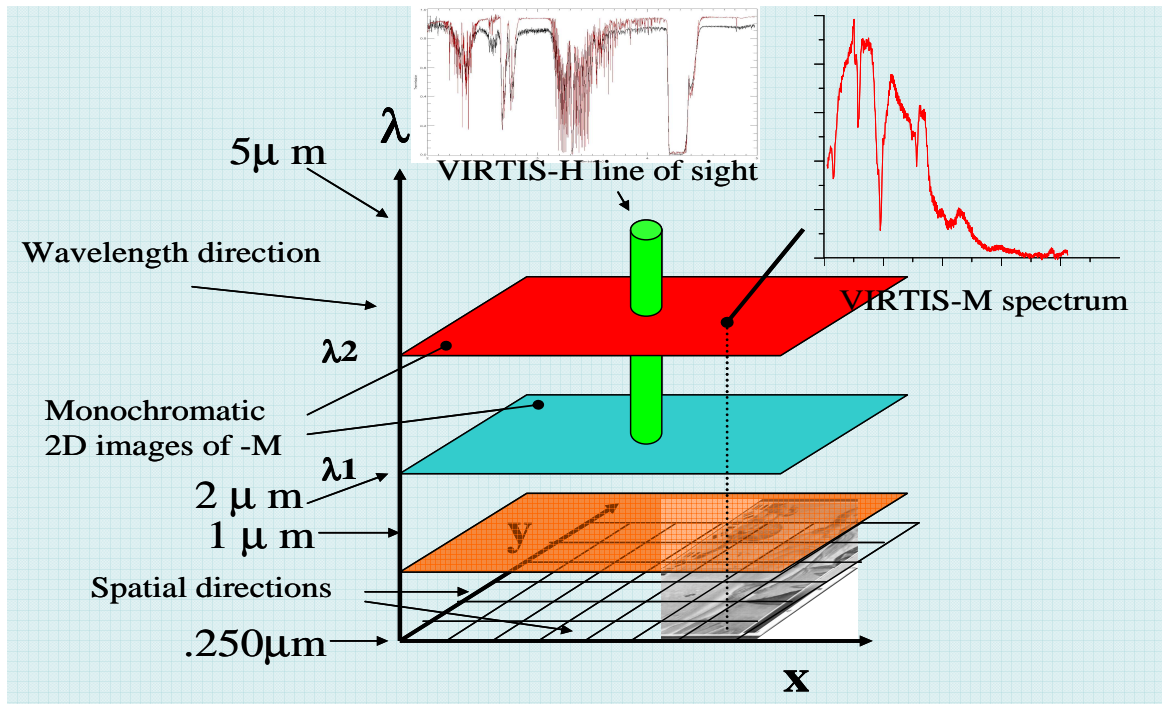


Figure 11. The output from VIRTIS-M can be considered to be a large set of stacked monochromatic two-dimensional images in the range between 0.25 to 5  $\mu\text{m}$ , at moderate spectral resolution. The field of view of VIRTIS-H centered in the middle of the  $-M$  image provides spectra at high spectral resolution in this small portion of the frame.

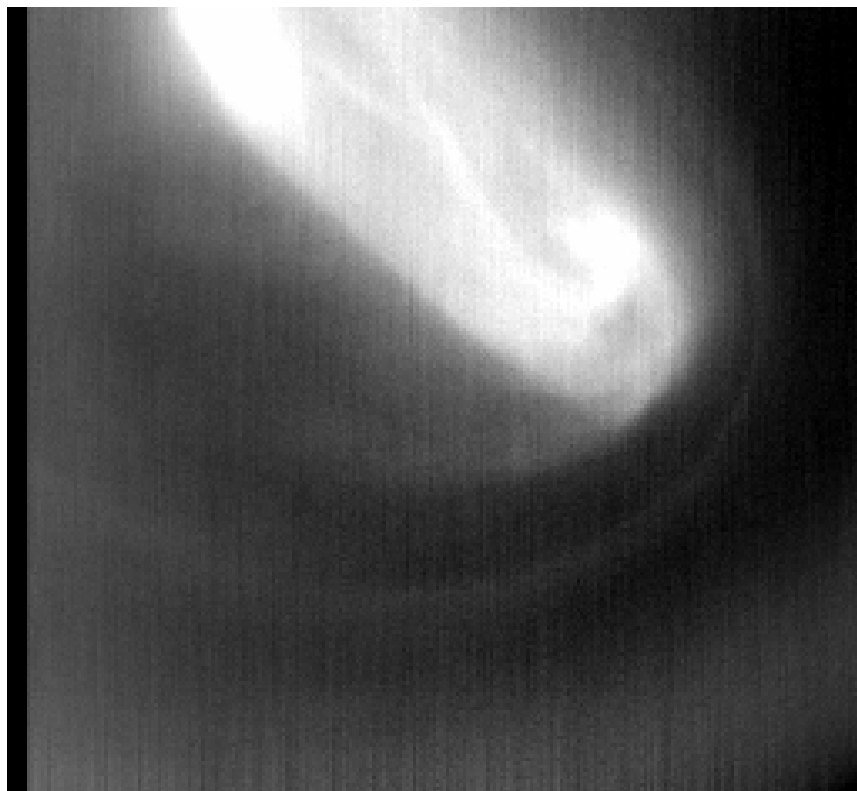
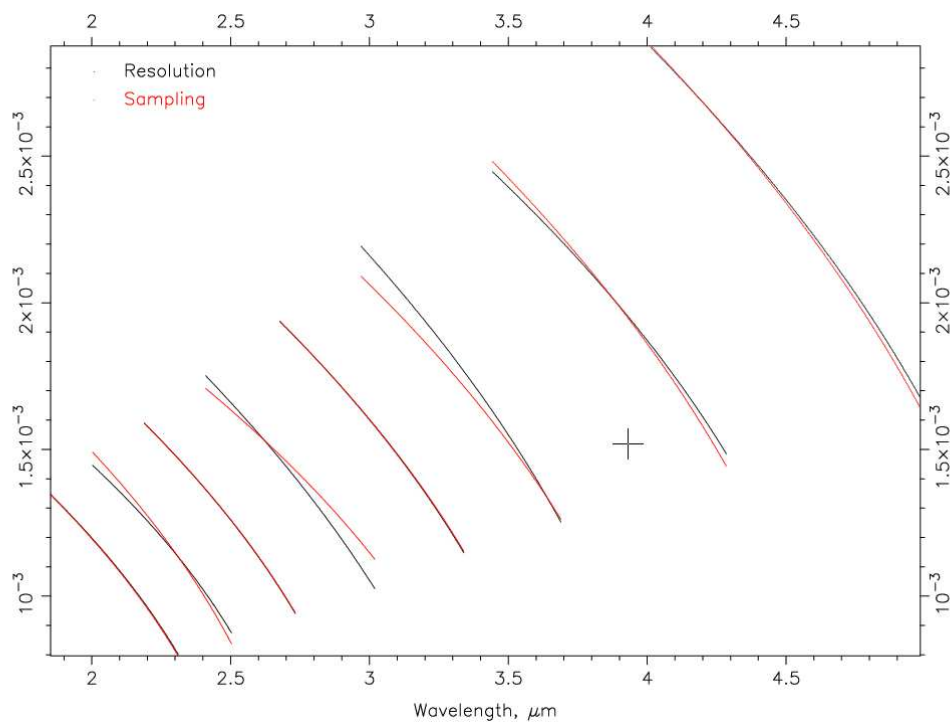


Figure 12. Example of an image acquired by VIRTIS-M. We can observe the polar vortex called "dipole" for its shape.

VIRTIS-H data are subdivided in 8 orders (see Figure 13) which overlap in a part of the spectral range (see Figure 14 where an example of VIRTIS-H spectrum with all orders is presented). Order 0 starts at 5 micron, till order 7 up to 2 micron. The resolution is higher in the spectral region at lower wavelengths of each order, but due to some residual stray light we should infer, case by case, the best order for our specific task.

In Figure 15 is showed the NER (Noise Equivalent Radiance) of VIRTIS-H instruments, for all orders, while in Figure 16 and Figure 17 we present respectively dayside and nightside synthetic spectra at VIRTIS-M and VIRTIS-H spectral resolution with indication of gaseous absorption bands and parameters which can be retrieved with the data.



**Figure 13.** Plot of the sampling and the resolution of VIRTIS-H spectra, divided in 8 orders which overlap with the closest ones in some part of the spectral range. We can observe that the resolution is higher in the spectral region at lower wavelengths of each order.

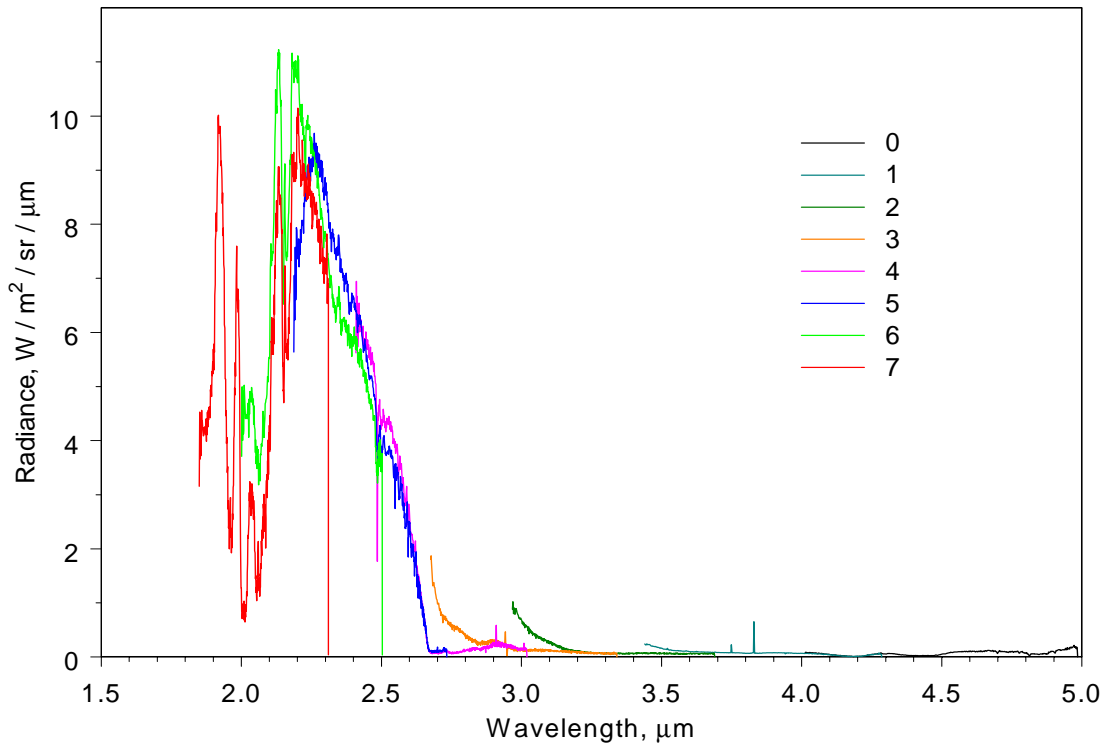


**Figure 14.** Venus spectrum acquired by VIRTIS-H in the dayside, we all 8 orders showed in the figure.

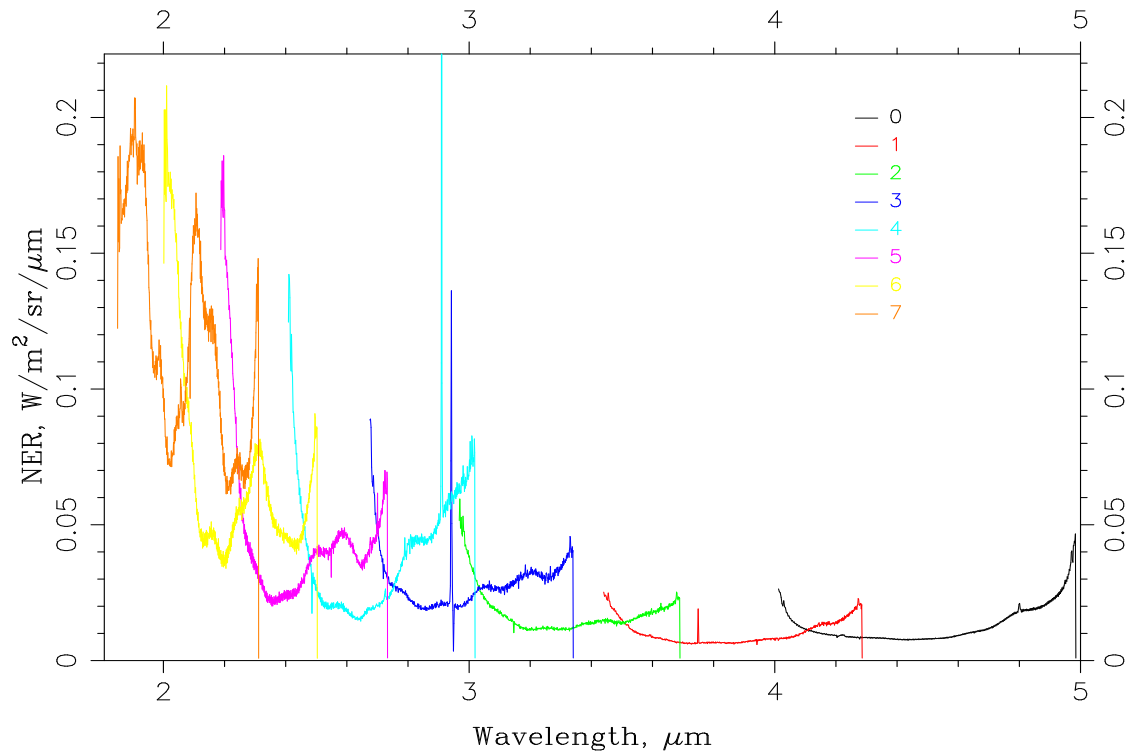


**Figure 15.** Noise equivalence radiance (NER) of VIRTIS-H for all orders.

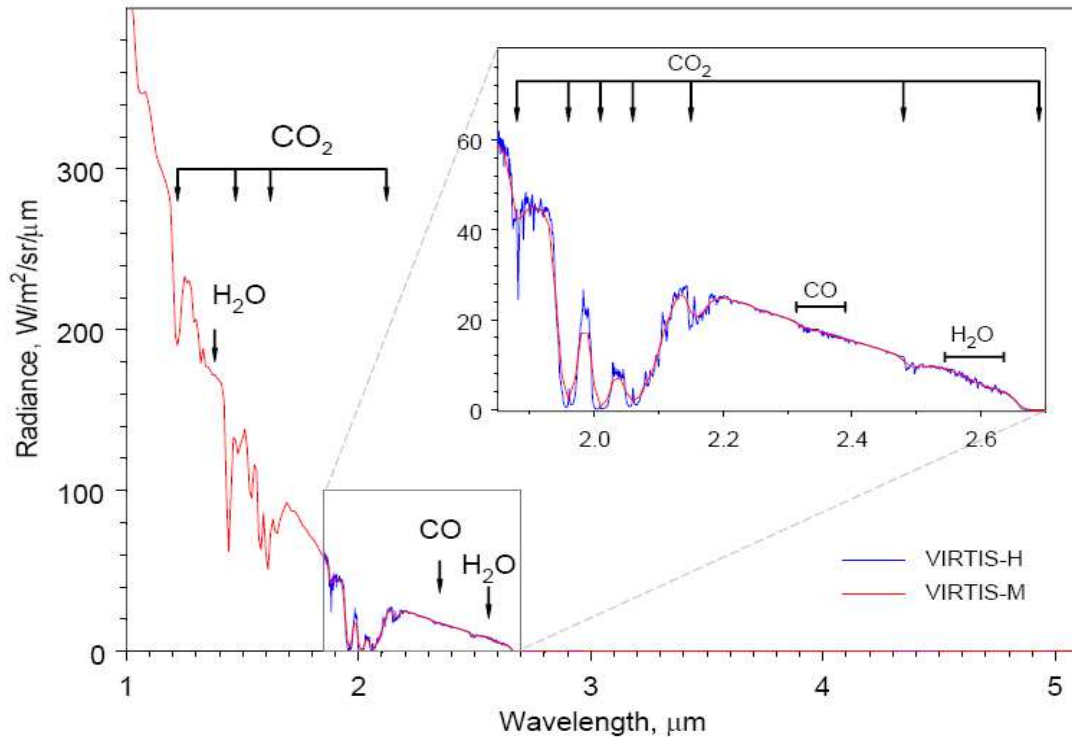


Figure 16. Venus dayside synthetic spectra at VIRTIS-M and VIRTIS-H spectral resolution with indicated gaseous absorption bands.

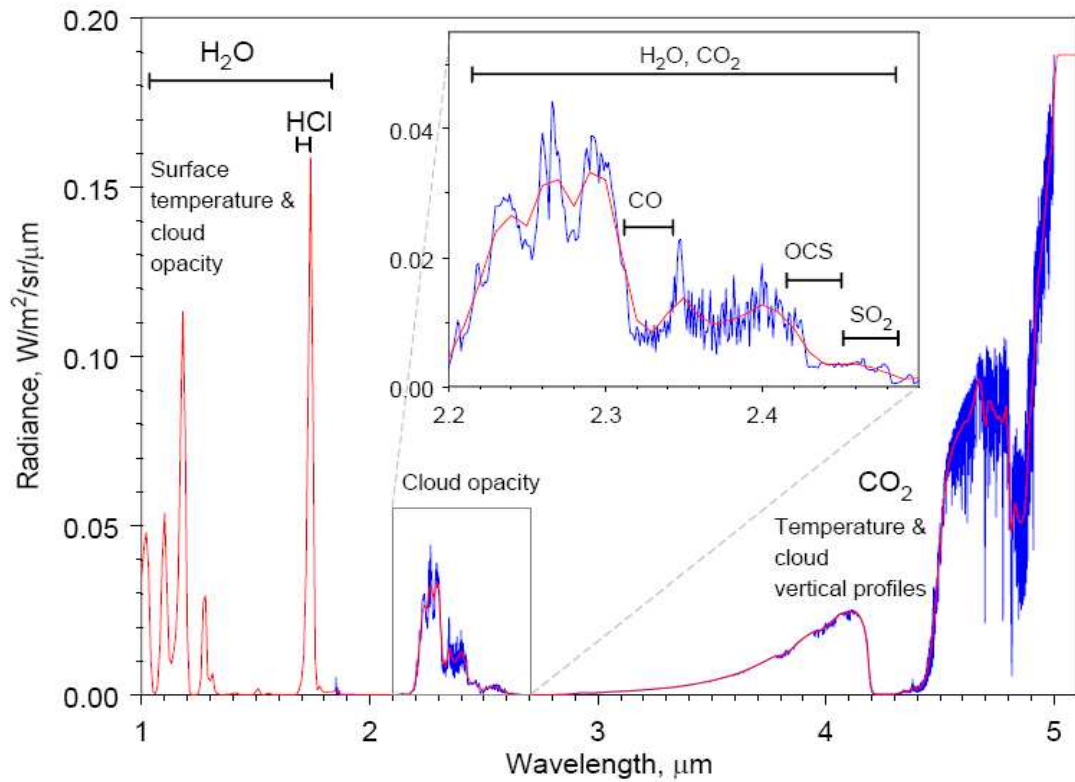


Figure 17. Venus nightside synthetic spectra at VIRTIS-M and VIRTIS-H spectral resolution with indicated gaseous absorption bands and retrieved parameters.

### 3.1.3 VIRTIS technical specifications

VIRTIS is made of 4 Modules: an Optics Module (-OM) containing the -M and -H Optical Heads, the two Proximity Electronics Modules for -M and -H (PEM-M and PEM-H) and the Main Electronics Module (-ME).

The Optics Module is externally mounted to the -X panel of the spacecraft with the -M and -H Optical Heads co-aligned and boresighted in the positive Z direction. Both optical systems have their slits parallel to the Y axis; the -M has the ability to point and scan by rotating the primary mirror around the Y axis.

VIRTIS-M channel, the mapping spectrometer, has moderate spectral resolution ( $R \sim 200$ ) and high spatial resolution of 0.25 mrad (250 m at 1000 km altitude), while VIRTIS-H is characterized by a much higher spectral resolution ( $R \sim 1200$ ). The main characteristics of the two instruments are summarized in Figure 18.

|   | VIRTIS – M Visible          | VIRTIS – M InfraRed       | VIRTIS - H (1)   |
|---|-----------------------------|---------------------------|--|
| Spectral Range ( $\mu\text{m}$ ) (4)        | 0.2882 – 1.1093             | 1.0305 – 5.1226           | Or0 4.01206-4.98496<br>Or1 3.44270-4.28568<br>Or2 3.01190-3.75586<br>Or3 2.67698-3.33965<br>Or4 2.40859-3.00570<br>Or5 2.18903-2.73220<br>Or6 2.00565-2.50468<br>Or7 1.85100-2.31194 |
| Spectral Resolution $\lambda/\Delta\lambda$ | 100 – 380                   | 70 – 360                  | 1300-3000  |
| Spectral Sampling (nm) (2)                  | 1.89                        | 9.44                      | 0.6  |
| Field of View (mrad x mrad)                 | 63.6 (slit) x 64.2 (scan)   | 63.6 (slit) x 64.2 (scan) | 0.567x1.73   |
| Max Spatial Resolution ( $\mu\text{rad}$ )  | 248.6 (slit) x 250.8 (scan) |                           |  |

Figure 18. Main characteristics of the three VIRTIS channels.

The -M utilizes a silicon charge coupled device (CCD) to image from 0.25  $\mu\text{m}$  to 1  $\mu\text{m}$  and a mercury cadmium telluride infrared focal plane array (IRFPA) to image from 1  $\mu\text{m}$  to 5  $\mu\text{m}$ .

The -H channel employs the same HgCdTe IRFPA to perform spectroscopy from 2  $\mu\text{m}$  to 5  $\mu\text{m}$ . The electronics to drive the CCD and the two IRFPAs are housed inside the Proximity Electronics Modules, while the remaining electronics boards are housed inside the Main Electronics Module. Both IRFPAs require active cooling to minimize the detector dark current (thermally generated Johnson noise). To minimize the thermal background radiation seen by these two IRFPAs, the Cold Box must be passively cooled to less than 130 K by radiating one of its surfaces toward cold space. While the coolers are housed inside the Optics Module Pallet, which directly interfaces with the warm spacecraft, the cold detectors and optical systems are housed in a cold structure that must be rigidly mounted to the much warmer Pallet while remaining thermally insulated from it.

The IR/FPA are high sensitivity detectors (arrays of 270 x 438 pixels) specially designed to provide high sensitivity and low dark current (10 fA at 80 K), with a read noise lower than 500 e<sup>-</sup>. For 1 sec integration, the noise equivalent spectral radiance is of the order of  $5 \cdot 10^{-5} \text{ W m}^{-2}\text{sr}^{-1} \mu\text{m}^{-1}$  for both Virtis H and M at 2.3  $\mu\text{m}$ . The maximum expected flux on Venus on the night side in this window is as high as  $0.15 \text{ W m}^{-2}\text{sr}^{-1}\mu\text{m}^{-1}$ , ensuring a S/N higher than 100, even for colder area. The FPA of both channels is actively cooled by cryocoolers down to the operating temperature of 80 K. On Rosetta, the spectrometer is passively cooled down to  $T= 130 \text{ K}$  by the radiator on the cold panel pointing to the deep space. Due to the thermal constraints on Venus Express, and the comfortable Signal to Noise ratio expected on Venus, the specification on the Optical Module temperature can be relaxed. Simulations on VIRTIS-H show that a temperature of  $T=150 \text{ K}$  on the optical module still provide a S/N higher than 100 for a 1 sec integration time.

## **3.2 The instrument: PFS - MEX**

### **3.2.1 The Planetary Fourier Spectrometer experiment (PFS)**

PFS is one of the instruments included in the scientific payload of Mars Express (MEX) mission to Mars. It was designed and manufactured in IFSI – CNR (now INAF) under the coordination of the principal investigator V. Formisano (Formisano et al., 1997). The concept of the experiment is based on a previous instrument developed jointly by IFSI – CNR and IKI, flown on the lost mission Mars96. Much detailed information is available in the PFS technical documentation (Formisano and the PFS team, 2003).

### **3.2.2 General instrumental set-up**

PFS is basically an interferometer. A complete description of this kind of instruments can be found in Hanel et al., 1992. Figure 19 shows the optical design of the instrument.

The incoming Martian radiation (with radiance  $I_{\nu, Mars}$ ) is divided, depending on the wavenumber  $\nu$ , in two main channels by a dichroic filter. These two channels are referred hereon as long wavelength channel (LWC or long) and short wavelength channel (SWC or short)<sup>4</sup>.

---

<sup>4</sup> In this work the word channel is used to designate LWC and SWC as well as an individual sampling point in the spectrum. Whenever ambiguity may raise, a clear assessment is made to distinguish the two concepts.

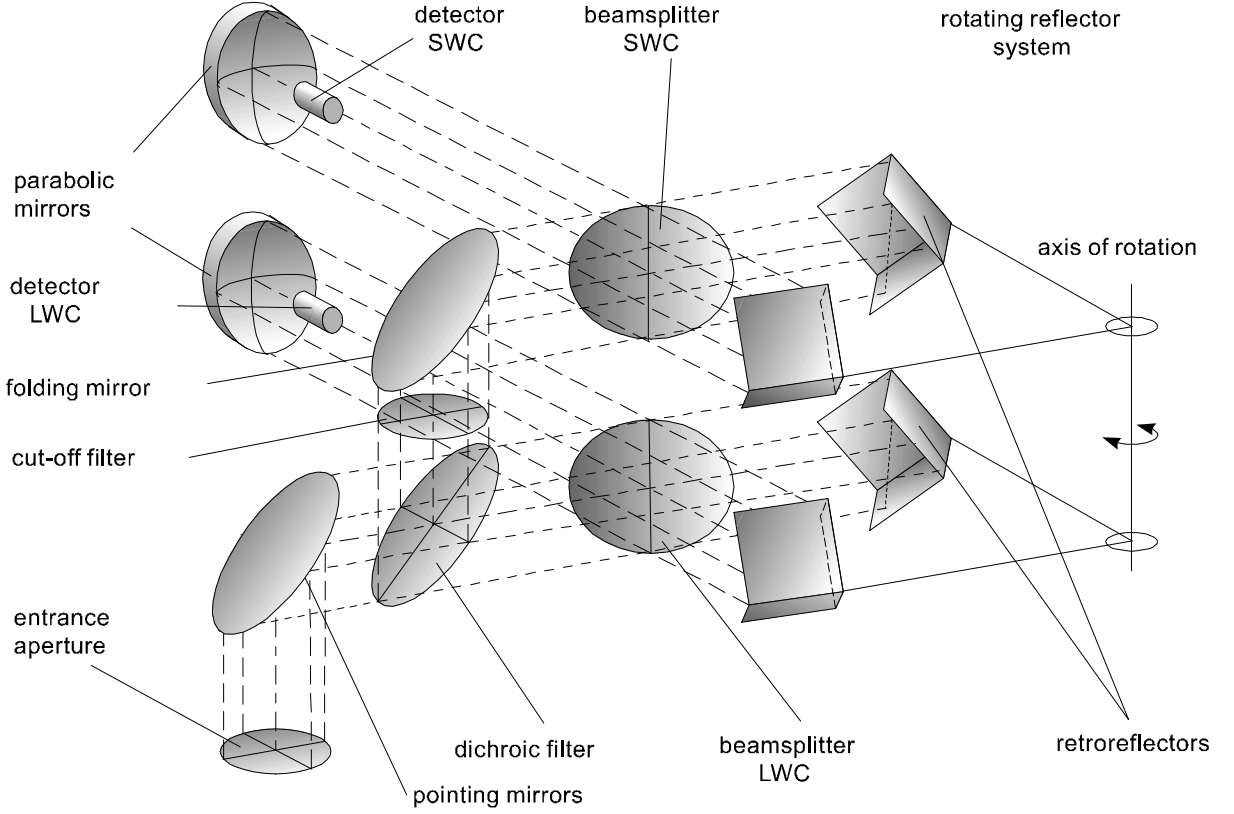


**Figure 19. Optical scheme of PFS instrument. From PFS proposal.**

The radiation inside each channel is further divided by a beamsplitter in two beams and redirected toward a couple of retro-reflectors fixed at the ends of the arms of a rigid double pendulum. The rotation of the double pendulum around its axis determines a  $\delta$  difference in the optical path of the two beams. This difference is two times the shift of each retro-reflector with respect to the beamsplitter. This design allows therefore a much more compact design compared to traditional interferometers (see, for example, Hanel et al., 1972). The two beams interfere each other, producing at the detector a variable component of the signal given by:

$$i(\delta) = \int_0^{\infty} K_{\nu} (I_{\nu, Mars} - I_{\nu, instrument}) e^{j(2\pi\delta\nu)} d\nu \quad (0.4)$$

where  $I_{\nu, instrument}$  is the thermal self-emission of the instrument and  $K_{\nu}$  a responsivity factor, that accounts for optical, detector and electronic

efficiencies at each wavenumber. A constant term (not depending on  $\delta$ ) also exists, but it is subtracted from output signal by a capacitor in the read-out electronics. The term inside parenthesis in Eq. (0.4) is the net energy gain/loss experienced by the detector in an infinitesimal wavenumber interval, i.e.: the actual signal as seen by the instrument point. The function  $i(\delta)$  is referred as interferogram: Eq. (0.4) demonstrates that its Fourier transform allows to recover  $I_\nu$  once  $K_\nu$  is known. In ideal conditions an interferogram is symmetric around  $\delta=0$ , therefore its Fourier transform is real and equivalent to the uncalibrated spectrum  $I_\nu K_\nu$ , with a zero imaginary part. Real interferograms are not symmetric and must be symmetrized prior to Fourier transform, according procedures described, for example, by Forman et al., 1966.

Due to the limited number of points where the interferogram can be sampled, the basic theory of Fourier discrete transform demonstrates that the resulting spectrum is limited in its resolution as well as in its range. Namely, being  $d\delta$  and  $\Delta\delta$  the sampling step of the interferogram and the maximum optical difference sampled, it can be shown that the maximum spectral range covered  $\nu_{max}$  is given by

$$\nu_{max} = \frac{1}{d\delta} \quad (0.5)$$

and the spectral resolution  $d\nu$  is limited according:

$$d\nu \propto \frac{1}{\Delta\delta} \quad (0.6).$$

Defining the spectral resolution as the FWHM of the transfer function of each sampling point in the resulting spectrum, the proportionality

constant of equation (0.6) varies according the apodization mask applied to the interferogram to reduce aliasing phenomena<sup>5</sup>.

The sampling of the interferometer is carefully controlled in PFS. Two laser diodes (one per channel) emit monochromatic radiations that experience the same optical path of Martian radiation. Devoted detectors (not shown in Figure 19) measure the intensity of the resulting sinusoidal interferogram, and command the sampling of scientific channels after a fixed number of zero-crossings in the reference one.

### **3.2.2.1 Resolution, transfer function and spectral range**

Due to its compact design PFS allows the sampling of a very wide range of optical differences. This results in a sampling step of the spectrum equal to  $1.0 \text{ cm}^{-1}$  for both channels in nominal operative conditions. During the calibration campaign, measurements of the response function of the single sampling point in the spectrum were possible, confirming, for unapodized spectra, the expected sinc shape and a value of  $1.2 \text{ cm}^{-1}$  for spectral resolution.

In each channel the spectral range is limited by Eq. (0.5) as well as by the behavior of  $K_\nu$  that in some spectral regions reduces the signal orders of magnitude below the noise. Calibration measurements allow to evaluate the responsivity of the instrument (see following paragraph) and to fix the indicative spectral ranges of  $[250; 1750] \text{ cm}^{-1}$  for LWC and  $[2000; 8200] \text{ cm}^{-1}$  for SWC. The ranges of the two channels correspond approximately to spectral regions dominated by thermal emission and solar reflection respectively.

---

<sup>5</sup> Apodization consists in a numerical mask applied to measured interferogram prior to Fourier transform. Numerical filter leaves the interferogram unchanged in its central parts, while tends to nullify it at the boundaries. This procedure avoids very sharp spurious features in the resulting spectrum (Fourier components of a step function).

### **3.2.2.2 Field of view**

PFS fields of view (FOV) for both channels were determined during the calibration campaign. The outputs of the instrument produced by a constant source were measured by varying the direction of the incoming beam. The FWHM of the resulting functions allow defining unambiguously the fields of view. The LWC has a field of view of  $2.8^\circ$  degrees, while SWC has a smaller one, being only  $1.7^\circ$  wide. The two channels are not perfectly co aligned, but are largely overlapping. These FOV values would correspond to a size of the footprints on the Martian surface of 7.7 km and 12.7 km at the pericenter (260 km). PFS cannot compensate for the motion of the spacecraft during data acquisition. Considering that each measure will take about 6 seconds, the resulting smearing of the image will produce elongated footprints of  $7.7 \times 22.5$  km and  $12.7 \times 27.5$  km at the pericenter.

PFS will acquire at Mars almost latitudinal tracks of spot observations. Footprints of different measurements will not overlap at the pericenter, due to the time spacing of 10 sec between the beginning of consecutive measurements. Therefore, it is not possible in these conditions to reconstruct the upwelling radiation field at sub-pixel resolution. In theory, these procedures would be possible for measurements acquired at higher altitudes. In the context of this work they were however not developed because:

we try to maintain, as far as possible, a uniform treatment of the dataset, the unknown magnitude, at the date, of errors in the location of footprint on the Martian surface.

*For our analysis we will assume that the physical conditions inside the two footprints are homogeneous and identical.* The atmospheric state is expected to vary on a greater scale than footprints, an exception is made for pressure variations related to topography. On the other hand, considering the albedo features as tracers of surface characteristic, MOC

images demonstrated variability on tenth meter scale, beyond the possibility of any remote sensing spectrometer. Therefore, it is important to remember that the retrieved quantities, even by single measurements, represent actually only an average situation inside the footprint.

### **3.2.3 Examples of PFS Martian spectra**

Figure 20 presents two examples of expected PFS observations at Mars, in very different conditions. Even a quick inspection of these plots allows identifying the main spectral features and the related quantities that can be investigated using PFS data:

1. The general signal level in the thermal infrared is driven mainly by the surface temperature, being that the Martian atmosphere is relatively optically thin in this spectral range. The low temperature of the polar cap (blue curve) determines a small signal compared to the one produced by the hot equatorial ground (red curve).
2. CO<sub>2</sub> bands in the thermal regions (namely 667 and 2300 cm<sup>-1</sup>) are sensitive to the total amount of this gas in the atmosphere as well as to the vertical temperature profile. The emission by the atmosphere in these opaque regions may become greater than the surface one (producing the lobes seen in the blue curve of Figure 20 a) around 630 and 690 cm<sup>-1</sup>).
3. Dust suspended in the atmosphere produces absorption bands centered at 480 and 1080 cm<sup>-1</sup>. Aerosol thermal emission may lead these features to appear in emission, depending on the actual thermal profile in the atmosphere.
4. Dust suspended in the atmosphere scatters the Solar radiation efficiently in the bottom of the CO<sub>2</sub> band at 3700 cm<sup>-1</sup>, completely saturated in a pure-gaseous atmosphere.
5. The general signal level in near infrared is driven by:
  - a. the incidence, emission and phase angles,

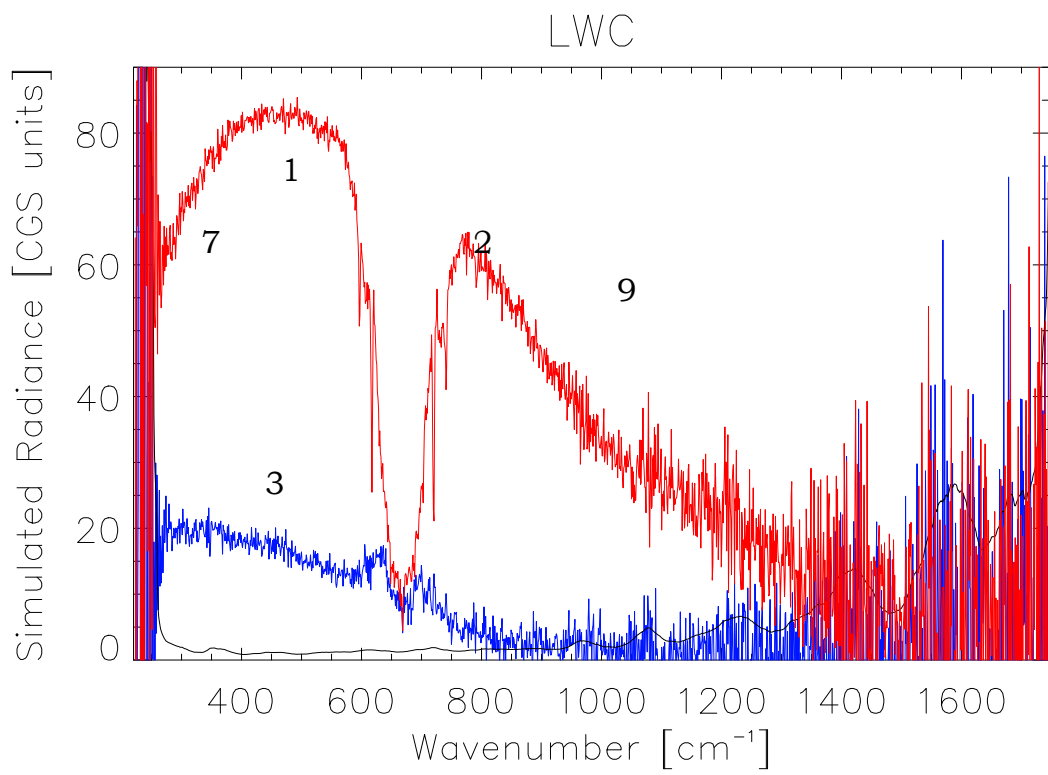
- b. actual Mars - Sun distance and,
- c. wavenumber dependence of Sun's flux.

Once these aspects have been taken into account, the SWC signal depends mainly on the reflectivity of the surface. For example, the broad shoulder going from 3700 to 4000  $\text{cm}^{-1}$  is interpreted as being related to hydrated materials ubiquitously spread on planet's surface. Scattering by suspended dust and water ice clouds may provide important contributions to the incoming radiation, producing almost featureless level variations of factor 2-3.

6. Non saturated  $\text{CO}_2$  bands in the near infrared probe the whole height of the atmosphere; their shapes depend mainly on the integrated amount of carbon dioxide. Assuming a uniform and known mixing ratio, this value can be translated in the total surface pressure.
7. Water vapor bands are present in a number of locations encompassed by the PFS spectral range, in LWC as well as in the SWC. Their details can be observed with the high spectral resolution achieved by our instrument.
8. Taking advantage of the adequate S/N ratio, a CO band is visible in SWC.
9. Deviations from ideal blackbody radiance in regions not affected by gaseous absorption may be related to non-unity emissivity of the surface.

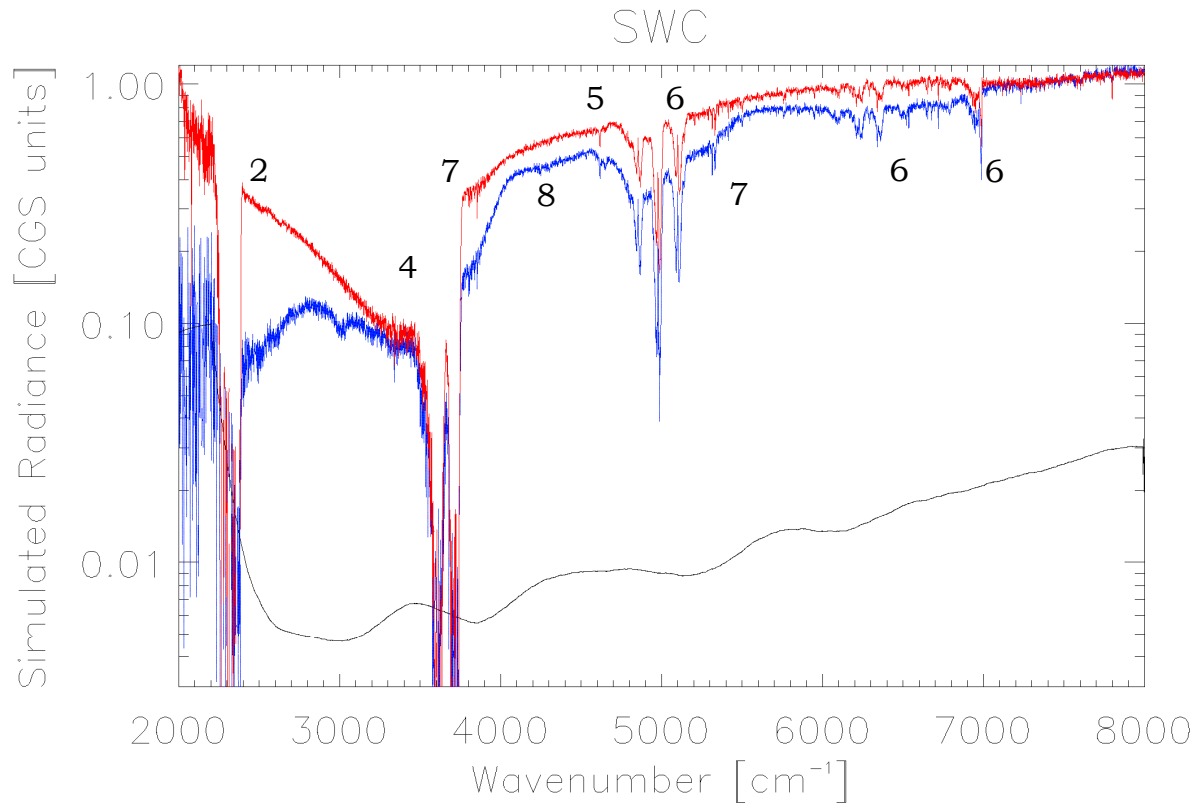
This list demonstrates heuristically the suitability of PFS design to study the Martian atmosphere. In this context, a key role is played by the wide spectral range and high resolution of our instrument, previously inexperienced

in satellite observations of Mars. PFS can also provide information on the chemical and physical conditions of the soil, from the reflectivity (or emissivity), of the surface. The relatively wide field of view and the lack of imaging capability make the geological sounding a second-order scientific objective for the instrument.



a

**Figure 20. cont.**



b

Examples of expected PFS spectra at Mars. A random noise (with a standard deviation equal to measured PFS NER) was added to the synthetic spectra computed on the basis of atmospheric and surface conditions extracted from EMCD v 3.1 (Forget et al., 2003). Both spectra refer to a nadir observing geometry. Blue:  $L_s=105^\circ$ , lat =  $80^\circ$ , Local time = 12 sol, polar cap surface; red:  $L_s=105^\circ$ , lat =  $0^\circ$ , Local time = 12 sol, low albedo region; black: PFS NER. CGS units are  $\text{erg}/(\text{sec. cm}^2 \text{ ster. cm}^{-1})$ . Numerical labels identify main spectral features, described in the text. Note that second picture has a logarithmic scale.

### **3.3 IR spectra of a planetary atmosphere**

This paragraph presents a brief outline of the interaction between IR radiation and matter. Of course, these notes should be considered only as simple background (with any purposes of completeness) aiming mainly to clarify the basic theory behind this topic (which represents the foundation of this work) and some used nomenclature. The reader can find an excellent review of these subjects in the book by Hanel et al., 1992, and references therein.

#### **3.3.1 Basic definitions**

The definition of infrared spectral range (IR) has its roots in the operative constraints of early electromagnetic detectors and consequently may vary between different authors. For our purposes, we consider the (quite arbitrary) indicative range of [1-100]  $\mu\text{m}$  for the wavelength  $\lambda$ .

The IR radiation field is particularly interesting for the planetary scientist for two main reasons:

it hosts the most prominent features of mineral spectra, in reflectivity as well as in transmittance,

it covers the roto-vibrational bands of several molecules present in planetary atmospheres.

Both aspects can provide information about the kind of materials that could be found in the investigated environment as well as on their physical conditions.

Let's define *radiance* or *intensity*  $I_\nu$  of a radiation field the energy  $dE_\nu$  associated to photons:

with wavenumber in the range  $[\nu ; \nu+d\nu]$ , with propagation directions included in the solid angle  $d\omega$  around the propagation direction, that cross in the time  $dt$  the area  $dA$  (showing  $dA$  an angle  $\theta$  between its normal and the propagation direction).

Therefore, it holds:

$$I_\nu \stackrel{\text{def}}{=} \frac{dE_\nu}{\cos \theta \cdot d\omega \cdot d\nu \cdot dA \cdot dt} \quad (0.7)$$

Depending on the radiance on the considered direction of propagation, it is convenient to define a polar reference system (Figure 21). The plane  $xy$  represents the planet's surface, with  $x$  pointing toward North Pole. The origin is the source of radiation on the surface, while P represents the observer. The direction of propagation is therefore unambiguously defined by the parameters  $(\phi, \theta)$ , or, more commonly,  $(\phi, \mu = \cos(\theta))$ . Once these conventions are established, the radiance can be defined in whichever point of the space as a function of  $\phi$ ,  $\theta$  and  $\nu$ .

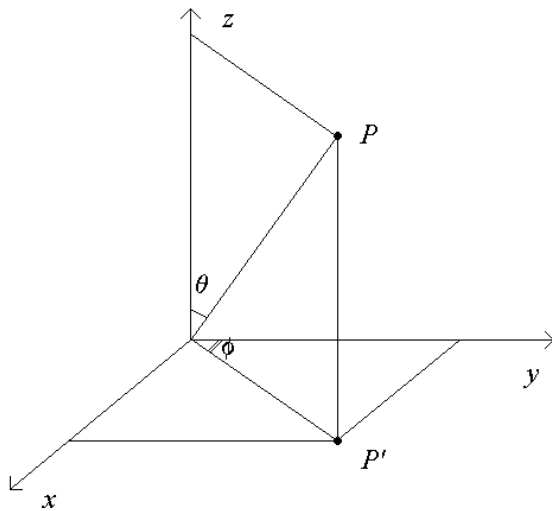


**Figure 21. Adopted reference system. The segment running from origin to point P (observer) defines the direction of photon propagation. Plane  $xy$  is the planet's surface.**

The most important characteristic of radiance holds in its spatial invariance: once the direction  $(\phi, \mu)$  is fixed, two points along this line have the same value of  $I_\nu(\phi, \mu)$  when no sources or sinks of radiation are interposed.

### 3.3.2 Effects of surface

Thermal emission is the simplest source of radiation, and by far the most important in planetary sciences. The surface of an *ideal black body* (a system able to absorb completely any incident radiation and to transform it into internal thermal energy) emits a radiation field given by the Planck function:

$$I_\nu(\mu, \phi) = \frac{2hc^2\nu^3}{\frac{hc\nu}{kT} - 1} \equiv B_\nu(T) \quad (0.8)$$

Thermal emission from the surface is the main factor driving the radiation field emerging from the planets in the range [100-2000]  $\text{cm}^{-1}$ , at least in the case of optical thin atmospheres (i.e. Mars, Earth, Mercury and other minor bodies apart from Titan). An actual planetary surface does not behave as an ideal black body and therefore the emitted radiation is more conveniently modeled by:

$$I_\nu(\mu, \phi) = \varepsilon(\nu, \mu, \phi) \cdot B_\nu(T_{\text{surface}}) \quad (0.9)$$

i.e.: the Planck emission is modulated by a function  $\varepsilon$ , known as emissivity, always less than 1. Emissivity depends on a number of factors, the most important being the mineralogical composition and the aggregation state of materials. A clear and simple introduction to these topics can be found in Salisbury et al., 1991, while a more general theory was developed by Hapke (1981, 1993). Simple thermodynamic

considerations show that emissivity is related to reflectivity  $r$  of a non-transparent surface by the so-called Kirchhoff law:

$$\varepsilon(\nu, \mu, \phi) = 1 - r(\nu, \mu, \phi) \quad (0.10).$$

Reflection of incident solar light by surfaces is the key player in determining the radiation fields from planets for  $\nu > 2500 \text{ cm}^{-1}$  (at least for those with optically thin atmospheres). Reflection from a granular surface can occur in two different ways (Fig. 1.2): we refer to *surface reflection* when the incident ray is reflected by the particles' most external surfaces, without penetration inside the grains. On the other hand, we have the *volumetric scattering*, by the rays refracted inside the grains and then reflected. A surface at the boundary of a semi-infinite, regular volume (i.e.: without cracks or other imperfections) produces only a surface reflection. In this case the reflection, as a function of  $\mu$  e  $\phi$ , can be calculated directly from Fresnel's equations and its dependence from  $\nu$  derives directly from the behavior of refractive indices  $n$  of the materials. These quantities can be expressed (being  $\omega$  the radiation frequency) by the following:

$$n(\omega) = n_r(\omega) + in_i(\omega) = \sqrt{\left[ 1 + \frac{Nq^2}{m\varepsilon_0} \sum_j \frac{s_j}{\omega_j^2 - \omega^2 - i\omega d_j} \right]} \quad (0.11)$$

This expression contains some factors ( $Nq^2/m\varepsilon_0$ ) related to the polarization of the material by incident radiation, but, most importantly, it models explicitly the bounds among minerals atoms as a series of  $J$  oscillators, each of them characterized by its proper frequency  $\omega_j$ , dumping parameter  $d_j$ , and relative weight  $s_j$ . From (0.11) it is easy to show that  $n_r$  presents a maximum (and consequently, reflectivity presents a minimum) where  $\omega = \omega_j$ . The situation becomes much more complex when realistic granular surfaces are considered. Now internal absorption in the material becomes important: reflections at the lower boundaries may occur when the dimensions of grains reach the same order of magnitude of mean free

optical path of photon (i.e.: average length run by a photon in the material before absorption). The description of reflectivity by analytical formulae becomes now almost impossible, due to the importance of reflections and refractions that occur at the void spaces between individual grains. Usually, a decrease in the average grain diameter produces an increase of reflectivity (as expected by common sense, due to extra diffuse reflection) only where thermal emission is negligible compared to incident radiation. In the thermal infrared the cavities formed by voids act as almost ideal black body radiators, increasing the emissivity (and, consequently, decreasing reflectivity) for smaller grains.

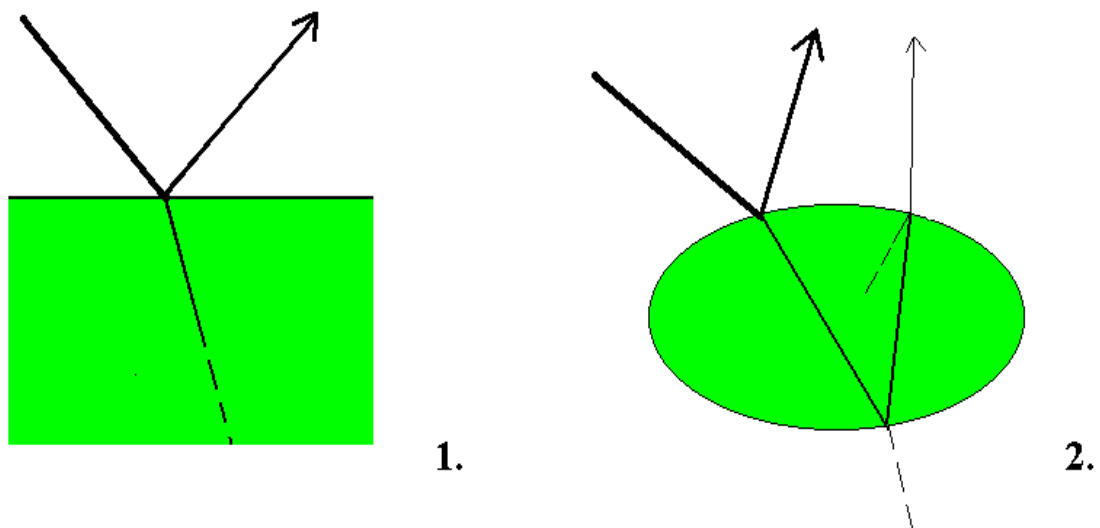


**Figure 22. Reflection of an electromagnetic wave by a solid geological surface. Case 1. The diameter of the grain is much greater than the photon's free path in the material. The refracted component (dashed line) is completely absorbed. Case 2. The diameter of grain is much smaller than the photon's free path in the material. Refracted component may be reflected by other discontinuities in the material and escape from the surface, producing a diffuse component randomly oriented.**

The emissivity and reflectivity properties can therefore be described only experimentally by empirical models. The dependence of  $r$  from direction (i.e.: the dependence from  $\mu$  and  $\phi$ ) becomes weak for actual geological surfaces, due to the presence, along the same line of sight, of rays

reflected in very different ways. The thermal radiation is satisfactory modeled by an hemispheric emissivity, measured by integration of the diffuse field in every possible direction. For the reflected Solar radiation, the Lambertian model is commonly adopted. In this approximation the surface acts as an ideal diffusive screen. Being  $F(\nu)$  the flux of incident radiation at the wavenumber  $\nu$  and  $\mu'$  the cosine of the angle between the incidence direction and the surface normal, the intensity of reflected radiation along  $\theta$  is:

$$I_{ref}(\nu, \phi, \theta) = \mu' \frac{F(\nu)}{\pi} \cos(\theta) \quad (0.12)$$

### 3.3.3 Microscopic effects of gases

Components of planetary atmospheres (gases as well as aerosols) have several important effects on the incoming radiation field.

**Absorption:** considering a given wavenumber, the radiation field experiences a net loss of energy due to the presence of suspended components in the atmosphere able to absorb the photons.

**Emission:** the atmosphere components produce a thermal emission, being at a temperature different from 0 K. This emission occurs not only at the wavenumbers where absorption actually occurs in the specific situation, but at every wavenumber where the particles *can* absorb. This represents a very efficient way to re-distribute the energy of the radiation field among different regions of the spectrum. The thermal radiation is spatially uniform.

**Scattering:** considering a given wavenumber  $\nu$ , the radiation field preserves its energy, that is anyway re-distributed spatially. Keeping fixed  $\mu$  and  $\phi$ ,  $I_\nu(\mu, \phi)$  can decrease due to photons redirected toward other directions, as well as to increase, due to the contributions of other photons, with different original directions of propagation, redirected along

$(\mu, \phi)$ . This extra fraction is the so-called diffuse field and is quite difficult to describe analytically because each photon may experience several direction' changes emerging from the atmosphere (multiple scattering).

Microscopic phenomena producing emission and absorption by atmospheric gases are related to the probability that a molecule performs a transition between two different states (namely, between two states described by different vibrational and rotational quantic numbers) at different energies.

Let's consider two states  $n$  and  $m$ , at energies  $E_n$  and  $E_m$  (the latter having an higher value): the absorption or emission associated to the transition between the two, at the wavenumber  $\nu = (E_m - E_n)/hc$ , is described by

$$I_{emi,\nu} = N_n A_{nm} h c \nu = N_n \frac{64\pi^4 c \nu^4}{3} |R_{nm}|^2 \quad (0.13)$$

and

$$I_{abs,\nu} = I_{0,\nu} N_m B_{nm} h \nu = N_m I_{0,\nu} \frac{8\pi^3 \nu}{3hc} |R_{nm}|^2 \quad (0.14).$$

Here  $|R_{nm}|^2$  is the square determinant of electric dipole matrix associated to the considered transition,  $A_{nm}$  and  $B_{nm}$  are defined as the so-called Einstein's coefficients for emission and absorption,  $N_n$  and  $N_m$  the number of molecules per unit volume in the  $n^{\text{th}}$  and  $m^{\text{th}}$  state respectively. These latter quantities can be computed, in conditions of local thermodynamic equilibrium, from the following relationship:

$$N_i = \frac{N d_i e^{-\frac{E_i}{kT}}}{\sum_{j=0}^{\infty} d_j e^{-\frac{E_j}{kT}}} \quad (0.15)$$

being  $d_j$  the degeneration of  $j^{\text{th}}$  state and  $N$  the total number of molecules per unit volume of the considered species. The complicated relationship between temperature and  $N_i$  represents one of most cumbersome computational tasks in the evaluation of synthetic spectra. A *real* transition between two states of different energy does not produce, even when observed with an ideal instrument, a perfectly monochromatic absorption or emission. Basic limitation is represented by quantum physics: shorter time of transition implies a wider spread of energy around the theoretical wavenumber  $\nu_0$ . For *isolated* molecules this phenomena produces a FWHM of spectral lines in the order of  $10^{-7} \text{ cm}^{-1}$  at  $1000 \text{ cm}^{-1}$ . In real planetary atmospheres the interactions between different molecules represent the limiting factor for the duration of transitions. These interactions are stronger at higher densities and, consequently, at higher pressures: for the Martian conditions (at the surface) a spread of lines in the order of  $0.1 \text{ cm}^{-1}$  can be considered an indicative value. The shape of lines determined by the energy-time indetermination can be represented by a Lorentzian function:

$$I_\nu = K \frac{w_c}{(\nu - \nu_0)^2 + w_c^2 / 4} \quad (0.16)$$

Here  $K$  represents the line intensity integrated over the entire spectrum and  $w_c$  is the FWHM of the function.  $w_c$  is proportional to the pressure. In the high atmosphere the pressure may become small, but air temperature remains high due to absorption by solar ultraviolet radiation. In these conditions, the Doppler broadening may become important. This effect consists in the variation of the ideal of a given transition due to the radial velocities of involved molecules along the line of sight. This motion is obviously related to the thermal shaking of molecules. The shape of line becomes in this case a Gaussian one

$$I_\nu = K \frac{2\sqrt{\ln 2}}{\pi w_d} e^{-4 \ln 2 (\nu - \nu_0)^2 / w_d^2} \quad (0.17),$$

being  $w_d$  the FWHM. It can be shown that this quantity is equal to

$$w_d = \frac{\nu}{c} \sqrt{\left( 8 \ln 2 k N_{avogadro} \frac{T}{\mu} \right)} \quad (0.18)$$

and depends therefore on temperature (representing a further complication in the computation of synthetic spectra), on average molecular weight  $\mu$  and on wavenumber  $\nu$ . Usually both sources of line broadening are noticeable and the resulting shape of spectral lines is actually a convolution between a Gaussian and a Lorentzian function. Resulting profile, usually referred as *Voigt* shape, shows a width that can be empirically expressed by:

$$w_v = \frac{w_c}{2} + \sqrt{\left( \frac{w_c^2}{4} + w_d^2 \right)} \quad (0.19).$$

The radiation scattering by gas molecules in a planetary atmosphere is described by the so called Rayleigh scattering. In this model, the molecules and its electron charge cloud act like an oscillating electric dipole. This means that a collimated beam of light, determining a flux  $F_0$  at the position of the molecule, has its energy redistributed spatially so that, at a distance  $r$  from the molecule, the flux is given by:

$$F = 8 \left( \frac{\pi^2 \alpha}{\lambda^2 r} \right)^2 (1 + \cos^2 \Theta) F_0 \quad (0.20).$$

$\Theta$  is the angle between the directions of incident and scattered radiation and  $\alpha$  the electric polarizability of the molecule. Due to the strong dependency on wavelength  $\lambda$ , the Rayleigh scattering is usually negligible in the range covered by PFS, but represents an important diffuse field source for visible and UV.

### 3.3.4 Microscopic effects of aerosols

Aggregated particles suspended in the atmosphere (aerosols) are very common in planetary atmospheres. Good examples are the water droplets of Earth low altitude clouds or water ice and silicate dust observed on Mars.

The absorption of the radiation field propagating across a medium is directly proportional to the imaginary part of its refractive index at the considered wavenumber. In any case, the interaction between radiation beam and particles can not be fully understood neglecting the effects occurring at the particles surfaces. Let's consider (Figure 23) a collimated beam, with a diameter much smaller than the particles radius. When the beam almost grazes the particle, the dominant effect consists in the Fraunhofer diffraction. This results in a narrow cone of diffracted radiation centered around  $\theta = 0^\circ$ . On the other hand, when the incidence point is far from the edge, usual Fresnel laws for refraction and reflection can be applied. The incoming ray splits in two components: one reflected, that becomes part of the diffuse field, and another refracted inside the grain. This last one propagates in the new medium being attenuated, until the boundary is met. Once again, a split can be observed, producing a reflected and a refracted component. The process goes on until the beam is completely absorbed or scattered out. Components labeled as  $j=0,1,2,3,\dots$  are the diffuse field.

Silicate dust aerosols usually show a low reflectance: consequently, radiation experiences few reflections inside the particles and only low values of  $j$  are important for the diffuse field. Namely, beam  $j=1$ , together with radiation diffracted at the particle's edge, produces a strong *forward scattering*, more and more collimated around  $\theta = 0^\circ$  while  $n_r$  decrease.

Analytic treatment of the interaction between suspended particles and light rays, even if conceptually very simple, results in a quite complex formulation, and may be reduced to explicit solutions only for the simplest cases. Results by Mie (1908) on spherical particles represent a milestone in this context.

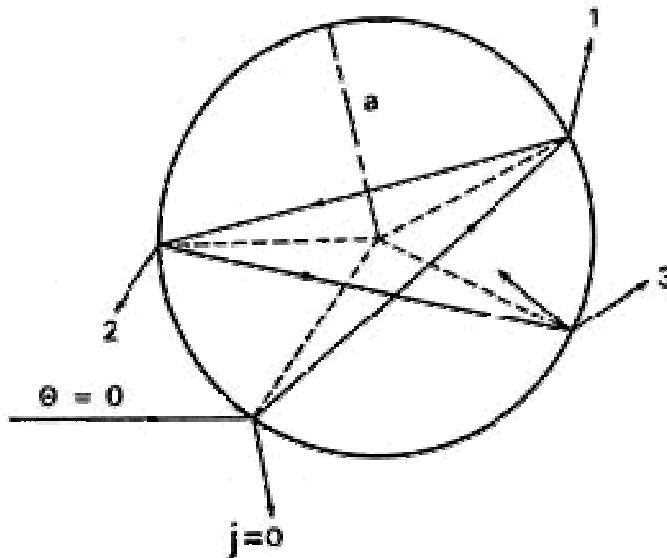


Figure 23. Reflected and refracted components of a light ray, incident with direction  $\theta$  on a spherical particle. From Hanel et al., 1992.

### 3.3.5 Macroscopic description

Once the physical processes at the origin of absorbing, emission and scattering in the atmosphere have been understood, a macroscopic treatment becomes possible. It provides a global description of the radiative field.

Let's consider an infinitesimal matter element  $dV$  (Figure 24) and a reference system centered on it (analogous of that shown in Figure 21).

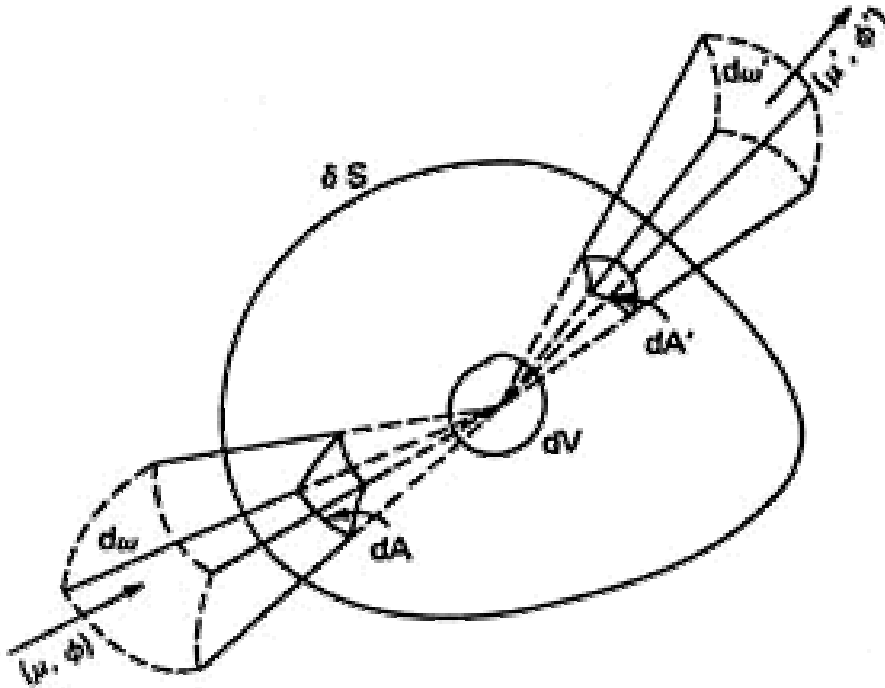


Figure 24. General scheme for the description of scattering processes. From Hanel et al., 1992.

If we have a radiation beam incident on  $dV$  from direction  $(\mu, \phi)$ , the interaction with matter determines a fraction  $E_\nu$  of the beam energy (per unit area, unit time and associated to radiation with a wavenumber in the range  $[\nu, \nu+d\nu]$ ) being absorbed or scattered. Being  $dE_\nu$  the energy scattered toward  $(\mu', \phi')$  inside the solid angle  $d\omega$ , we can define a phase function for single scattering  $p_\nu$  as:

$$\frac{dE_\nu(\mu', \phi')}{E_\nu(\mu, \phi)} = p_\nu(\mu, \phi, \mu', \phi') \frac{d\omega}{4\pi} \quad (0.21)$$

Usually, the great number of scattering particles involved produces a natural cylindrical symmetry in the system, where the axis is obviously represented by the direction of incoming light. In these conditions, the dependence of  $p_\nu$  from direction becomes a function of the angle between

incoming and scattered light beam  $\Theta$  only. This angle can simply be calculated by:

$$\cos \Theta = \mu\mu' + \sqrt{(1-\mu^2)}\sqrt{(1-\mu'^2)} \cos(\phi' - \phi) \quad (0.22).$$

Moreover, it can be useful to define a *single scattering albedo*  $\bar{\omega}_\nu$ , that represents the ratio between the total lost energy and the scattered one (no matter which direction):

$$\bar{\omega}_\nu \equiv \frac{1}{E_\nu(\mu, \phi)} \int dE_\nu(\mu', \phi') = \int_0^{4\pi} p_\nu(\cos \Theta) \frac{d\omega}{4\pi} \quad (0.23).$$

Particles suspended in the atmosphere are usually not perfectly identical, but composed by several populations (differing in composition, size, shape, etc.). The first step to describe inhomogeneous populations is the definition of an *extinction cross section*  $\chi_\nu$ . Let's consider the case of an infinitesimal control volume  $dV$ , with a geometrical section  $d\sigma$  normal to incidence direction, filled with identical particles. Being  $P$  the probability that an incoming photon of wavenumber  $\nu$  is absorbed or scattered,  $\chi_\nu$  associated to that class of particles at the considered wavenumber can be defined as:

$$P = \frac{N\chi_\nu dV}{d\sigma} \quad (0.24),$$

where  $N$  is the number of particles per unit volume. It is important to point out that the concept of extinction cross section encompasses absorption as well as extinction and that it can be applied to aerosols as well as to gases.

Keeping fixed the wavenumber, it is useful to classify the particles according to their extinction cross section. We introduce a normalized distribution function  $D(\chi_\nu)$ , such that the number  $N(\chi_\nu)$  of particles per

unit volume with extinction cross section in the range  $[\chi_\nu, \chi_\nu+d\chi_\nu]$  and the total number of particles per unit volume  $N_0$  are related by:

$$N(\chi_\nu) = D(\chi_\nu)N_0 \quad (0.25).$$

Now, we can redefine consequently the phase function, the single scattering albedo and the extinction probability as  $p_{\nu,\chi}$ ,  $\bar{\omega}_\nu(\chi)$  and  $P(\chi)$ , as the quantities that describe the effects on the beam exerted by the particles with extinction cross section in the range  $[\chi \text{ e } \chi+d\chi]$ .

Average population characteristics can eventually be described by:

an *effective* extinction cross section  $\chi_{E,\nu}$

$$\chi_{E,\nu} \equiv \int_0^\infty D(\chi_\nu)\chi_\nu d\chi_\nu \quad (0.26),$$

an effective single scattering albedo  $\bar{\omega}_{0,\nu}$ , that quantifies the overall reflectance of the material in the atmosphere at the considered wavenumber  $\nu$ ,

$$\bar{\omega}_{0,\nu} \int_0^\infty D(\chi_\nu)\chi_\nu d\chi_\nu = \int_0^\infty \bar{\omega}_\nu(\chi)D(\chi_\nu)\chi_\nu d\chi_\nu \quad (0.27),$$

an effective normalized phase function  $p_{0,\nu}$ , such that:

$$p_{0,\nu}(\cos \Theta) \int_0^\infty \bar{\omega}_\nu(\chi)D(\chi_\nu)\chi_\nu d\chi_\nu = \int_0^\infty D(\chi_\nu)\chi_\nu p_{\nu,\chi}(\cos \Theta)d\chi_\nu \quad (0.28).$$

With this formalism, the fraction of incident radiation from  $(\mu, \phi)$  being scattered toward  $(\mu', \phi')$  by the interaction with  $dV$  is given by:

$$\tilde{p}_\nu(\mu, \phi, \mu', \phi') \equiv \bar{\omega}_{0,\nu} p_{0,\nu}(\mu, \phi, \mu', \phi') \quad (0.29).$$

Quantities described by equations (0.26) - (0.29) can be described in terms of microscopic quantities.

For aerosol, Mie theory allows their evaluation from complex refractive indices and particles radius. For gases, comparison between (0.13), (0.14) e (0.24) allows the expression of

$$\chi_{E,\nu} = \delta(\nu - \nu_{0,i}) \frac{d_i e^{-\frac{E_i}{kT}}}{\sum_{j=0}^{\infty} d_j e^{-\frac{E_j}{kT}}} \frac{8\pi^3 \nu_{0,i}}{3h^2 c} |R_{nm}|^2 \quad (0.30)$$

for an ideal monochromatic line located at  $\nu_{0,i}$ .

Another fundamental concept is the *optical thickness*  $\tau_\nu$ . Considering an homogeneous layer of atmosphere, bounded by two infinite and parallel planes at distance  $dz$ , filled by particles with effective extinction cross section  $\chi_{E,\nu}$  and density  $N_0$ , this quantity can be defined by:

$$d\tau_\nu \equiv N_0 \chi_{E,\nu} dz \quad (0.31).$$

It can be interpreted heuristically as the average number of interactions with matter experienced by a photon with wavenumber  $\nu$  in crossing the layer along a path normal to layer boundaries. This interpretation allows us to write the fundamental relationship relating the extinction  $dI_\nu$  of an incident radiation field  $I_\nu$  over the infinitesimal layer with its optical thickness  $d\tau_\nu$ , i.e.:

$$dI_\nu = I_{0,\nu} \frac{d\tau_\nu}{\mu} \quad (0.32).$$

Describing the atmosphere as a stack of plane-parallel layers, each of them thin enough to be considered homogeneous inside its boundaries, we get in a path between altitudes  $z=0$  e  $z=z_1$  an optical thickness of

$$\tau_{\nu}(z_1) = \int_0^{z_1} N_0(z) \chi_{E,\nu}(z) dz \quad (0.33).$$

This formalism can describe simultaneously gases as well as aerosols. Applying averages introduced by (1.19) and (1.20) it is clear that

$$N_0(z) \chi_{E,\nu}(z) = N_{0,aerosol}(z) \chi_{E,\nu,aerosol}(z) + N_{0,gas}(z) \chi_{E,\nu,gas}(z) \quad (0.34)$$

and, therefore

$$\tau_{\nu}(z_1) = \tau_{\nu,aerosol}(z_1) + \tau_{\nu,gas}(z_1) \quad (0.35).$$

### 3.3.6 Total field

Previous considerations can be summarized in an expression that describes analytically the expected radiance measured by a spacecraft in orbit around a planet. The actual state of the atmosphere is modeled as a stack of *internally homogeneous* infinitesimal plane parallel layers. Therefore, the spatial dependencies of radiance, single scattering albedo, phase function and temperatures are (strongly) simplified, being functions of altitude only (and therefore, at a given  $\nu$ , function of optical depth via Eq.(0.33). Adopting the convention that at the surface  $\tau_{\nu}(z=0) = 0$  and at the top of the atmosphere  $\tau_{\nu}(z=\infty) = \tau_{\nu,total}$  it can be shown that:

$$\begin{aligned}
I_\nu(\tau_{\nu, total}, \mu, \phi) = & \\
A. & I_\nu(\tau_\nu = 0, \mu, \phi) e^{-\tau_{\nu, total}/\mu} + \\
B. & \frac{1}{\mu} \int_0^{\tau_{\nu, total}} (1 - \bar{\omega}_{o,\nu}(\tau_\nu = \tau_\nu')) e^{-(\tau_{\nu, total} - \tau_\nu')/\mu} B_\nu(T(\tau_\nu = \tau_\nu')) d\tau_\nu' + \\
C. & \frac{1}{4\pi\mu} \int_0^{\tau_{\nu, total}} \int_0^{2\pi} \int_0^1 e^{-(\tau_{\nu, total} - \tau_\nu')/\mu} e^{-\tau_\nu'/\mu'} \tilde{p}_\nu(\tau_\nu = \tau_\nu', \mu, \phi, \mu', \phi') I_\nu(\tau_\nu = 0, \mu', \phi') d\mu' d\phi' d\tau_\nu' + \\
D. & \frac{1}{4\pi\mu} \int_0^{\tau_{\nu, total}} \int_0^{2\pi} \int_{-1}^1 e^{-(\tau_{\nu, total} - \tau_\nu')/\mu} \tilde{p}_\nu(\tau_\nu = \tau_\nu', \mu, \phi, \mu', \phi') I_\nu(\tau_\nu = \tau_\nu', \mu', \phi') d\mu' d\phi' d\tau_\nu' + \\
E. & \frac{F_{\nu,0}}{4\pi} \int_0^{\tau_{\nu, total}} \tilde{p}_\nu(\tau_\nu = \tau_\nu', \mu, \phi, \mu_0, \phi_0) e^{-(\tau_{\nu, total} - \tau_\nu')/\mu} e^{-(\tau_{\nu, total} - \tau_\nu')/\mu_0} d\tau_\nu'
\end{aligned}
\tag{0.36}$$

This equation can be easily interpreted in its terms:

- represents the emission from the surface, attenuated by the passage in the overlying layers. Approximations described in paragraph 3.3.2 allow modeling this emission as Eq. (0.9), i.e.: as a thermal one, modulated by an emissivity function. The attenuation factor comes from a simple integration of (0.32);
- describes the thermal emission by the atmosphere. As expected, the emission by the atmospheric layers follows, at every given wavenumber, the Kirckhhoff law and therefore is equal to one minus the reflectance of the layer, given by (0.27). This radiation is attenuated along the path from source point to the observer by the extinction of overlying layers, which have an optical thickness of  $(\tau_{\nu, total} - \tau_\nu')$ ;
- provides the field associated to the single scattering of radiation emitted at the surface. Photons emitted at the surface along the direction  $(\mu', \phi')$  travel in the atmosphere until the level at optical depth  $\tau_\nu'$  (some of them are eliminated, as described by the attenuation factor  $\exp[-\tau_\nu'/\mu']$ ). Here, their direction of propagation is deviated toward  $(\mu, \phi)$ . They go on along their path up to the

observer, experiencing further extinction by atmospheric layers overlying scattering point, described by  $\exp[-(\tau_{\nu, total} - \tau'_{\nu})/\mu]$ ;

- describes photons that experienced several scattering events emerging from the atmosphere. Here, the radiance at the scattering point is indicated explicitly by  $I_{\nu}(\tau'_{\nu}, \mu, \phi)$ , because the variety of phenomena at the origin of multiple field cannot be reduced to simpler representations;
- describes the contribution of Solar radiation reflected by atmospheric layers. The interpretation is very similar to C, keeping in mind that  $(\mu_0, \phi_0)$  represents the Sun position and that  $F_{\nu,0}$  the Sun flux at the planet' distance. The integral spans up to  $\tau_{\nu}=0$  and therefore encompasses also the reflection from the surface.

A further term, related to the reflection by the surface of the diffuse field from the atmosphere, has been neglected due to the very high emissivity (implying low reflectivity) of Martian surface.

The presence of field intensity on both sides of equation (0.36) - and of one of them inside an integral - suggests that it is not usually possible to provide a general analytical expression of  $I_{\nu}$  as a function of physical conditions (temperature, absorbers concentrations) only. Particular solutions for very specific cases represent classical problems for astronomy and Earth's sciences, but their treatment is well beyond the purpose of this introduction.

Equation (0.36) demonstrates however the great information content potentially present in IR observation, due to the number of atmospheric and surface parameters that contribute to the upwelling field. Among them:

Chemical composition is the main factor that defines, for aerosol as well as for gases, the dependence of  $\chi_{E,\nu}$  from  $\nu$ .

Equation (0.33) shows how the concentration of particles as a function of altitude plays a key role in determining the optical depth at a given wavenumber.

Gases absorbing coefficients depend strongly on temperature (that defines the distribution of the molecules population among the different energetic levels and the Doppler broadening of spectral lines) and pressure (collisional broadening).

Mie theory relates the  $\chi_{E,\nu}$  of aerosols with their sizes (being the dependencies from refractive indices included in point 1).

B term of (0.36) demonstrates how the thermal emission from the atmosphere derives essentially from the behavior of air temperature with altitude.

One could think the inversion of (0.36) would allow the computation of  $T(z)$ ,  $P(z)$ , and  $N(z)$  for each components of the atmosphere and the sizes of suspended aerosol.

Following chapters will show the main characteristics of the instruments PFS and VIRTIS and which parameters can actually been retrieved with their data and finally how it can be done.

## **4 General retrieval method**

### **4.1 Introduction**

Once we have available the infrared spectra of Mars and Venus acquired by PFS and VIRTIS, we need to produce models which properly describe (simulate) what the instrument measures, in order to get information on the atmosphere of the planets and to retrieve important quantities, namely the composition.

Many factors contribute to the formation of a spectrum emerging from a planet: the chemical and physical state of the surface, the atmospheric composition and thermal structure, the aerosols content and their nature, the observational and illumination's geometry (emission, incidence and phase angles) and also the instrument's properties as the response function and resolution, since our measured spectrum consist actually in the convolution of the radiance with the instrumental function.

We need to take into account all these factors when working to model the atmospheres and the radiance spectra emerging from it.

In this chapter we illustrate the methods and models we used and built with the aim of computing synthetic spectra, which are essential for comparison with the data produced from the instruments.

We will describe in general the Forward Model for the resolution of the radiative transfer equation, (previously explained with a theoretical approach in paragraph 3.3.6 and now presented in a form applicable to this work), discussing not only the basic background but also the practical choices made to solve the various physical equations; the main mathematical equations required for the retrieval of atmospheric state observed by the instruments will be also introduced. Afterwards we will present the specific methods and results for Venus. In this part we will

include the description of the first approach on modelling the Venus atmosphere; then we will describe the specific task in the investigation of this planet, i.e.: the water content and its variation in the mesosphere, just above the thick Venusian clouds of sulphuric acid. We will show after the atmospheric model developed to solve the RT equation, then we will explain the retrieval methods we implemented to analyse the atmospheric quantities and finally we will show the results, the interpretation, their validation and the implementation of a formal method to quantify the errors.

Next we will describe both the methods and results obtained for Mars, with the task of investigating the CO<sub>2</sub> isotopomers ratio in the atmosphere and the content of carbon monoxide, being these important tracers of atmospheric physical and dynamical phenomena. For this last part we will discuss more briefly the model built up to simulate the Martian spectrum, a mention of the methods to retrieve the physical quantities and then the results, since the retrieval procedure are similar (despite the model changes completely) to the ones used to study Venus atmosphere.

## **4.2 Forward model: resolution of RT equation**

The Forward Model simulates the radiance a specific instrument would measure, once the atmospheric (as quantified by an input state vector) is fixed. The radiance is calculated by solving the RT equation for the specific condition given by the chosen spectral range and the observative conditions.

For this aim we have used and adapted for the different tasks of the work some basic radiative transfer procedures which implement line-by-line calculations of gaseous and aerosol opacities, transmittance, atmospheric radiance spectra, and other related quantities, being local thermodynamic equilibrium (LTE) condition the only assumption.

General radiative transfer problem can be subdivided in two independent tasks: computation of opacity (and other properties for aerosols) and radiative transfer itself. From a practical point of view, the most important steps needed to solve the RT problem are:

- to extract information about spectral lines parameters from a HITRAN-formatted spectroscopic database and converts it to a reduced format. In this step it is possible to consider and modify isotopic ratios of the gases and the Lorentz line half-widths
- to create a wavenumber grid optimized according line positions, widths and strengths
- to calculate monochromatic gaseous absorption coefficients which are then used by radiative transfer programs
- to implement radiative transfer computation to calculate the transmittance of the atmosphere and the outgoing radiance possibly taking into account multiple scatterings
- to convolve the monochromatic spectrum with the instrumental response function.

The *input* state vector and the others input data are:

- *spectroscopic data* (derived from, e.g. HITRAN or CDS database): information on molecular spectral lines adapted to Venus and Mars atmospheric conditions (temperature and pressure profile)
- *air temperature as a function of pressure and altitude* along the height of the atmosphere and at the surface. Parameters describing *observative conditions* (geometry) and solar illumination ( $\theta_{inc}$ ,  $\theta_{emis}$ ,  $\theta_{phase}$ , dist M-S, altimetry)
- boundary conditions of *incident solar flux* at the top of the atmosphere and *albedo*
- *aerosols* properties and distribution
- instrumental function

while the *output* is the monochromatic spectrum (I.e. solution of RT equation) and its convolution with instrumental function.

A simplified scheme of the methods is showed in Figure 25.

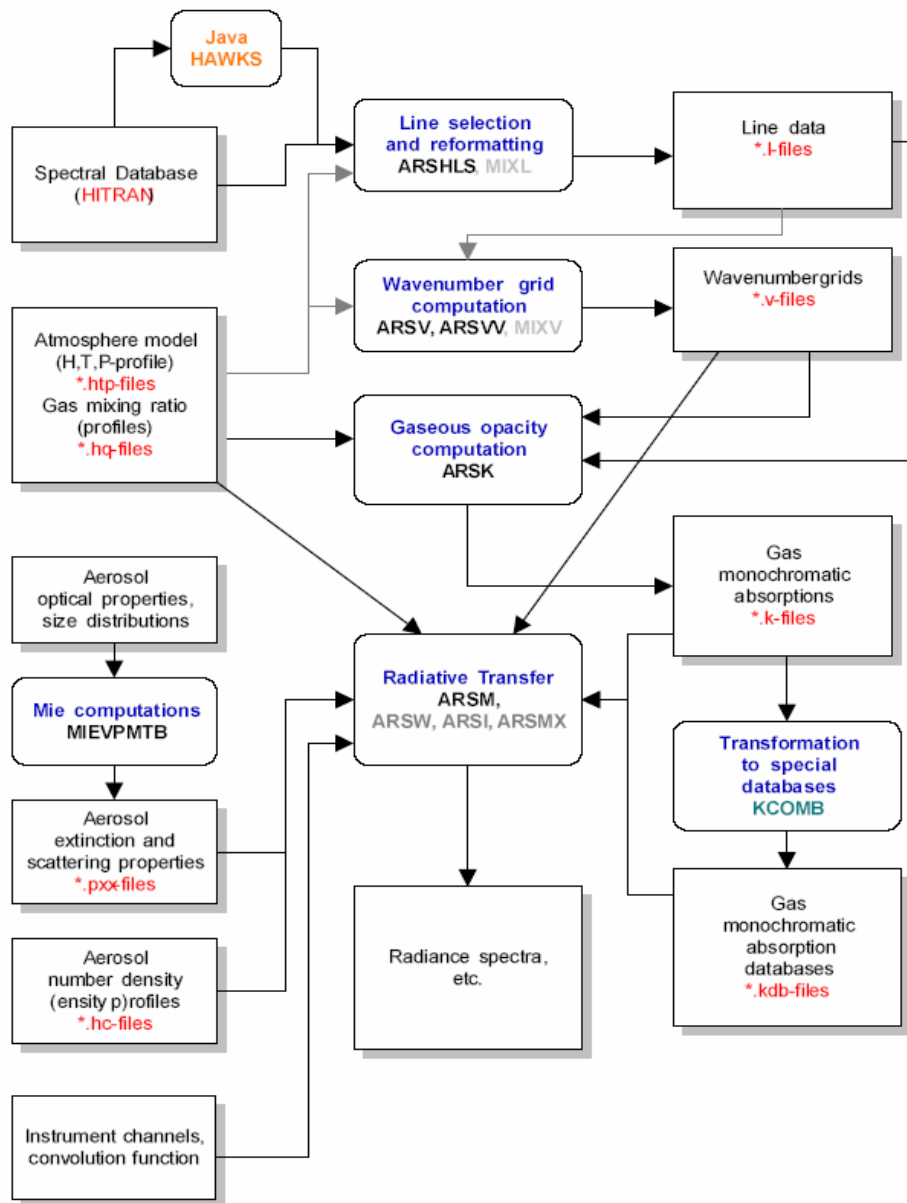


Figure 25. Simplified chart of the software package for radiative transfer computations: the actions in blue color correspond to the steps described in the text; names in upper case represent the procedures which implement those actions; in red color are shown the input and output files of each step; in black lowercase are evidenced the input and output information, while in yellow it is pointed out an external program which can eventually be used instead the personal one.

The information for each line which is extracted from spectroscopic databases consists in the following parameters:

- $\nu_0$  - line center position at standard atmospheric conditions ( $T_0 = 296$  K,  $p_0 = 1$  atm = 101325 Pa);

- $S(T_0)$  - line intensity in  $\text{cm}^{-1}$  / (molecule  $\text{cm}^{-2}$ ) at temperature  $T_0$  ;
- $\alpha_{\text{air}}(P_0, T_0)$  - halfwidth at half maximum (HWHM) of the line width induced by collisional broadening by other gases of the terrestrial atmosphere (air broadened halfwidth), measured in  $\text{cm}^{-1}$  /atm;
- $\alpha_{\text{self}}(P_0, T_0)$  - HWHM of the line in the pure gas (self broadened line halfwidth);
- $E''$  — lower state energy of the transition, measured in  $\text{cm}^{-1}$ ;
- $m$  — index of the dependence of the temperature on the Lorentz halfwidth
- $Q(T)$  total statistical sum (rotational + vibrational).

From this information are then computed the gaseous absorptions following the method by Rothman et al., (1992, 1996).

Line intensity for any temperature (for the HITRAN-96 database from 70 to 2000 K) is defined as follows:

$$S(T) = S(T_0) \frac{Q(T_0)}{Q(T)} \exp\left\{-c_2 E'' \left(\frac{1}{T} - \frac{1}{T_0}\right)\right\} \frac{1 - \exp(-c_2 \nu_0 / T)}{1 - \exp(-c_2 \nu_0 / T_0)} \quad \text{with}$$

$$c_2 = \frac{hc}{k_B} \quad (0.37).$$

$S(T_0)$  is the line intensity at the temperature  $T_0$ ,  $E''$  is the lower state level energy of the transition,  $Q(T)$  is the full (rotational + vibrational) statistical sum.

Absorption cross-section per molecule [ $\text{cm}^2$ ] in a spectral line (Voigt line profile) is given by the formula:

$$\sigma_\nu = \frac{Sa}{\pi^2 \beta} \int_{-\infty}^{+\infty} \frac{e^{-t^2} dt}{a^2 + (x-t)^2} \quad \text{with} \quad a = \frac{\alpha}{\beta}, \quad x = \frac{\nu - \nu_0}{\beta} \quad (0.38)$$

and where  $S$  is the line intensity,  $\nu_0$  is the line center,  $\alpha$  is the Lorentz halfwidth,  $\beta$  is the Doppler halfwidth defined as

$$\beta = \frac{\nu_0}{c} \sqrt{\frac{2RT}{M}} \quad (0.39)$$

where  $R$  is the universal gas constant,  $T$  is the temperature, and  $M$  is the molecular weight [g/mole] of the gas. Integral over  $t$  of the cross section can be calculated using special interpolation procedures, e.g. Humlicek (1984) or Matveev (1972).

If the Lorentz halfwidth  $\alpha(P_0, T_0)$  at the pressure  $p_0$  and temperature  $T_0$  is known, then for other pressures and temperatures it can be computed by the formula:

$$\alpha(p, T) = \alpha(p_0, T_0) \frac{p}{p_0} \left( \frac{T_0}{T} \right)^m \quad (0.40)$$

where  $m$  is a particular parameter for each individual line. When the collision cross-section does not depend on temperature, the theory gives  $m = 0.5$ . In practice,  $m$  is slightly different. In addition, the difference in the broadening conditions on the Earth and other planets should be taken into account.

Note, that the formula from Rothman et al. (1996) for the Lorentz line halfwidth includes both air and self- broadening:

$$\alpha(p, T) = (\alpha_{air}(p_0, T_0)(p - p_s) + \alpha_{self}(p_0, T_0)p_s) \frac{1}{p_0} \left( \frac{T_0}{T} \right)^m \quad (0.41).$$

However, the validity of this formula is not evident (more reasonable seems to sum up self- and foreign-broadened opacities rather than

Lorentz line halfwidths), and for minor gases it could give only a very small correction to the spectra. For this reason, we use here the previous formula. Pressure line shift is ignored due to its usually limited effects and lack of reliable experimental data on it for many species.

The total opacity produced by all the lines is equal to the sum of the individual line opacities:

$$\sigma_\nu = \sum_i \sigma_{\nu_i} . \quad (0.42) .$$

Now, it is possible to use a line-by-line computational method, summing the contributes of all lines for each wavenumber.

Absorption coefficient per unit path length for 100% mixing ratio<sup>6</sup> is equal to

$$K_\nu^1 = \sigma_\nu n \quad \text{with} \quad n = \frac{p}{K_B T} \quad (0.43).$$

To describe the extinction of a beam of radiation crossing an homogenous atmospheric layer  $dl$  with an incidence angle  $\cos\theta$ , we define the optical depth  $\tau_\nu$ .

This quantity, once divided for  $\cos\theta$ , is interpreted as the average number of interactions with matter of a photon with wavenumber  $\nu$ , crossing the depth  $dl$ :

$$d\tau_\nu = K_\nu^1(l)q(l)dl \quad (0.44).$$

Assuming an atmosphere composed of a finite number of plane and parallel layers each with uniform temperature and pressure in its interior, to radiation crossing between the levels  $l=0$  and  $l=z_1$  is associated an optical depth of:

$$\tau_\nu = \int_{l_0}^{l_1} K_\nu^1(l)q(l)dl \quad (0.45).$$

Therefore optical depth is the integral of absorption coefficient  $K$  multiplied by the mixing ratio  $q(l)$  along the line of sight.

In the above approach the opacity is linear with respect to number density of molecules. This cannot hold true, when both self- and foreign-broadening are important. In these cases, monochromatic gaseous absorption coefficient computed for some mixing ratio profile cannot be used for different abundances. The only way to consider such problems is to compute the opacity for some temperature, pressure and abundance profiles, and to repeat the entire computation for any other conditions. This is the approach we adopted in all the computations of synthetic spectra for data simulations.

Transmittance is simply the exponent of the optical depth along the line of sight:

$$t_\nu = e^{-\left(\frac{\tau_\nu}{\cos \vartheta}\right)} \quad (0.46).$$

In the solar region, we often deal with the total transmittance of the atmosphere from the space to the surface and back:

---

<sup>6</sup> The *mixing ratio* is the *molar*

*concentration*:  $\frac{\text{total number of molecules of the considered gas}}{\text{total number of molecules}}$  for each point.

$$t_{\nu} = e^{-\tau_{\nu} \left( \frac{1}{\cos \vartheta_0} + \frac{1}{\cos \theta} \right)} \quad (0.47)$$

where  $\tau_{\nu}$  is the total optical depth in the nadir (strictly vertical) direction,  $\vartheta_0$  is the Sun zenith angle and  $\theta$  is the line of sight zenith angle.

In most of the cases we performed an exact line-by-line computation, without approximations which in general increase performance but reduce precision. For this reason, the adopted method is not very fast (in computations of gaseous opacity and simple spectra) with respect to the codes with special short cuts, as FASCODE, LBLRTM, MODTRAN, which give ready approximate solutions for fast simulations of transmission and radiance spectra and radiative transfer for Earth's atmosphere. They are useful to get a ready solution but are not flexible being difficult to deal with the details of their computation. Since my work implied often the investigation of subtle effects of radiative transfer options in a non-Earth atmosphere, the slower but more robust approach was preferred.

#### 4.2.1 Radiative transfer without scattering

The Radiative Transfer Equation for the thermal emission from a plane parallel atmosphere in local thermodynamic equilibrium, as seen by a nadir viewing instrument, predicts that the upward monochromatic radiation intensity, or radiance, is given by the integral of the Planck function on transmittance (0.48) (which depends on altitude) from the bottom (or from a reference altitude) to the top of the atmosphere, plus an added term describing the surface emission:

$$I_{\nu} = \varepsilon_{\nu} B_{\nu}(T_{suolo}) e^{-\frac{\tau_{\max}}{\cos\theta}} + \int_0^{\tau_{suolo}} B_{\nu}(T(\tau_{\nu})) e^{-\frac{\tau_{\nu}}{\cos\theta}} d(\tau_{\nu} / \cos\theta) \quad (0.48).$$

$$\Rightarrow I_{\nu} = \varepsilon_{\nu} B_{\nu}(T_{suolo}) \cdot t_{\nu \cdot suolo} \int_{t_{\min}}^1 B_{\nu}(T(t_{\nu})) dt_{\nu}$$

In other words the FIRST member is composed by: the emission from the surface, attenuated by the passage in the overlying layers; the other term is total contribution of the thermal emissions by the atmospheric layers, each of them attenuated by overlying layers. This term plays a major role in the definition of the signal level of the Martian spectrum observed by PFS in its LWC where CO<sub>2</sub> isotopes are investigated. Furthermore, this last term makes the thermal infrared observations very different from the ones in the near infrared in which the molecules between the surface and the observer act just as a filter of the solar radiance reflected from the surface of the planet. In cases where it is present for example a thermal inversion (air in a layer hotter than the lower one), radiation coming from the surface may become smaller than the one produced from the atmospheric gases. This appears in the spectrum as an excess of radiation in respect to the planckian corresponding to surface's temperature and in the wavenumber where the optical depth of the gas is much higher than one.

This can be easily observed in Martian polar zones or in the early morning, when the surface is colder. PFS LWC show sometimes this features, which are difficult to be modeled unless the atmospheric temperature profile is well known.

This part is obviously important in the thermal part (LWC) of the Martian spectrum but even in the SWC up to 3000 cm<sup>-1</sup> (see section 6). It is also main in the thermal part of the Venus spectrum where the lower part of the atmosphere is probed in nightside acquisition around 5 microns.

In the near infrared, where the solar radiation dominates, the radiance is simply the solar radiation flux  $F_{\nu}^0$  outside the atmosphere (divided by  $\pi$ )

times total atmosphere transmission, with account for the surface albedo  $A_v$  :

$$I_v = \frac{F_v^0 \cos \theta}{\pi} \cdot A_v \cdot e^{-\tau_v \left( \frac{1}{\cos \theta_0} + \frac{1}{\cos \vartheta} \right)} \quad (0.49).$$

This term plays a major role in defining the signal level observed by PFS in its SWC and it contributes to the radiation out coming from the dayside acquisitions of Venus, together with the scattered radiation term.

The spectrum of the radiation emerging from a planetary atmosphere can be obtained directly numerically integrating the (0.48) o (0.49) once we know both the temperature profile and the concentration profile through the atmosphere of the optically active component.

In the regions where contributes of thermal emission and solar radiation are both important they will be both included in the computation.

This is the case of the investigation of carbon monoxide in Martian atmosphere in the band at 2600  $\text{cm}^{-1}$ .

The final step of a synthetic spectrum computation, for comparison with the measured one, is the convolution with the instrumental function:

$$I(\nu) = \int I_{\nu'} \Phi(\nu - \nu') d\nu' \quad (0.50).$$

This convolution makes necessary the integration of (0.48) o (0.49) on a grid with a spectral step much lower than the one of the observed spectrum.

Even this can be an important point on the final quality of a computed spectrum; for example, the relative low atmospheric pressure at the surface, produces thin lines in the Martian spectrum. For this reason, to properly simulate it, it's needed a monochromatic grid with a very small step ( $5 \cdot 10^{-3}$ ), while some tests showed in the following chapter, demonstrated that, because of the high pressure, in Venus atmosphere

lines are much broadened and a wider monochromatic step is enough to compute the spectrum.

The same procedure is adopted for the monochromatic transmittance and reflectance to compute the corresponding convoluted quantities.

The efficiency of calculations can be increased by the usage of various time-saving procedures as line selection, decomposition of the line profile, appropriate choice of the altitude and wave number mesh width, interpolation between levels in the  $T(p)$  profile and many others, which are eventually adopted case by case if they do not produce important changes in the results.

#### **4.2.2 Radiative transfer with multiple scattering**

In addition to the case of pure gaseous atmosphere considered above, it can often be important to simulate an atmosphere in which some aerosols are present.

In Martian atmosphere at least two different types of aerosols can be found (silicate dust and water ice particles) while in the Venusians' one we expect aerosols of sulphuric acid, droplets of liquid water and probably dust of some particular minerals found in the surface.

On Mars, dust is particularly important, being able to strongly modify the energetic balance of soil and atmosphere through the absorption of the visible solar radiation. Water ice forms usually clouds and its presence gives information on the atmospheric temperature and its water vapour content. On the other hand, the great amount of aerosols in the Venusians' atmosphere is responsible of the strong greenhouse effect present on the planet. This is due to relative transparency of the clouds to the solar ultraviolet radiation, which is absorbed and reemitted in the infrared range at which the atmosphere becomes opaque, trapping radiation between the surface and the clouds.

The emerging field, in the presence of aerosols, have some added terms due to: the contribute to the field of the photons which are emitted at the surface in any direction and then send towards the observer after a single interaction with the particles; the contribute of photons which went towards multiple scattering events or diffusion of photons emitted by the atmosphere.

These contributes contain the intensity of the field, whose presence in both the left and right terms of the radiative transport equation makes impossible to achieve an analytic solution of  $I_v$ .

Moreover the aerosols extinction crossing section, even if not dependent from temperature, has very complicate relation on the particles size and their complex refractive indices. Finally aerosols concentrations may go thought strong spatial (in 3 dimensions) and temporal variations (see Mie theory for details on a complete analytical solution of Maxwell's equations for the scattering of electromagnetic radiation by spherical particles).

For these reasons usually the problem is faced trough the use of numerical models which approximate the continuum radiation field present in the atmosphere with a finite number of streams along some fixed directions.

There are several ways to make computations for a scattering atmosphere and the choice among some options is done for each different case.

For the particular task of the treatment of scattering we implement within our code different approaches which in some part include currently used procedures.

These approaches consist in:

1. Approximation of black aerosol. Aerosol absorption is simply added to the gaseous absorption. This is an acceptable approximation for the thermal region, while for the solar region it is usually absolutely invalid.
2. Single scattering and other approximate solutions for multiple scattering. Two stream approximation is used to estimate the multiple scattering part of the source function as average values on two hemispheres only. The source function is then integrated to give the intensity of outgoing radiation. This approach is similar to the one

described for example in Isaacs *et al.* (1987). We use three options for the computation of fluxes: the first is the TWOSTR code by Kylling *et al.* (1995); the second is the layer flux adding procedure similar to that used in Modtran 3 (Isaacs *et al.*, 1987); the third is the combination of them — the first for thermal emission and the second for the solar radiation (however, this option is implemented only together with a “correlated-I” correction).

3. DISORT (Discrete Ordinate Radiative Transfer) code (Stamnes *et al.*, 1988, 2000), which can be considered as a “precise” solution.

4. “Correlated-I” correction (Ignatiev *et al.*, 2005) to the approximate solution. This approach provides the spectrum almost coinciding with that given by DISORT, but in hundreds times faster.

5. SHDOMPP code by F. Evans (1998).

## **5 Results for Venus**

The spectrum of Venus in the whole range observed by VIRTIS, offers many topics which can be successfully investigated.

The reflected solar spectra of Venus provide information on atmospheric composition and aerosol. In the visible and the near-IR range, the reflected spectrum exhibits signatures of CO<sub>2</sub>, H<sub>2</sub>O and CO, while observed on the dayside, it probes the middle atmosphere above the sulfuric cloud level, at a pressure of about 1 bar.

The infrared spectrum presents instead a very peculiar property: while usually thermal contribution dominates planetary spectra only beyond 3–4 μm, the thermal emission of Venus is detected at much smaller wavelengths in a limited number of spectral windows (down to about 1 μm) on the night side of the planet, due to the very high temperature of surface and lower atmosphere. This fact provides an excellent tool for probing the chemical composition of the lower Venusian atmosphere.

It is possible to see through the clouds by observing the night-side of the planet at infrared wavelength: only through spectral “windows” we can see thermal radiation from the lower atmosphere down towards the surface. This makes it possible to study the atmospheric composition and properties in regions which would be hard to reach using in-situ probes, due to the extreme temperatures and pressures.

Beyond 5 μm, the strong CO<sub>2</sub> band at 15 μm which dominates the thermal spectrum of Venus is anyway not included in the VIRTIS spectral range.

In the next paragraph we will describe briefly the initial approach to simulate the night side spectrum, outside the atmospheric windows, in order to build the simulations of the spectra and validate the atmospheric model and the computation procedure. Then we will show with more

details the methods for water vapor retrieval, which needed to model the dayside spectrum of Venus.

## **5.1 Venus spectra computation to model VIRTIS-M data**

The spectrum of the radiation emerging from Venus atmosphere can be subdivided in three main parts which we need to model, depending on the spectral range and consequently on the different observations of the planet:

*Night side observations in the spectral region 3.5 – 5.0  $\mu\text{m}$ .* In this part of the spectrum, in the data acquired on the night side of the planet we observe mainly the *thermal emission from the clouds*.

*Night side observations in the spectral region 1.0 - 3.5  $\mu\text{m}$ .* In this range we can look through the atmospheric windows toward the deep atmosphere; in this range, depending on the wavelength, we can get information from different altitudes in the atmosphere, almost reaching the surface. The problems to face in modeling this spectral range are due to the possible unknown variability of the clouds vertical profile and the CO<sub>2</sub> spectral properties at high temperatures and pressures. Line broadening produces a continuum on the spectrum as a sum of the contributes of the wings of the lines, which is not known and not easy to simulate. Moreover in the high atmosphere airglow emissions (nonLTE) may also be present in the spectra.

*Day side observations in the spectral region 1 - 5  $\mu\text{m}$ .* In this case we observe the solar radiation scattered from the clouds in the range 1.0 - 3.5  $\mu\text{m}$  and the solar radiation contribute plus the thermal emission (which becomes important close to 5  $\mu\text{m}$ ) in the range 3.5 – 5.0  $\mu\text{m}$ . The problems related to this region are due to the importance of a proper treatment of the scattering in the simulations, which may need the use of a precise

solution of the radiative transfer equation such as the ones provided by DISORT. Moreover is possible to find in this range NLTE emission of CO<sub>2</sub> which are not considered in our models.

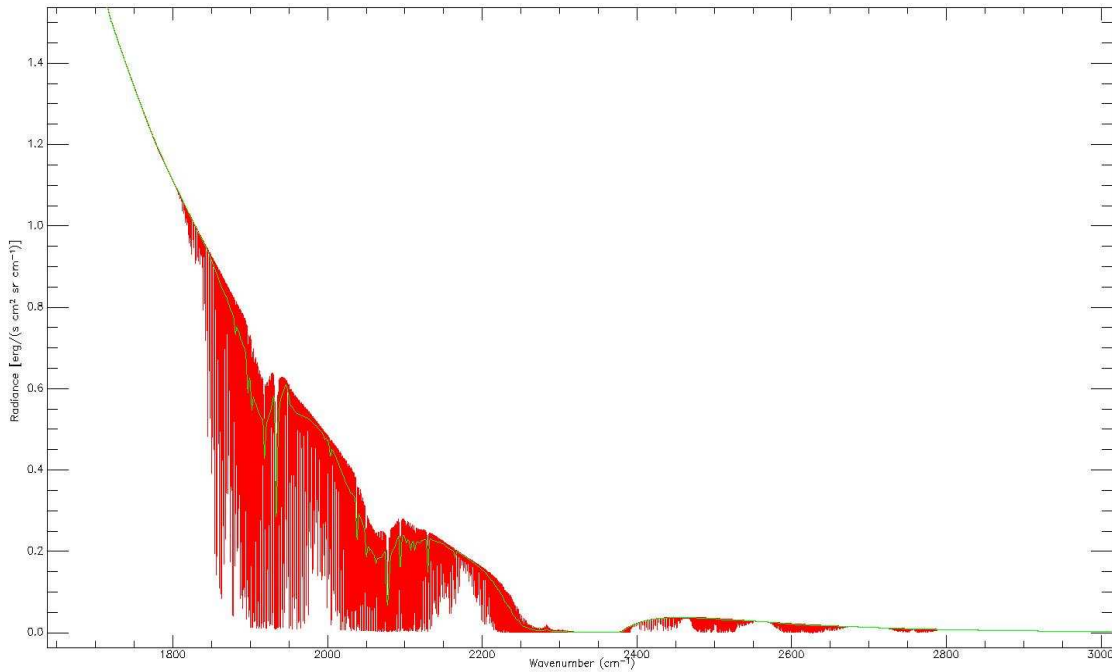


**Figure 26. Example of a simulation of a night side spectrum, monochromatic (red) and convolved at VIRTIS H resolution (green).**

### **5.1.1 Models for night side spectra in the region 3.5 – 5.0 $\mu\text{m}$**

We have chosen to perform the validation of the night side model in the 3.5-5.0 micron spectral range being this the simplest case: there are no high pressure's effects which are instead present in the deep atmosphere probed at lower wavelengths and there is no relevant scattering of the solar radiation.

The method we used to obtain a proper simulation of this region consisted in the selection of a “nominal” case for the synthetic spectra computations

and subsequent implementation of some sensitivity tests to assess the effects of the variation of some key parameters.

In the nominal case we used:

- HITRAN database for spectroscopic lines information
- A uniform monochromatic spectral grid with step of  $10^{-2} \text{ cm}^{-1}$
- $\text{CO}_2$  as only atmospheric absorbing gas
- Line cut-off of  $200 \text{ cm}^{-1}$  for the wings of  $\text{CO}_2$  line
- Mode (2) aerosols (Esposito et al.,) which means droplets of a mixture of  $\text{H}_2\text{SO}_4$  and water
- Aerosol vertical profile according to Zasova et al., 1999 (as derived from FTS Venera 15 data)
- Two stream approximation for the treatment of scattering
- Simple initial convolution with a sinc function with resolution of  $1.8 \text{ cm}^{-1}$

The validity of these assumptions was investigated by means of a series of specific tests, described below.

### **5.1.2 Test: comparison of $\text{CO}_2$ spectroscopic databases**

We compared the results obtained using some databases – HITRAN (Rothman et al., 1996), CDSD (Carbon Dioxide Spectroscopic Database for Venus; Tashkun, 2006),  $\text{CO}_2$  “HOTBASE” for Venus (derived from HITRAN at high temperatures; Pollack et. al., 1993) - and some combinations of them. The HITRAN spectroscopic database is the most common database which provides the spectroscopic quantities needed to compute absorption coefficients and then the transmittance of a gas and the radiance spectrum. The information contained in HITRAN for some species and for particular spectral regions are derived either from theoretic computations

or retrieved from experimental measurements. It is a good starting database, but there are some conditions in which some problems related with its usage may occur. Primarily, it pertains to Earth atmospheric standard conditions of pressure and temperature, while near-surface Venusian conditions of high pressure and temperature at the surface may require a more suitable database, e.g.: HOTBASE. Noteworthy, this problem is not very relevant when the simulated radiation forms mostly above the clouds where the T and P values become closer to the standard ones. On the other hand, this becomes important for the use of a correct lines' shape when modeling the lowest part of the atmosphere. Another problem of HITRAN usage is due to its incompleteness. This point may become very relevant since in condition of high pressure the integrated effects of weak lines may become dominant.

In general HOTBASE contains weaker lines than CDS, but in total CDS contains more lines than HOTBASE. Then something is missing in both databases (in particular CDS, lacks some CO<sub>2</sub> isotopomers effects).

In Table 6 we show the comparison on the number of CO<sub>2</sub> lines present in the mentioned spectroscopic databases which we have performed while searching the best database to use for our models.

Due to huge amount of lines, the attempt to make simulations using CDS failed, because of very long radiative transfer computation time (in the order of months for CO<sub>2</sub> absorption coefficient computation). For these reason we tried also to combine all the information of the two databases, but we found difficult to compare weak lines in CDS and HOTBASE, because the quantum numbers' indications of the transitions are in different (and incompatible) format and sometimes totally absent precluding therefore a unequivocal cross identification of lines.

In this situation was impossible to recognize which lines were present in the three databases. The final compromise was to combine the databases on spectral range basis, selecting just some parts from different sources: we created a database based on HOTBASE with the integration of some CDS and HITRAN parts, that is a substitution of a whole spectral interval with the one of the other database, in the parts which are more

complete and important for our simulations. In the same way we created a database based on CDSD with some parts of HOTBASE or HITRAN. These combined databases were eventually used in subsequent investigations.

| Isotopomer | HITRAN-04<br>(Rothman et al.) | HITEMP-02<br>1000K<br>(Rothman et al.) | CO <sub>2</sub> HOT BASE<br>(Pollack et al., 1993) | CDSD<br>(Tashkun et al., 2006) |
|------------|-------------------------------|--|--|--------------------------------|
| Total      | 62913                         | 1032269                                | 7088178  | 10041959                       |
| 1 (626)    | 27979                         | 741495                                 | 3716014  | 5773233                        |
| 2 (636)    | 8836                          | 141469                                 | 1233325  | 1727545                        |
| 3 (628)    | 13445                         | 137775                                 | 1727069  | 1673836                        |
| 4 (627)    | 7739                          | 6625                                   | -  | 867345                         |
| 5 (638)    | 2312                          | 2312                                   | 411770   | -                              |
| 6 (637)    | 1593                          | 1584                                   | -  | -                              |
| 7 (828)    | 721                           | 721                                    | -  | -                              |
| 8 (728)    | 288                           | 288                                    | -  | -                              |

**Table 6.** On the comparison of CO<sub>2</sub> spectroscopic databases

### 5.1.3 Choice of the monochromatic grid

A correct choice of the monochromatic grid for the computation of the spectrum may result very important; to properly simulate Martian atmosphere we need a grid with a step of at least  $10^{-3} \text{ cm}^{-1}$  because pressure is low and consequently lines result thin. This fact eventually requires a very dense grid to properly model their shape. A wider step of the monochromatic spectrum would cause the exclusion of many

information (line total intensity) when integrating the lines' contributes along in the wavenumber domain.

The high pressure of the Venus atmosphere causes a broadening of the lines, making less important the use of a thick grid. On the other hand, it is important to stress that the finer is the grid the longer is the computation time (linear dependence in computation of opacities); for this reason we need to choose the grid with the widest spectral step which does not produce an appreciable loss of information in the spectrum.

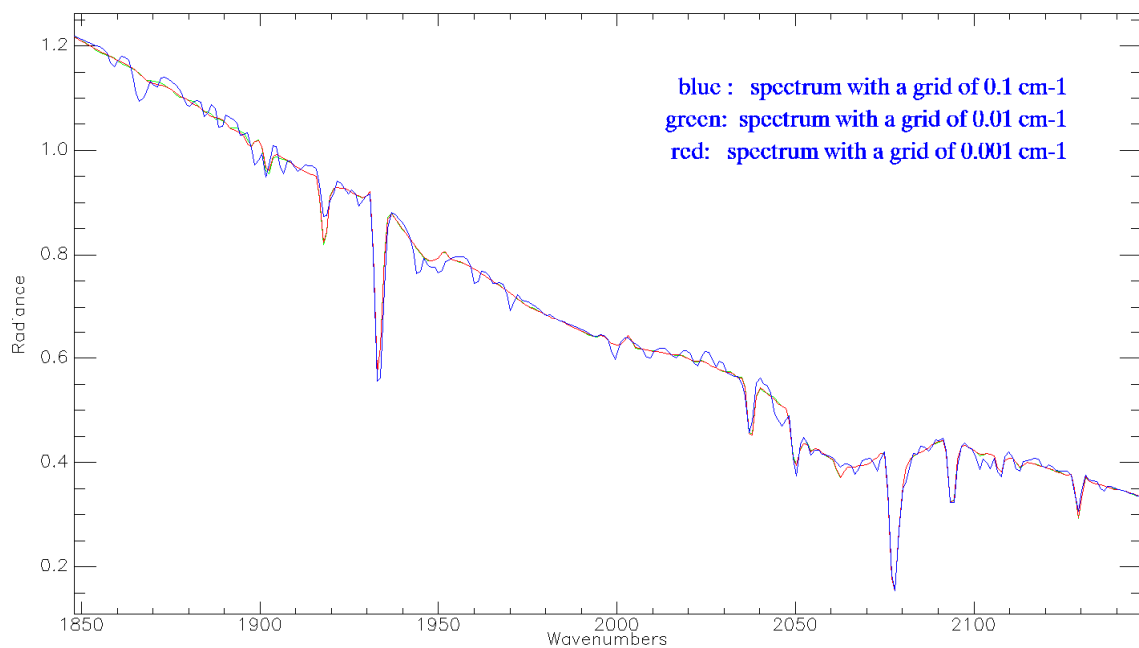


**Figure 27. Comparison among spectra computed on grids with three different steps: 0.1, 0.01, 0.001  $\text{cm}^{-1}$ . In the picture wavenumbers are in  $\text{cm}^{-1}$  while radiance in  $\text{erg s}^{-1} \text{cm}^{-2} \text{sr}^{-1} / \text{cm}^{-1}$ .**

We computed spectra on monochromatic grids with different step of  $10^{-1}$ ,  $10^{-2}$  and  $10^{-3} \text{ cm}^{-1}$  (Figure 27), concluding that  $10^{-1}$  is surely not enough to obtain a correct spectrum, while the spectra computed with the other two steps are almost identical. For this reason we chose the widest one  $10^{-2} \text{ cm}^{-1}$  (for computational speed up), which is enough for a correct simulation.

### 5.1.4 Test of different CO<sub>2</sub> line cutoff

When implementing a line-by-line radiative transfer computation, for each wavenumber the contributions of all the lines are summed. A line has wings of infinite length so it becomes important to decide at which value of width the line's wings become negligible, keeping in mind that for high pressures lines are much broadened and their contribution to the spectrum may become important even at wavenumbers very far from the line center. We tested the radiance's computation using a value for CO<sub>2</sub> line cut-off of 200 and 1000 cm<sup>-1</sup>.

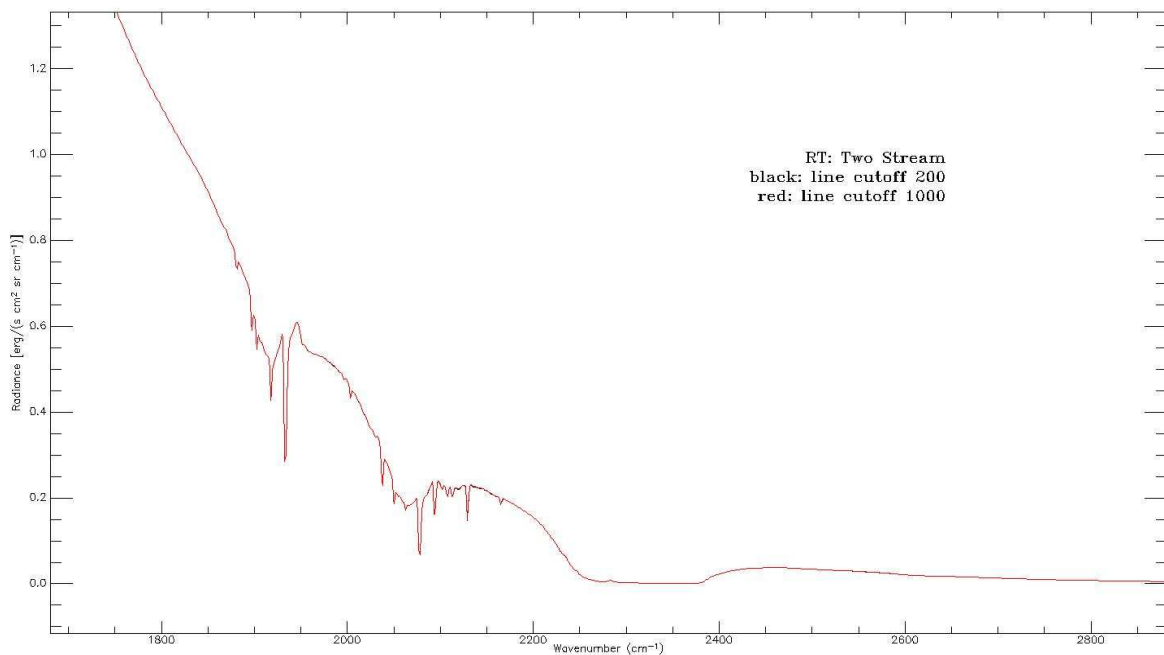


**Figure 28.** Synthetic spectra computed with a CO<sub>2</sub> line cut-off of 200 and 1000 cm<sup>-1</sup>. We can observe that the smaller value is enough to consider the mayor contribute of the lines.

As we can see from Figure 28, the difference in the spectrum with the two values is very small, also in respect to the instrumental Noise Equivalent Radiance (NER); for this reason we chose the smaller, 200 cm<sup>-1</sup>, which reduces much the computation time.

### 5.1.5 Test of different radiative transfer options for the treatment of scattering

Different methods for the treatment of scattering in the radiative transfer equation were briefly described in paragraph 4.2.2.

We tested the resulting spectrum using TWO STREAM approximation and DISORT.

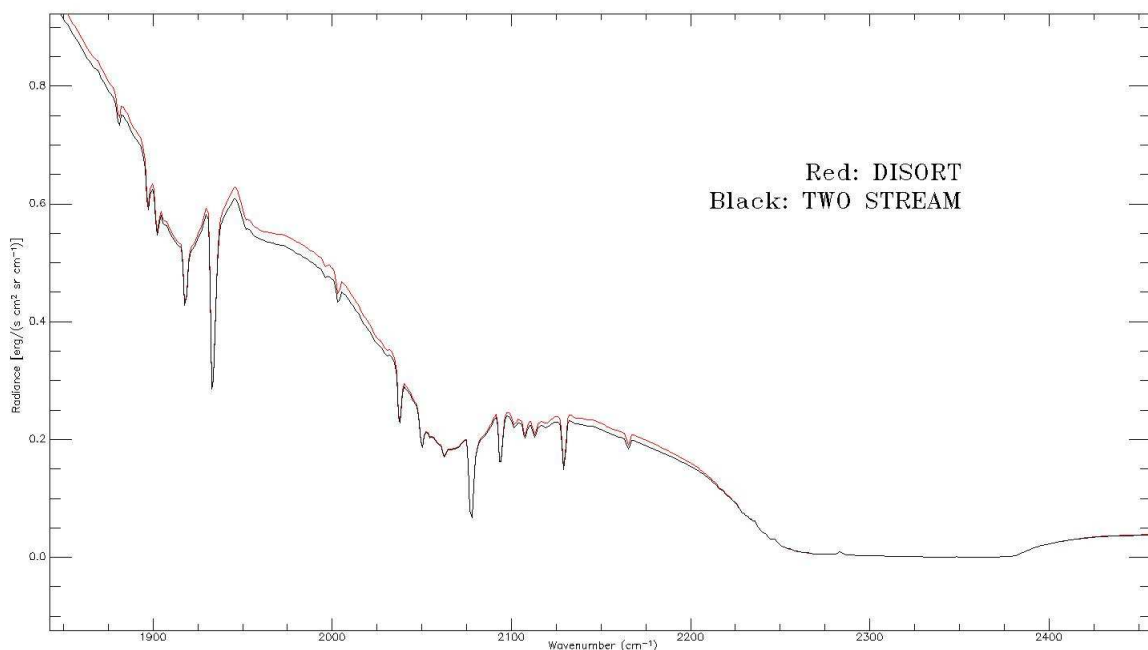


**Figure 29. Synthetic spectra computed with TWO STREAM approximation for scattering computation and the "exact" solution obtained with DISORT. We can observe in some part of the spectrum small difference in the continuum. Anyway this test has been done also for others spectral range and different observation and illuminating geometry because the difference between the two method can become negligible or important at different conditions.**

As we can see from Figure 29 there is some difference in the level of the continuum but not so high. For this reason we can use TWO STREAM if short computation time is required, otherwise implementation of DISORT computation could be more precise, especially when modeling observations acquired at great emission angle and with the sun at high

incidence angle for whom scattering effects are expected to be more critical.

### **5.1.6 Validation of a fast direct RT method for the retrieval of the atmospheric temperature profile**

Simulations of the radiation emerging from an atmosphere in the thermal infrared region require the use of a pressure-temperature profile which represents atmospheric conditions. This is important especially when modeling the spectra of the night side of the planet, when the thermal emission contributes of the atmosphere becomes predominant. The T(P) profile is expected to be more stable, but not well known, in the lower atmosphere, where the greenhouse effect thermalizes the region under the thick clouds layer. On the contrary it is necessary to know the variations of the temperature vertical profile to simulate the thermal emission in the mesosphere above the clouds. This task is reached with the implementation of an inverse code for the retrieval of the temperature profiles in the atmosphere by means of an inversion method applied on the CO<sub>2</sub> band in the range 4250 - 5000 nm. (Grassi)

This model is the same used to retrieve the Martian temperature-pressure profiles from the PFS data but it was needed to validate it for the usage in Venusian atmosphere as observed in VIRTIS data. Due to huge amount of spectra acquired from the image spectrometer, it was necessary to implement a fast direct radiative transfer method to speed up the computation of the models used by the retrieval inverse code.

This method is used for calculation of atmospheric transmittance in planetary atmospheres, as an approximate replacement of the line-by-line method described above, to be considered the most accurate technique since it takes directly into account the contribution of numerous lines to the absorption at each wavenumber.

In the fast method, the gaseous absorption coefficient is represented as a product of two functions:  $k(p,T,\nu) = G(p) \cdot F(T,\nu)$ , where  $G(p) = p/p_0$ , and  $F(T,\nu)$  is a function of temperature and wave number which describes the contribution of many lines to absorption at wave number  $\nu$ . Time consuming line-by-line calculations are involved in  $F(T,\nu)$ . They are performed only once on a specified temperature and wavenumber grid. This created matrix is then used for fast interpolative determination of the absorption coefficient at any atmospheric level.

Expansion of transmittances takes directly into account the convolution with instrumental function (CT or “ $\beta\alpha$ ” method).

CO<sub>2</sub> transmittances are evaluated on a fixed pressure grid by a non-linear expansion as a function of temperature

$$\ln Tr(\nu_i, p_j) = \ln Tr(\nu_i, p_{j-1}) + \left[ \ln Tr_0(\nu_i, p_j) - \ln Tr_0(\nu_i, p_{j-1}) \right] \left( \frac{\bar{T}_0(p_j)}{\bar{T}(p_j)} \right)^{\beta(\nu_i, p_j)} e^{\left( \alpha(\nu_i, p_j) \frac{\bar{T}(p_j) - \bar{T}_0(p_j)}{\bar{T}(p_j) \bar{T}_0(p_j)} \right)}$$

$$\bar{T}(p_j) = \frac{T(p_j) + T(p_{j-1})}{2}$$

$$\bar{T}_0(p_j) = \frac{T_0(p_j) + T_0(p_{j-1})}{2} \quad (0.51)$$

In order to validate the procedure we performed a comparison of radiances derived with the convolved transmittance (CT) method and the line-by-line (LBL) calculations, together with the NER. This was done on a set of temperature-pressure profiles thought to be representative of a variety of Venus conditions (173 cases in total).

We computed, for each case of temperature-pressure profile, the difference between spectra obtained with the two methods and the averaged value and its standard deviation.

As we can see in the examples in Figure 30, the errors related to CT method are usually small when compared to NER, confirming that it can be used when really fast computation are needed, as in the case of temperature profiles retrievals.

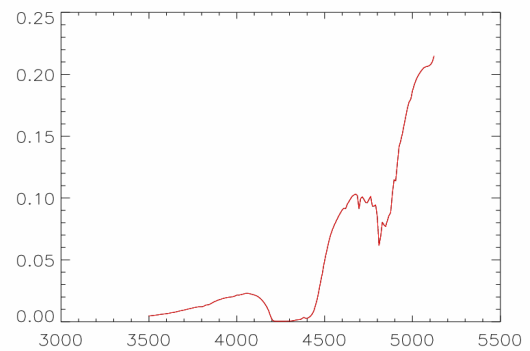
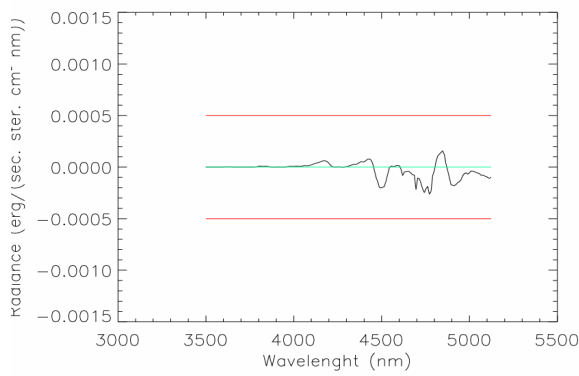
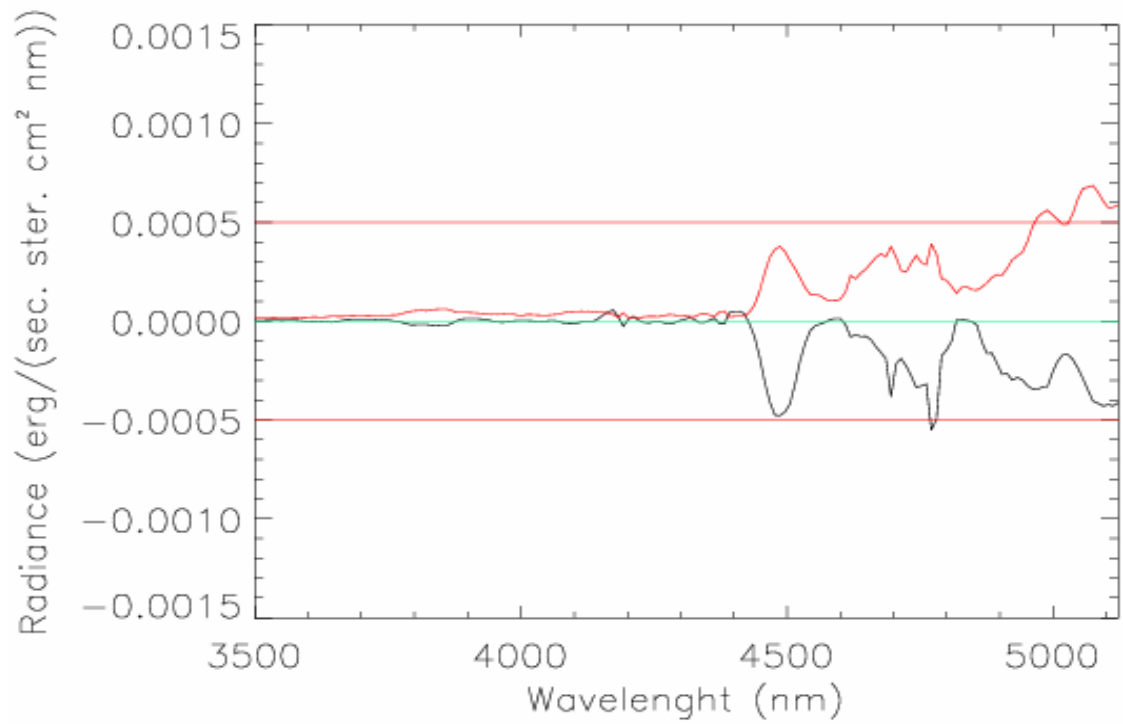


**Figure 30. Upper panel: in black systematic errors in red random errors. In lower panels are shown the difference among the spectra (left) and the spectrum computed with CT (right).**

## **5.2 Task: search for water in Venus atmosphere**

The water vapor abundance in the middle atmosphere of Venus, within and above the main cloud deck, has been a controversial issue for many decades.

Understanding why Venus is so much drier than Earth is crucial to understand the evolution of the Venus atmosphere. The role of water as a trace constituent is also key to illuminating the present-day Venus atmosphere, particularly with respect to the global cloud layers of Venus. The sulfuric acid cloud particles form from water by thermal chemistry in the lower atmosphere, where  $\text{SO}_2$  reacts with water dissociation products to form  $\text{SO}_3$ , and  $\text{SO}_3$  then reacts directly with  $\text{H}_2\text{O}$  to form  $\text{H}_2\text{SO}_4$ .  $\text{H}_2\text{SO}_4$  combines physically with  $\text{H}_2\text{O}$  to form (liquid or solid) solution particles of varying acid concentration (Esposito et al., 1997).

The Earth based observations before acquired 1975, summarized in von Zahn et al. (1983), made with high resolution airborne spectrometers, resulted in mixing ratios between 0 and 40 ppm. At that time Barker (1975) attributed this discrepancy to the presence of localized wet spots and indeed, the fleet of in situ instruments which visited Venus during the 1980s reported mixing ratios between 50 and 5000 ppm. These studies include all the Venera and Pioneer Venus entry probes and the two Vega balloons (Oyama et al., 1980; Mukhin et al., 1982; Surkov et al., 1982). The Orbiter Infrared Radiometer experiment on board the Pioneer Venus spacecraft discovered the presence of a wet area in the afternoon equatorial region whereas the night-side yielded only trace amounts of water vapor (Schofield et al., 1983). More recently, high resolution Earth-based spectroscopic observations of the night-side have revealed a constant global abundance of  $40 \pm 20$  ppm over a wide range of sub-cloud altitudes (Bézard et al., 1990; Crisp et al., 1991; de Bergh et al., 1995; Meadows and Crisp, 1996) and trace amounts ( $3.5 \pm 2.0$  ppm) above the main cloud deck at 65 km (Encrenaz et al., 1991, 1995). The

spectroscopic data of the Near-Infrared Mapping Spectrometer (NIMS) recorded during the Galileo flyby of Venus were in good agreement with the Earth-based studies and yielded a deep atmosphere water vapor mixing ratio of  $30 \pm 15$  ppm (Carlson et al., 1991; Drossart et al., 1993). A recent re-analysis of the Venera 15 Fourier Transform Spectrometer observations (Ignatiev et al., 1999) further confirms these findings.

Anyway Venera 15 data did not include observations at noon, leaving open the controversies about the high values of water abundance found at noon by Pioneer Venus data (Schofield, 1983; Irwin, 1997, Koukouli, 2005) in the equatorial cloud-top region shortly after the sub-solar point, that is 100 ppm.

In this work we try to clear this question giving a contribute to the knowledge on this topic, by retrieving the water content in the proximity of the clouds deck.

Since the reflected solar spectrum of Venus, observed on the dayside, probes the middle atmosphere above the sulfuric cloud level, at a pressure of less than 0.1 bar, we focused the work on the Venus dayside spectra for the water retrieval.

### **5.2.1 Water from VIRTIS M data**

In the case of Mars, the lines are very narrow, because the Lorentz broadening (proportional to the pressure) is very small. Thus, very high spectral resolution is required to search for minor species.

In the case of Venus atmosphere we may try to study minor species even with the VIRTIS-M resolution (10 nm) because of the strongly broadened lines with respect to Martian ones.

For this reason we have initially searched water in VIRTIS-M data, which is characterized by an high spatial resolution to the detriment of the spectral one and, as an image spectrometer, it acquires a huge amount of spectra which covers simultaneously a high percentage of the planet, being this convenient for mapping the atmospheric components.

In the spectral range (1 – 5  $\mu\text{m}$ ) of the VIRTIS-M instrument four  $\text{H}_2\text{O}$  bands can be found:

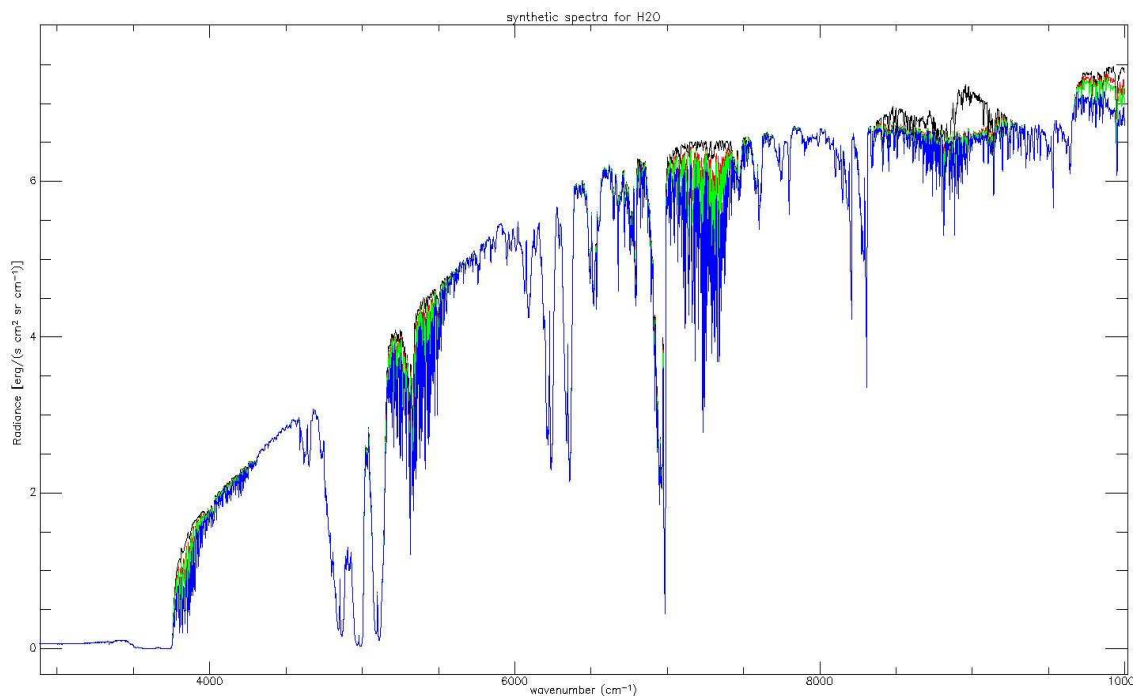
1. (3790 - 4315)  $\text{cm}^{-1}$ , (2,5 – 2,64)  $\mu\text{m}$
2. (5170 - 5670)  $\text{cm}^{-1}$ , (1,81 – 1,93)  $\mu\text{m}$
3. (7000 - 7430)  $\text{cm}^{-1}$ , (1,34 – 1,43)  $\mu\text{m}$
4. (8350 - 9100)  $\text{cm}^{-1}$ , (1,1 – 1,2)  $\mu\text{m}$

In the computation of synthetic spectra we simulated the radiation coming from the dayside part of the planet taking into account the scattering. Spectra computed for different amounts of  $\text{H}_2\text{O}$  are presented (see Figure 31), to highlight the positions of the water absorption's bands. Looking at these simulations we realized the difficulties on the retrieval of water from these bands. We can observe, from the picture showing the spectra convolved with the VIRTIS-M instrumental function, that

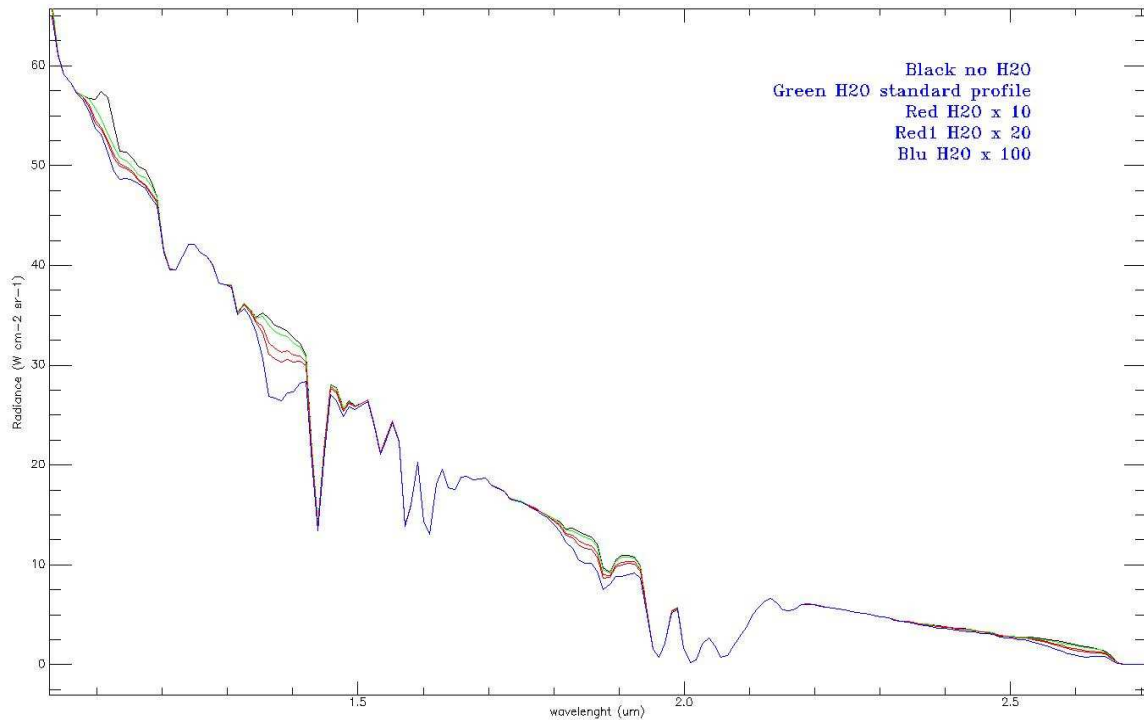
- the band 1) is too weak to be retrieved at this spectral resolution,
- bands 2) and 3) are contaminated by the  $\text{CO}_2$  absorption which makes unclear the definition of the continuum and the absorption channels,
- the band 2) is poorly sensitive to water variations (it is important to notice that we plotted spectra with huge amount of water in order to show clearly the band's positions, but the expected amount of  $\text{H}_2\text{O}$  should be one or two orders of magnitude less, making very difficult in this case a quantitative retrieval),
- band 4) and 3) revealed a very peculiar shape of the continuum which makes impossible its definition in the

measured data. The continuum of these bands, of which we can have some information looking at the synthetic spectrum computed without the water as absorbing gas, present a shape much far from being correctly assumed as linear, which is in effect the only way we are able to construct the continuum of a band.

To confirm quantitatively the above mentioned observations we tried to compute, for a great numbers of simulated cases, the value of the water band depths (this will be described in section 5.2.2.1 for VIRTIS-H data). In the case we were able to find reasonable results (that is values around a positive number which means detectable water absorption band depths) we could try to investigate more deeply the possibilities on the continuum assumptions. Anyway this tentative failed, having retrieved values for the band area scattered around zero (which means that we were not able to detect water lines). For these reasons we preferred to search the water signatures in data acquired from the VIRTIS-H instrument with higher spectral resolution.



a)



b)

**Figure 31. Synthetic spectra computed with different amounts of H<sub>2</sub>O (from 0 to 100 ppm) to highlight the positions of the water absorption's bands. In the figure a) are the spectra as a function of wavenumber (cm<sup>-1</sup>), while in figure b) are showed the spectra convolved with the VIRTIS-M instrumental function in wavelength units (micron).**

### 5.2.2 Water from VIRTIS H data

In the spectral range of VIRTIS-H (1 – 5 μm) we can observe the absorption of water only in one band:

$$(3790 - 4315) \text{ cm}^{-1}, \quad (2,5 - 2,64) \text{ μm}.$$

This band is the smallest among the bands we can observe in VIRTIS-M spectra (Figure 31 on the right, 2.6 μm), anyway, at VIRTIS-H resolution we were able to clearly detect its signature on spectra.

### **5.2.2.1 Calibration problems and data selection by means of H<sub>2</sub>O and CO<sub>2</sub> band depths analysis**

While searching the water lines in the spectra we had to face some problems related with the data. This happens every time we go to deeply investigate small features in the spectra, task that requires a huge correctness of calibrations.

This led us to deepen our knowledge of the spectra, their characteristics and behaviors, trying to find eventual correlation with calibration's procedure in order to give support for the validation and improvements of the calibration's methods.

Since this task required constant efforts we briefly mention in this section some of the problems we have dealt with, together with a study of the data trends and behaviors to find where problems were present.

The calibration of VIRTIS-H is something difficult, because of two effects:

- 1) the response function of the detector has non negligible non linearity,
- 2) the pixel to pixel response vary strongly between "odd" and "even" pixels of the CCD, resulting in two very different response functions.

These effects are taken in principle into account when calibrating the data: the applied calibrating procedure is found to not work badly for the night side spectra, but it happens anyway that, while acquiring day side spectra, the instrument is in a different regime of the detector. This explicates in having high flux on the "object" spectra compared to low flux on the "dark" and hence in getting a different response function. In this case we can infer that the optimization of the response function for the night side - low level spectra does not work perfectly for the day side - high level ones.

About the so called 'odd-even channels effect', we noticed that on the dayside, with short exposure time, both VIRTIS-H and M experience odd/even problem (Figure 32). Different calibration should be applied to the two channels due to their different response functions, but which are basically not known. Moreover, even considering only odd or even bands,

the spectrum is subjected to distortions, which have to be considered carefully on dayside spectra for minor species studies, as those distortions are much higher than random noise.

Besides the described effects we have also found a shift in wavelengths (see for example Figure 33) due probably to small changes of the detector temperature during the all session, while we have in a calibrated files' session only one wavelength grid for all spectra, which is hardly possible in reality.

Besides these problems, concerning the calibration of Virtis-H for small bands, it was to be corrected the so called "bad dark" effect, before the on-board software upgrade in June 2007 solved it: it was performed a reinterpolation of the dark currents which were due to some object contamination into dark files.

While we failed to find some reasonable behavior in H<sub>2</sub>O features in VIRTIS-M, when we first tried to look at the VIRTIS-H data we got the same or even worse conclusion. This because, despite the bands/lines were present and visible (see Figure 34), the spectrum on the dayside was poorly simulated (Figure 35), appearing therefore impossible to use it for quantitative estimates, due to the mentioned problems.

Together with the attempt to obtain a good simulation of the dayside spectra and a better understanding of the data, some of the above mentioned problems were found when we searched for data and orbits which did not present instrumental problems. This was performed by computing and mapping for all the data the relative band depth of both a CO<sub>2</sub> and H<sub>2</sub>O band and their ratio.

To characterize the relative depth of CO<sub>2</sub> band we define the depth index  $D$  as difference between the continuum  $cont(\lambda_D)$  and the spectrum inside the band  $S(\lambda_D)$  normalized to the continuum at wavelength  $\lambda_D$ :

$$D = \frac{cont(\lambda_D) - S(\lambda_D)}{cont(\lambda_D)} \quad (0.52),$$

being the continuum defined by a straight line drawn between the two points on the sides of the band.

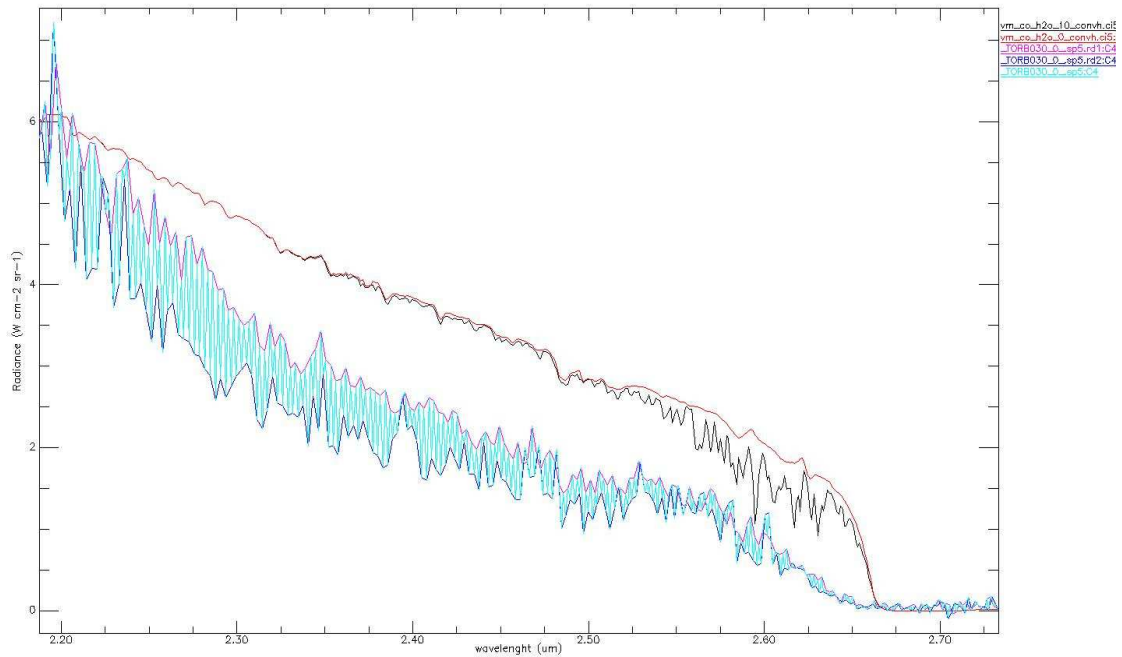


**Figure 32.** From this picture is clear the effect of the difference between odd and even channels: are shown two synthetic spectra (the ones with higher radiance) and one measured VIRTIS-H spectrum (with lower radiance). This spectrum is plotted in three ways: the complete spectrum with all the channels (in light blue), and the plot of just odd or even channels respectively in the higher and lower boundary.

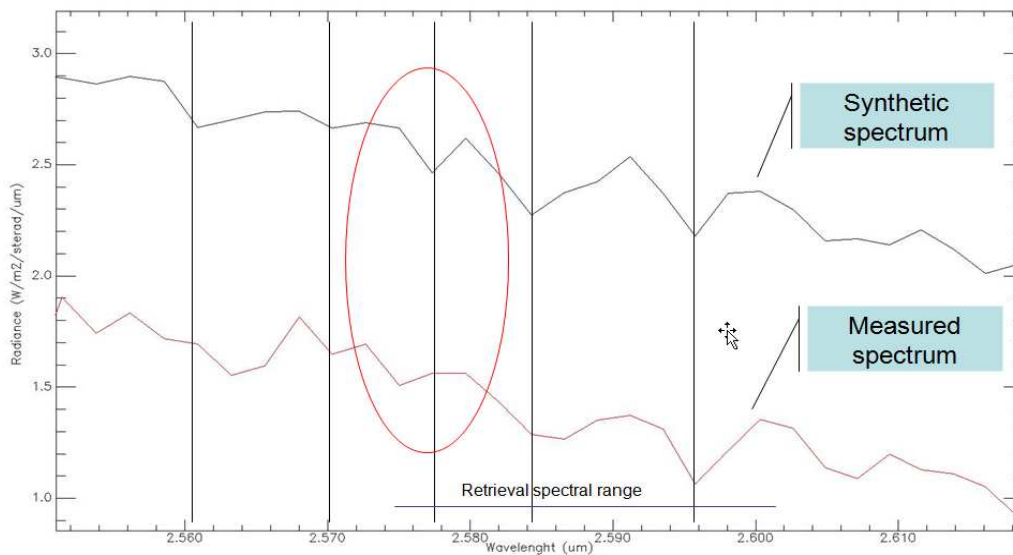


**Figure 33.** This is an example of the shift in wavelengths we have found in some parts of the spectral range. Some lines don't show an evident shift while others sometimes have this problem (see the water line in the red curve).

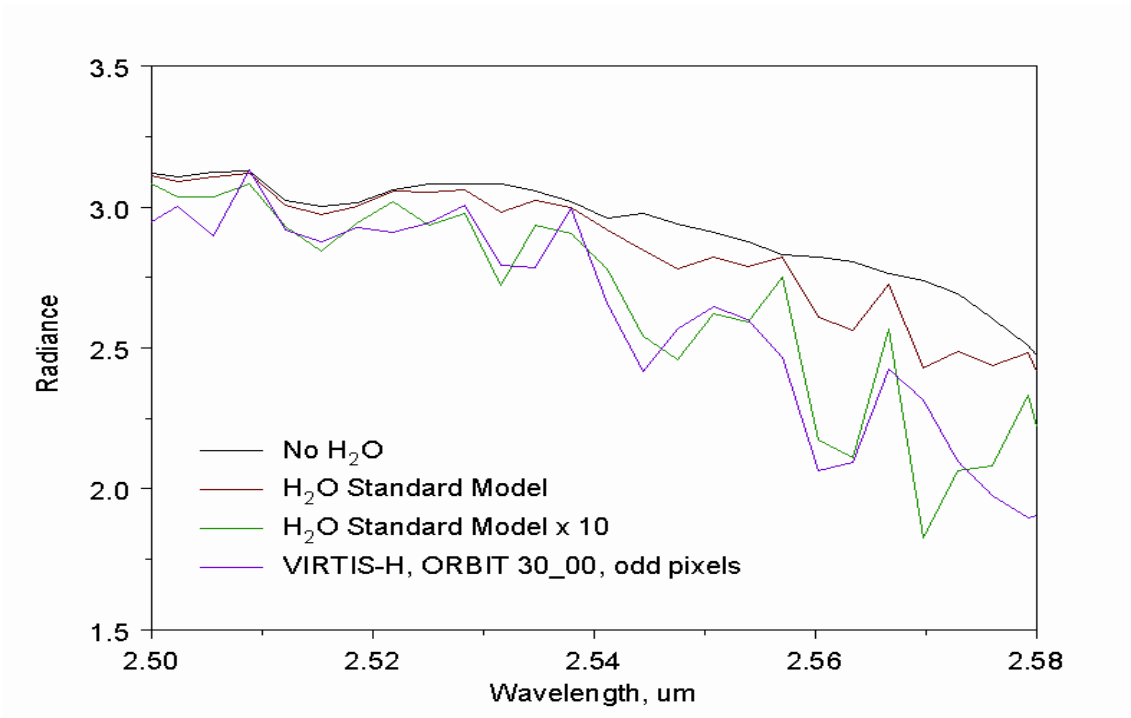


**Figure 34. First attempt to reproduce the 2.56  $\mu\text{m}$   $\text{H}_2\text{O}$  band: measured and synthetic VIRTIS-H spectra, order 4 and odd spectral bands selected. By comparison of spectra with different water amount we easily single out the  $\text{H}_2\text{O}$  lines.**

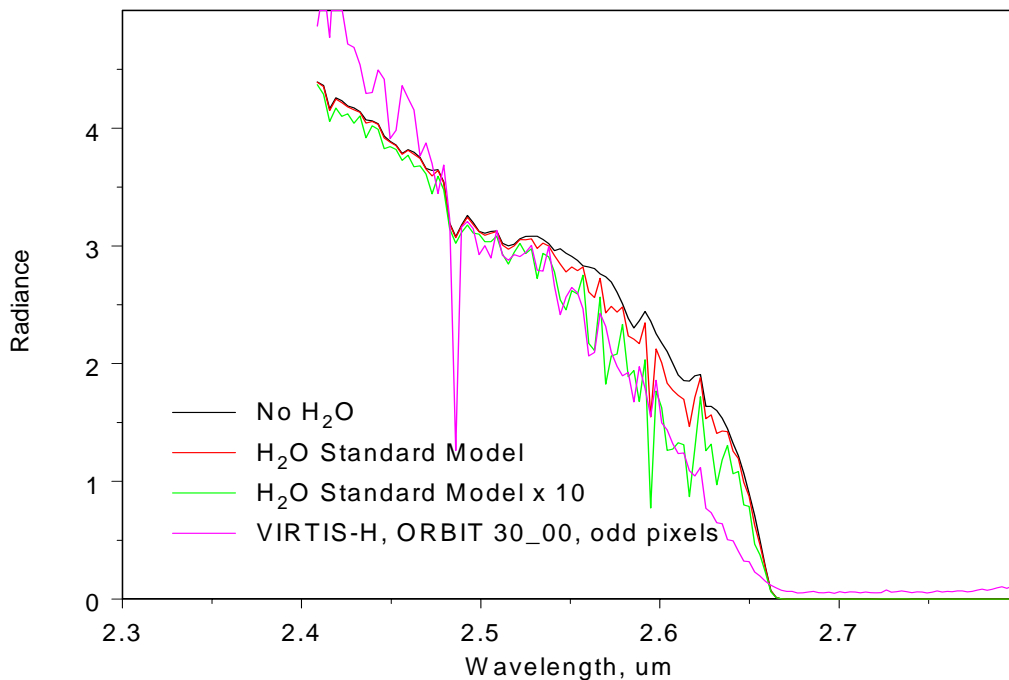


**Figure 35. Measured and synthetic VIRTIS-H spectra on a wider range; we can notice that the spectrum is not fitted at all.**

This was done to get a quick idea of the band depths' values and especially their trends in function of latitude and angles, in order to understand if unpredicted behaviors were present in the observations and also to select the data with more stable values, even if the band depths, without comparison with simulated data, cannot give absolute information but can just help to individuate some eventual calibration's problems.

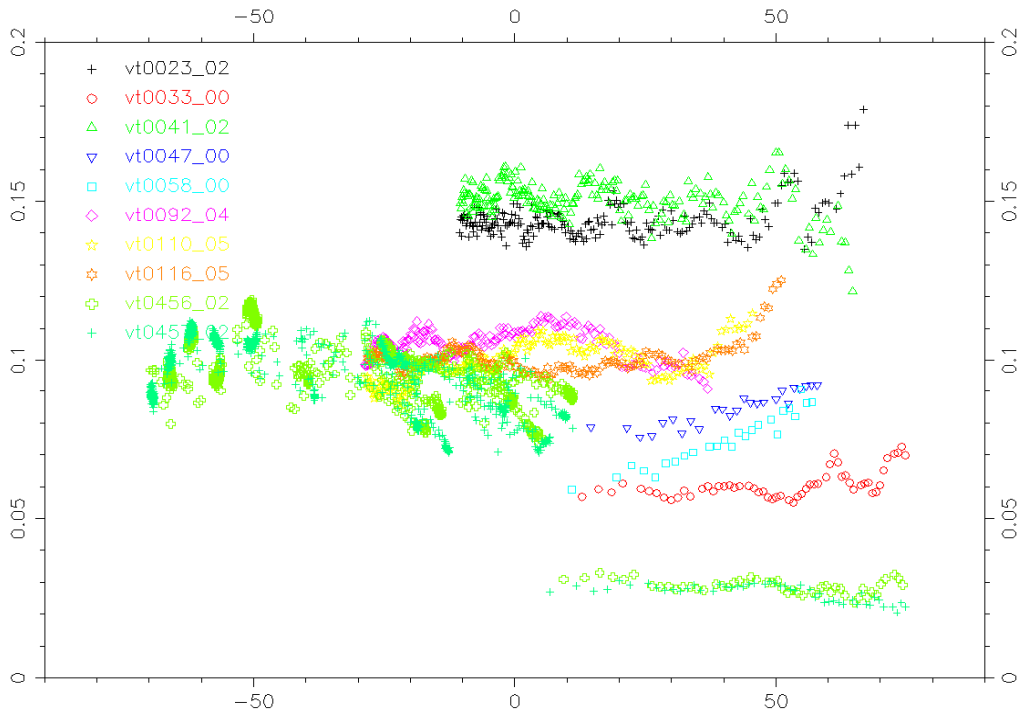
We found that sometimes the behavior was reasonable: e.g. 116\_05, 58\_00 in Figure 36. We observed that while in these sessions the increase to the pole corresponding to lower clouds and higher angles, and therefore longer path, is a reasonable trend, the so big difference between orbits (compare 23\_02 and 33\_00) and jumps within a session (457\_02, at latitude = 10) are not. In these cases the feature looked like being more instrumental than produced by water lines.

We can observe this peculiar trend also by looking and the three pictures in Figure 37, (in which are plotted the band depths for many more orbits). It is clear the peculiar subdivision of the results in two set of data, which then we discover that was due to the above mentioned "bad dark effect".

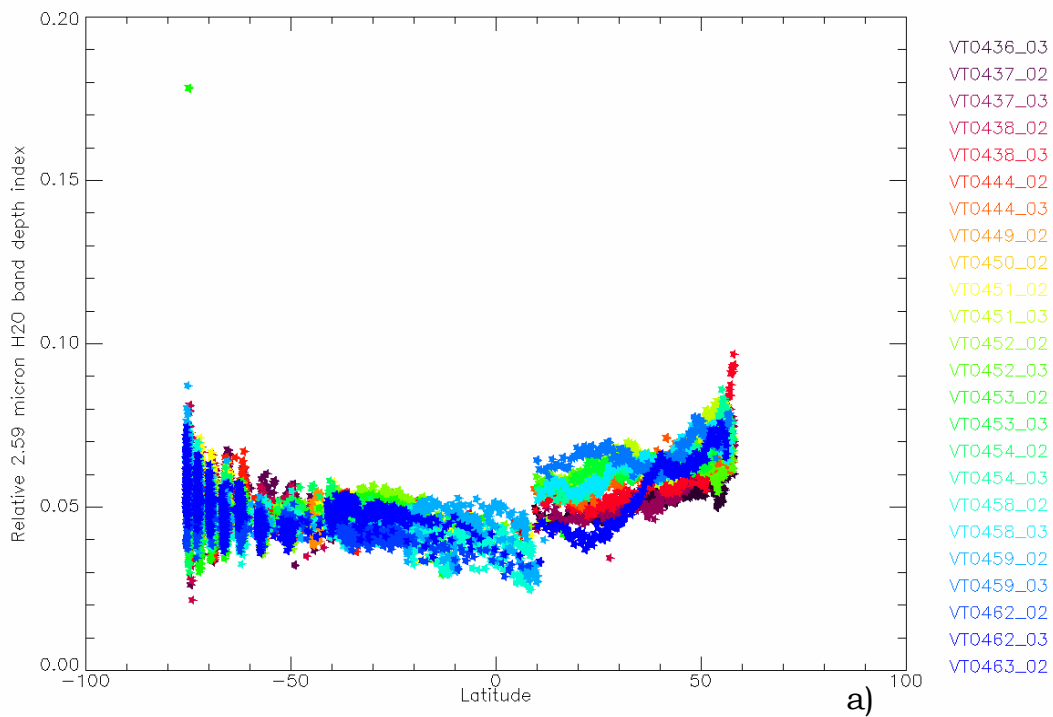
This last problem is for the moment overcome just by having considered for this study, just the data sessions starting from VT0500, which are the data acquired after July 2007 when the problem was corrected.

As with the choice of the best order, the other described problems are faced every time by a careful investigation of their behaviors and the eventual influence on our studies, in order to exclude a dependence of the obtained results on instrumental characteristics.

About the presence of a spectral shift, we simply avoid using the lines, for the retrieval of the researched quantities, which present this effect. Moreover we are also performing some test with the aim of correcting the wavelengths grids.



**Figure 36. Band depth index versus latitude for 10 sessions of data.**



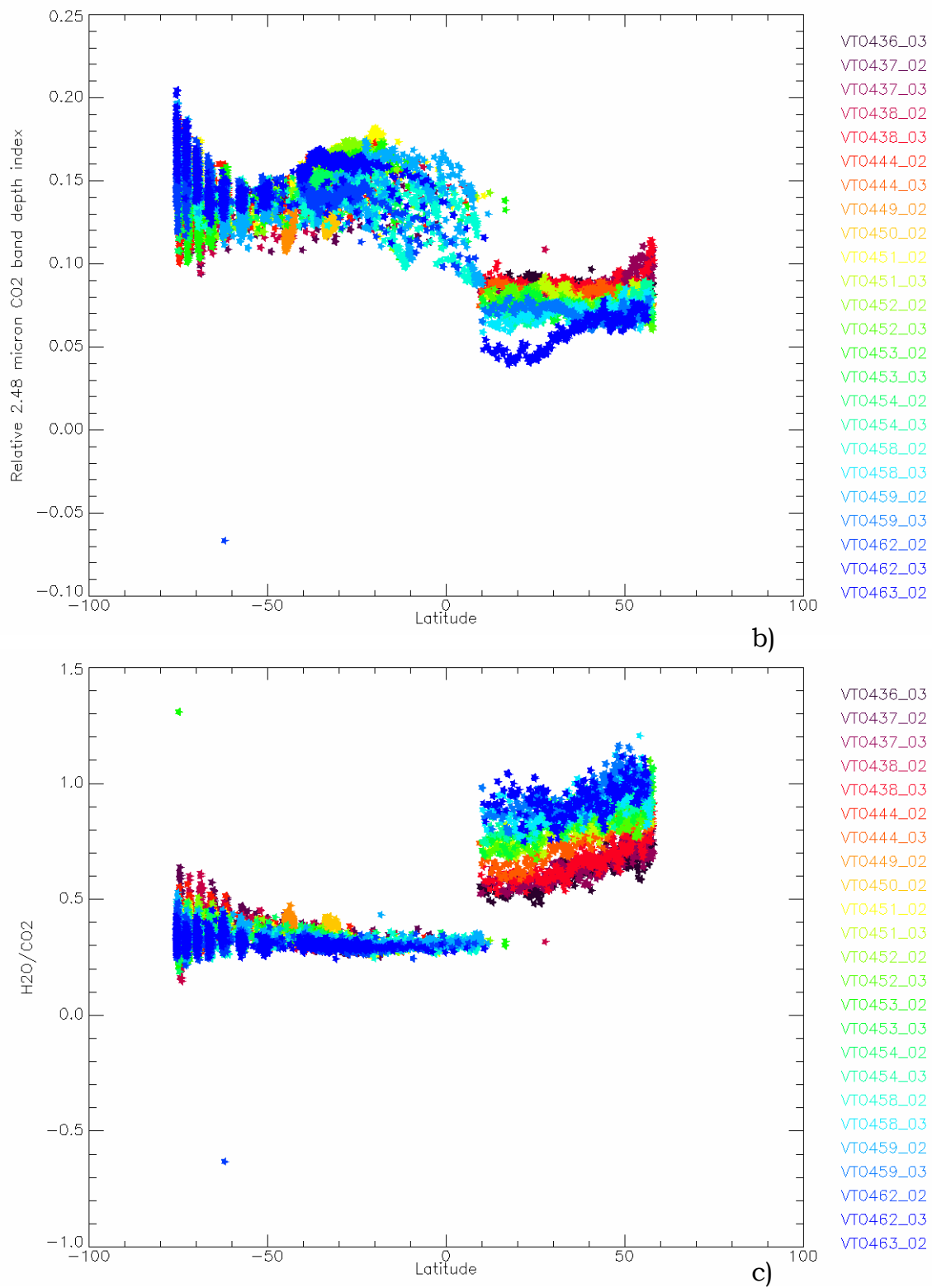


**Figure 37. There are shown for many orbits the computed band depth indexes, plotted versus latitude: a) H<sub>2</sub>O band, b) CO<sub>2</sub> band, c) H<sub>2</sub>O/CO<sub>2</sub> band. It is clear the peculiar subdivision of the results in two set of data.**

About the odd-even effect, we study each time which are the channel with the correct response function, even with the help of simulation which can give important information on the quality of the fit and hence on the choice of the channels.

Here we will not give further descriptions on this topic and on the solutions to overcome eventual problems we faced during the study. Anyway in this section we wanted just to give to the reader an idea on the topics we have to deal with while studying small features and to underline that every behavior of the and each eventual problem is deeply examined, avoided and however taken into account.

### **5.2.3 Atmospheric model**

The atmosphere of Venus has been discussed qualitatively in section 1.1. In order to create a mathematical model of this atmosphere, vertical profiles for temperature, pressure, volume mixing ratios for each radiatively active gaseous species and aerosol properties, we referred to previous measurements and published results, plus to results of some test which we performed to improve the model.

#### **5.2.3.1 Choice of $T(p)$ profile**

The inverse code for the retrieval of the temperature profiles, despite the implemented fast direct radiative transfer method to speed up the computation (see paragraph 5.1.6), requires some computation time before the implementation of our retrieval procedures.

For this reason, to define the temperature and pressure profile used in the atmospheric model for radiative transfer computations we referred to the data obtained by the Venus International Reference Atmosphere (VIRA)

model [Seiff *et al.*, 1985] which is based on the data of the extensive space investigations of Venus in the 1960s and 1970s.

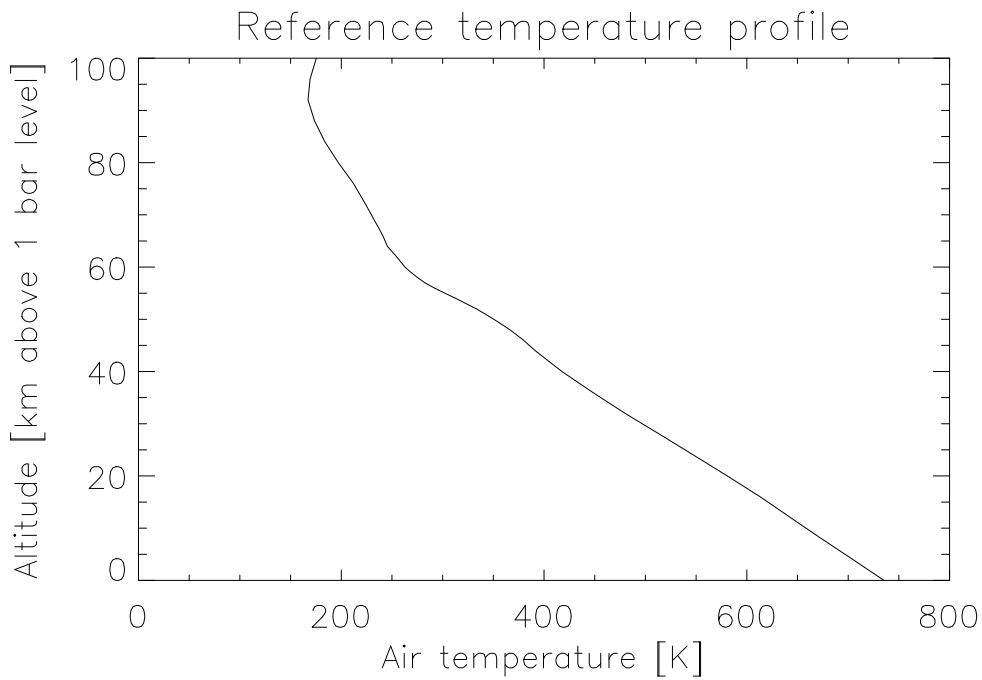


**Figure 38.** Temperature and pressure profile used for the atmospheric model.

A  $T(p)$  profile for low latitudes has been considered in the model. The choice of a single profile is due to the minor importance of considering different atmospheric temperature profiles to simulate the atmosphere when modeling data acquired in the dayside part of the planet, in a spectral range which does not include the thermal infrared radiation; on the contrary in case of nightside spectra simulations high attention has to be given to the use of a  $T(p)$  which reproduce the real atmospheric profile as better as possible.

In Figure 38 the adopted temperature profile is presented.

### 5.2.3.2 Models of aerosols

Aerosol model (Figure 39 and Figure 40) cannot be as well defined as the temperature profile. We took a commonly accepted model: droplets of 75% water solution of  $\text{H}_2\text{SO}_4$ , with optical constants in IR and VIS taken from Palmer and Williams (1975). For particle size distribution, 4 mode models are commonly accepted: “1” (small particles), 2 and 2’ (~1 micron particles), and 3 (large particles in the lower cloud layer). This model is based on particle size spectrometer on Pioneer Venus. (Knollenberg & Hunten, 1980). Vertical profiles, measured by various entry probes are different in details, although they have common features: upper haze (mode 1), intermediate clouds (modes 2 and 2’), and lower clouds (mode 3). We adopted the values (Figure 39) of Zasova *et al.* (1985) for the number density profile. In this midlatitude model, total optical depth at 1 micron is equal to 40, which, in fact, is a maximum value, while expected variations range is 20–40 (i.e.: 1  $\mu\text{m}$  optical depth measured by Venera 11 and 13 descent probes was 28–32).

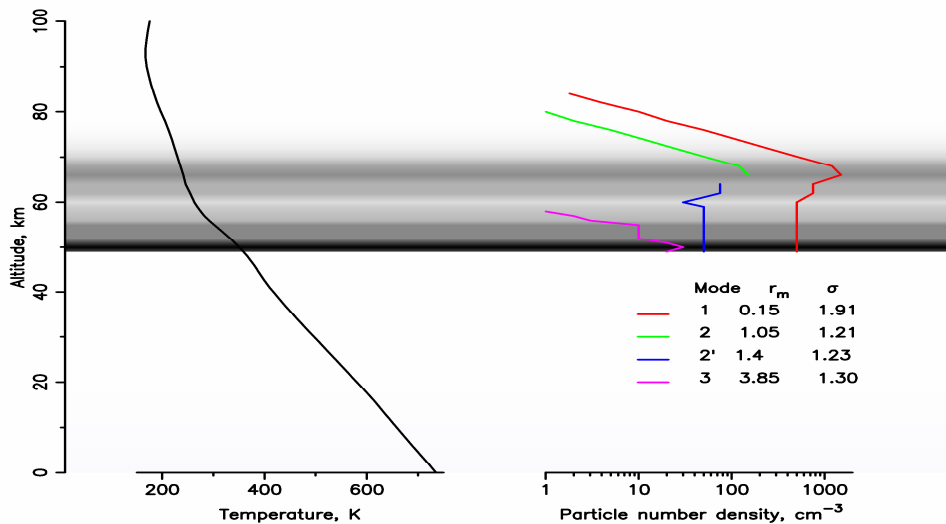
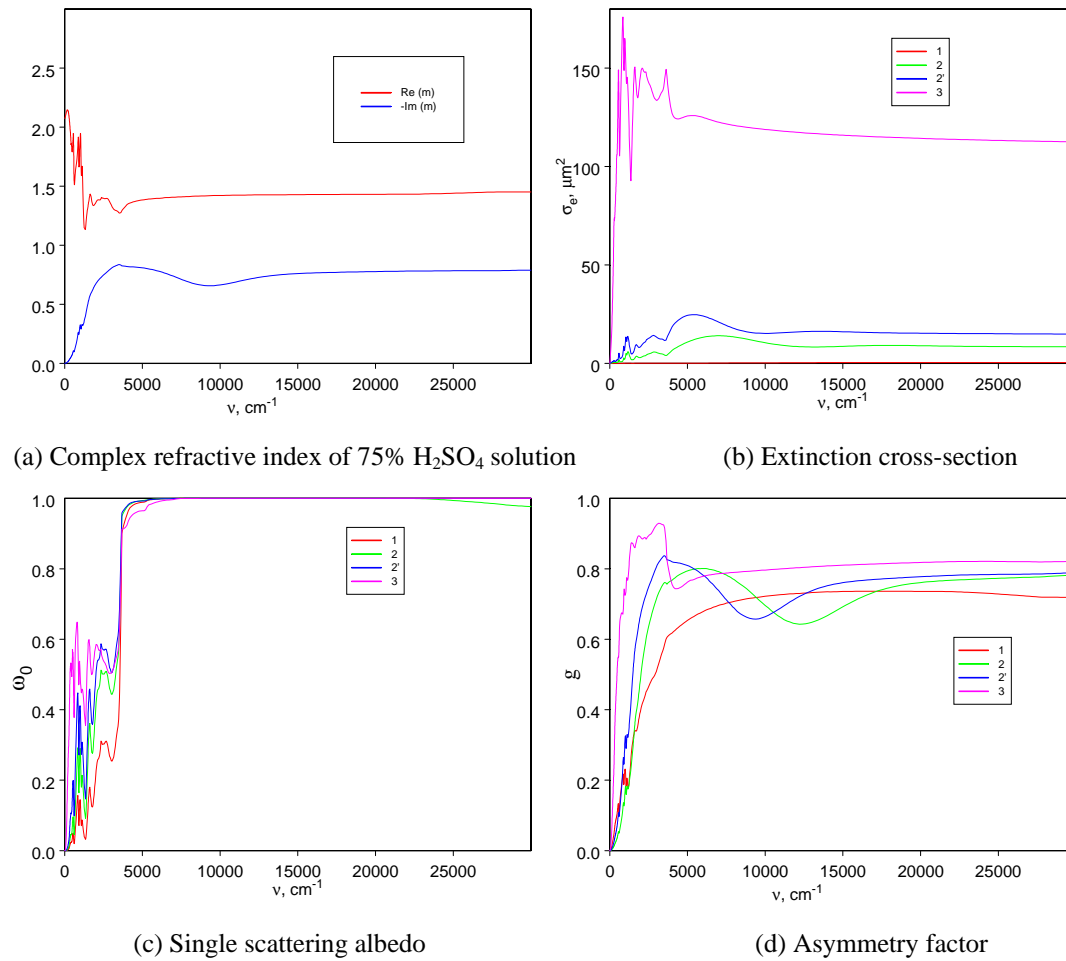


Figure 39. Temperature profile and aerosol model.



**Figure 40. Optical properties of Venus aerosol model**

Extinction cross-section, single scattering albedo and the phase function Legendre expansion were computed according to the Mie theory.

Ultraviolet absorber, whose nature is not clear yet, is simulated with the addition of 0.7% FeCl<sub>3</sub> in mode 2. (Zasova *et al.*, 1981).

### 5.2.4 Retrieval method

The main problem of the H<sub>2</sub>O retrieval above the clouds is an accurate determination of the cloud top. The depth of CO<sub>2</sub> band can be used to

determine the cloud level because it depends on the optical path in the scattering and absorbing atmosphere as it was shown by Ignatiev et al.

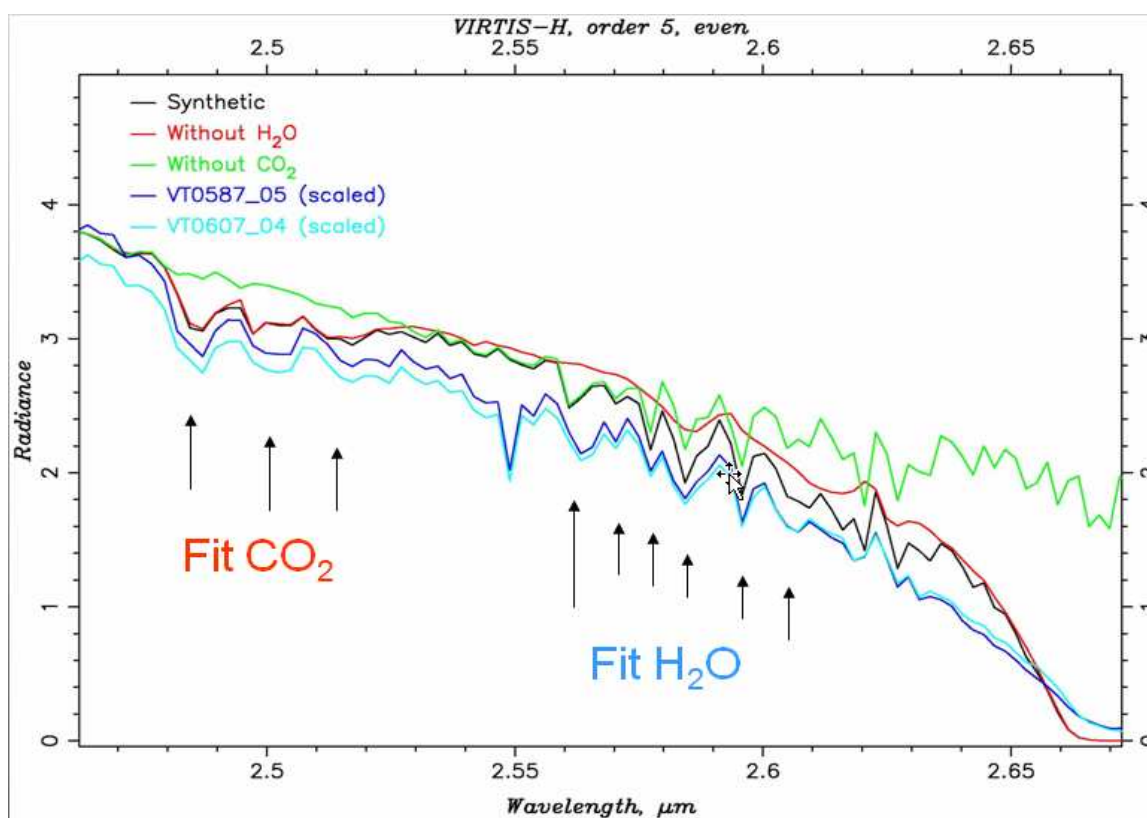


**Figure 41.** In this picture is shown a dayside VIRTIS-H spectrum in which we can observe the CO<sub>2</sub> and H<sub>2</sub>O bands used for the retrieval of respectively the altitude of the clouds tops and the content of water. The mentioned bands are singled out by comparison of synthetic spectra with or without the considered species.

The method we have used to retrieve the abundance of the water in the mesosphere is basically to retrieve simultaneously the altitude of the clouds from a CO<sub>2</sub> band (a component of constant and well known mixing ratio) and the abundance of the H<sub>2</sub>O in the mesosphere, above the cloud layer. With this procedure we can get the correct optical path of the radiation in the atmosphere, taking into account in the simulation the proper pressure of the region which mainly contributes to the absorption in the spectrum. In Figure 41 we show the CO<sub>2</sub> and H<sub>2</sub>O bands chose for the retrieval..

### 5.2.4.1 Computation of aerosol and water profiles

The cloud vertical distribution can be modeled by the cloud top (the unit column optical depth) and the scale height  $H$ <sup>7</sup>. The assumptions made to model the CO<sub>2</sub> band for different cloud models are the use of a fixed temperature-pressure profile and aerosol modeled by the mode 2 of H<sub>2</sub>SO<sub>4</sub> (75%) particles (as described in paragraph 5.2.3.2), beside we needed to assume the scale height  $H$  of upper clouds on Venus. We choose a fixed value of 4 km that is close to SPICAV/SOIR upper haze measurements at high northern altitudes. Previous observations indicated that the aerosol scale height at the cloud tops can vary from less than 1km at high latitudes (Zasova et al., 1993, 2007) to 4–5 km at the equator (Ragent et al., 1985; Zasova et al., 1993, 2007; Koukouli et al., 2005). The scale height of 4-5 km is the most accredited value and anyway better for low latitudes simulations.

We used the aerosol's extinction coefficient relative to 1.51  $\mu\text{m}$ . We chose this wavelength to have the possibility to compare the results with the ones obtained with VIRTIS-M data (Ignatiev et al., submitted).

With this input values we compute the aerosols density profile

$$q = q_0 e^{-z/H} \quad (0.53)$$

being  $q$  the density.

The computation of an initial density  $q_0$  is performed imposing the opacity to be equal 1 at the altitude of clouds tops  $h_1$ :

$$1 = \int_{h_1}^{\infty} \sigma_{EXT} q(z) dz = \sigma_{EXT} \int_{h_1}^{\infty} q_0 e^{-z/H} dz = -\sigma_{EXT} q_0 H \left( e^{-z/H} - e^{-z/H} \right) \Big|_{h_1}^{\infty}$$

$$\Rightarrow 1 = \sigma_{EXT} q_0 H e^{-h_1/H} \quad (0.54)$$

---

<sup>7</sup> For planetary atmospheres a scale height is the vertical distance upwards, over which the pressure of the atmosphere decreases by a factor of  $e$ .

Then we find

$$q_0 = \frac{e^{\frac{h_1}{H}}}{\sigma_{EXT} H} \quad (0.55)$$

In the same way we can find an altitude  $h_{max}$  corresponding to a reasonable  $\tau_{max}$  (for example we found 40 is enough) so that it is possible to put equal zero the density of the levels under this  $h_{max}$  in the aerosol profile:

$$40 = \int_{h_{max}}^{\infty} \sigma_{EXT} q(z) dz = \sigma_{EXT} \int_{h_{max}}^{\infty} q_0 e^{\frac{-z}{H}} dz = \sigma_{EXT} q_0 H e^{\frac{-h_{MAX}}{H}}$$

$$\Rightarrow h_{MAX} = -H \ln \left( \frac{40}{\sigma_{EXT} q_0 H} \right) \quad (0.56)$$

Now for each level  $i$  of the profile we compute the density:

$$q_i = q_0 e^{-z_i/H} \quad (0.57).$$

In this way we computed the density  $q_0$  for all the clouds tops altitude's values (at 1.51  $\mu\text{m}$ ). Successively we computed the altitudes at 2.58  $\mu\text{m}$  (inside the water band used for the retrieval) by taking the extinction coefficient relative to this channel:

$$h_{(2.58)} = \ln(\sigma_{EXT} q_0 H) H \quad (0.58).$$

In Figure 43 is presented the relation between the clouds top altitude at 2.58  $\mu\text{m}$  and at 1.5  $\mu\text{m}$ .

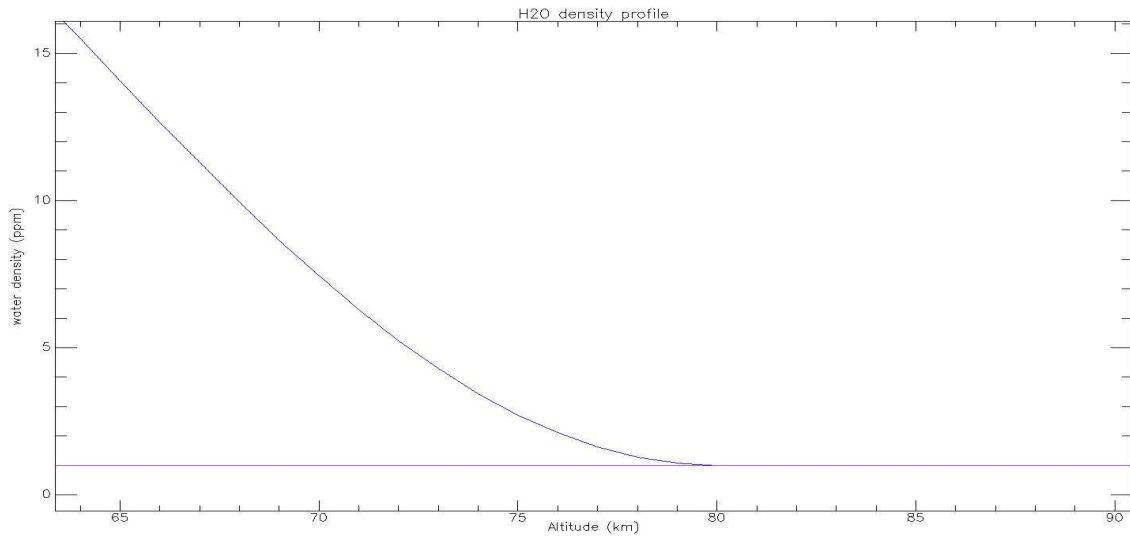


**Figure 42. Adopted water profiles. In blue a not constant profile (following models, e.g. Krasnopolsky-Pollack, 1994), with values from 30 ppmv under the cloud layer up to 1 ppmv above the clouds; for a continuum connection between the two different values we used a cosine function. In purple water profile with constant value of 1 ppmv.**

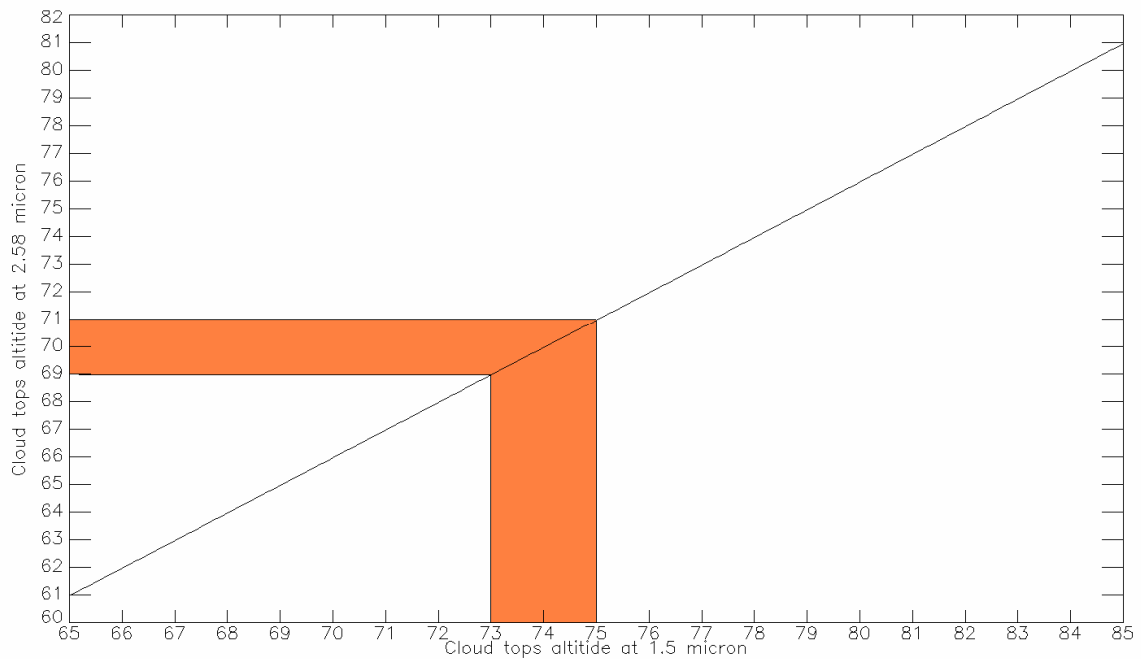


**Figure 43. Clouds top altitude at 2.58  $\mu\text{m}$  (channel of water content retrieval) versus 1.5  $\mu\text{m}$  (used to compare results with those obtained by VIRTIS-M data). In orange is highlighted the retrieved average values of the altitude of the top of the clouds.**

To simulate the water vertical distribution we have initially adopted (following models, e.g. Krasnopolsky-Pollack, 1994), a not constant profile (Figure 42) which goes from 30 ppmv under the cloud layer up to 1 ppmv above the clouds. For a continuum connection between the two different values we used a cosine function. Then we preferred to use a constant profile of 1 ppmv, due to better legibility of the results. In paragraph 5.2.6 will be described the comparison of the results obtained with the two models.

#### **5.2.4.2      *Software for automatic processing of the data***

To perform the retrieval of the altitude of the clouds and the water content in the mesosphere I wrote a program which is able to ingest the data, process them and provide the two results (clouds' altitude and water content) for each single observation. This code computes the synthetic spectra taking into account the correct observation and illumination geometry from the data, builds the aerosol density profile as already described, fit the CO<sub>2</sub> band, then simulates again the radiance in order to fit the H<sub>2</sub>O band and finally returns the results plus many useful parameter computed for later analysis and check of the obtained values. To compute the band depth indexes it calculates the integral of the normalized band in a chosen spectral region. This gives more correct results than an index computed just with the band depth of a line, because it is less subject to variations due to noise.

The channels we chose to evaluate the continuum of the band for the retrieval procedure are:

co<sub>2</sub> continuum = [2.4777, 2.4942] μm

h<sub>2</sub>o continuum =[2.5797, 2.5912, 2.6003] μm

In Figure 44 a simplified scheme to describe the main conceptual passages is shown.

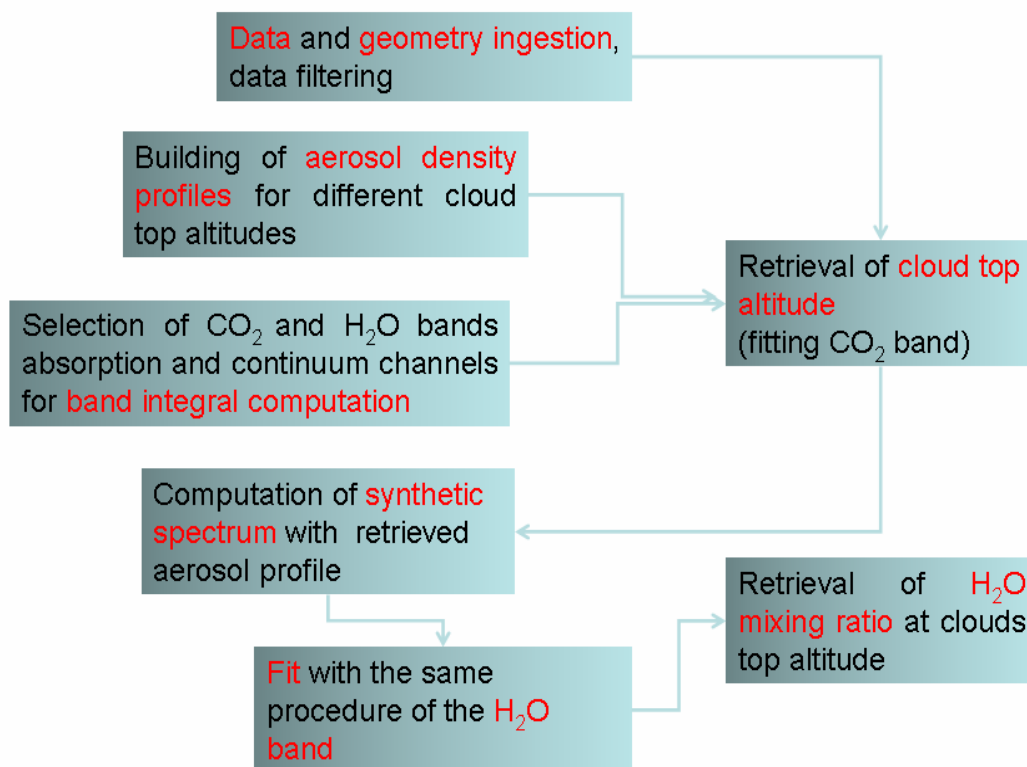


**Figure 44.** Basic structure of the program for simultaneous retrieval of  $h$  of cloud tops and  $H_2O$  abundance. The fit and the retrieval is made on single spectra.

In the output, the program produces and stores all the simulations. This is an unusual procedure because of the huge space on the hard disk occupied by the results, but it is much less time consuming, so that we decide to save time in respect of space. Moreover having stored the simulations we were able to check in any moment the results of the fit, in order to understand quickly, if some peculiar behaviour found, what was going on, both in the retrieval methods and in the data.

In Figure 45 there is an example of the initial simulations performed by the code to fit the  $CO_2$  band and find the clouds tops altitude.

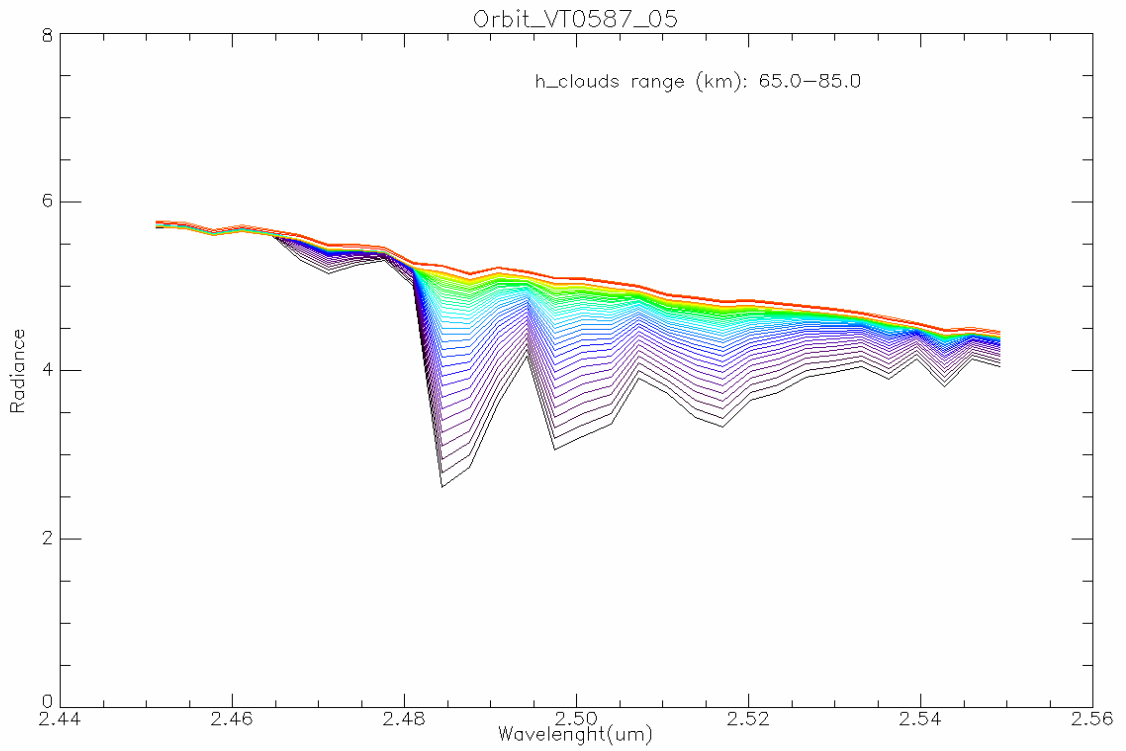


**Figure 45. Example of the simulations performed by the code to fit the CO<sub>2</sub> band and find the clouds tops altitude; the spectra are computed with the built aerosol profiles for the tops of the clouds positioned from 65 to 85 km (at 1.5 μm).**

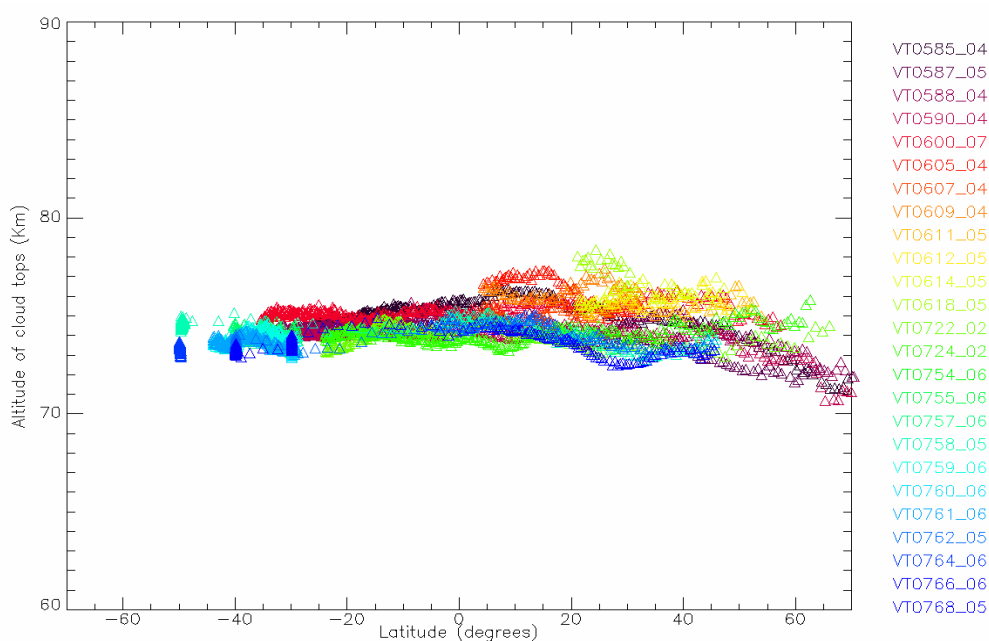
## 5.2.5 Results for the cloud tops altitude

With the procedure described above we have obtained the altitude of the cloud top from single observations acquired during 25 orbits on the dayside part of the planet.

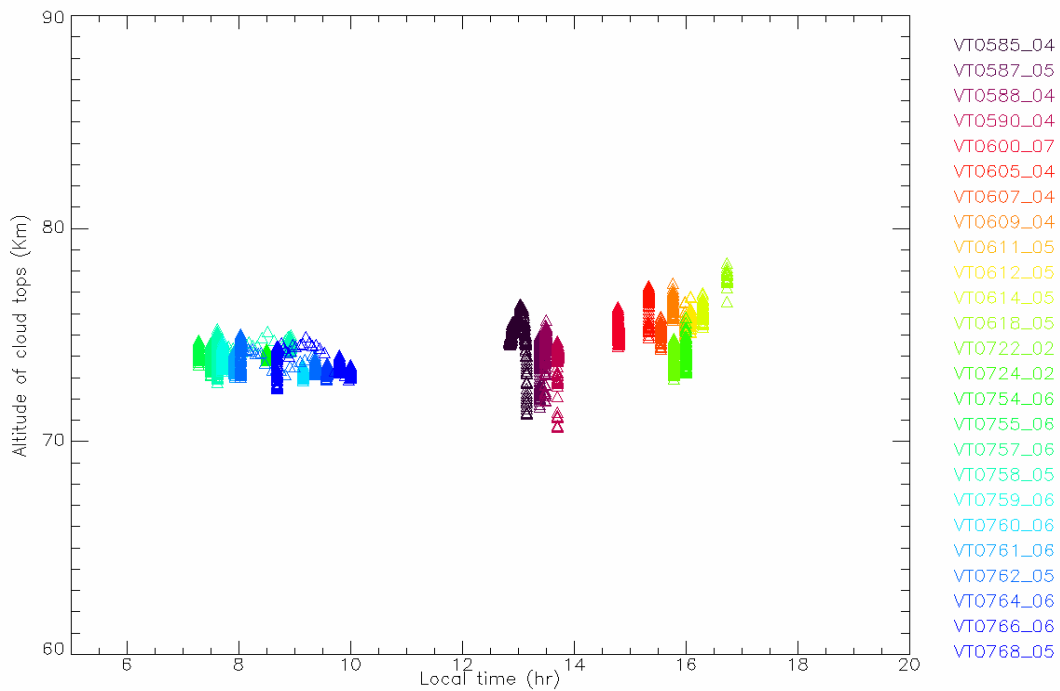
We have retrieved an average value of 74-75 km at 1.5  $\mu\text{m}$ .

To study some possible behavior and trends with the location on the planet, local time and observative conditions we can analyze the plots of the altitude of the clouds as a function of these parameters.

In Figure 46 is shown the clouds top altitude function of the Latitude. Most of the spectra show a value around 74 Km, with a maximum of 78 km and a decrease toward the Nord Pole down to 71 Km. This is due to the presence around the pole of the cold collar (see session 2.1.1) in which the clouds tops are located in a lower region of the atmosphere. If we observe the behavior with Local time (Figure 47) we can see that the highest clouds are located in the late afternoon.

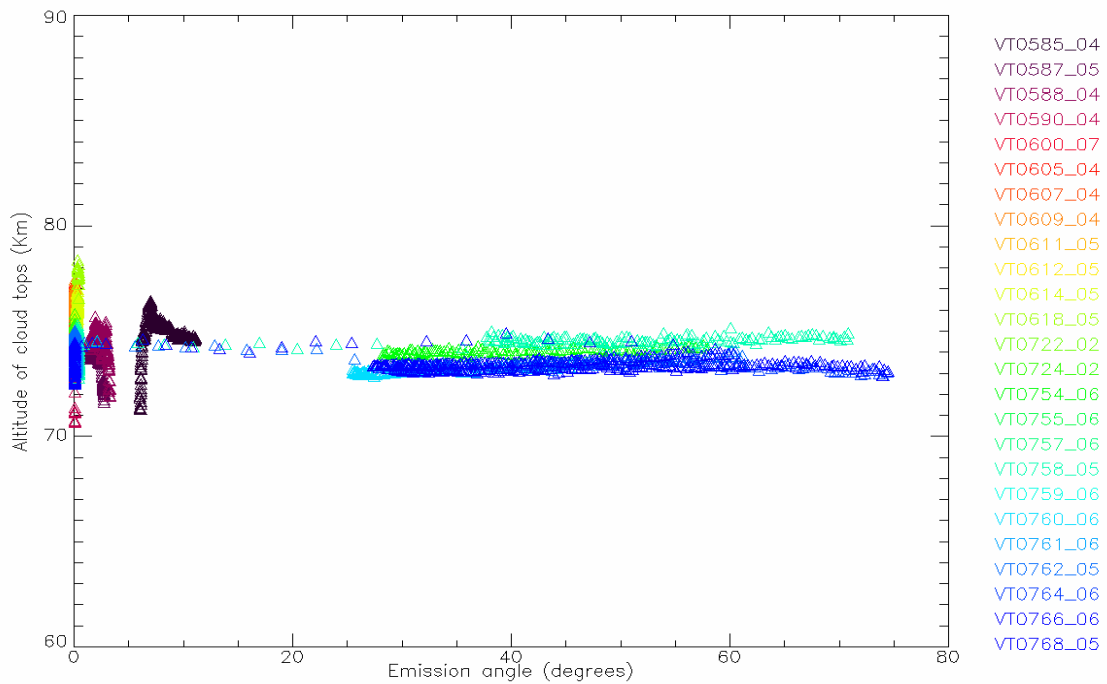


**Figure 46. Results for the clouds top altitude as a function of the Latitude. The average altitude shows a value of about 74 Km, with a decrease toward the Nord Pole to 71 Km.**

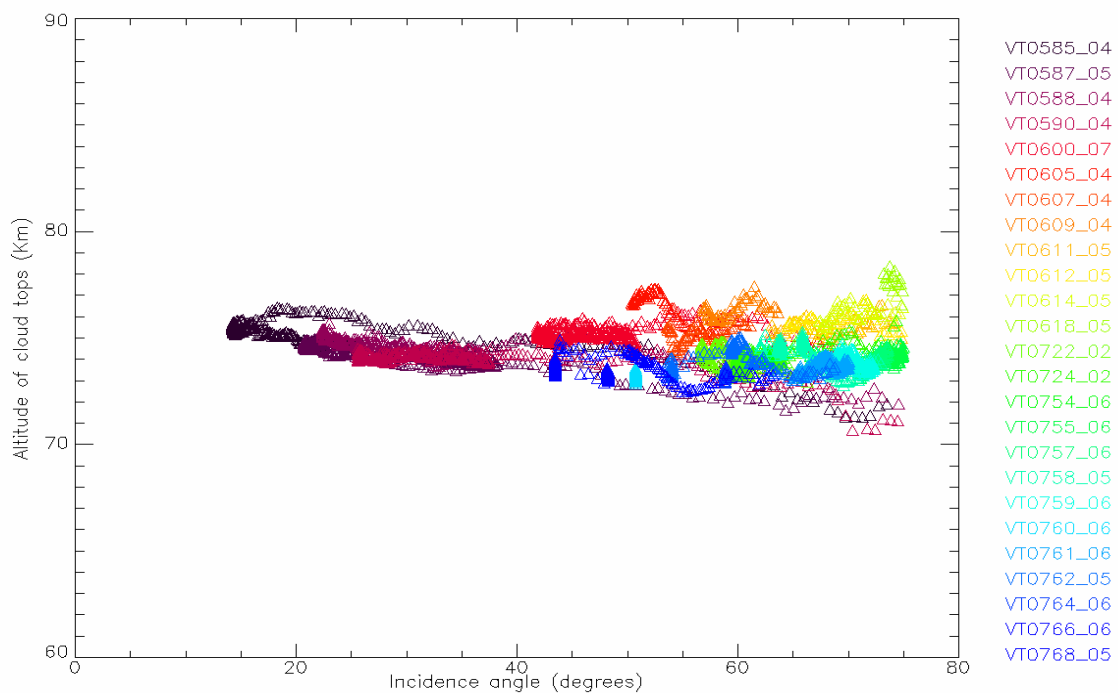


**Figure 47. Results for the clouds top altitude as a function of the Local time.**

In Figure 48 and Figure 49 the results are plotted as a function of the Emission angle (angle between the perpendicular to the surface and the direction of the spacecraft) and the Incidence angle (angle between the perpendicular to the surface and the direction of the Sun) respectively. No trends as a function of these parameters are observed as it should be when the observation's and illumination's geometry are properly taken into account in the computation of synthetic spectra for the retrieval procedure. The orbits with lower altitude's value at higher Incidence angles in Figure 49 on are biased by the fact that those data are acquired towards the North Pole, where the clouds altitude decreases.

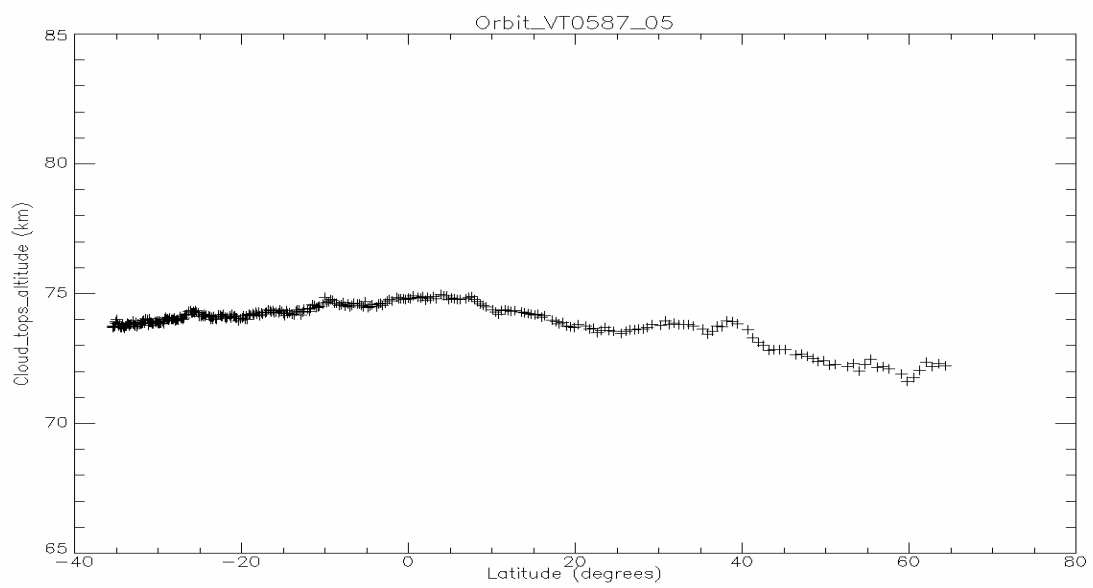
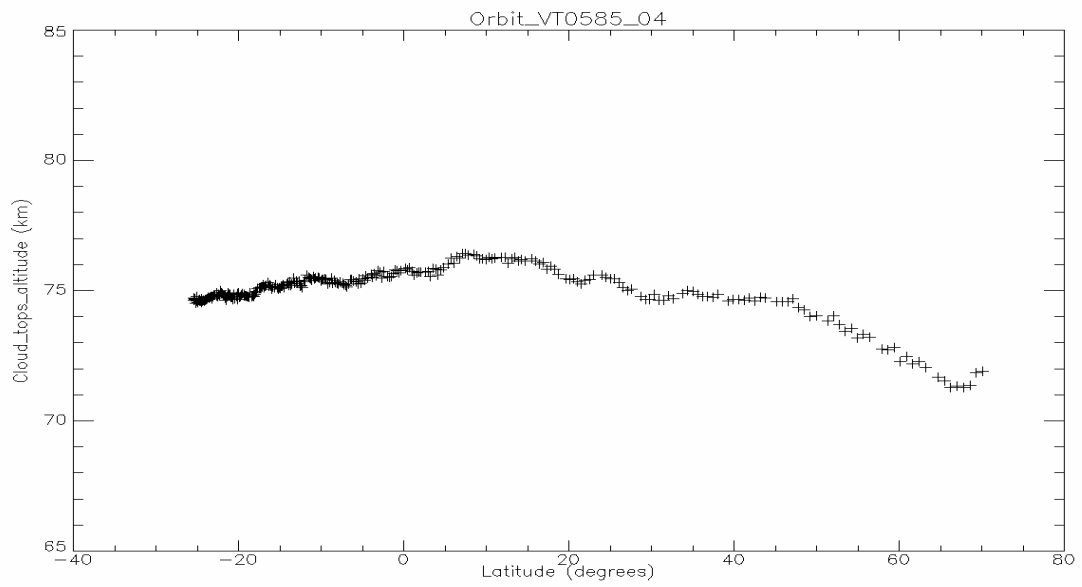


**Figure 48. Results for the clouds top altitude as a function of the Emission angle. No trends are found as expected once the observational geometry is properly taken into account in the retrieval procedure.**



**Figure 49. Results for the clouds top altitude as a function of the Incidence angle. Also in this case there is no particular trend because the illumination geometry has been modelled in the retrieval procedure. The orbits with lower altitude's value on the right side are biased by the fact that those data are acquired towards the North Pole, where the clouds altitude decrease.**

In Figure 50 we present the results for three individual orbits. Also in these cases we can easily recognize the trend of decrease towards the North Pole.



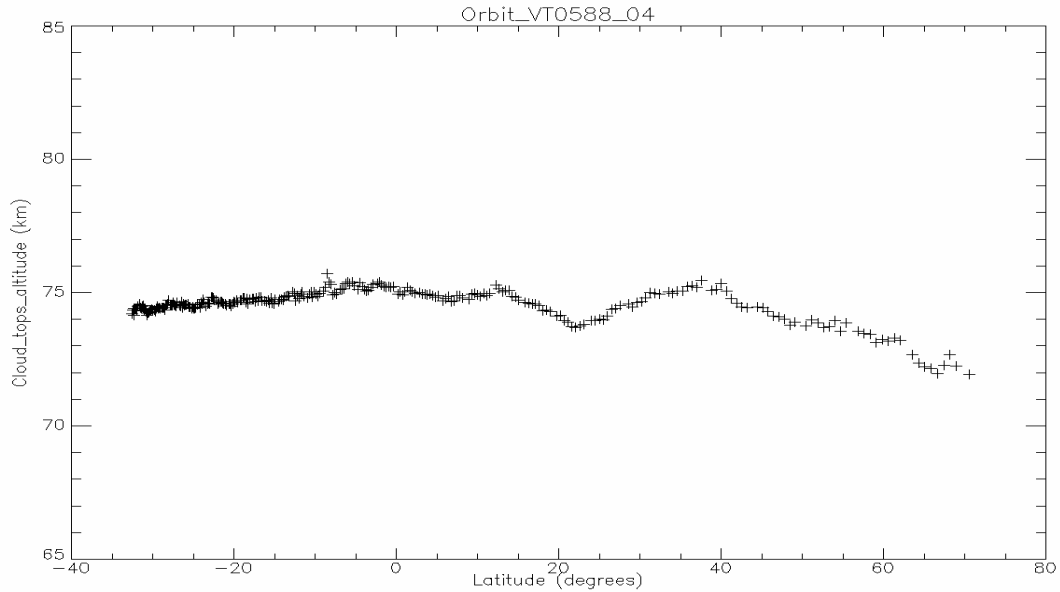


**Figure 50. Retrieval of the clouds tops altitude of individual spectra acquired in three single sessions of data. We can observe the decrease towards the North Pole.**

All the results considered in this paragraph refer to the altitude of the cloud tops at 1.5 microns. We can find the corresponding results for the 2.58 microns water band from the relation shown in Figure 43. We see that the obtained average value of 74 km at 1.5 microns corresponds at 70 km at 2.58 microns.

### **5.2.5.1 Evaluation of the error**

The evaluation of the error can be carried on taking into account each error source separately.

While the NER of this spectral region is very low, less than  $0.03 \text{ W/m}^2/\text{sterad}/\mu\text{m}$  (see Figure 15) and consequently negligible, the systematic calibration error is not well known. For the model we can roughly adopt an error equal to half of the atmospheric scale height which we used in the retrieval procedure; in our case, using a scale height of 4 km the error can be in a first approximation evaluated in  $\pm 2 \text{ km}$ . To overcome those uncertainties we had the possibility to use the comparison between our results and the ones obtained with the retrieval of the cloud

tops altitude from VIRTIS-M data (Ignatiev et al., manuscript in progress). The results from the two different data were obtained independently, using two instruments which work separately (VIRTIS -H and -M) and with completely different retrieval procedures. We found that in one section of data acquisition the two instruments worked almost simultaneously acquiring spectra of the same region and Local Time. We compared these observations presenting the result in Figure 51.

We can observe an excellent agreement of the results, with the VIRTIS-H retrieved values coinciding with the VIRTIS-M for all the latitude until 50 degrees. For higher latitudes the trend of the two sections becomes different. This can be mostly ascribed to the change of signal level between high and low latitudes, so that the calibration errors (5.2.2.1) at low signal levels may become relatively more important.

This result can be used for a valuation of the error on the cloud top altitude retrieval, which can be considered of 1 km when data are not affected by calibration's problems.

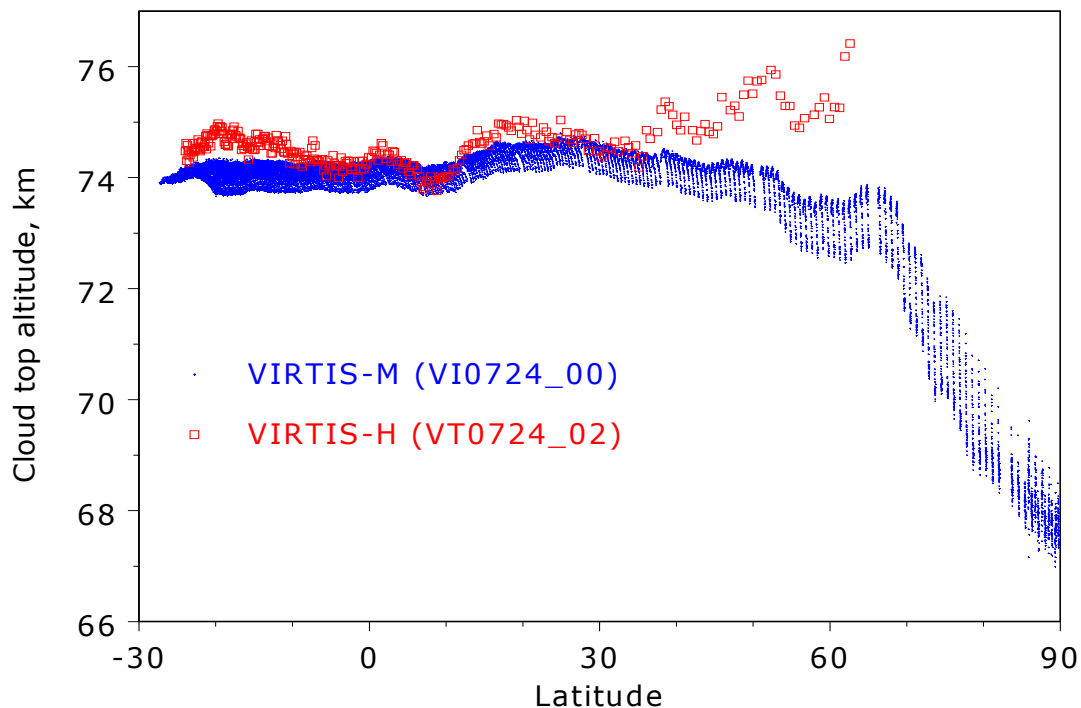


**Figure 51.** Comparison between our results (VIRTIS-H) on the cloud top altitude and the ones obtained independently by Ignatiev (manuscript in progress) from VIRTIS-M data.

## 5.2.6 Results for water abundance

From the same individual data, after evaluating the altitude of the clouds to get the correct optical path, we retrieved the content of water in the mesosphere above the clouds deck.

As done for cloud top altitude, we analysed the behaviour of the water mixing ratio as a function of the main observational parameters.

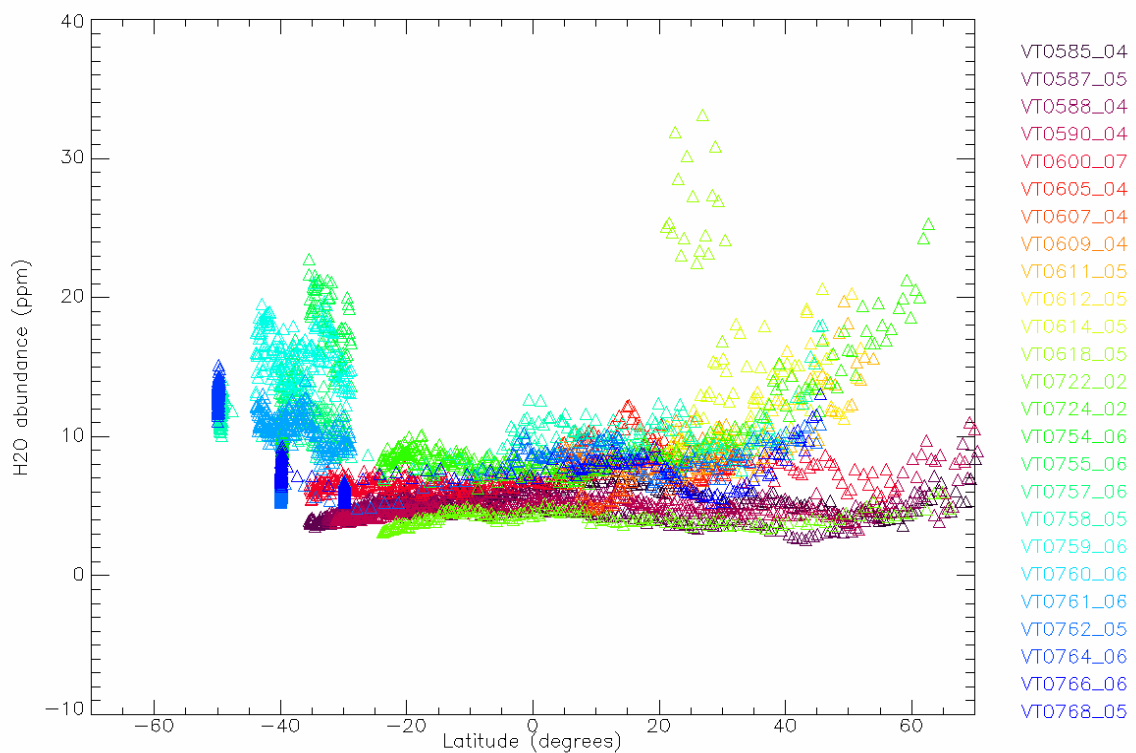


**Figure 52. Results for the water content as a function of the Latitude. The average value of the mixing ratio is ranging from 5 to 8 ppm. Some session of data shows higher content of water up to more than 30 ppm.**

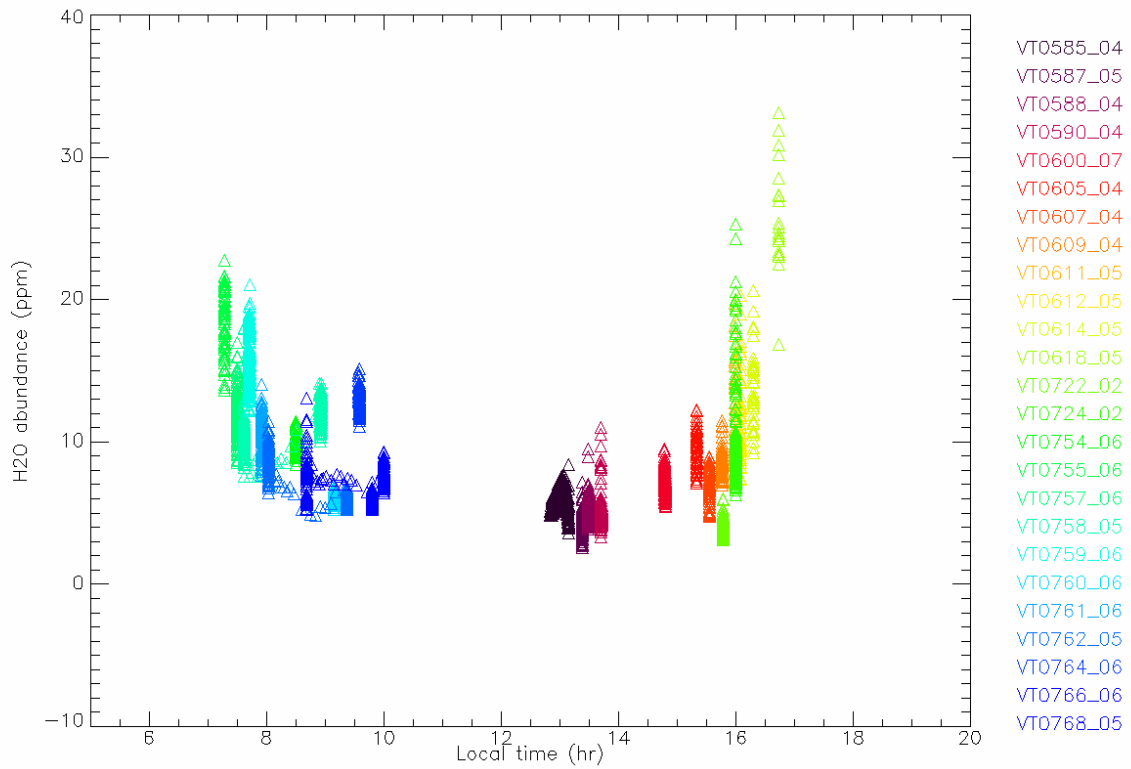


**Figure 53. Results for the water content as a function of the Local time. From the picture we can notice a minimum near noon and an increase in the early morning and late afternoon.**

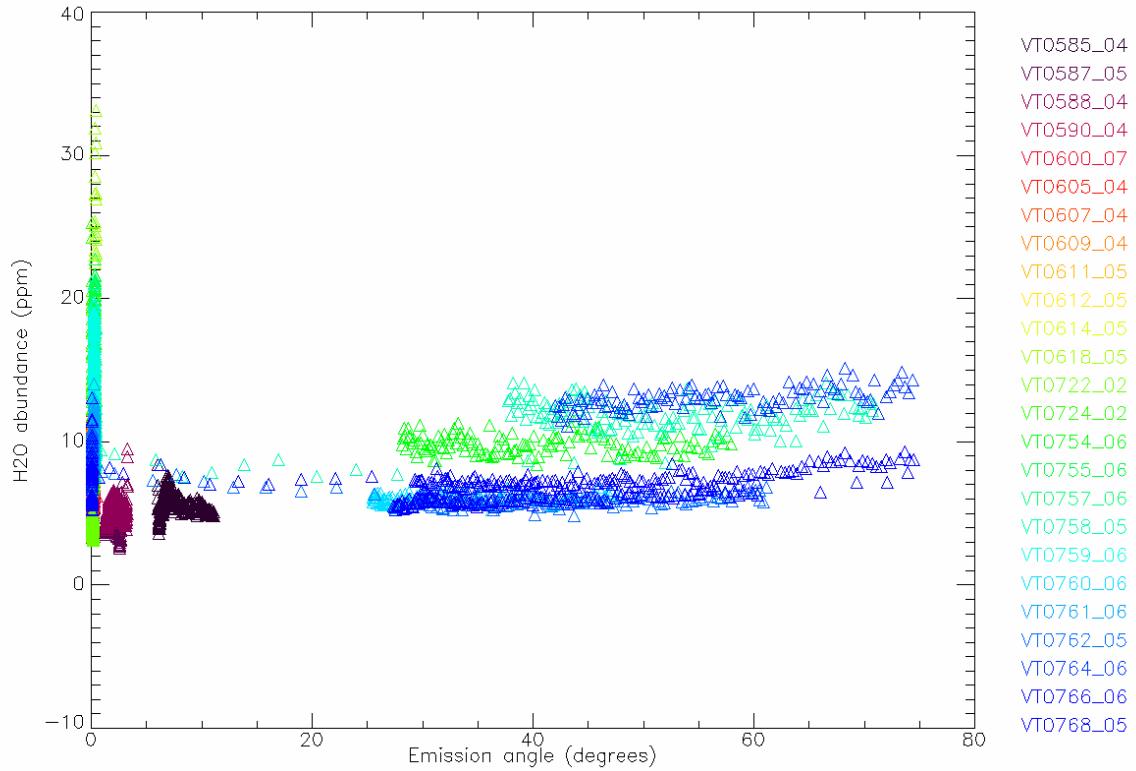


**Figure 54. Results for the water content as a function of the Emission angle.**

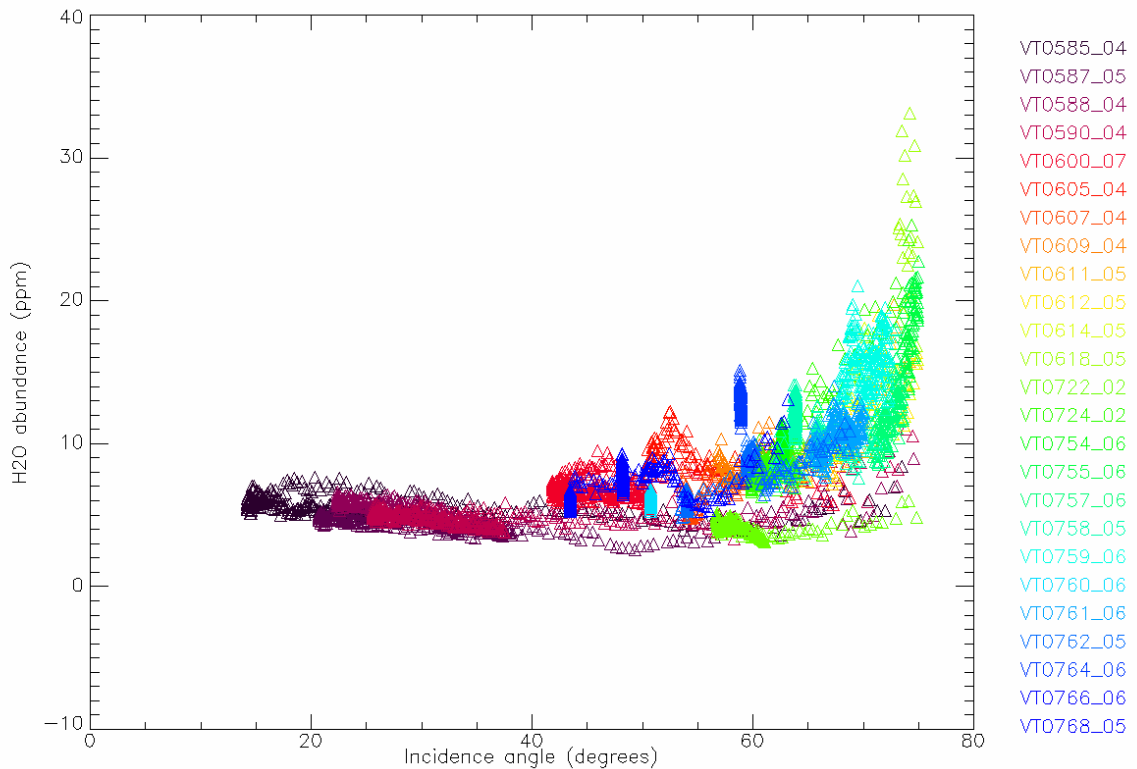


**Figure 55. Results for the water content as a function of the Incidence angle.**

From Figure 52 and Figure 53 we note that water content is highly variable in the mesosphere and many results indicate for its mixing ratio a value around 5 ppm, with some peaks up to more than 30.

In particular, Figure 53 shows the water content as a function of Local time. We find a decrease of water at noon, in the subsolar point, which does not confirm previous results obtained by Schofield et al. (1983) indicating an higher amount of water at midday.

Instead we see an enhancement of water in the early morning and late afternoon observations, which is probably correlated with the chemistry of H<sub>2</sub>O involved with SO<sub>2</sub> to form clouds of H<sub>2</sub>SO<sub>4</sub>.

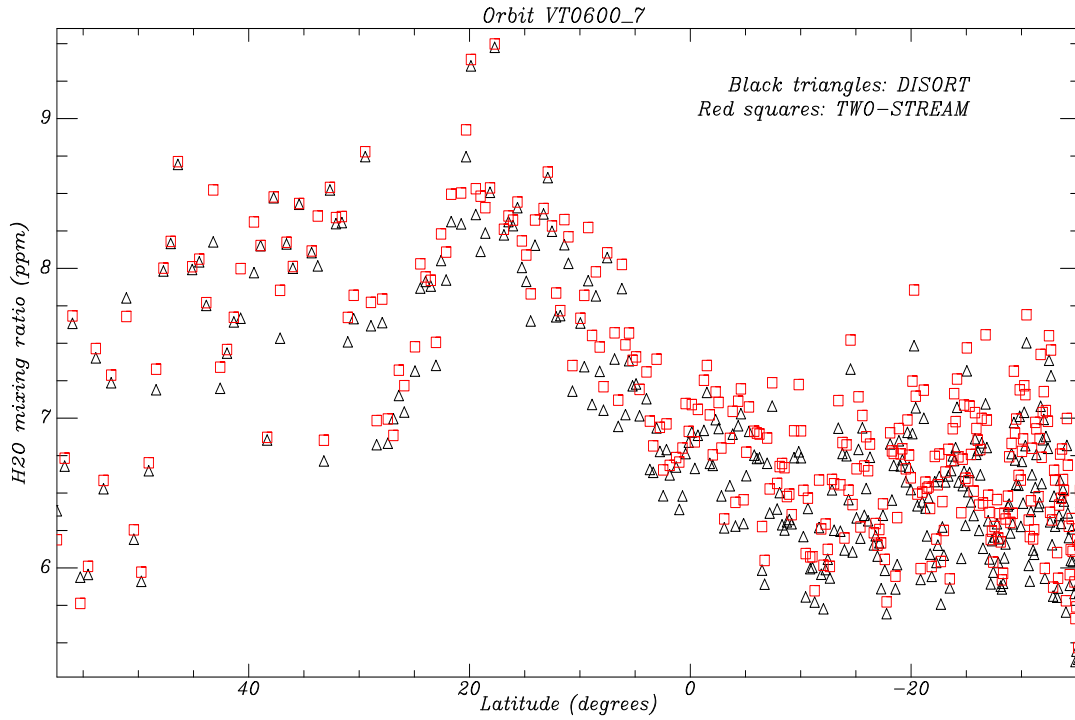
Figure 54 and Figure 55 indicates, as for the clouds altitude, no particular trend of water content as a function of the emission angle and also of the incidence angle, apart for angles higher than 60 degrees. There is an observative bias that imposes a correlation between data observed when Sun was illuminating the considered region at high incidence angle and high latitudes, due to the negligible inclination of Venus rotation's axis.

For the characteristic of the observation's geometry, which poses the spacecraft in a polar orbit, there is an observative bias also between high Sun's incidence angles and Local Time, in particular the regions close to the terminator (early morning and late afternoon).

Consequently, if data cannot rule out an enhancement of the water at noon- but eventually a decrease - it is not so straightforward to confirm the observed increase in the data acquired near the terminator. Actually, the much abundant water we find from 7 to 8 in the morning and from 17 to 18 in the afternoon is retrieved from data of regions with the Sun at incidence angles higher than 60 degrees. High angles can make the assumption of plane parallel layers in the atmosphere failing with the use of TWO-STREAM (see 4.2.2) approximation for the treatment of the scattering. For this reason we repeated the water content retrieval for orbits with high angles using the Discrete Ordinate methods (see 4.2.2) to properly account for scattering contribution. The trend of water content as a function of parameters as incidence angle, Local Time or Latitude anyway did not basically change its characteristic when using DISORT computations as we can see in the plots of the results obtained using the two methods, presented in Figure 56: water content's retrieval shows very similar values.

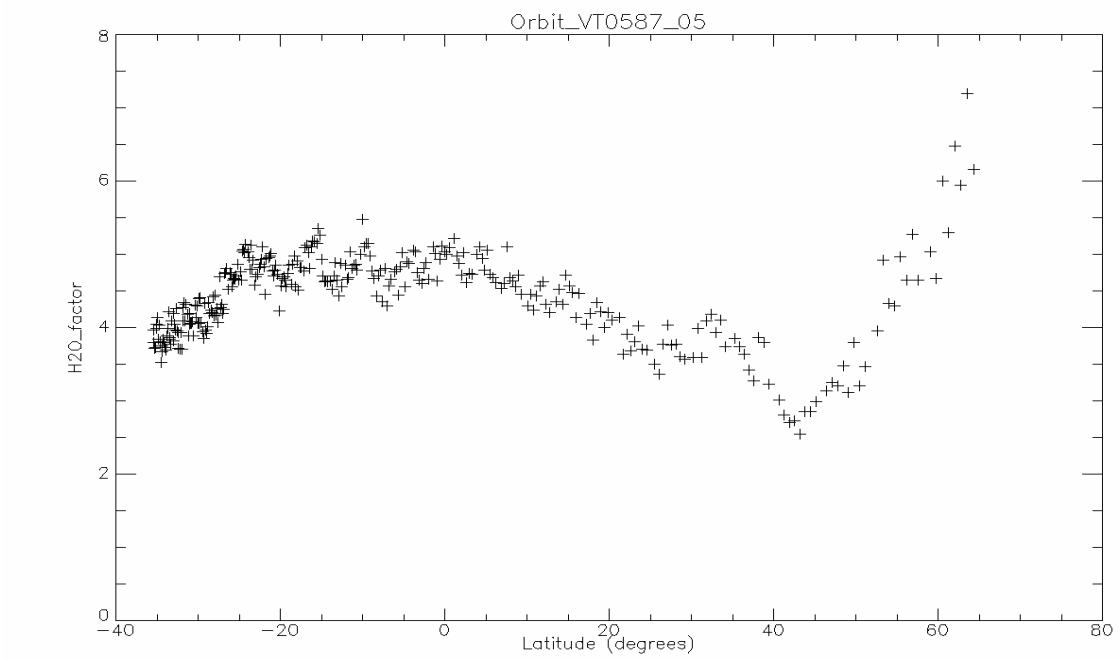
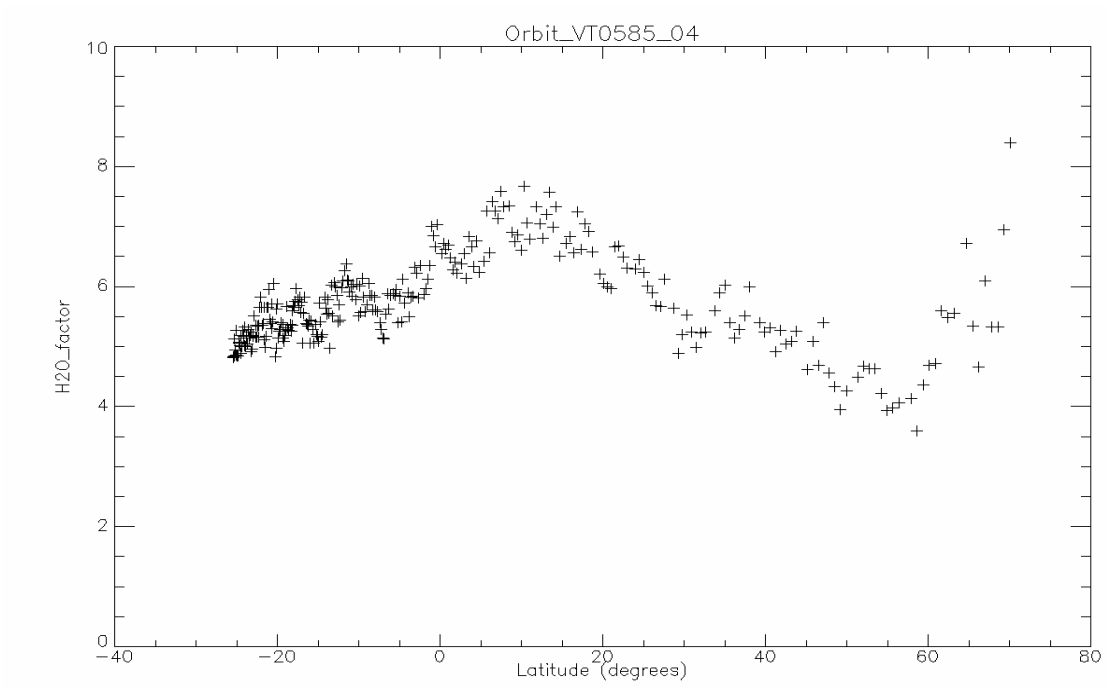
Moreover, from the retrieval of the altitude of the clouds top we don't observe the same trend of water with local time, especially in the morning. This is a confirmation of the correctness of the retrieval method, which, if failing for high incidence, emission, phase or azimuth angles, should have failed also on the clouds altitude's retrieval.

We interpret this result not in the direction of attributing a dependence of the retrieved values on the Sun illumination's direction, because phenomena correlated with photo-dissociation occurs in a much higher region of the atmosphere (> 110 km) and also dynamics models does not foresee diurnal variability. The behaviour it is most probably correlated with the chemistry occurring with the species which forms sulphuric acid in the clouds.



**Figure 56.** Comparison between results obtained with DISORT (black) and TWO-STREAM (red) for the scattering's treatment in synthetic spectra computations.

From the plots of single acquisition session (the same orbits showed for clouds altitude results in Figure 50) we observe a high variability of the mesospheric water content and in particular a sort of oscillating behavior that can be due to gravity and planetary waves in the atmosphere.



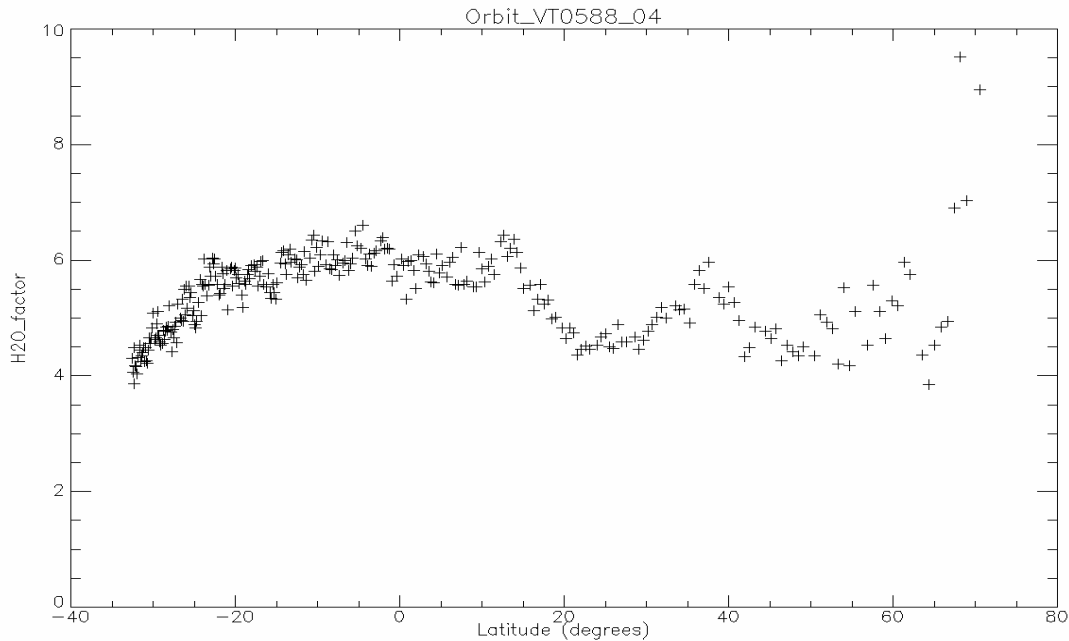


**Figure 57.** Retrieval of the H<sub>2</sub>O mixing ratio of individual spectra acquired in three single sessions of data. We can observe a high variability of the mesospheric water content and in particular a sort of oscillating behaviour that can be due to gravity waves along the atmosphere.

## 5.2.7 Inverse Method

### 5.2.7.1 *Test of the sensitivity of the water vertical profile to the altitude*

We have initially retrieved the water abundance using for water a non constant vertical profile following the models proposed by Krasnopolsky & Pollack, 1994; there are anyway no measurements supporting these models so that the real profile is still unknown. With this profile there was a problem of interpreting the results for water abundance having retrieved a scalar multiplicative factor to the vertical profile, instead of the mixing ratio. Assuming that the absorption is more sensible to the clouds top, we could give the results multiplying the factor to the ppm corresponding at

the altitude of stronger absorption. The problem was that around the region of the clouds top the adopted profile varies with an high gradient, so that we could just give an approximate results, valid for water concentration *around* the clouds top altitude, in the region of approximately  $\tau = 1$ . To give a less ambiguous result, we considered more appropriate to adopt a constant vertical profile for water. For this reason we retrieved again the H<sub>2</sub>O abundance using a profile along the vertical path in the atmosphere with a constant value of 1 ppm and considering as unknown free parameter to be retrieved a scalar multiplicative factor, constant along the height of atmosphere. In this case the results of abundance can be read directly in ppm. The results we obtained in this case had the same shape (for example along latitude) of the previous, but much less ambiguous in its meaning.

Despite of the fact that a constant profile is usually used for this kind of studies and that we can anyway give a result valid for an approximate altitude on the atmosphere, we performed a deeper investigation to clarify which atmospheric region water absorption contributes mainly to form the observed spectra.

The method we developed to test this altitude consisted in inducing small variations from the constant water vertical profile - *separately for each level* - in order to assess the sensitivity of the data on these variation.

In details, for each layer of the water vertical profile we produced a profile with constant mixing ratio for all the other layers (number of layer considered in the profile:  $l=100$ ) and a value of 0.9 and 1.1 ppm in the considered layer, in total  $2l + 1$  profiles. Then we computed synthetic spectra for all these cases. This made possible to compute for each spectral channel the partial derivative of the radiance as a function of the H<sub>2</sub>O concentration at a given level, i.e.: Jacobian of the water abundance in the atmosphere.

The synthetic spectra were computed for a clouds top *altitude of 75 Km*.

As we can see from Figure 58 we got a very interesting result: the higher sensitivity to water is found between 62 and 76 Km, with a peak at 68 Km

that is the upper part of the clouds which is responsible for the main absorption.

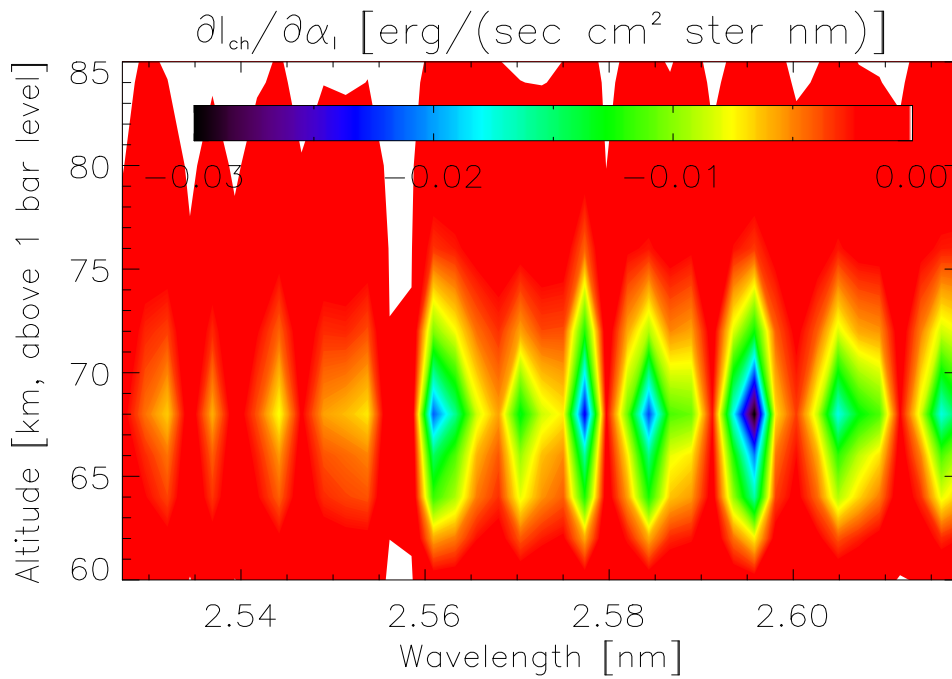


**Figure 58.** Study of the sensitivity of the spectra on the variation of water profile (around a constant value of 1 ppm), computed for a cloud top altitude of 75 km at 1.5 microns. We observe that spectra are sensible to the water absorption which occurs in the altitude range 62 – 76 km, with a peak of maximum sensitivity at 68 km.

The same procedure has been applied to spectra computed considering the cloud top altitude positioned at 70 km (Figure 59).

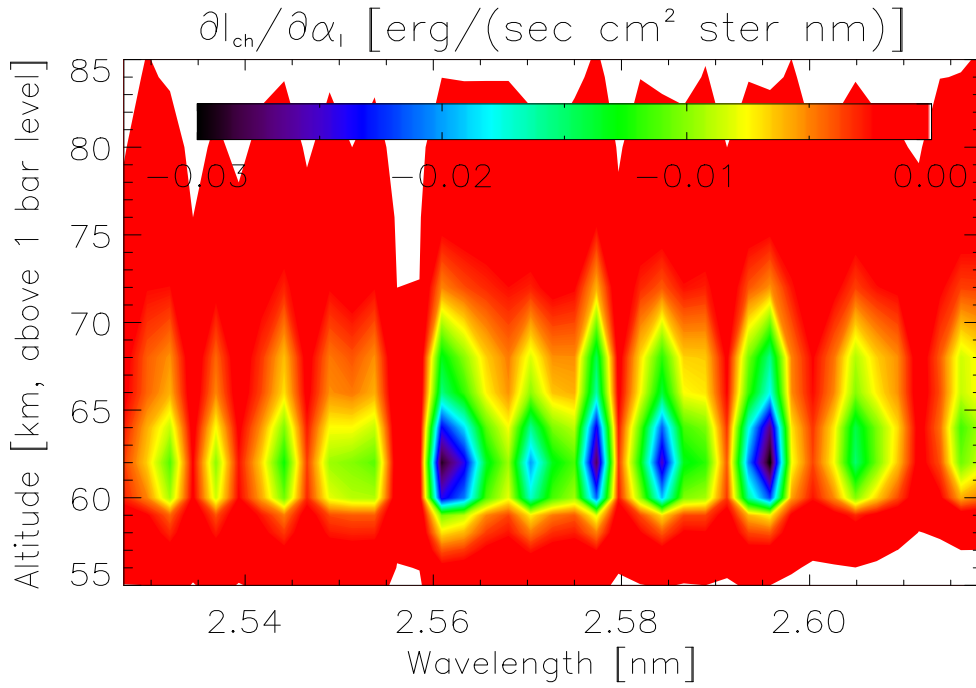


**Figure 59.** Study of the sensitivity of the spectra on the variation of water profile (around a constant value of 1 ppm), computed for a cloud top altitude of 70 km at 1.5 microns. We observe that spectra are sensible to the water absorption which occurs in the altitude range 58 – 73 km, with a pick of maximum sensitivity at 63 km.

### **5.2.7.2 Evaluation of the error on the retrieval of water abundance**

The estimation retrieval scheme chosen for this evaluation is based on the formalism of Rodgers (1976, 2000), which uses Bayes theorem of probability functions (Bayes, 1763) and Gaussian distributions for both a priori and measurement errors. The cost function minimized in order to attain the most probable value for the unknown atmospheric state,  $x$  (water vapor mixing ratio profile in our case), given the real measurements,  $y$  and a priori knowledge of the state of the atmosphere,  $x_a$ , is given by:

$$\phi_x = (y - y_x)^T S_\epsilon^{-1} (y - y_x) + (x - x_a)^T S_a^{-1} (x - x_a) \quad (0.59)$$

where,  $y_x$  is the modeled radiance,  $S_\epsilon$  is the measurement covariance error and  $S_a$  is the a priori covariance error. The Newton–Gauss method for iteratively solving the retrieval problem then provides a new, better estimate of the atmospheric state given by:

$$x_{i+1} = x_a + (S_a^{-1} + K_i^T S_\epsilon^{-1})^{-1} \cdot K_i^T S_\epsilon^{-1} \{(y - y_i) + K_i (x_i - x_a)\} \quad (0.60)$$

where  $x_{i+1}$  is the new solution of the state vector,  $x_i$  is the current solution, and  $K_i$  represents the sensitivity of the radiative transfer model to the quantities that are being retrieved, referred to hereafter as the K-matrix. This K matrix in our case corresponds to the jacobian matrix presented in previous paragraph. Rodgers (2000) shows that the total error covariance of the final retrieval error, given by

$$\hat{S} = (K_i^T S_\epsilon^{-1} K_i + S_a^{-1})^{-1}$$

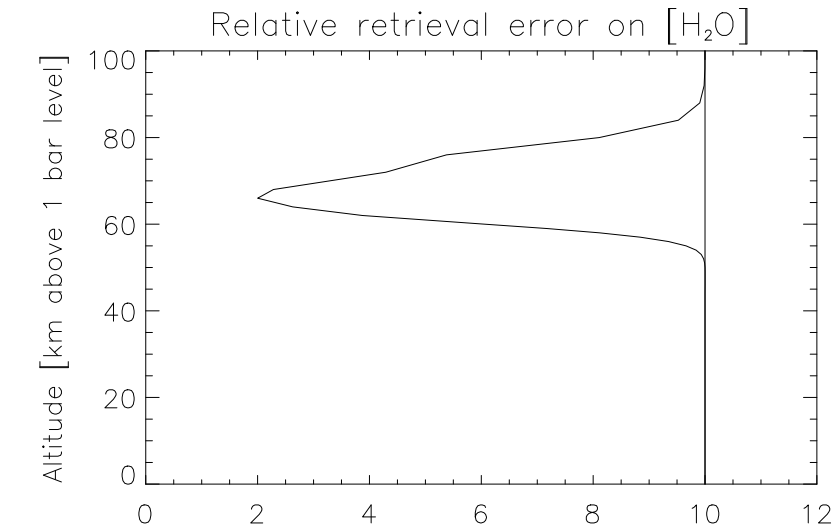
is composed of two main sources, the measurement error,  $S_m$ , which represents the uncertainty in the retrieval introduced by the measurement noise, and the smoothing error,  $S_s$ , which represents the uncertainty introduced by possible components of the state vector that the measurements cannot detect.

In this retrieval technique, the selected a priori vector  $x_a$  and covariance matrix,  $S_a$ , should cover and in a sense predict all possible observable atmospheric conditions so as to encompass the atmospheric variability observed by the measurements. In our case we considered as a priori a constant mixing ratio profile of 1 ppm. Diagonal elements of  $S_a$  are the squares of uncertainties on this a priori value at each atmospheric level. For the purposes of this numerical experiment, a constant variability of 10 ppm was adopted. In the case of the water mixing ratios, there is a correlation between the different atmospheric levels (as expected by the

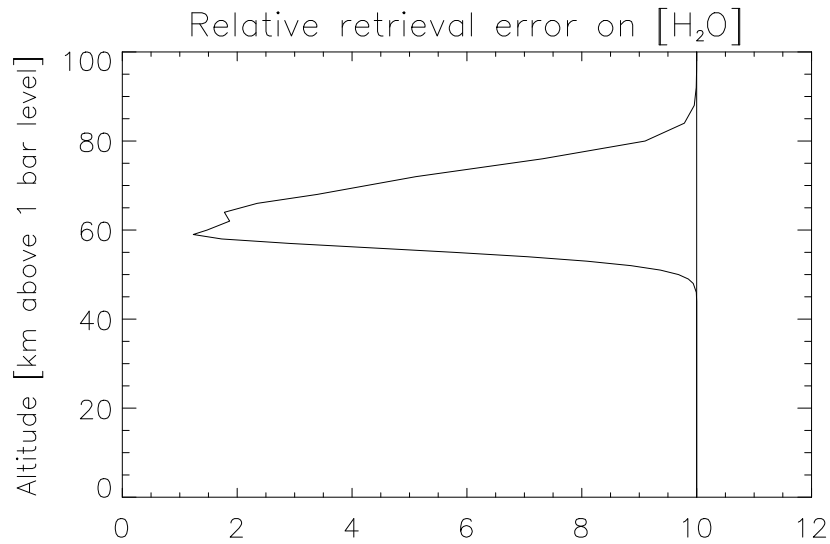
mixing of the atmosphere) and in this case, the off-diagonal elements are calculated using the following (Irwin, 1997):

$$S_{ij} = S_{ji} = \sqrt{S_{ij}S_{ji}} \exp\left(-\frac{|(z_i - z_j)|}{H}\right)$$

where H is known as the correlation length and is set to 10 km.



a)



b)

**Figure 60.** a) Error for an ideal retrieval system, computed considering the cloud top positioned at 75 km. b) Error for an ideal retrieval system, computed considering the cloud top

positioned at 70 km. The minimum error occurs in the region of maximum sensitivity of the spectra to the water absorption. Being computed for variations of a water profile with 1 ppm of mixing ratio, in x-axis we can read directly the error in mixing ratio units, instead of relative error.

These plots provide the error for an ideal retrieval system, where the unknowns are represented by the 1 (100, in our case) levels used to sample the mixing ratio profile. Nevertheless, they again confirms that our data are basically sensitive to the region “just above” clouds tops, where, taking a constant mixing ratio as the only unknown, an retrieval error of 2 ppm can be quoted as a figure of merit. Further numerical experiments demonstrated that this value has weak dependence from assumed covariance matrix on a priori and shall therefore be considered as robust.

## **6 Results for Mars**

Although studied for long, the problem of the stability of the CO<sub>2</sub>-dominated Martian atmosphere remains a topical question. It raised when it was noticed that CO<sub>2</sub> photolysis by solar light penetrating deeply in Mars thin atmosphere might have led to an accumulation of CO and O<sub>2</sub> giving an abundance for these two constituents of up to 10%. Indeed, this would have been possible as the spin-forbidden inverse reaction (CO + O → CO<sub>2</sub>) is very slow. However, observational evidences show that the amount of CO and O<sub>2</sub> remains very modest (approximately 0.08% and 0.12% respectively) and that therefore CO<sub>2</sub> is somehow efficiently recycled. Clancy et al., 1990 and Encrenaz et al., 1991, show CO mixing ratios in the range of 550-800 ppm. However, it is considerably smaller, by a factor of 3--5, than those of Kakar et al. (1977) and of Good & Schloerb (1981). Measurements of CO from a variety of studies performed during different Martian seasons consistently give CO mixing ratios in the above mentioned range. This is puzzling also since the main atmospheric constituent, CO<sub>2</sub>, is subject to substantial seasonal variations due to condensation (fall and winter) and sublimation (spring) on the polar caps. Measured variations in CO<sub>2</sub> should result in measurable variations in CO by a factor of 2-4 according to predictions from Mars general circulation models, while (Clancy et al., 1983) have shown the mixing ratio in the Martian atmosphere to be variable and with possible seasonal fluctuations, but without a clear evidence for a significant change of the CO abundance over a timescale of about 5 years, although F. Billebaud et al. attributed to the range of CO variability values from 0 to 100%. Further, the altitude distribution of CO is not well constrained. Krasnopolsky (1993b) has also shown that the solar cycle could have an effect on the CO mixing ratio, inducing a variation which could reach 35%. In all cases, the problem remains however of the apparent lack of variation

of the O<sub>2</sub> abundance, which makes it difficult for the CO abundance to vary. Concerning the question of possible spatial variations of the CO abundance, Lellouch et al. (1991), from millimetric observations, have shown that spatial variations, if any, could not exceed 40% on spatial scale comparable to a Martian radius. The photochemistry, transport properties and thermal structure of the atmosphere of Mars, and the temporal variations of those properties on daily and seasonal time scales, are important to understanding the basic questions about the Martian environment - its origin, evolution and stability. The photochemistry of Mars is currently uncertain in several aspects. One is the question of the suitability of homogeneous (gas phase) chemistry to explain the abundance of trace species, including CO as well as H<sub>2</sub>O, O<sub>2</sub> and O<sub>3</sub> in the atmosphere. Atreya & Gu (1994, 1995) have suggested that some kind of heterogeneous catalytic process, perhaps involving aerosols of ice or dust, may be required to explain the recycling rate of CO<sub>2</sub> on Mars: specifically, aerosol surface chemistry may be required to provide a sink for some of the trace species which participate efficiently in the recycling of CO<sub>2</sub>. We investigated CO in Martian atmosphere in order to give contribute to the atmospheric stability's comprehension and to still open questions.

In the case of Mars, the lines are very narrow, because the Lorentz broadening (proportional to the pressure) is very small. Thus, very high spectral resolution is required to search for minor species and PFS data.

## ***6.1 Carbon monoxide abundance (CO) in Martian atmosphere***

Carbon monoxide represents the main product of CO<sub>2</sub> photolysis and therefore it is strictly correlated to the stability of the Martian atmosphere of CO<sub>2</sub>.

However, although studied since a long time, the problem of the stability of the CO<sub>2</sub>-dominated Martian atmosphere remains a controversial question. It raised when it was noticed that CO<sub>2</sub> photolysis by solar light penetrating deeply in Mars thin atmosphere might have led to an accumulation of CO and O<sub>2</sub> giving an abundance for these two constituents of up to 10%. Indeed, this would have been possible as the spin-forbidden inverse reaction (CO + O → CO<sub>2</sub>) is very slow. However, observational evidences show that the amount of CO and O<sub>2</sub> remains very modest (approximately 0.08% and 0.12% respectively) and that therefore CO<sub>2</sub> is somehow efficiently recycled. Clancy et al., 1990 and Encrenaz et al., 1991, show CO mixing ratios in the range of 550-800 ppm. However, it is considerably smaller, by a factor of 3-5, than those of Kakar et al. (1977) and of Good & Schloerb (1981). Measurements of CO from a variety of studies performed during different Martian seasons consistently give CO mixing ratios in the above mentioned range. This is puzzling also since the main atmospheric constituent, CO<sub>2</sub>, is subject to substantial seasonal variations due to condensation (fall and winter) and sublimation (spring) on the polar caps. Measured variations in CO<sub>2</sub> should result in measurable variations in CO by a factor of 2-4 according to predictions from Mars general circulation models, while (Clancy et al., 1983) have shown the mixing ratio in the Martian atmosphere to be variable and with possible seasonal fluctuations, but without a clear evidence for a significant change of the CO abundance over a timescale of about 5 years, although Billebaud et al., (1998) attributed to the range of CO variability values from 0 to 100%. Further, the altitude distribution of CO is not well constrained. Krasnopolsky (1993b) has also shown that the solar cycle could have an effect on the CO mixing ratio, inducing a variation which could reach 35%. In all cases, an additional puzzle is represented by the apparent lack of variation of the O<sub>2</sub> abundance, which makes it difficult for the CO abundance to vary. Concerning the question of possible spatial variations of the CO abundance, Lellouch et al. (1991), from millimetric observations, have shown that spatial variations, if any, could not exceed 40% on spatial scale comparable to a Martian radius. The photochemistry,

transport properties and thermal structure of the atmosphere of Mars, and the temporal variations of those properties on daily and seasonal time scales, are important to understanding the basic questions about the Martian environment - its origin, evolution and stability. The photochemistry of Mars is currently uncertain in several aspects. One is the question of the suitability of homogeneous (gas phase) chemistry to explain the abundance of trace species, including CO as well as H<sub>2</sub>O, O<sub>2</sub> and O<sub>3</sub> in the atmosphere. Atreya & Gu (1994, 1995) have suggested that some kind of heterogeneous catalytic process, perhaps involving aerosols of ice or dust, may be required to explain the recycling rate of CO<sub>2</sub> on Mars: specifically, aerosol surface chemistry may be required to provide a sink for some of the trace species which participate efficiently in the recycling of CO<sub>2</sub>. We investigated CO in Martian atmosphere in order to give contribute to the atmospheric stability's comprehension and to the still open questions. In Martian spectrum, lines are very narrow, because the Lorentz broadening (proportional to the pressure) is very small. Thus, very high spectral resolution is required to search for minor species and PFS, with a spectral resolution of 1.3 cm<sup>-1</sup> is suitable for this task.

### **6.1.1 Retrieval method and Atmospheric model**

For the atmospheric CO abundance detection, in the present analysis we have used data from the Short Wavelength Channel in which CO is present with two bands centred around 2130 and 4270 cm<sup>-1</sup> of respectively transitions (1-0) and (2-1). The first, being much more intense, is the one used for this task.

In the spectral range of the CO investigation, the spectrum is simulated by a radiative transfer equation in which the sources of reflected solar radiation and thermal infrared emission from the surface and the atmospheric layers are both important, giving a comparable contribute to the formation of the radiance spectrum.

Lines spectral parameters are extracted from spectroscopic database HITRAN 2004 (Rothman et al., 2005), with the correction for the CO<sub>2</sub>-broadening parameter according to the values calculated by Sung and Varanasi (2005).

The model assumes a plane-parallel geometry. Vertical pressure and temperature profile used for the simulation has been extracted from theoric European Mars Climate Database (EMCD, Forget et al., 2006) for the time and location of the observed spectrum while retrievals of the T(p) profile directly from the data were available and therefore used for the analyses of a first dataset of observations. The computation of the synthetic spectra used to fit the data has required as well taking into account observational geometry, Sun incidence angle and surface temperature pressure and albedo. Indeed, since through the thin Martian atmosphere radiation reaches the surface and is reflected back in a percentage given by its albedo, this parameter is important in the spectra computation. Surface pressure is taken by interpolating the Viking Lander 1 vertically recorded data on the MOLA topography (Smith et al., 2001a). CO content is estimated assuming to have a uniform mixing ratio, i.e. constant with height all along the atmospheric column and ignoring scattering due to aerosols.

As for Venus simulations, also for this work a line-by-line radiative transfer algorithm has been developed to simulate observed Martian spectra. This allows evaluating CO content by modelling *individual* spectra, obtaining *simultaneously* CO mixing ratio, surface temperature and an estimated value of the *albedo* in the considered spectral region. This radiative transfer modelling has been applied to the spectrum in the interval between 2030 and 2300 cm<sup>-1</sup>, including the gaseous absorption by CO<sub>2</sub> and CO in computation of synthetic spectra computation. This wide interval for fitting the spectrum has been selected to make possible a subsequent check of the fit of the adjacent CO<sub>2</sub> absorption lines and band, as will be described later. Fitting of CO abundance has instead been performed in a smaller interval which includes 34 spectral channels inside the CO lines in the range 2068 - 2208 cm<sup>-1</sup>.

In Figure 61 and Figure 62 examples of the CO spectrum fit at two different radiance's levels are presented.

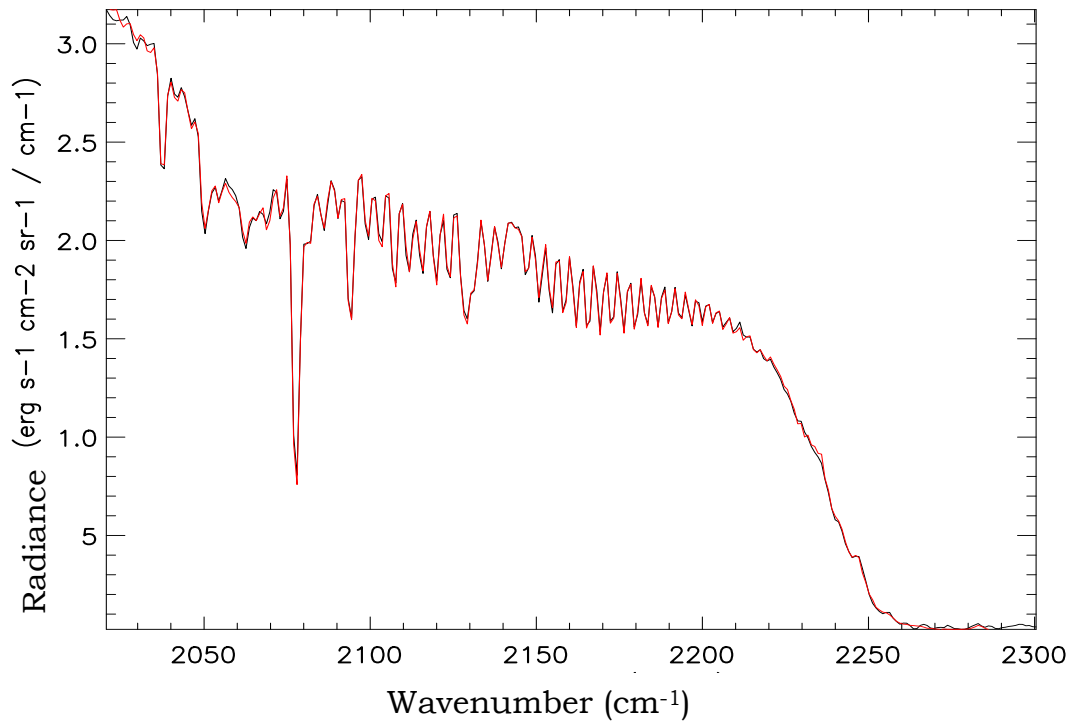


**Figure 61. Fit of the CO spectrum: in black and red respectively observed and synthetic spectrum.**

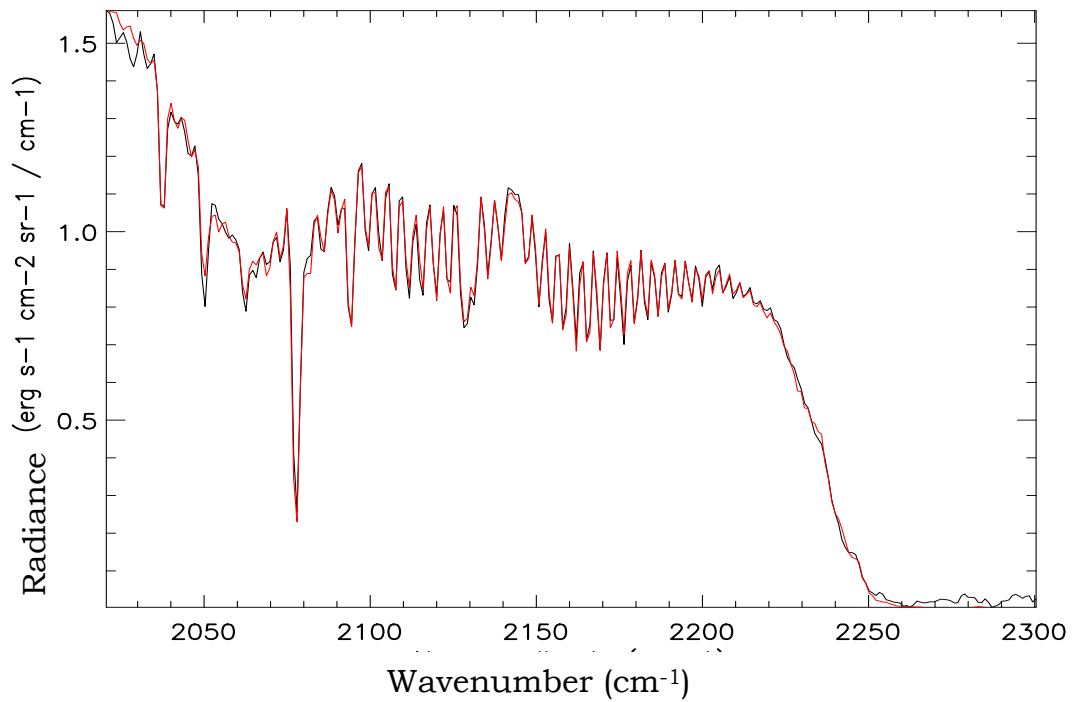


**Figure 62. Fit of the CO spectrum: in black and red respectively observed and synthetic spectrum.**

The spectrum is fitted by an iterative process. In an ideal case, the only unknown parameter to be fitted simultaneously with mixing ratio is the surface albedo  $A_s$ . In practice, the surface temperature  $T_s$  is also not precisely known and can be derived in addition to the surface albedo. Thus the process takes a general form which includes: surface temperature fitting, surface albedo fitting, gas mixing ratio fitting and finally a convergence check.

For each of the first three steps we have used a simple and robust fitting procedure, assuming that the initial guess of retrieved parameters may be quite far from its true value, and the absolute calibration of the PFS spectra may be not perfect.

*Surface temperature fitting.* A set of temperatures  $T_s^k$ ,  $k = 1..K$  around the current value of  $T_s$  are chosen and the corresponding synthetic spectra are calculated. Then the best fit value  $T_s^*$  is defined as the one that provides a minimum difference (in terms of root mean square deviation) between the synthetic and measured spectra in the “continuum” channels (previously defined together with gas channels). The size of the “window”  $[T_1, T_k]$  is decreasing with iterations. Then the dependence of the difference  $\text{RMSD}(S-S_0)$  on the surface temperature is approximated by a parabola, and then its minimum is defined.

A similar procedure is used for *surface albedo fitting*. We define the formal best fit albedo  $A_s(\nu_c)$  for each continuum channel  $\nu_c$  (practically we take just the points where no gas absorption is present, that is continuum points and produce a broken curve from these points), and then obtain a smooth albedo curve  $A_s(\nu)$  by convolving this usually noisy curve with a smooth function. Surface temperature and albedo are defined using “continuum” channels.

*Mixing ratio* (or, more precisely, its logarithm) is defined using “gas” channels in a way similar to the surface temperature fitting.

The process is stopped if the relative change of the gas column density between iterations is less than some predefined value (e.g. 1%), or a maximum number of iterations is reached (e.g. 10).

Moreover, at the end of the retrieval procedure, selection of the obtained fits was performed. We selected only the retrievals in which both CO<sub>2</sub> lines and band adjacent to the considered CO band resulted properly modelled, to exclude any problems on data calibrations (e. g. the bottom of the CO<sub>2</sub> band had sometimes a wrong radiance level) or fitting procedure due to any possible reasons.

### **6.1.2 Data**

During MEX operative period PFS instrument has reached a good spatial and temporal covering.

Among available calibrated data, two different dataset have been modelled for this study: 8000 observations taken at the beginning of the mission at Ls between 330 e 50 degrees (end of winter and beginning of spring in north hemisphere) and about 31000 spectra observed at Ls in the range 100 – 200 degrees (all summer and the beginning of autumn in north hemisphere, therefore winter in the southern one).

For simulations of the first dataset we used pressure and temperature profiles directly derived from data, while EMCD profiles were used to model the second dataset of observations since T(P) profile retrieved from the data were not yet available. The most part of the data were acquired during the morning until the early afternoon, with two peaks around 8 and 12 local time.

### **6.1.3 Error evaluation**

The PFS spectrum is not affected only by the noise, which can be characterized by NER. PFS spectra are adversely affected by spacecraft vibrations, resulting in variable distortions of the spectrum. In general, we

cannot characterize those distortions as random noise with some fixed and known  $NER$  measured in the laboratory and reported by Giuranna et al. (2005). That is why we tried to evaluate “noise” from the difference between the measured spectrum  $S^0$  and synthetic spectrum  $S$ . In an ideal case this value must have a standard deviation equal to  $NER$ , provided our model of the synthetic spectrum is good.

Error due to parameters of the model, e.g., due to the difference of the EMCD temperature profiles and real conditions, is to be considered separately.

Uncertainties due to aerosol effects are also to be considered separately.

Error of the numerical model is well below other systematic and random errors and uncertainties and is therefore neglected.

Error due to random noise and other uncertainties in the spectrum caused by vibrations etc. is evaluated in a simplified manner from the considerations given below. More complex and formal procedure would take more efforts without any considerable improvement in the quality of error evaluation and is beyond the scientific purpose of this thesis.

After the last iteration, when the process is considered to have converged, a spectrum for a slightly different mixing ratio is evaluated and then the error is derived.

Let the final value be  $q$ , and  $x = \log_{10}(q)$ , and the corresponding spectrum  $S$ .

Then

$$x_1 = x + \delta x, \tag{0.61}$$

where  $\delta x = 0.1$  (a good choice for  $\delta x$  is evidently a value of the order of the expected error), or, in terms of mixing ratio

$$q_1 = q \cdot 10^{\delta x} \tag{0.62}.$$

The mixing ratio is derived from fitting the spectrum in “gas” and “continuum” channels, that is in fact from the depth of the band  $D$ , which, independently of the particular definition, reduces to the difference between the average spectra in “continuum” channels and “gas” channels

$$D \sim \bar{S}_c - \bar{S}_g, \quad \text{where } \bar{S}_c = \frac{1}{N} \sum_{i=1,N} S_i, \quad \bar{S}_g = \frac{1}{M} \sum_{j=1,M} S_j \quad (0.63),$$

$i$  enumerates “continuum” channels and  $j$  – “gas” channels.

The error in terms of mixing ratio logarithm  $\varepsilon_x$  can be evaluated as follows:

$$\varepsilon_x \approx \frac{\sigma_D}{\partial D / \partial x} \sim \frac{\sqrt{\sigma_c^2 + \sigma_g^2}}{\delta D / \delta x} \quad (0.64).$$

$$\text{where } \delta D = D(x_1) - D(x), \quad \sigma_c^2 = \frac{1}{M} \sum_{i=1,M} (S_i - S_i^0)^2, \quad \sigma_g^2 = \frac{1}{N} \sum_{j=1,N} (S_j - S_j^0)^2 \quad (0.65).$$

Error in terms of mixing ratio  $\varepsilon_q$  is therefore different in + and – directions. In the file we obtain in output error in positive direction  $\varepsilon_q^+$  is written:

$$\varepsilon_q^+ = \left( q + \varepsilon_q^+ \right) - q = 10^{x + \varepsilon_x} - 10^x \quad (0.66),$$

while in the negative direction:

$$\varepsilon_q^- = q - \left( q - \varepsilon_q^- \right) = 10^x - 10^{x - \varepsilon_x} \quad (0.67).$$

To plot correctly an error bar one should take  $q$  and  $\varepsilon_q^+$ , and calculate  $\varepsilon_q^-$ ,  $q + \varepsilon_q^+$ , and  $q - \varepsilon_q^-$ .

### 6.1.4 Results

In the following graphics we present the correlations between the retrieved CO mixing ratio and some observative parameters: latitude, incidence angle of the Sun, planet Altimetry and Local Time.

Plots were obtained averaging the retrieved mixing ratio values of the data falling inside every bin of the considered parameter, weighting each individual retrieval with the corresponding error (see paragraph 6.1.3).

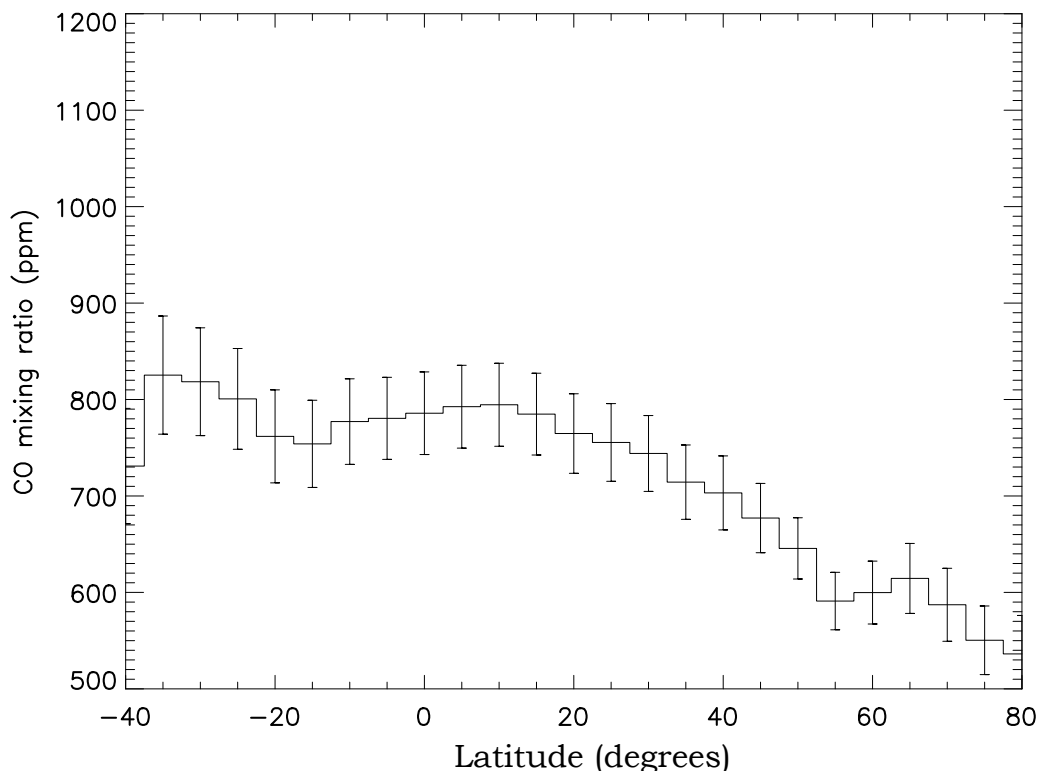


**Figure 63.** CO mixing ratio variation with Latitude, averaged in bins of 5°. Data for Ls range: 90° - 200°.

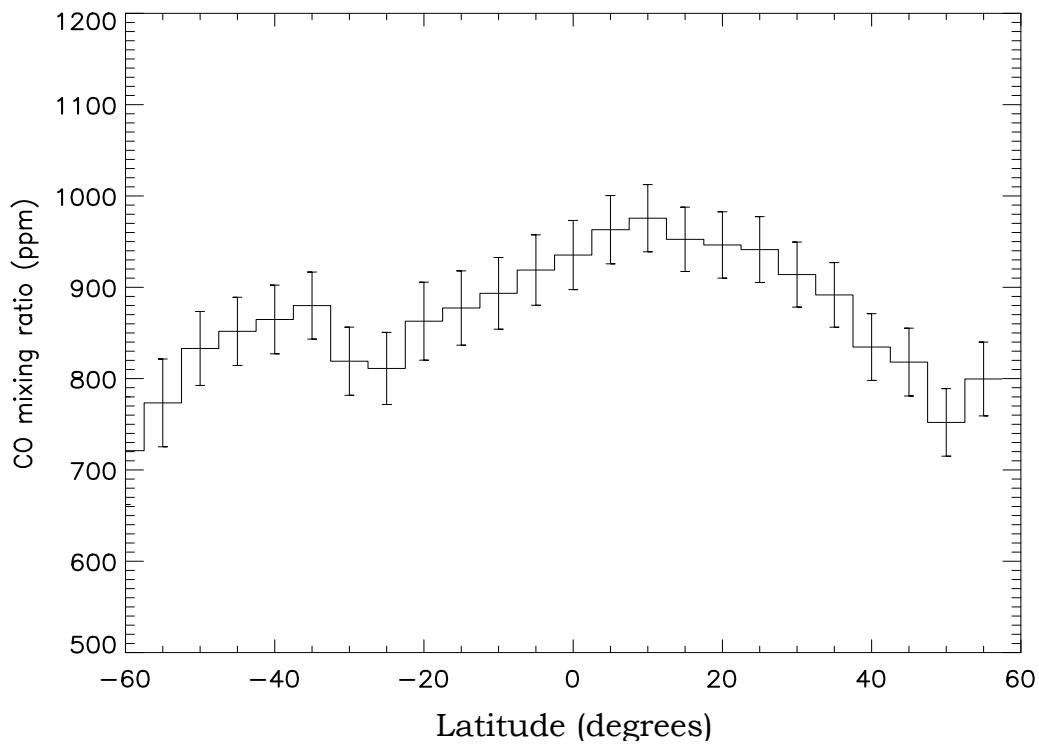


**Figure 64. CO mixing ratio variation with Latitude, averaged in bins of 5°. Data for Ls range: 330° - 95°.**

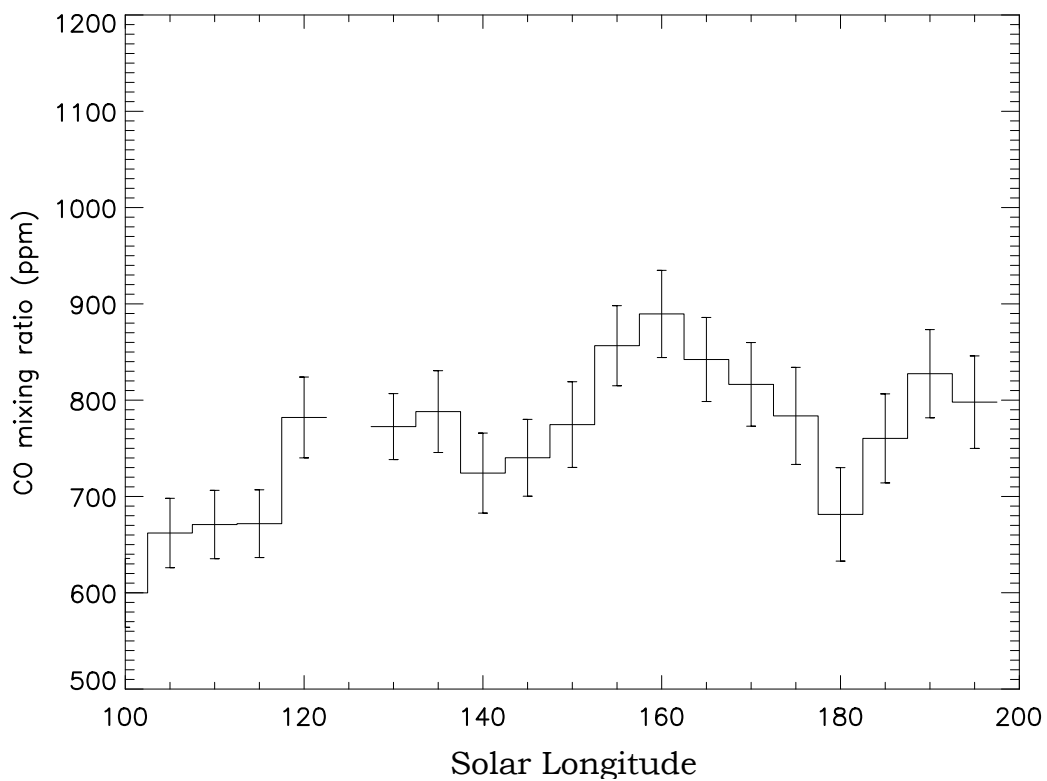


**Figure 65. CO mixing ratio variation with Season (Ls), averaged in bins of 5°. Data for Ls range: 90° - 200°.**

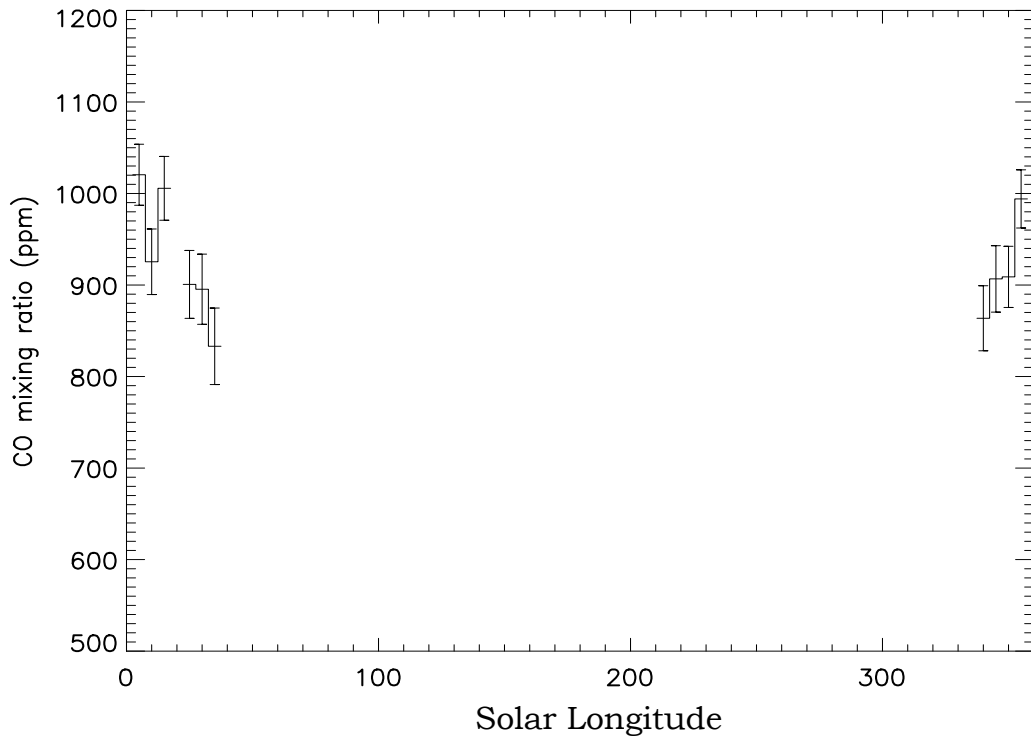


**Figure 66. CO mixing ratio variation with Season (Ls), averaged in bins of 5°. Data for Ls range: 330° - 95°.**

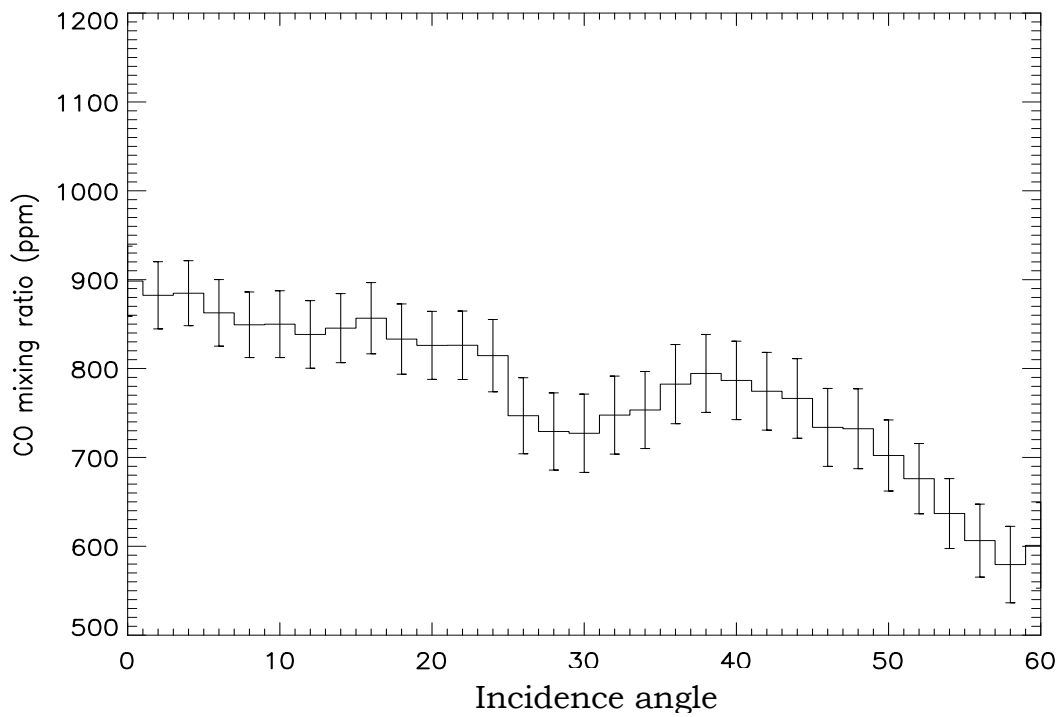


**Figure 67. CO mixing ratio variation with the solar incidence angle (Theta Sun), averaged in bins of 2°. Data for Ls range: 90° - 200°.**

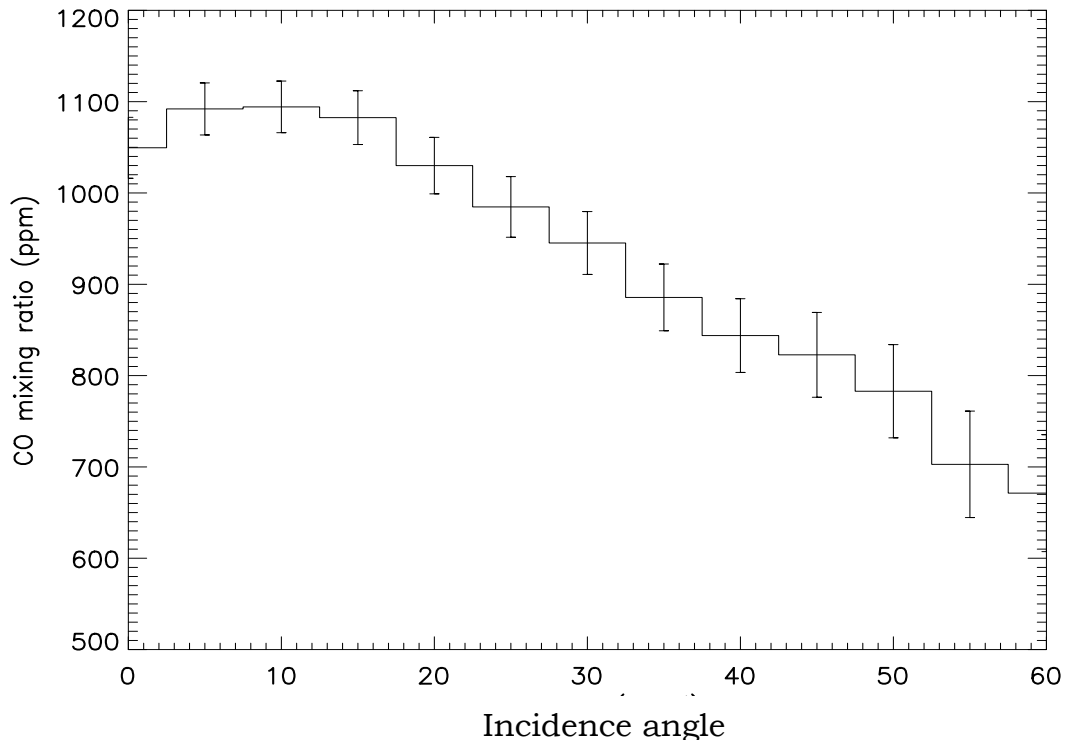


**Figure 68.** CO mixing ratio variation with the solar incidence angle (Theta Sun), averaged in bins of 5°. Data for Ls range: 330° - 95°.

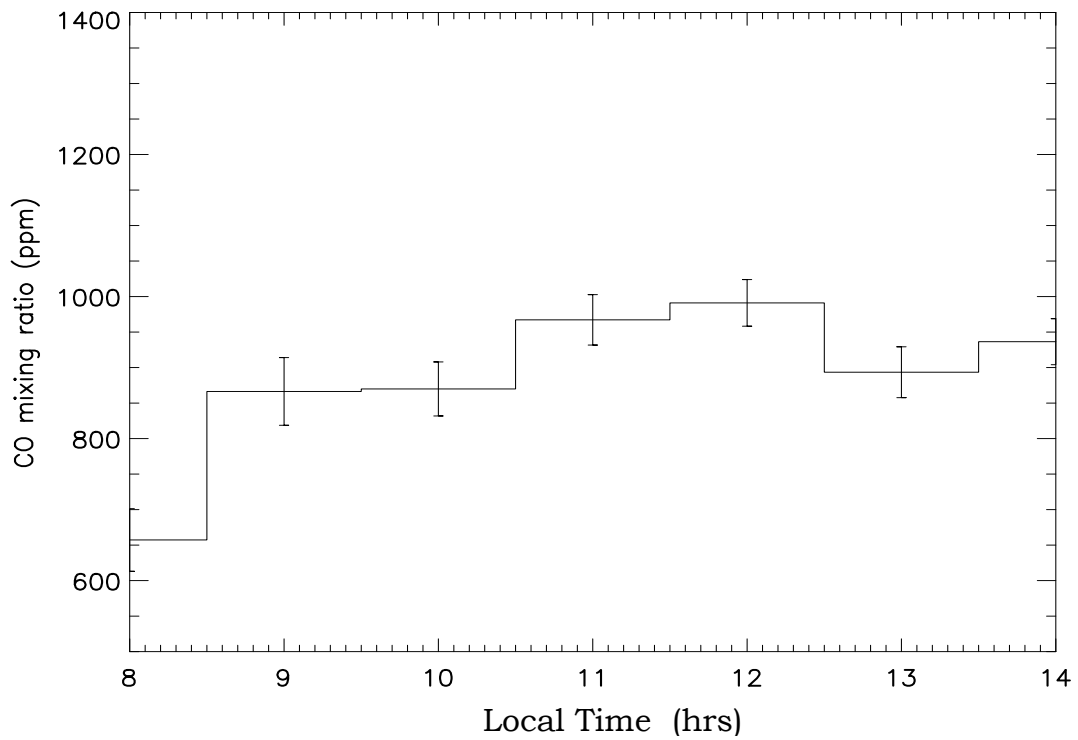


**Figure 69.** CO mixing ratio variation with the Local Time, averaged in bins of 1 hour. Data for Ls range: 90° - 200°.

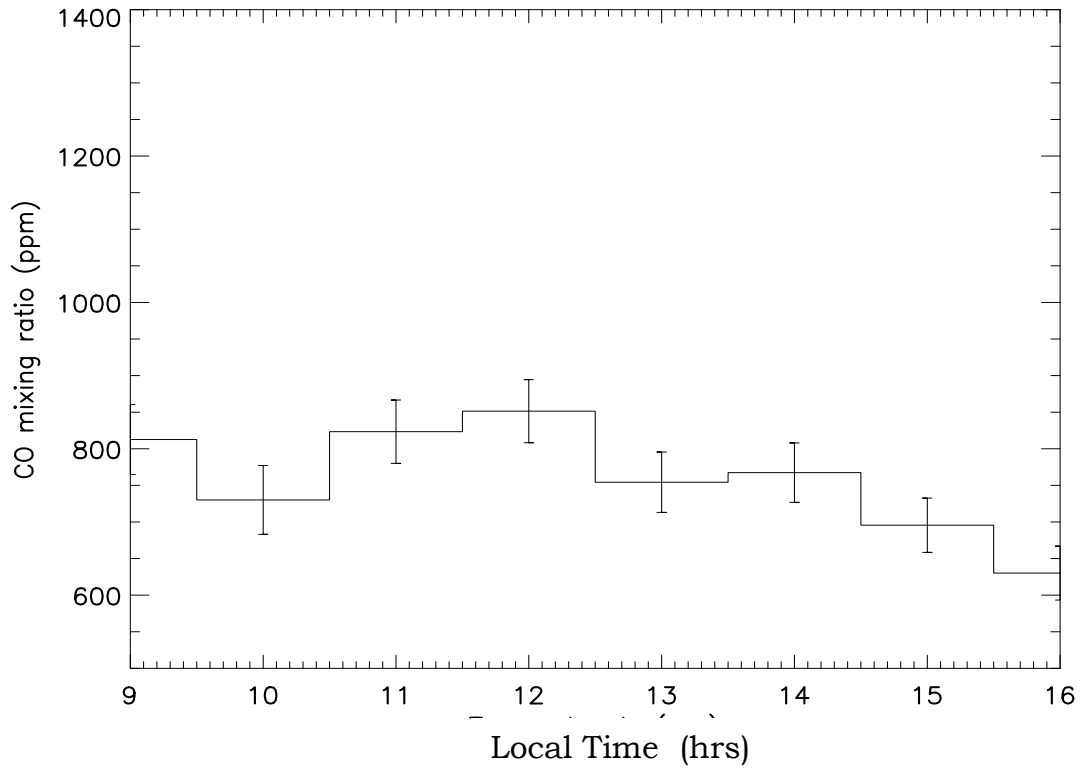


**Figure 70.** CO mixing ratio variation with the Local Time, averaged in bins of 1 hour. Data for Ls range:  $330^\circ - 95^\circ$ .

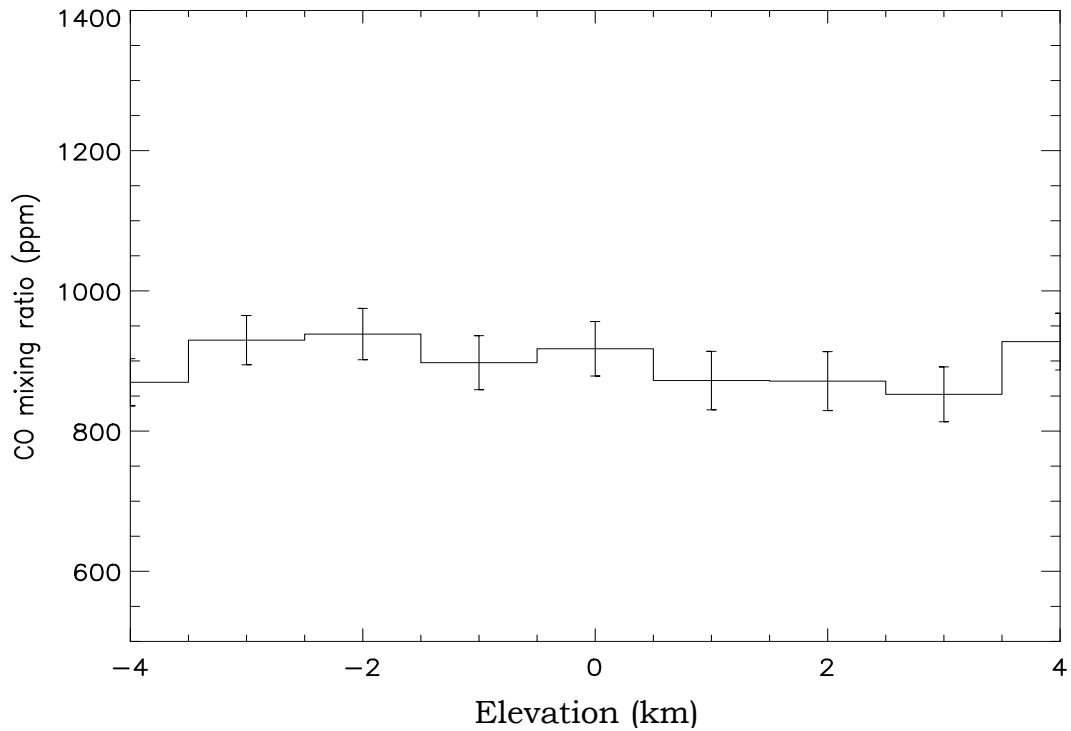


**Figure 71.** CO mixing ratio variation with the Elevation averaged in bins of 1 Km. Data for Ls range:  $90^\circ - 200^\circ$ .

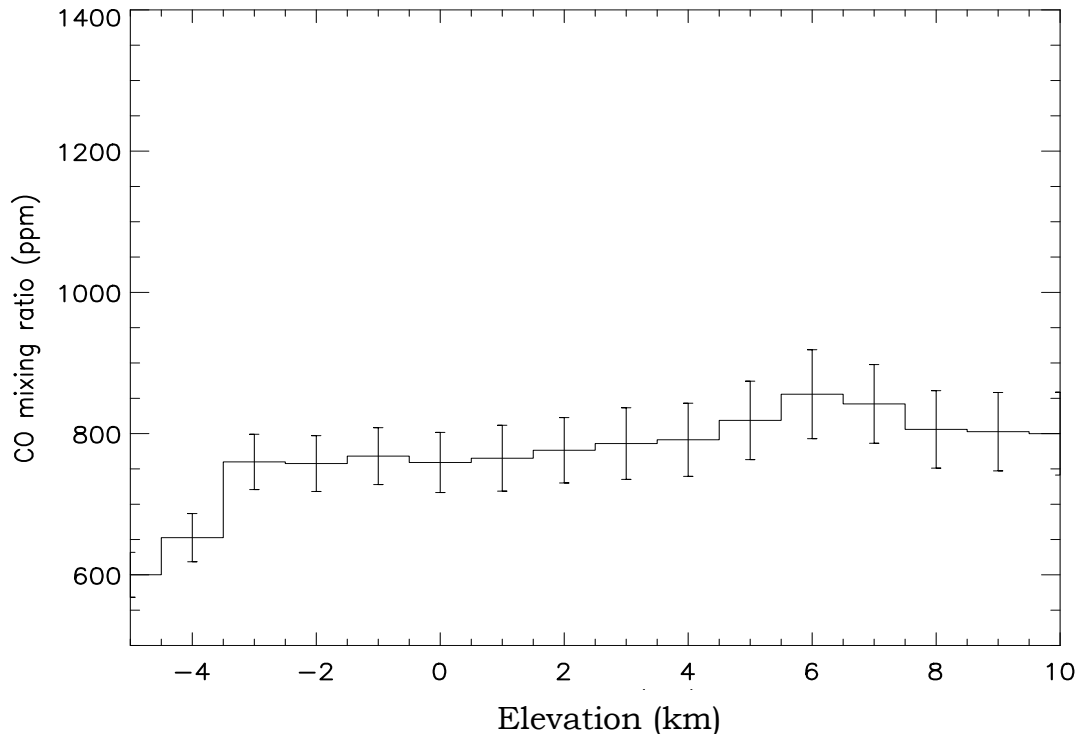


**Figure 72.** CO mixing ratio variation with the Elevation averaged in bins of 1 Km. Data for Ls range: 330° - 95°.

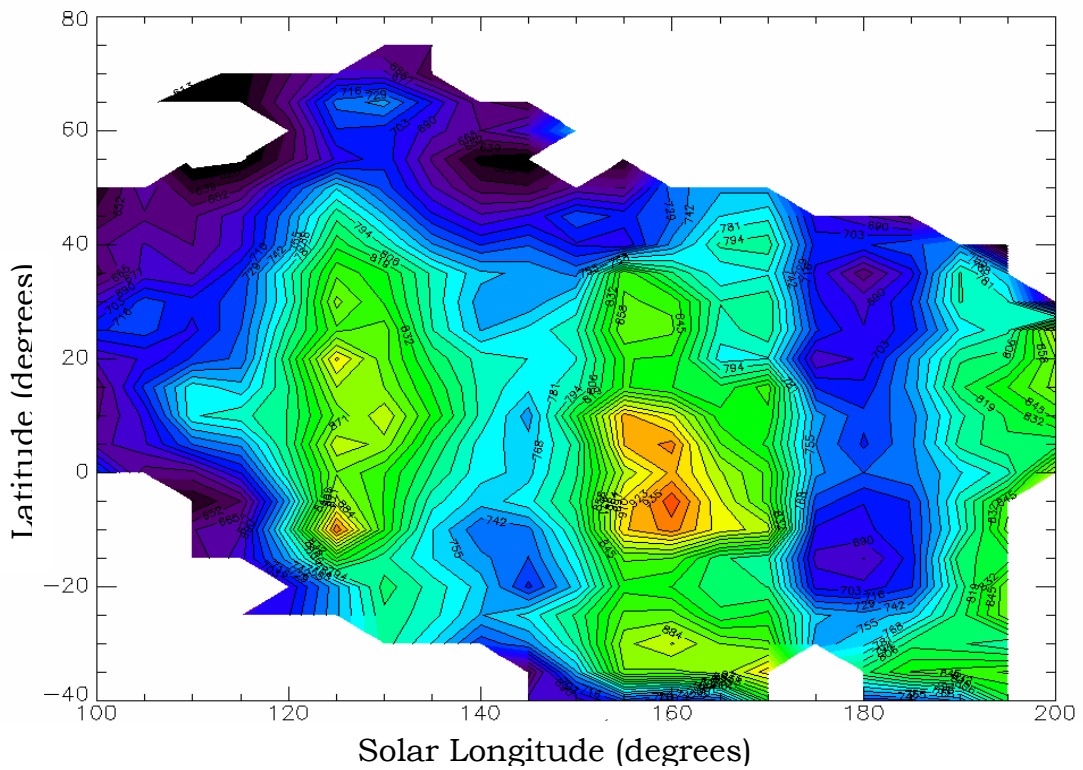


**Figure 73.** CO mixing ratio combined variation with Season (Ls) and Latitude.

### 6.1.5 Discussion

From this analysis appears a variability of the CO content at different atmospheric conditions, however not so strong in percentage (25 % for the first observed dataset, 35% for the second) as resulted from other studies (Billebaud et al.- 1998, attributed to the range of CO variability values from 0 to 100%); results show a variable mixing ratio with an average value of about 800 ppm in the latitude range approximately between - 60 and + 60 degrees and in a solar longitude range which encompass the summer and the beginning of autumn in the north hemisphere, therefore winter in the southern one (Ls range: 90° - 200°). Higher average values of about 900 ppm are found in the second dataset which comprises observations at the end of winter and beginning of spring in the northern hemisphere (Ls range: 330° - 95°).

Since the two datasets differ in the atmospheric model (see description in paragraphs 6.1.1) absolute values of CO atmospheric content may depend on the model. For this reason we report both results, which anyway are comparable within the computed errors, stressing more the observed variability and trends.

We have found an independence of the mixing ratio from planet altimetry (Figure 71 and Figure 72) and this is in agreement with a uniform mixing ratio along the atmospheric column. In fact the eddy diffusion coefficient is  $K \approx 10^6 \text{ cm}^2 \text{ s}^{-1}$  in Mars' troposphere [Korablev et al., 1993], and the vertical mixing time  $H^2/K$  is two weeks (H is the scale height.) Being this mixing time much shorter than CO lifetime, carbon monoxide should be vertically well mixed.

Our results confirm totally this observation. We stress also that we did not yet study observations in proximity of great volcanoes, where mixing ratio could eventually vary in case of founding outgassing processes.

From Figure 69 and Figure 70 we can observe an absence of strong diurnal CO variability.

Actually, the global mean photolysis rate of CO<sub>2</sub> is  $9.2 \times 10^{11} \text{ cm}^{-2} \text{ s}^{-1}$  [Krasnopolsky, 1995]. The CO column abundance is  $1.7 \times 10^{20} \text{ cm}^{-2}$  for the pressure of 6 mbar and the CO mixing ratio of  $8 \times 10^{-4}$ .

A ratio of the column abundance to the production rate is the CO lifetime, which is equal to 6 years. Therefore the diurnal variations should be very low, and this agrees with the observational data. The observed low variations with local time suggest a weak enhance on midday, where the Sun is high and the photolysis rate is more efficient.

There is an evident correlation with the Sun incidence angle (Figure 67 and Figure 68). From both analyzed dataset we can observe a decrease of CO mixing ratio increasing the incidence angle.

This trend may be correlated with the energy present in the atmosphere depending on solar illumination, which could enhance CO production when the incident solar beams density is higher (small angles).

Mars Express satellite orbits are rather elliptical ( $e=0.6$ ), with a period of 7.6 h (three times per day) and are not Sun synchronous, therefore bringing to a not unimportant bias for observations in Ls (season), Latitude and Local Time. This bias can affect the dataset, and consequently the interpretation of the variability, which anyway is clearly observed in the results.

The main observed correlation is with latitudes closer to the subsolar point in a given season. Due to the mentioned bias we can mainly attribute the CO variations with incidence angle to the latitudinal dependence on the subsolar point. In the plots where mixing ratio versus Latitude is showed (Figure 63 and Figure 64) a variable trend is observed, which presents a maximum around latitudes in which the Sun rays meet the surface with the minimum angle in the considered season. We can observe a maximum at low latitudes in the southern hemisphere winter, which could be correlated with CO<sub>2</sub> decreasing due to intense condensation of CO<sub>2</sub> on the south polar cap.

In this case, the actual CO column density does not vary, but what changes is the mixing ratio which is related to the total atmosphere (almost totally made of CO<sub>2</sub> in Martian case). In fact condensation and

sublimation of CO<sub>2</sub> result in enhancement and depletion, respectively, in the mixing ratios of incondensable species like CO.

Indeed, Figure 65 shows a variation of the CO mixing ratio in function of Solar Longitude (Ls), and Figure 73 shows that these seasonal features are more pronounced at equatorial latitudes. Moreover, the meridian profiles of the mixing ratio (for individual orbits) show a seasonal shift of the maximum versus the sub solar point. However, the orbital constraints of the observations do not yet allow a significant seasonal coverage (in solar longitude).

## **6.2 CO<sub>2</sub> isotopes retrieval in Martian atmosphere**

The stable isotope record contained within carbon and oxygen on Mars may provide important constraints regarding the origin of the planet and its relationship to that of other bodies in the Solar System, especially the Earth. Stable oxygen isotopes are particularly useful in the study of Mars because oxygen is abundantly present in both the Martian atmosphere and lithosphere. In particular it is present in CO<sub>2</sub>, the main atmospheric constituent (95%).

Despite their important roles, the precise O and C isotope compositions of Mars' atmosphere remain poorly known and both measurement and interpretation are difficult. Ground based and spacecraft studies of CO<sub>2</sub> established for <sup>12</sup>C/<sup>13</sup>C and <sup>18</sup>O/<sup>16</sup>O values similar to that of the Earth (the "terrestrial" value) within various uncertainties (Kaplan et al., 1969; Young, 1971; Maguire, 1977; Schrey, 1985; confirmed by Viking measurements reported in Nier and McElroy, 1977). The values reported for the Viking mass spectrometers are for high altitudes (120-180 km), and may not pertain to the bulk atmosphere. Maguire's results have been obtained for carbon isotope while on oxygen are based on the goodness of general fits. Earth-based estimates of <sup>18</sup>O/<sup>16</sup>O show a lighter value (Eiler

et al., 2000). Other values found from ground-based observations include those of Bjoraker et al. (1989) on oxygen in water, and Krasnopolsky (1996).

Most of the previous results are based on the study of the thermal radiation emerging from the planetary atmosphere. It should be noted, however, that the interpretation or fitting of these data with a synthetic spectrum depends essentially on the vertical temperature vs. pressure profile. We obtained this profile by inversion of the  $667\text{ cm}^{-1}$   $\text{CO}_2$  band. However it is well known that the temperature profile retrieved may not be unique; therefore the results on the isotopic composition usually quoted may be affected by these problems, unless they are verified with data out of thermal radiation regime. This possibility become available for the first time with the PFS measurements, and this is the main justification of the present study in which we performed the analysis of the oxygen and carbon isotopes in  $\text{CO}_2$  in the Martian atmosphere from the data returned by the PFS- LWC (where the contribute of thermal infrared emission from surface and atmospheric layer becomes of primary importance in the computation of models, therefore a correct temperature - pressure profile is needed), with a simultaneous check of results (when possible) with data acquired from the SWC.

### **6.2.1 Data**

The radiation provided from the long-wavelength channel covers the thermal infrared region between  $250$  and  $1700\text{ cm}^{-1}$ , dominated by the thermal emission of the planet and therefore produces a measured spectrum in the LWC with a rough Planckian shape, corresponding to surface temperature; deviation from this ideal shape is given by non-unit emissivity of the surface, by the action of aerosols and by the absorption and emission of the gases present in the atmosphere. In the SWC

measures the incoming Solar radiation, between 1700 and 8200  $\text{cm}^{-1}$ , reflected by the surface and aerosols, with a thermal part dominating below 2500  $\text{cm}^{-1}$ ; therefore the measured general level of signal depends on the surface reflectance and the spectrum presents several bands and lines of the main gases, including solar spectrum.

In the PFS spectral range, several  $\text{CO}_2$  isotopic bands are present. In this work we have studied the main  $\text{CO}_2$  absorption band centered at 667  $\text{cm}^{-1}$  (LWC). Here, we can observe many Q-branches, i.e. set of spectral lines so close each other that they appear as single lines in a spectrum measured at the PFS resolution (1.3  $\text{cm}^{-1}$ ).

In the SWC there are many isotopic bands, but several of them lie inside the 4.3 microns absorption band of the main isotope. The most prominent of the three isotopic bands out of the 4.3 microns band range, which will be considered in this work, is centred at 2614  $\text{cm}^{-1}$ .

## 6.2.2 Retrieval method and Atmospheric model

For the *identification* of  $\text{CO}_2$  isotopes, an *average* of 2041 spectra has been used to reduce noise. This subset was selected by requiring a high surface temperature (around 280 K) to increase the signal, and consists of spectra acquired near local noon and near the subsolar latitude; the average solar longitude was  $L_s = 340^\circ$  with a heliocentric distance of 1.50 AU, the representative solar zenith angle for the average spectrum around  $31.5^\circ$ , while the emission angle was  $13.9^\circ$ .

To *identify* the  $\text{CO}_2$  isotopes and *derive their abundances*, we compare observed spectra with computed models, adopting the representative average parameters described above.

Computation of synthetic spectra was performed using a line-by-line radiative transfer code (see section 4) to compute gaseous opacity and obtaining a quasi-monochromatic spectrum which includes both the

thermal component and the *solar reflected spectrum* (Fiorenza & Formisano, 2005). Lines parameters have been taken from molecular database HITRAN 2004 ([www.hitran.com](http://www.hitran.com)). The atmosphere is modeled as a stack of 67 plane-parallel levels. The adopted temperature-pressure profile, as stressed above, was retrieved from the observed average spectrum by means of an inversion method applied to the main CO<sub>2</sub> absorption band, centred at 667 cm<sup>-1</sup> (Grassi).

### **6.2.2.1 Methodological problems**

We list here some problems that may affect our study:

- There may be some ambiguities caused by the use of average spectra. Non-homogeneous conditions, associated with different positions and times of the observed spectra, may give physically inconsistent results if an average spectrum is used to retrieve the atmospheric profile.
- The radiative transfer solution is in principle not unique in the band under consideration (centered at 667 cm<sup>-1</sup>) as previously stated, when we attempt to retrieve thermal profile and isotopic abundances at the same time. However, once appropriate initial conditions are selected, this problem may become of second order.
- Nominal PFS instrumental function has been used to convolve synthetic spectra. Residual discrepancies from this ideal function in the LWC cannot be ruled out and may provide some misfit in the lines.
- Difficulties related to scattering in SWC (thermal and solar region) may induce problematic definitions of the continuum.

### 6.2.3 Results on isotopic abundances

In this section we present the best fits obtained in each channel separately.

#### 6.2.3.1 Long wavelength Channel

PFS resolution is sufficient to resolve the Q-branches separately in the main absorption CO<sub>2</sub> band at 667 cm<sup>-1</sup>. All the eight CO<sub>2</sub> isotopes have been identified in the averaged spectrum, by comparison with the synthetic spectra and lines positions derived from spectral database.

In Figure 74 we present the averaged observed spectrum with the identification of CO<sub>2</sub> isotopes, adopting the common short form to indicate isotopes, e.g. 626 for <sup>16</sup>O<sup>12</sup>C<sup>16</sup>O, while in Table 7 we report the identified isotopes and corresponding detection position.

Within this absorption band all isotopes may give some contributes at different wavenumbers and it happens that more than one isotope contributes to the same observed line (we can clearly take this information from synthetic spectra computed with one isotope per time and from line positions). Wavelengths in which contribute of more than one isotope is present are indicated in the figure.

Figure 75 shows the best global fit achieved for the main CO<sub>2</sub> band, taking into account average observational conditions, input T(p) profile and reference isotopic ratio values (from here after called “terrestrial values” and which can be found in HITRAN database description, *Rothman et al., 2001*).



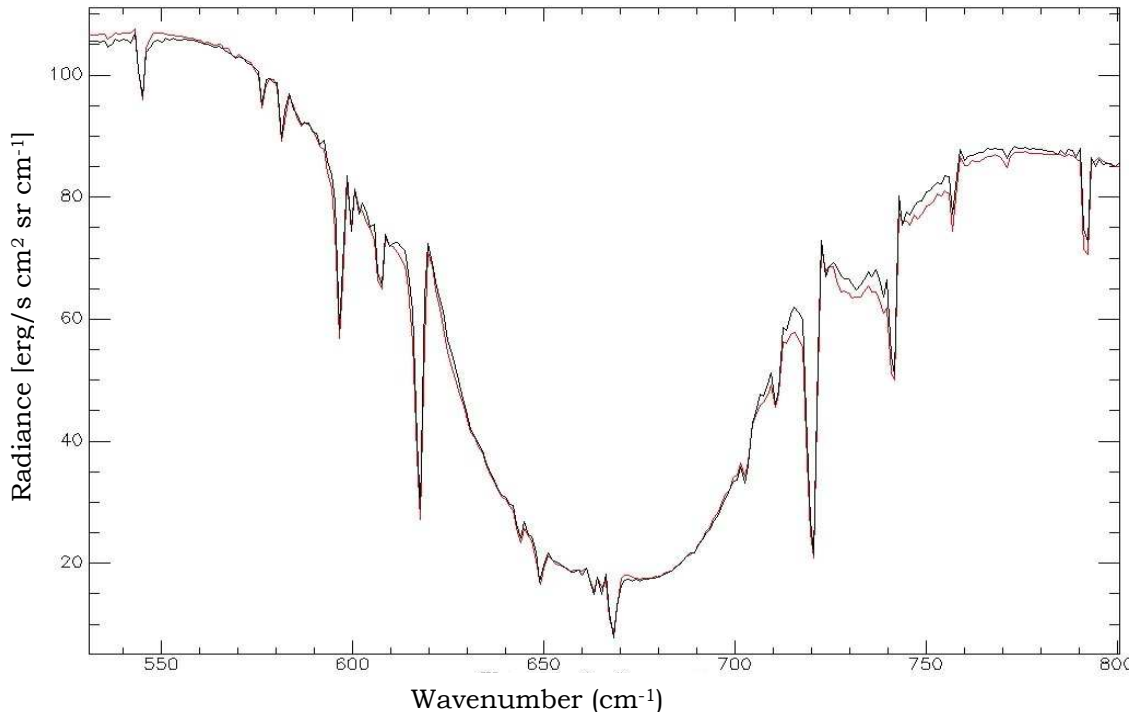


**Figure 75. Global fit of the main CO<sub>2</sub> band: in black average spectrum measured, in red synthetic.**

Some systematic misfits are evident. Namely, the band level outside the main Q-branches appears depressed in the entire 700-780 cm<sup>-1</sup> range. The wide extension of the structure suggests an origin likely related to: either the adopted temperature profile (possibly inconsistent, being retrieved from an average spectrum) or inappropriate aerosols models, or finally an effect due to the wrong isotopic composition assumed to start with. This fact point out that the study of isotopic ratio shall rely more on the Q-branch depth with respect to the surrounding general CO<sub>2</sub> band level than on their absolute magnitudes.

Study of the three CO<sub>2</sub> main isotopes has been done by comparison of the averaged spectrum with synthetic spectra computed at several abundances around terrestrial values.

The carbon isotope 636 has been studied in two spectral ranges: 599 and 649 cm<sup>-1</sup> (Figure 76 and Figure 77). Both lines, even if probing two different altitudes in the atmosphere, suggest for this isotope abundance close to the terrestrial value.

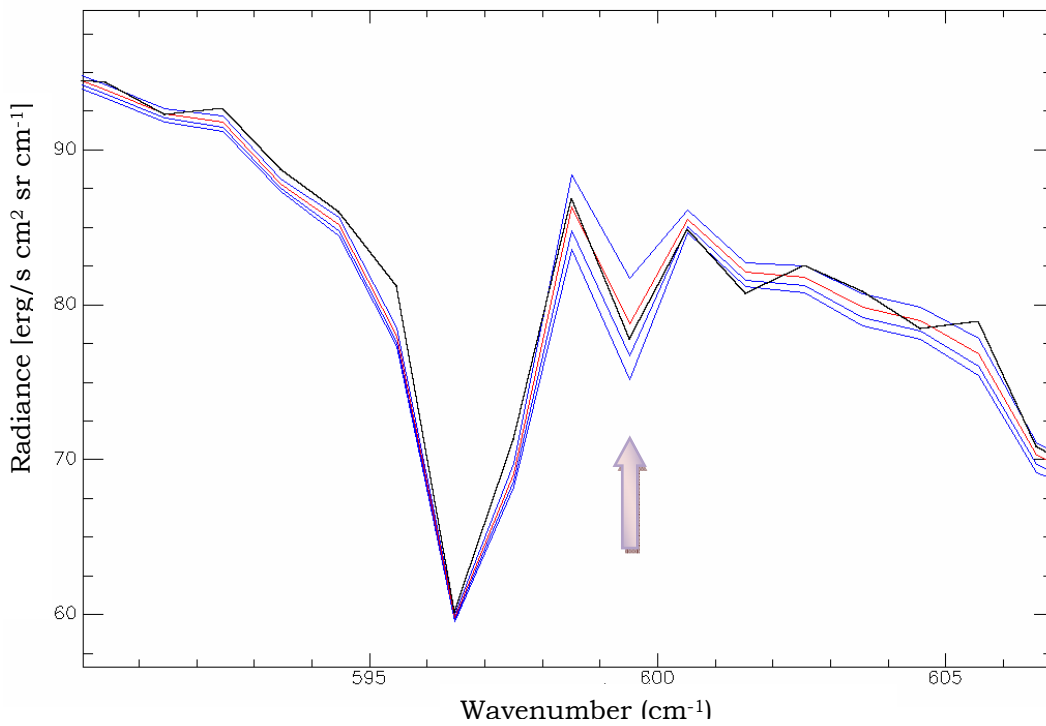


**Figure 76. Isotope 636 at 599  $\text{cm}^{-1}$ . In black is the average spectrum, in red the terrestrial value and the three blue synthetic spectra have respectively 0.5, 1.5, 2 times the terrestrial values.**

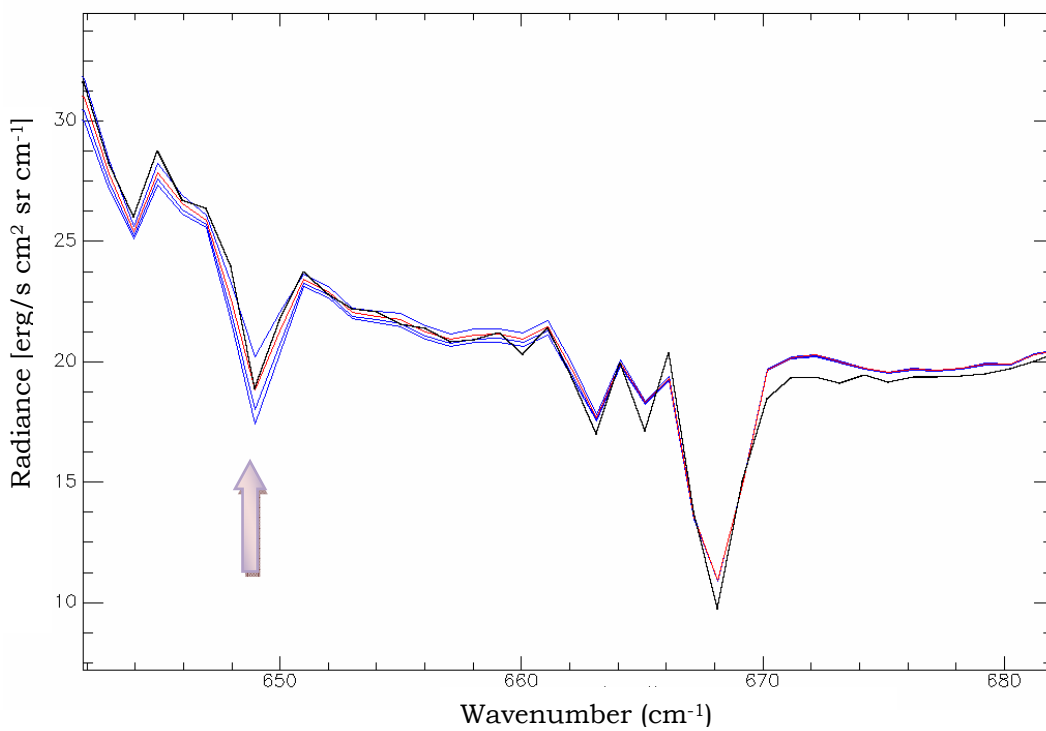


**Figure 77. Isotope 636 at 649  $\text{cm}^{-1}$ : blow up of the center of the band. In black average spectrum, in red and blue synthetic spectra with respectively 1, 0.5, 1.5, 2 terrestrial values.**

Oxygen isotope 628 has been detected at wavenumbers 663 and 576  $\text{cm}^{-1}$  (Figure 78 and Figure 79), while oxygen isotope 627 is observed at wavenumbers 665 and 607  $\text{cm}^{-1}$  (Figure 80 and Figure 81). In these two cases there are some differences in best-fit values retrieved at center of the band with respect of those derived from other wavenumbers. Namely, 628 and 627 fits with synthetic spectra at respectively 576 and 607  $\text{cm}^{-1}$ , provide for these isotopes approximately terrestrial values, while in the center of the band the values seems to be higher. Reasons for this behavior are still uncertain. Since the center of this  $\text{CO}_2$  absorption band probes higher atmosphere (around 35-50 Km), a possible interpretation can be a variation of isotopic abundance with altitude, possibly related to the escaping processes (escaping oxygen has been observed by Aspera experiment on board the Mars Express mission, Barabash et al., 2006). An alternative interpretation is that this region is affected by some residual misfit problems (particularly evident for 627 at 665  $\text{cm}^{-1}$ , but not for the 628 at 663  $\text{cm}^{-1}$ ).

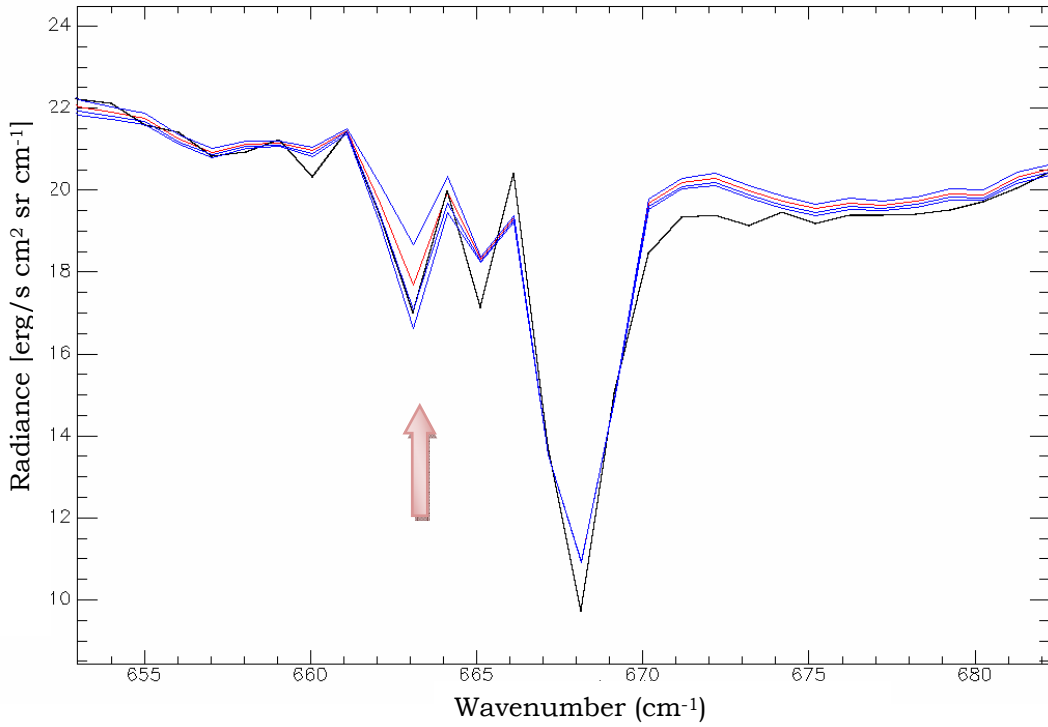


**Figure 78. Isotope 628 at 663 cm<sup>-1</sup>: blow up of the center of the band. In black average spectrum, in red and blue synthetic spectra with respectively 1, 0.5, 1.5, 2 terrestrial values.**

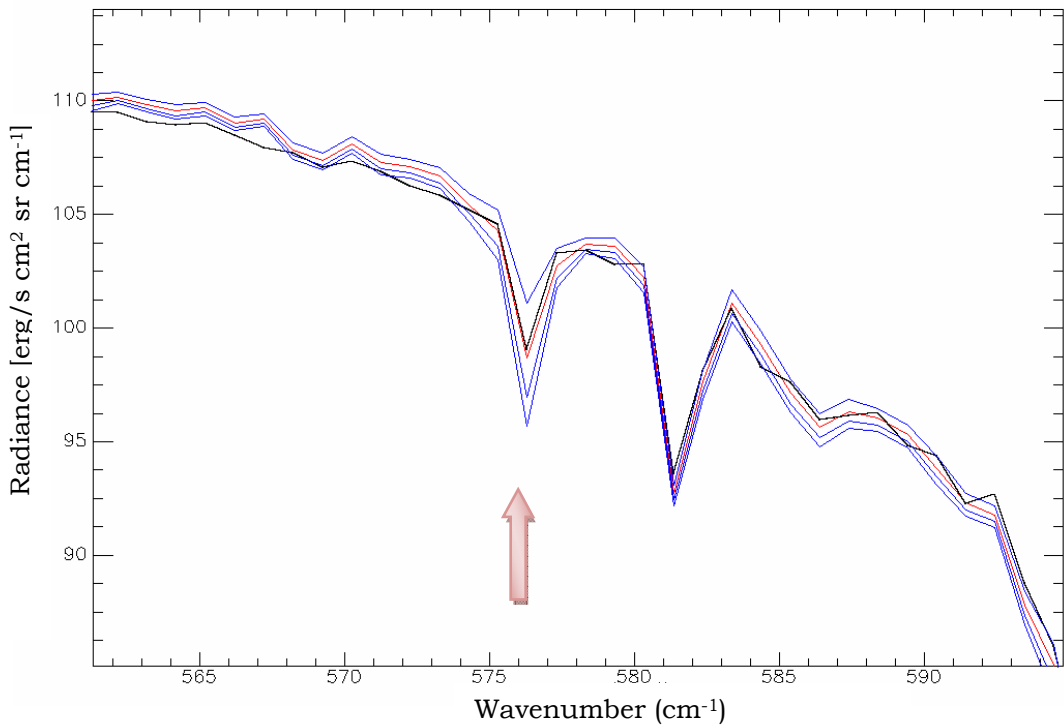


**Figure 79. Isotope 628 at 576 cm<sup>-1</sup>. In black average spectrum, in red and blue synthetic spectra with respectively 1, 0.5, 1.5, 2 terrestrial values.**

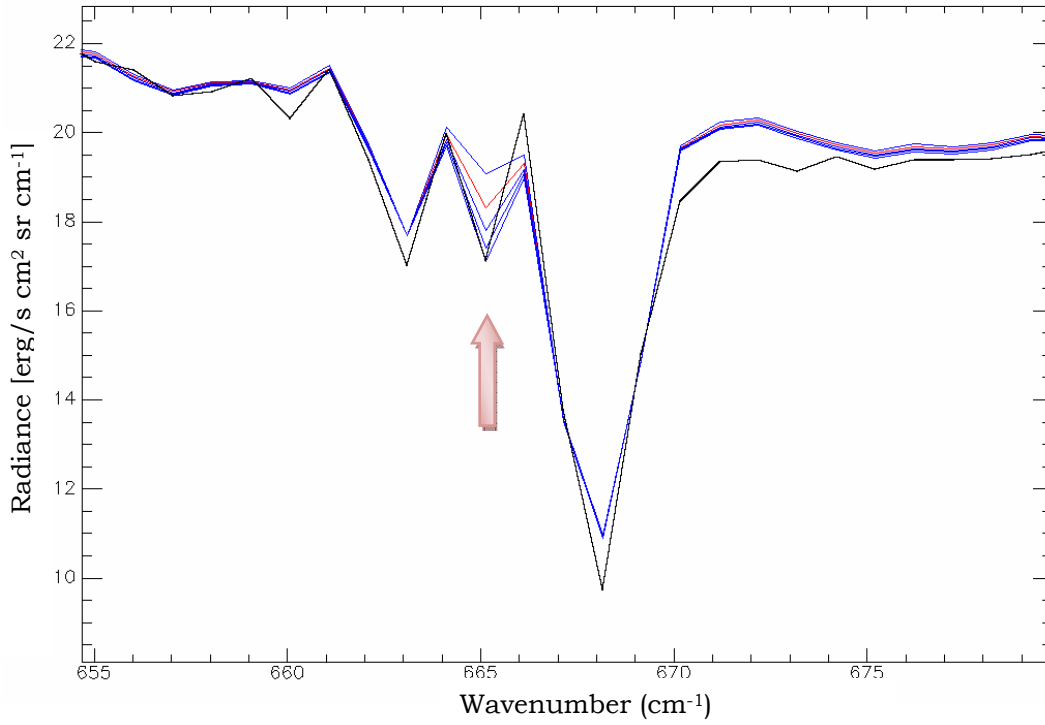


**Figure 80. Isotope 627 at 665 cm<sup>-1</sup>: blow up of the center of the band. In black average spectrum, in red and blue synthetic spectra with respectively 1, 0.5, 1.5, 2, 2.5 terrestrial values.**

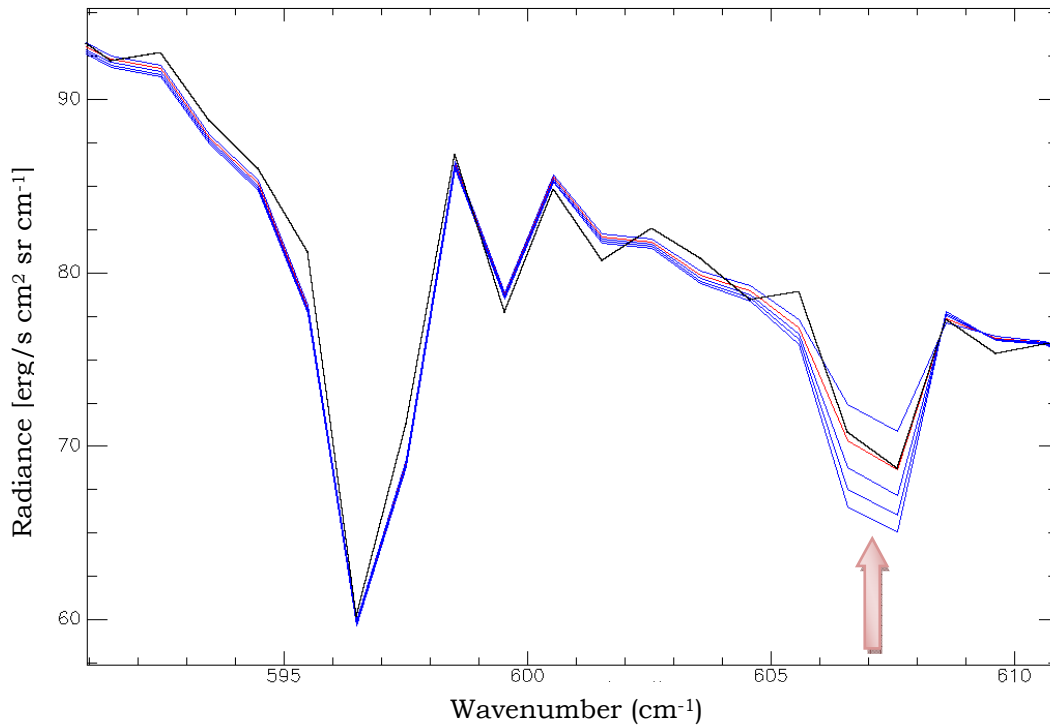


**Figure 81. Isotope 627 at 607 cm . in black average spectrum, in red and blue synthetic spectra with respectively 1, 0.5, 1.5, 2, 2.5 terrestrial values.**

Consequently, deeper investigation is required to better understand these differences.

For these purposes, we developed another analysis to reduce the problems associated with averaged spectra and improve at the same time the estimate of corresponding error.

We have considered some spectral channels where is possible to study the isotopic abundance of the three main isotopes. For each of these lines we have found the distribution of the relative depth of the considered Q-branch, defined as  $1 - [\text{radiance (center of the line)} / \text{radiance (continuum)}]$ , computed for each of the individual spectra adopted to build the average spectrum.

This quantity is more correlated just to the isotopic abundance and in general more suitable to discriminate the isotopic ratio in respect to variations of the other parameters described above.

In order to convert the observed relative depths to isotopes abundances, we have used a synthetic spectrum computed with isotopic terrestrial values.

Dividing the measured depths by the synthetic ones, we obtain isotopic abundances expressed in terrestrial units.

The use of this procedure is correct if a linear relationship between relative depths and abundances exists. In turn this is true for small differences of the absorption coefficients between the center of the line and the adjacent continuum and for small abundances, as it is verified in all the considered cases about CO<sub>2</sub> isotopes in this band.

Usage of standard deviation of the averaged spectrum to determine an error can be overestimated by the fact that the used set of data is not homogenous in surface and atmospheric conditions, observational geometry and incident solar flux; the derived  $\sigma$  will measure all these differences besides the variation in abundance of isotopic ratio. On the contrary, the adopted method allows estimating the variability of isotopic ratio only and obviously the NER of the instrument.

The distributions of the three main CO<sub>2</sub> isotopes' abundances at different wavelengths are shown in the following set of figures.

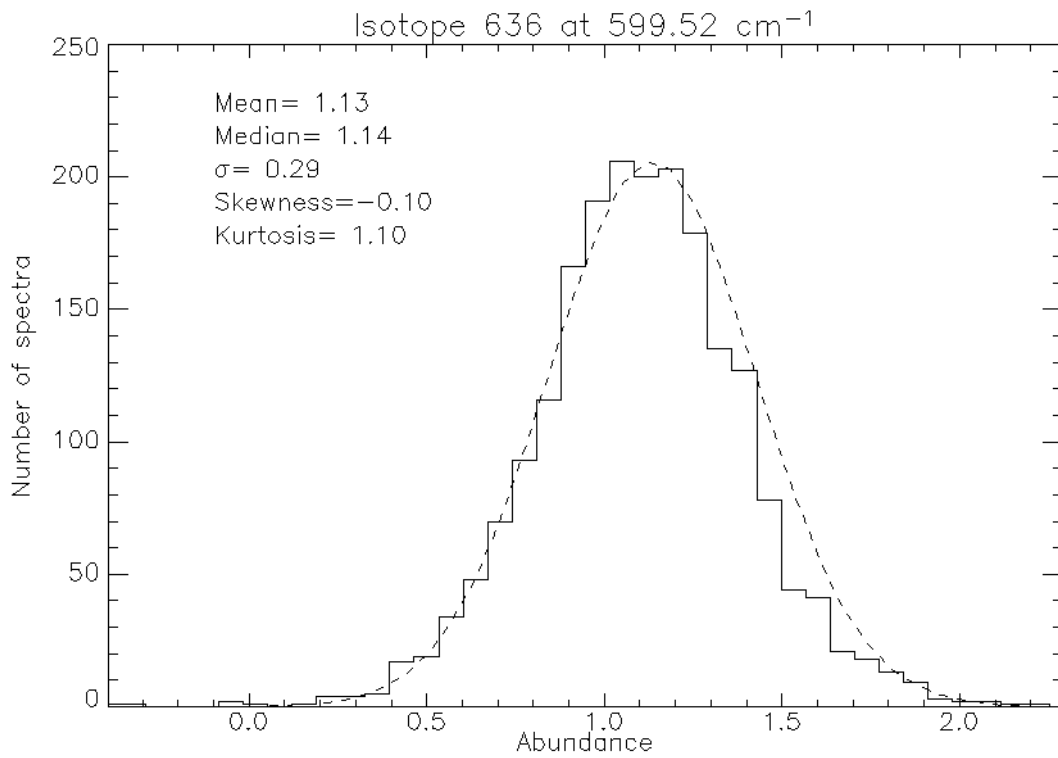


**Figure 82. Isotope 636 at 599 cm<sup>-1</sup>. Distribution and its moments of the abundance relative to terrestrial one of 2041 spectra. The mean value gives the retrieved result.**

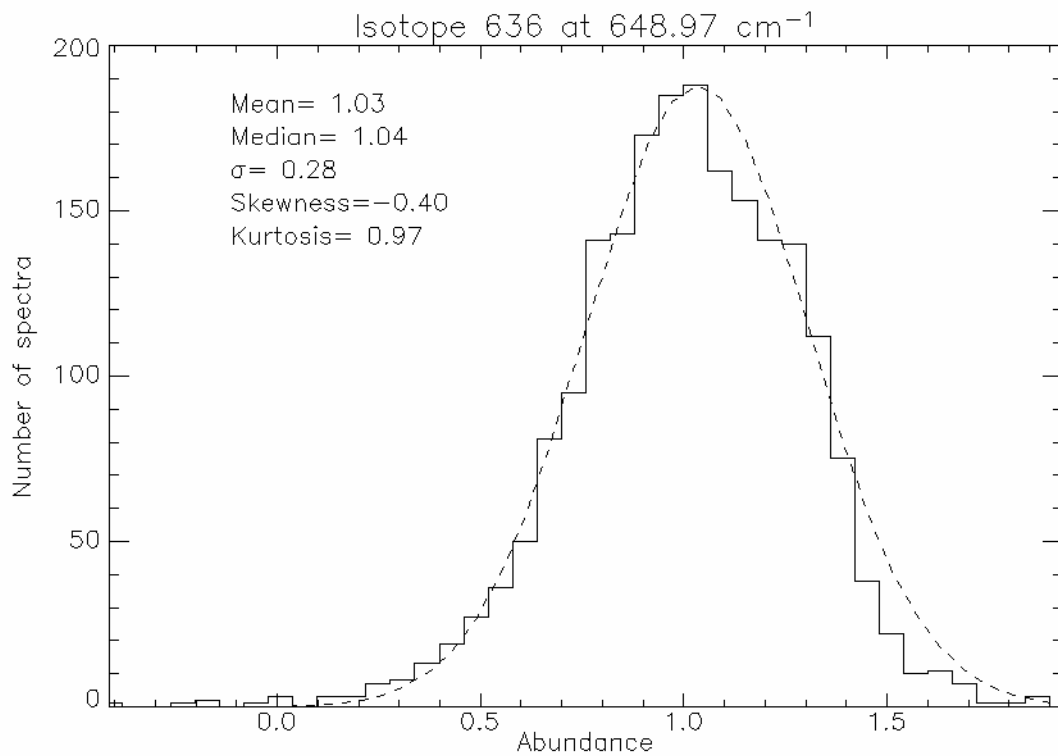


**Figure 83. Isotope 636 at 649 cm<sup>-1</sup>. Distribution and its moments of the abundance relative to terrestrial one of 2041 spectra. The mean value gives the retrieved result.**

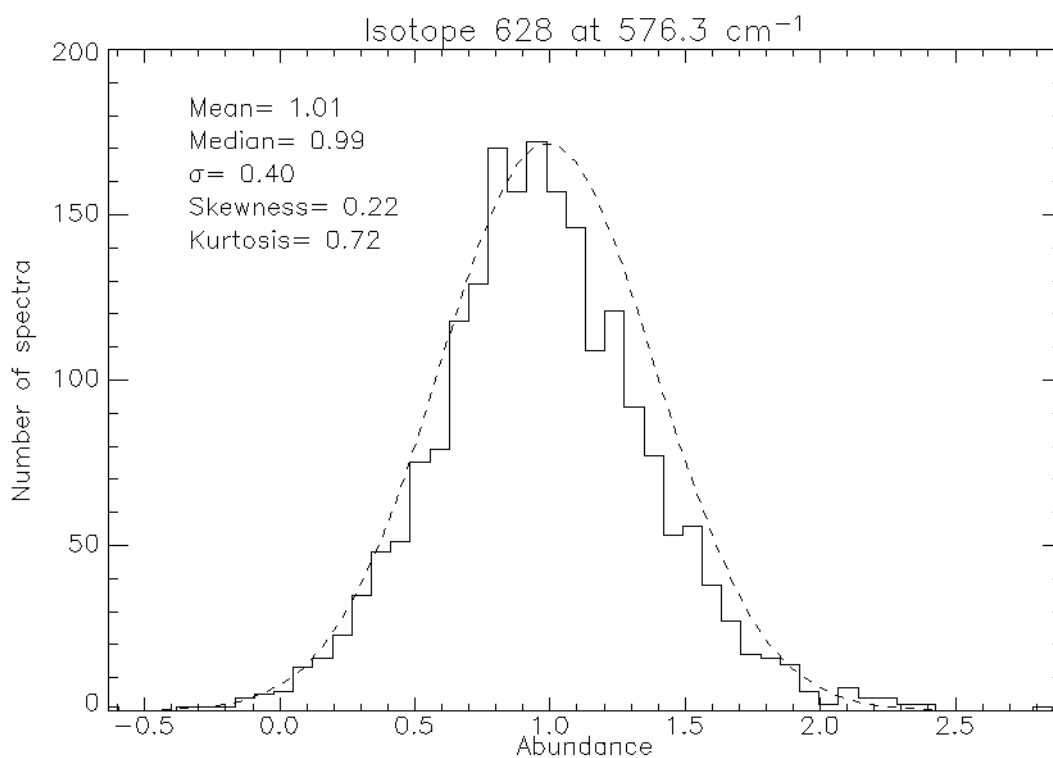


**Figure 84. Isotope 628 at 576 cm<sup>-1</sup>. Distribution and its moments of the abundance relative to terrestrial one of 2041 spectra. The mean value gives the retrieved result.**

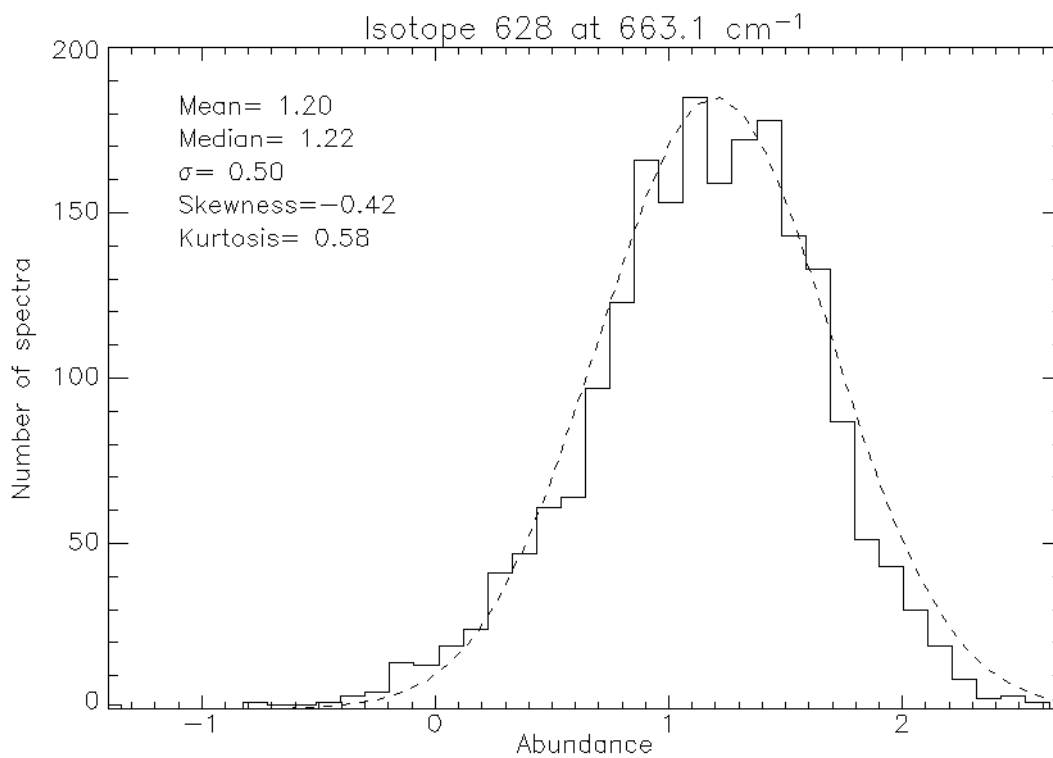


**Figure 85. Isotope 628 at 663 cm<sup>-1</sup>. Distribution and its moments of the abundance relative to terrestrial one of 2041 spectra. The mean value gives the retrieved result.**

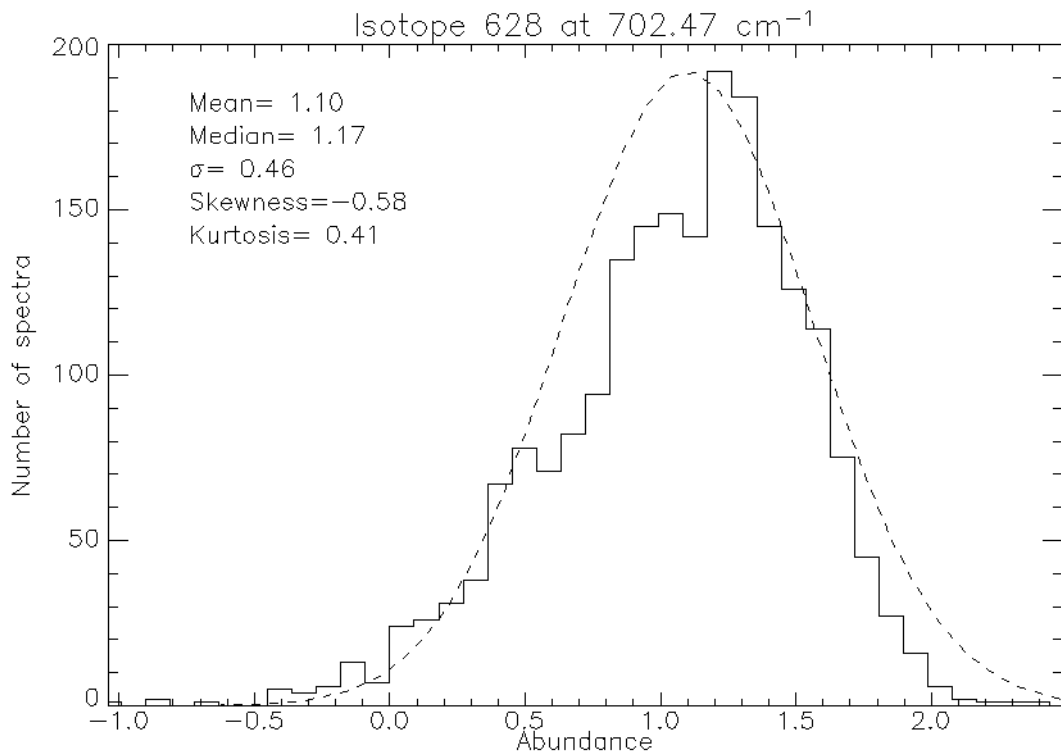


**Figure 86. Isotope 628 at 702 cm<sup>-1</sup>. Distribution and its moments of the abundance relative to terrestrial one of 2041 spectra. The mean value gives the retrieved result.**

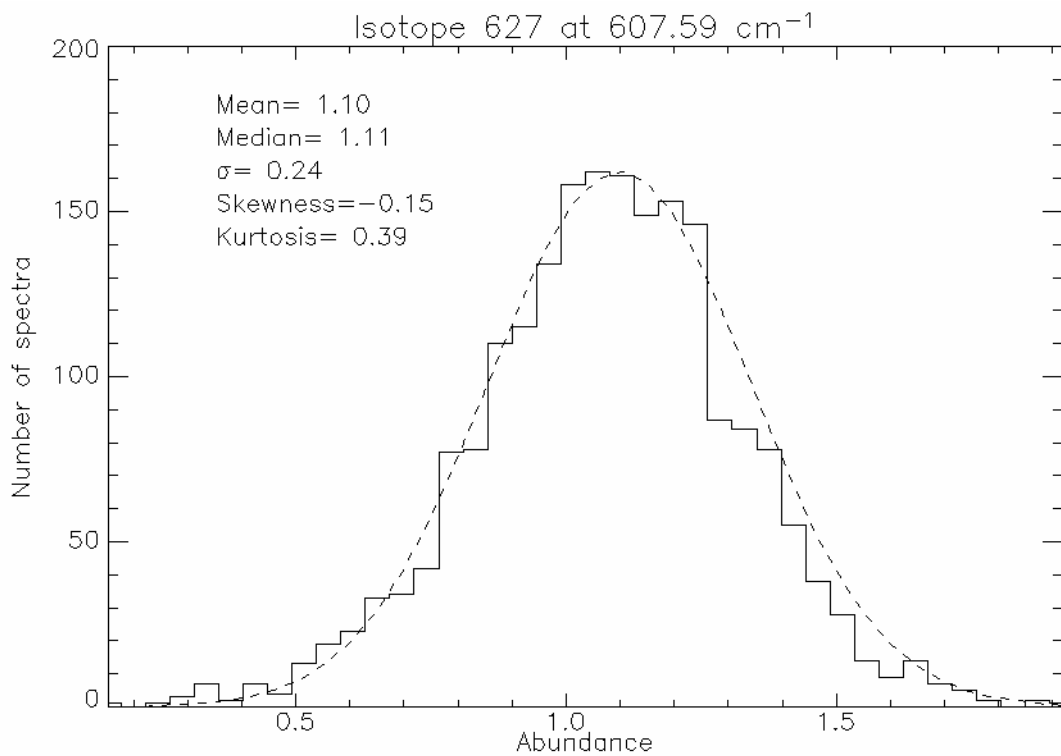


**Figure 87. Isotope 627 at 607 cm<sup>-1</sup>. Distribution and its moments of the abundance relative to terrestrial one of 2041 spectra. The mean value gives the retrieved result.**

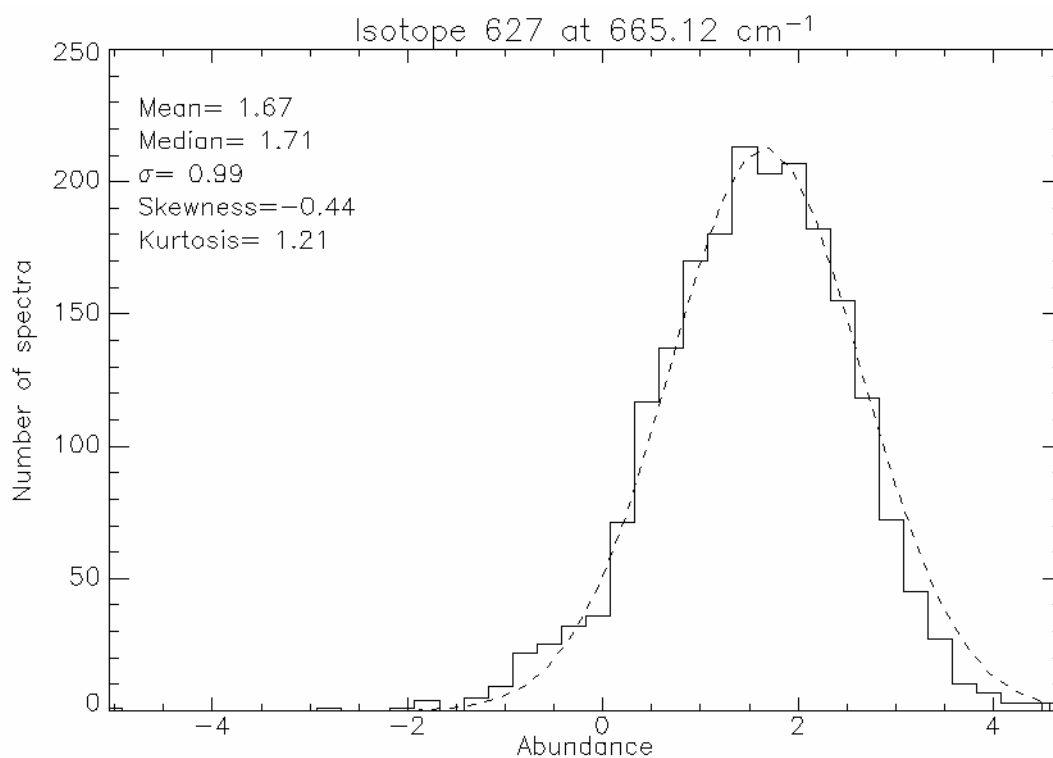


**Figure 88. Isotope 627 at 665 cm<sup>-1</sup>. Distribution and its moments of the abundance relative to terrestrial one of 2041 spectra. The mean value gives the retrieved result.**

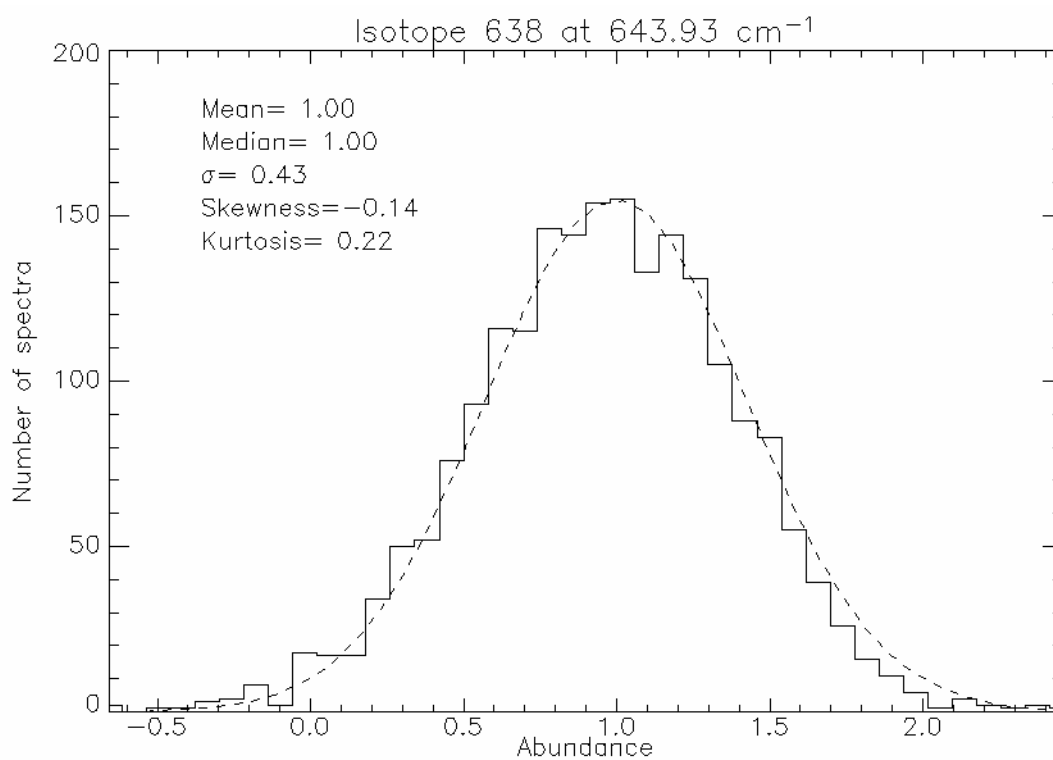


**Figure 89. Isotope 638 at 644 cm<sup>-1</sup>. Distribution and its moments of the abundance relative to terrestrial one of 2041 spectra. The mean value gives the retrieved result.**

The values of parameters and moments characteristic of the considered distributions are provided inside the figures. The mean value gives the isotopic abundance derived from the considered set of data with an error given by the standard deviation of the distribution. This  $\sigma$  is still overestimated, due to the diversities among the data, above discussed, but anyway much smaller than the unrealistic values provided by the usage of absolute depths. The Kurtosis is subtracted to the ideal gaussian one (which has value=3). The gaussian functions showed on the histograms are computed using the retrieved mean values and  $\sigma$  of the distributions. Noteworthy, Isotope 636 has been studied at the same wavenumbers of the previous semi-quantitative fits (Figure 82 and Figure 83), obtaining the same result. For 628 (Figure 84 and Figure 85) this procedure made possible to consider even the Q-branch at 702  $\text{cm}^{-1}$  (Figure 86). For isotope 627 (Figure 87 and Figure 88) only abundance from the line at 607  $\text{cm}^{-1}$  provided satisfactory results (Figure 87), because of the difficulties related to a reliable definition of the continuum in the center of the band at 665  $\text{cm}^{-1}$ , anyway in Figure 88 is shown the result obtained at this wavenumber; this provided an higher value in respect of terrestrial one but with a bigger error. Also isotope 638 has been analyzed with this procedure at its main absorption spectral range, e.g. 644  $\text{cm}^{-1}$ . This molecule is composed by the two main isotopes of carbon and oxygen and its study can contribute to a better comprehension of the results; the obtained abundance value is provided in Figure 89. The results of this study are summarized in Table 8.

| Isotope (wavenumber)        | Abundance $\pm \sigma$<br>(terrestrial units) |
|-----------------------------|---|
| 636 (649 cm <sup>-1</sup> ) | 1.03 $\pm$ 0.50                               |
| 636 (599 cm <sup>-1</sup> ) | 1.13 $\pm$ 0.29                               |
| 628 (576 cm <sup>-1</sup> ) | 1.01 $\pm$ 0.40                               |
| 628 (663 cm <sup>-1</sup> ) | 1.20 $\pm$ 0.50                               |
| 628 (702 cm <sup>-1</sup> ) | 1.10 $\pm$ 0.46                               |
| 627 (607 cm <sup>-1</sup> ) | 1.10 $\pm$ 0.50                               |
| 627 (665 cm <sup>-1</sup> ) | 1.67 $\pm$ 0.99                               |
| 638 (644 cm <sup>-1</sup> ) | 1.00 $\pm$ 0.43                               |

**Table 8. Results of the retrieved isotopic abundance at different wavenumbers with relative standard deviation.**

Accordance with 1.1 terrestrial value of the abundance was found for all the three main CO<sub>2</sub> isotopes, outside the center of the band in which higher values seems to be observed. Experimental errors do not allow ruling out, on the basis of PFS-LWC, isotopic ratios equal to terrestrial ones, but a possible trend of increasing abundance with higher altitudes in the Martian atmosphere appears suggested by the data but can not be confirmed without further information..

### **6.2.3.2 Short wavelength Channel**

In this channel some isotopic bands are present. Among these, the ones that fall outside the most abundant CO<sub>2</sub> isotope absorption bands are mainly due to oxygen isotope 628, in particular at 2500, 2614 and 2760 cm<sup>-1</sup>; absorption of 627 gives also a contribute in the first two regions covered by 628 bands. Here we focus our attention to the major of the three bands, which is centered at 2614 cm<sup>-1</sup>.

An average of the same observations described in the LWC section, has been adopted. Fitting this band is usually problematic due to differences

between the continuum of observed and synthetic spectra in this spectral range.

Consequently, the fit of the measured averaged spectrum in SWC with synthetic spectra (Figure 90) was obtained by an iterative procedure (similar to the one adopted to retrieve CO abundance, see paragraph 6.1.1) to model simultaneously both the surface albedo and the isotopic abundance of 628. Content of 627 isotope (which contributes at the absorption in the right side of the band) was arbitrarily fixed to the terrestrial value.

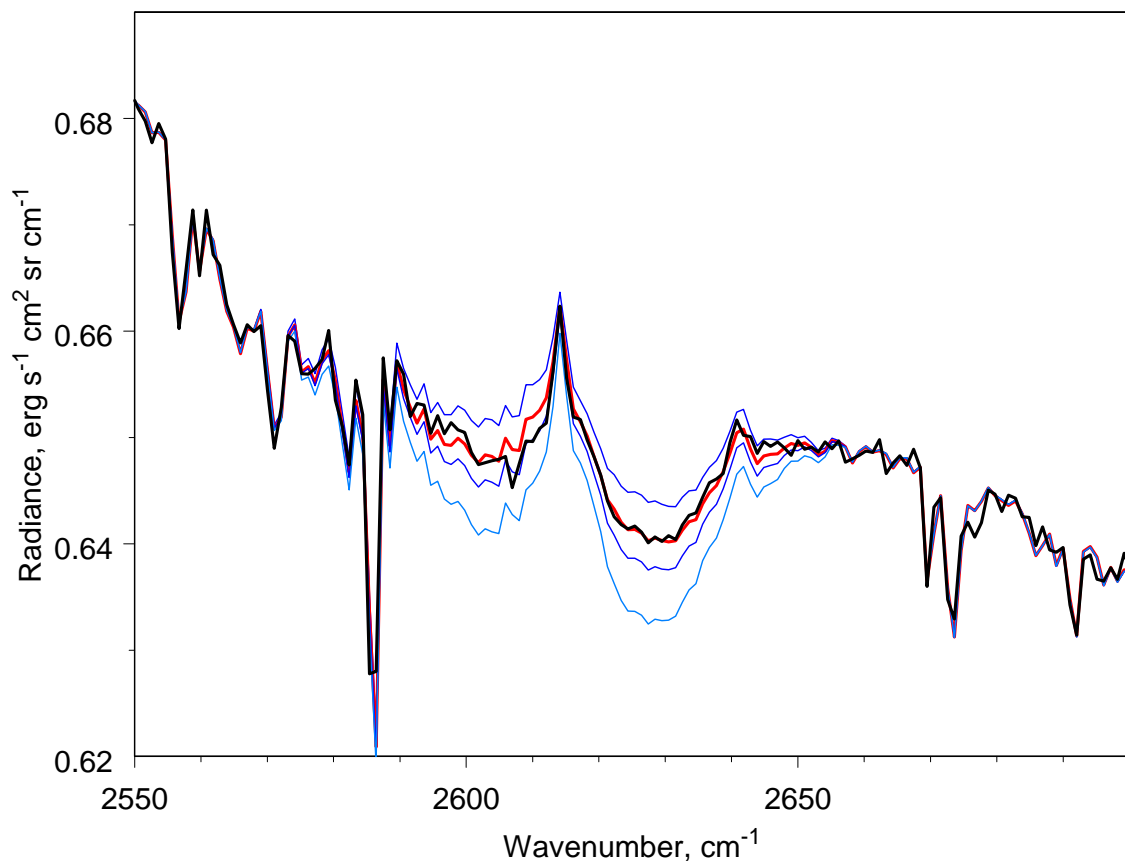


**Figure 90.** CO<sub>2</sub> 628 isotopic band centred at 2614 cm<sup>-1</sup>: in black colour — average spectrum, in red colour — synthetic spectrum for the best fit value of 0.80 ± 0.2 of the terrestrial abundance; for reference blue curves show synthetic spectra for CO<sub>2</sub> 628 abundances of 0.5, 1, and 1.5 terrestrial values.

The adopted least squares procedures computed directly the error on the basis of NER on the average spectrum. The result indicates an isotopic abundance of 0.8 times the terrestrial value.

This value is smaller than the one obtained with the study in LWC but the two results, within the errors, are still coherent.

#### 6.2.4 Discussion

The retrieved abundances of the main isotopes outside the center of the main CO<sub>2</sub> absorption band at 667 cm<sup>-1</sup> (LWC) resulted to be close to terrestrial values and are reported in Table 9, expressed in isotopic ratios and in Table 2 in terrestrial value units.

|   |
|---|
| Isotopic ratio                            |
| <sup>12</sup> C/ <sup>13</sup> C = 82.4   |
| <sup>16</sup> O/ <sup>18</sup> O = 479.5  |
| <sup>16</sup> O/ <sup>17</sup> O = 2437.9 |

**Table 9. : Isotopic ratios.**

In these observations there are some differences between the observed abundance of 628 isotope (the most important CO<sub>2</sub> isotopomer - together with the 627- which gives indication of the CO<sub>2</sub> oxygen isotope's content) at different wavelengths: at 576 cm<sup>-1</sup> is similar to the terrestrial value, while in the bottom of the band (663 cm<sup>-1</sup>) it is found to be a little higher. From the last spectral range even the 627 isotope seems to have much higher abundance than terrestrial value.

The retrieved abundance of 628 in the SWC (the band at 2614 cm<sup>-1</sup>) is about 0.8 times the terrestrial value. In general, the quantity retrieved

from this spectral range pertains to the atmospheric mass of the first scale height of the atmosphere.

For this reason, a realistic interpretation of the results of this study can be a variability of mixing ratio of the oxygen isotopes with the altitude. We pass from a lower value obtained in the first layers of the atmosphere (from SWC), less than terrestrial value, to values similar to the terrestrial one from the ranges of the band in LWC pertaining an altitude around 20-30 Km, to higher values in the center of the band which probes an altitude around 30-50 Km. This decreasing trend with altitude could be explained by the escape of lighter isotopes from the top of the atmosphere, with enrichment of the heavier ones going closer to the surface. Anyway some further considerations should be developed.

The column CO<sub>2</sub> abundance in the Martian atmosphere is  $2 \times 10^{23} \text{ cm}^{-2}$ , the column photolysis rate is  $10^{12} \text{ cm}^{-2} \text{ s}^{-1}$ . Their ratio is the mean CO<sub>2</sub> lifetime relative to chemical processes which is 6000 years. Local lifetimes may be shorter or longer; for example, the CO<sub>2</sub> lifetime is 30 years at 80 km. Mixing time is  $H^2/K$  where H is the scale height and K is eddy diffusion. Mixing time varies from two weeks in the lower atmosphere to 15 hours at 80 km. Mixing time is very much shorter than the chemical lifetime of CO<sub>2</sub>; therefore all CO<sub>2</sub> isotopes should be well mixed in the atmosphere and the CO<sub>2</sub> isotope ratios do not depend on height up to a homopause at 120-135 km where the diffusive separation begins.

The 628 abundances obtained in this study from various bands are  $1.01 \pm 0.40$ ,  $1.20 \pm 0.50$ ,  $1.10 \pm 0.46$ , and  $0.8 \pm 0.20$ . The uncertainty intervals for all values are well overlapping, and we can calculate a weighted-mean value which is equal to  $0.91 \pm 0.18$ .

The weighted-mean abundances of the other isotopes are  $1.10 \pm 0.35$  for 636 and  $1.21 \pm 0.63$  for 627. The abundance of 627 is equal to square root of 628 for mass-dependent fractionation, that is,  $0.95 \pm 0.42$ . The abundance of 638 is equal to product of 636 and 628, that is,  $1.00 \pm 0.38$ . The former agrees with the measured value within their uncertainties, the latter perfectly fits the measured value.

For the above reasons, without further information, we can conclude that retrieval of CO<sub>2</sub> isotopic abundance performed from the short and long wavelength channel of PFS spectrometer suggest results close to “terrestrial one” with a weighted-mean value which is equal to  $0.91 \pm 0.18$ .

## 7 Conclusions

Investigation of minor species in Martian and Venusian atmosphere by using the data of PFS-MEX and VIRTIS-VEX spectrometers gave a unique possibility to pose important experimental constraints on a variety of problems still unresolved. High resolution spectroscopy achieved by Earth-based instruments provides small spatially resolved observations and gives few opportunities to investigate content variations as a function of observational parameters since information is usually integrated across the planetary disk.

The progress in space-borne satellites' technology and infrared spectroscopy reached with the latest planetary missions gives for the first time an opportunity to study atmospheric and superficial properties with acquisitions of spectra highly spatially and spectrally resolved.

These two improvements together gave us the chance to investigate minor species (therefore characterized by small spectral features) which are important tracers of the main atmospherics' processes, evolution and stability, dynamics and chemistry.

The ***water vapor abundance*** in the *mesosphere of Venus* has been already measured in a number of ground-based and spaceborn experiments. Various experiments gave approximately the same values from several ppm to a bit more than 10 ppm. An intriguing exception was the strong local enhancement up to  $10^2$  ppm soon after the subsolar point in the equatorial region observed by the Pioneer Venus OIR (Schoefield et al., 1982; Irwin et al., 1997; Koukouli et al., 2005). Thus our present study had two main goals: to measure the water vapor abundance at the cloud tops with high spatial resolution, and to search for the wet spots observed by the Pioneer Venus. As a byproduct we measured the cloud top altitude.

The Venus Express and VIRTIS observation strategy was particularly favorable for measurements at low latitudes around noon. Here the water vapor abundance near cloud top level at 2.5  $\mu\text{m}$  was found to be  $6 \pm 2$  ppm. Our best horizontal spatial resolution was about 10 km on the cloud “surface”, giving for the first time the chance with our high spatial resolution to measure local variations.

Pixel-to pixel variations were within 20% and do not exceed random measurement error. Thus we did not observe any anomalously wet regions reported by the Pioneer Venus OIR experiment team. To be precise we have to note that the cloud top region in the far IR is located lower by several kilometers than that at 2.5  $\mu\text{m}$ , and therefore we were sensitive to a higher level of atmosphere. The level of maximum sensitivity to the variations of water vapor is equal to 68 km, the corresponding cloud top altitude at 1.5  $\mu\text{m}$  being equal to  $75 \pm 1$  km.

We observed an increase of water vapor abundance up to 20 ppm near both morning and evening terminator. However, the result is highly sensitive to the absolute precision of the continuum level calibration, since in this region the intensity of outgoing radiation is low due to high incidence solar angle. With the instrumental uncertainties related to the removal of the dark current and absolute calibration of the VIRTIS-H spectra, a systematic bias is possible. Thus this result needs additional confirmation.

The future attempts should be devoted to the improvements of spectral and radiometric calibration of the VIRTIS-H & M instruments to get rid of the possible systematic biases related to calibration uncertainties and to increase the data amount suitable for studies of minor species. A next step would be a complex high spatial resolution study of water vapor abundance and its correlation with cloud properties, UV absorber, and abundances of other minor species.

Results show a **CO mixing ratio** with an average value of about 800 ppm from a first analyzed dataset observations acquired in a latitude range of approximately  $(- 60) \div (+ 60)$  degrees and in a solar longitude range which

encompass the summer and the beginning of autumn in the northern hemisphere, therefore winter in the southern one (Ls range: 90° - 200°). Higher average values of about 900 ppm are found in the second dataset which comprises observations at the end of winter and beginning of spring in the north hemisphere (Ls range: 330° - 95°).

Since the two datasets differ in the atmospheric model (used temperature-pressure profile), absolute values of CO atmospheric content may depend on the model. For this reason besides reporting both results of absolute CO content values, which anyway are comparable within the computed errors, we particularly stress the observed variability and trends.

From the analysis of carbon monoxide in Martian atmosphere it appears a variability of the CO content at different atmospheric conditions (25 % for a first dataset, 35% for a second), however not so strong in percentage as resulted from other studies (e.g. Billebaud et al. – 1998, which attributed to the range of CO variability values from 0 to 100%).

We have found an independence of the mixing ratio from planet altimetry in agreement with a uniform mixing ratio along the atmospheric column. In fact the eddy diffusion coefficient is  $K \approx 10^6 \text{ cm}^2 \text{ s}^{-1}$  in Mars' troposphere [Korablev et al., 1993], and the vertical mixing time  $H^2/K$  is two weeks ( $H$  is the scale height). Being this mixing time much shorter than CO lifetime, carbon monoxide should be vertically well mixed.

Our results confirm this observation; we however stress that we did not yet study observations in proximity of great volcanoes, where mixing ratio could possibly vary in case of founding outgassing processes. Due to the PFS high spatial resolution, as soon as calibration over high elevated Martian features will be improved, the study of carbon monoxide over a higher altitude range will give further clarifications on previous results indicating altitude's dependence (Rosenqvist et al., 1992)

We observe an absence of strong diurnal CO variability in agreements with models predicting the CO lifetime to be equal to 6 years, assessing for diurnal variations a very low range.

The however observed low variations with local time suggest a weak enhance on midday, where the Sun is high and the photolysis rate is more efficient.

There is an evident correlation with the Sun incidence angle. From both analyzed dataset we can observe a decrease of CO mixing ratio increasing the incidence angle.

This trend may be correlated with the energy present in the atmosphere depending on solar illumination, which could enhance CO production when the incident solar beams density is higher (small angles).

The main observed correlation is however with latitudes closer to the subsolar point in a given season. Mars Express satellite elliptical and not Sun synchronous orbits, bring to a not unimportant bias for observations in Ls (season), Latitude and Local Time, which can affect the dataset and consequently the interpretation of the variability.

Due to the mentioned bias we can mainly attribute the CO variations with incidence angle to the latitudinal dependence on the subsolar point. The observed trend of mixing ratio versus Latitude presents a maximum around latitudes in which the Sun rays meet the surface with the minimum angle in the considered season. We can observe a maximum at low latitudes in the southern hemisphere winter, which could be correlated with CO<sub>2</sub> decreasing due to intense condensation of CO<sub>2</sub> on the south polar cap.

In this case, the actual CO column density does not vary, but what changes is the mixing ratio which is related to the total atmosphere (almost totally made of CO<sub>2</sub> in Martian case). In fact condensation and sublimation of CO<sub>2</sub> result in enhancement and depletion, respectively, in the mixing ratios of incondensable species like CO.

**Summarizing** *results on carbon monoxide, we find an increase in the Southern winter and at the latitudes of subsolar point where solar flux is higher and therefore CO<sub>2</sub> photolysis is more efficient. In general seasonal features are more pronounced at equatorial latitudes and meridian profiles of the mixing ratio (for individual orbits) present seasonal shift of the*

*maximum versus the sub solar point. We find an enhancement also at low incidence angles and at midday local time.*

Results on **CO<sub>2</sub> isotopes** consisted primarily in the identification of all the CO<sub>2</sub> isotopes in PFS data (LWC), with an instrumental spectral resolution never available before.

The retrieved abundances of the main isotopes outside the center of the main CO<sub>2</sub> absorption band at 667 cm<sup>-1</sup> (LWC) resulted to be close to terrestrial values and are reported and are presented in Table 10 in the form of isotopic ratios.

| Isotopic ratio                         |
|--|
| $^{12}\text{C}/^{13}\text{C} = 82.4$   |
| $^{16}\text{O}/^{18}\text{O} = 479.5$  |
| $^{16}\text{O}/^{17}\text{O} = 2437.9$ |

**Table 10.** Results expressed as isotopic ratios.

In these observations there are some differences between the observed abundance of 628 isotope (the most important CO<sub>2</sub> isotopomer - together with the 627- which gives indication of the CO<sub>2</sub> oxygen isotope's content) at different wavelengths: at 576 cm<sup>-1</sup> is similar to the terrestrial value, while in the bottom of the band (663 cm<sup>-1</sup>) it is found to be a little higher. From the last spectral range even the 627 isotope seems to have much higher abundance than terrestrial value.

The retrieved abundance of 628 in the SWC (the band at 2614 cm<sup>-1</sup>) is about 0.8 times the terrestrial value. In general, the quantity retrieved from this spectral range pertains to the atmospheric mass of the first scale height of the atmosphere.

For this reason, a realistic interpretation of the results of this study can be a variability of mixing ratio of the oxygen isotopes with the altitude. We pass from a lower value obtained in the first layers of the atmosphere (from SWC), less than terrestrial value, to values similar to the terrestrial

one from the ranges of the band in LWC pertaining an altitude around 20-30 Km, to higher values in the center of the band which probes an altitude around 30-50 Km. This decreasing trend with altitude could be explained by the escape of lighter isotopes from the top of the atmosphere, with enrichment of the heavier ones going closer to the surface. Anyway some further considerations should be developed.

The column  $\text{CO}_2$  abundance in the Martian atmosphere is  $2 \times 10^{23} \text{ cm}^{-2}$ , the column photolysis rate is  $10^{12} \text{ cm}^{-2} \text{ s}^{-1}$ . Their ratio is the mean  $\text{CO}_2$  lifetime relative to chemical processes which is 6000 years. Local lifetimes may be shorter or longer; for example, the  $\text{CO}_2$  lifetime is 30 years at 80 km. Mixing time is  $H^2/K$  where  $H$  is the scale height and  $K$  is eddy diffusion. Mixing time varies from two weeks in the lower atmosphere to 15 hours at 80 km. Mixing time is very much shorter than the chemical lifetime of  $\text{CO}_2$ ; therefore all  $\text{CO}_2$  isotopes should be well mixed in the atmosphere and the  $\text{CO}_2$  isotope ratios do not depend on height up to a homopause at 120-135 km where the diffusive separation begins.

The 628 abundances obtained in this study from various bands are  $1.01 \pm 0.40$ ,  $1.20 \pm 0.50$ ,  $1.10 \pm 0.46$ , and  $0.8 \pm 0.20$ . The uncertainty intervals for all values are well overlapping, and we can calculate a weighted-mean value which is equal to  $0.91 \pm 0.18$ .

The weighted-mean abundances of the other isotopes are  $1.10 \pm 0.35$  for 636 and  $1.21 \pm 0.63$  for 627. The abundance of 627 is equal to square root of 628 for mass-dependent fractionation, that is,  $0.95 \pm 0.42$ . The abundance of 638 is equal to product of 636 and 628, that is,  $1.00 \pm 0.38$ . The former agrees with the measured value within their uncertainties, the latter perfectly fits the measured value.

For the above reasons, without further information, we can conclude that retrieval of  $\text{CO}_2$  isotopic abundance performed from the short and long wavelength channel of PFS spectrometer suggest results close to “terrestrial one” with a weighted-mean value which is equal to  $0.91 \pm 0.18$ .

## 8 *References*

- Andrews, D. A., Holton, J. R., and Leovy, C. B. (1987). *Middle Atmosphere Dynamics*. Academic Press.
- Armstrong, B. H. (1967). Spectrum line profiles: The Voigt function. *J.Q.S.R.T.*, 7:66^88.
- Artru J., P. Lognonné, and E. Blanc, Normal modes modeling of post-seismic ionospheric oscillations, *Geophys. Res. Letters*, 28, 697, 2001
- Atreya, S. K., and J. E. Blamont, Stability of the Martian atmosphere: Possible role of heterogeneous chemistry, *Geophys. Res. Lett.*, 17, 287– 290, 1990.
- Aumann, H. H. and Orton, G. S. (1979). The 12 to 20 micron spectrum of Venus: Implications for temperatures and cloud structure. *Icarus*, 38:251^266.
- Baines et al (2001) (2000), Detection of Sub-micron radiation from the surface of Venus by Cassini/VIMS. *Icarus*, 148, 307-311.
- Barabash, S., Lundin, S., ASPERA-3 on Mars Express, *Icarus*, Volume 182, Issue 2, June 2006, Pages 301-307
- Barker, E. S. (1975a). Comparison of Simultaneous CO<sub>2</sub> and H<sub>2</sub>O observations of Venus. *J. Atmos. Sci.*, 32:1071^1075.
- Barker, E. S. (1975b). Observations of Venus Water Vapour over the Disk of Venus: The 1972-1974 data using the H<sub>2</sub>O lines at 819.7 and 817.6 nm. *Icarus*, 25:268^ 281.
- Bayers, R. M. (1763). An Essay towards solving a problem in the Doctrine of Chances. *Phil. Trans. R. Soc. Lond.*, 53:370.
- Bell III, J. Crisp, D., Lucey, P. C, Ozoroski, T. A., Sinton, W. M., Willis, S. C, and Campbell, B. A. (1991). Spectroscopic Observations of Bright and Dark Emission Features on the Night Side of Venus. *Science*, 252:1293 1296.

Belton, M. J. S., Gierasch, P. J., Smith, M. D., and collaborators. (1991). Images from Galileo of the Venus cloud deck. *Science*, 253(5027): 1531-1536.

Belton, M. J. S., Hunten, D. M., and Goody, R. M. (1968). Quantitative spectroscopy of Venus in the region 800-1100 nm. In Brandt, J. C. and McElroy, M. B., editors, *The Atmospheres of Venus and Mars*, pages 694-8. New York:Gordon and Breach.

Belton, M.J.S., Gierasch, P.J., Smith, M.D., Helfenstein, P., Schinder, P.J., Pollack, J.B., Rages, K.A., Morrison, D., Klaasen, K.P., Pilcher, C.B., 1991. Images from Galileo of the Venus cloud deck. *Science* 253, 1531-1536.

Belton, M.J.S., Smith, R.S., Schubert, G., Del Genio, A.D., 1976. Cloud patterns, waves and convection in the Venus atmosphere. *J. Atmos. Sci.* 33, 1394-1417.

Bertaux, J. L., Widemann, T., Hauchecorne, A., I., M. V., and Economov, A. P. (1996). Vega 1 and Vega 2 entry probes: an investigation of local UV absorption 220-440 nm in the atmosphere of Venus (SO<sub>2</sub>, aerosols, cloud structure). *J. Geophys. Res.*, 101 (E5): 12709-12745.

Bezard, B., de Bergh, C, Crisp, D., and Maillard, J. (1990). The deep atmosphere of Venus revealed by high-resolution night side spectra. *Nature*, 315:508-511.

Bezard, B., de Bergh, C, Maillard, J. P., Crisp, D., Owen, T., Pollack, J. B., and Grinspoon, D. (1993). The abundance of sulphur dioxide below the clouds of Venus. *Geophys. Res. Lett.*, 20:1587-1590.

Biermann, U., Luo, B. P., and Peter, T. (2000). Absorption Spectra and Optical Constants of Binary and Ternary Solutions of H<sub>2</sub>SO<sub>4</sub>, HNO<sub>3</sub> and H<sub>2</sub>O in the mid-infrared at atmospheric temperatures. *J. Phys. Chem. A.*, 104:783-793.

Billebaud, F., J. P. Maillard, E. Lellouch, and T. Encrenaz, The spectrum of Mars in the (1-0) vibrational band of CO, *Astron. Astrophys.*, 261, 647, 1992.

Billebaud, F., J. Rosenqvist, E. Lellouch, J. P. Maillard, T. Encrenaz, and F. Hourdin, Observations of CO in the atmosphere of Mars in the (2-0) vibrational band at 2.35 microns, *Astron. Astrophys.*, 333, 1092- 1099, 1998.

Billebaud, F., Rosenqvist, J., Maillard, J.-P., Lellouch, E., & Encranaz, T., Search for Spatial Variations in the CO Abundance on Mars at 2.3 Micron, Bulletin of the American Astronomical Society, Vol. 23, p.1214

Bjoraker, G. L.; Mumma, M. J.; Larson, H. P., Isotopic Abundance Ratios for Hydrogen and Oxygen in the Martian Atmosphere, Bulletin of the American Astronomical Society, Vol. 21, p.991, 1989

Blamont, J. E., Young, R. E., Seiff, A., Ragen, B., Sagdeev, R., Linkin, V. M., Kerzhanovich, V. V., Ingersoll, A. P., Crisp, D., Elson, L. S., Preson, R. A., Golistyn, G. S., and Ivanov, V. N. (1986). Implications of the Vega balloon results for Venus atmospheric dynamics. *Science*, 231 (4744): 1422-1425.

Bottema, M., Plummer, W., and Strong, J. (1964). Water vapour in the atmosphere of Venus. *The Astrophysical Journal*, 139(3):102H022.

Bougher, S. W. and Roble, R. G. (1991). Comparative terrestrial planet thermospheres. 1. Solar cycle variation of global mean temperatures. *J. Geophys. Res.*, 96,11045-11055.

Bougher, S. W., Dickinson, R. E., Ridley, E. C, and Roble, R. G. (1988). Venus mesosphere and thermosphere III. Three-dimensional general circulation with coupled dynamics and composition. *Icarus*, 73,515 573.

Bullock, M. A. and Grinspoon, D. H. (2001). The recent evolution of climate on Venus. *Icarus*, 150:19^37.

Bullock, M.A., Grinspoon, D.G., 1996. The Stability of Climate on Venus. *J. Geophys. Res.* 101, 7521–7529.

Carlson R.W. et al. (1991) Galileo infrared imaging spectroscopy measurements at Venus. *Science*, 253, p. 154.

Carlson, R. W., Kamp, L. W., Baines, K. EL, Pollack, J. B., Grinspoon, D. EL, Encranaz, T., Drossart, P., and Taylor, F. W. (1991). Variations in Venus cloud particle properties: a new view of Venus' cloud morphology as observed by the Galileo Near-Infrared Mapping Spectrometer. *Planet. Space Sci.*, 11(7), 177 185.

Carlson, R.W., Taylor, F.W., et al., 1991. Galileo infrared imaging spectroscopy measurements at Venus. *Science* 253, 1541–1548.

Chahine, M. T. (1970). Inverse problems in Radiative Transfer: Determination of Atmospheric Parameters. *J. Atmos. Sci.*, 27,960-967.

Chahine, M. T. (1972). A general relaxation method for Inverse Solution of the Pull Radiative Transfer Equation. *J. Atmos. Sci.*, 29,711 717.

Chahine, M. T. (1974). Remote Sounding of Cloudy Atmospheres. I. The Single Cloud Layer. *J. Atmos. Sci.*, 31,233-243.

Chamberlain, J. W. and Hunten, D. M. (1987). *Theory of Planetary Atmospheres*. Academic Press.

Chamberlain, J. W., and D. M. Hunten, *Theory of Planetary Atmospheres: An Introduction to Their Physics and Chemistry*, Academic, San Diego, Calif., 1987.

Clancy, R. T., A. W. Grossman, M. J. Wolf, P. B. James, D. J. Rudy, Y. N. Billawala, B. J. Sandor, S. W. Lee, and D. O. Muhleman, Water vapor saturation at low altitudes around Mars aphelion: A key to Mars climate?, *Icarus*, 122, 36–62, 1996.

Clough, S. A., Kneizys, F. X., and Davies, R. W. (1989). Line shape and the water vapour continuum. *Atmospheric Research*, 23, 229-241.

Clough, S. A., Kneizys, F. X., Davies, R. W., Gamache, R. R., and Tipping, R. (1980). Theoretical line shape for H<sub>2</sub>O vapour: Application to the continuum. In Deepak, A., Wilkerson, T. D., and Ruhnke, L. EL, editors, *Atmospheric Water Vapour*, pages 25 16. Academic Press, New York.

Clough, S.A., Kneizys, F.X., and Davies, R.W. (1989). Line shape and the water vapour continuum. *Atmospheric Research*, v. 23, p. 229–241.

Colin, L. (1980). The Pioneer Venus Program. *J. Geophys. Res.*, 85(A13):7575-7598.

Collard et al (1993). Latitudinal distribution of carbon monoxide in the deep atmosphere of Venus, *Planet. Space Sci.* 41, 487.

Collard, A. D., Taylor, F. W., Calcutt, S. B., Carlson, R. W., Kamp, L. W., Baines, K. EL, Encrenaz, T., Drossart, P., Lellouch, E., and Bezaud, B. (1993). Latitudinal distribution of carbon monoxide in the deep atmosphere of Venus. *Planet. Space. Sci.*, 41(7),487-494.

Collard, A.D., Taylor, F.W., Calcutt, S.B., Carlson, R.W., Kamp, L., Baines, K., Encrenaz, Th., Drossart, P., Lellouch, E., Berzard, B., 1993. Latitudinal distribution of carbon monoxide in the deep atmosphere of Venus. *Planet. Space Sci.* 41 (7), 487–494.

Connes, J. and Connes, P. (1966). Near-infrared planetary spectra by Fourier Spectroscopy. I. Instruments and results. *J. Opt. Soc. Amer.*, 56:869-910.

Cousin, C, Le Doucen, R., Boulet, C, and Henry, A. (1985). Temperature dependence of the absorption in the region beyond the 4.3  $\mu\text{m}$  band head of CO<sub>2</sub>. 2: N<sub>2</sub> and O<sub>2</sub> broadening. *Applied Optics*, 24(22) , 3899-3907.

Crisp, D. (1986a). Radiative Forcing of the Venus Mesosphere I. Solar Fluxes and Heating Rates. *Icarus*, 67, 181-511.

Crisp, D. (1986b). Radiative Forcing of the Venus Mesosphere II. Thermal Fluxes, Cooling Rates and Radiative Equilibrium Temperatures. *Icarus*, 77, 391-113.

Crisp, D., Allen, D., Grinspoon, D., and Pollack, J. (1991a). The dark side of Venus: Near-Infrared Images and Spectra from the Anglo-Australian Observatory. *Science*, 253:1263-1266.

Crisp, D., McMurdock, S., Stephens, S. K., Sinton, W. M., Hagen, B., Hodapp, K. W., Probst, R. C, Doyle, L. R., Allen, D. A., and Elias, J. (1991b). Ground-based near-infrared imaging observations of Venus during the Galileo encounter. *Science*, 253(5027):1538-1541.

Dave, J. V. (1969). Scattering of electromagnetic radiation by a large, absorbing sphere. *IBM J. Res. Dev.*, 13(3):302-313.

de Bergh, C, Bezard, B., Crisp, D., Maillard, J., Owen, T., Pollack, J., and Grinspoon, D. (1995). Water in the deep atmosphere of Venus from the High-Resolution Spectra of the night side. *Adv. Space. Res.*, 15:(4)79-(4)88.

Del Genio, A. D. and Rossow, W. B. (1990). Planetary-scale waves and the cyclic nature of cloud top dynamics of Venus. *J. Atmos. Sci.*, 47:293-318.

Delderfield, J., Schofield, J. T., and Taylor, F. W. (1980). Radiometer for the Pioneer Venus Orbiter. In *IEEE Transactions on Geoscience and Remote Sensing*, volume 18, pages 70-76.

Donahue, T. M. and Hodges, R. R. (1992). Past and Present Water Budget on Venus. *J. Geophys. Res.*, 97:6093-6091.

Donahue, T. M. and Hodges, R. R. (1993). Venus Methane and Water. *Geophys. Res. Lett.*, 20:591-594.

Drossart et al (1993). Search for spatial variations of the H<sub>2</sub>O abundance in the lower atmosphere of Venus from NIMS Galileo. *Planet. Space Sci.* 41, 495.

Drossart, P. Bezdard, B., Encrenaz, T., Lellouch, E., Roos-Serote, M., Taylor, F. W., Collard, A., Grinspoon, D., Carlson, R., Baines, K., and Kamp, L. (1993). Search for spatial variations of the H<sub>2</sub>O abundance in the lower atmosphere of Venus from NIMS-Galileo. *Plan. Space Sci.*, 41:495-504.

Eiler, J.M., Kitchen, N., and Rahn, T. (2000) Experimental constraints on the stable isotope systematics of CO<sub>2</sub> ice/vapor systems and relevance to the study of Mars. *Geochimica et Cosmochimica Acta*, 64, 733-746.

Encrenaz, T., E. Lellouch, J. Rosenqvist, P. Drossart, M. Combes, F. Billebaud, I. de Pater, S. Gulkis, J. P. Maillard, and G. Paubert, The atmospheric composition of Mars: ISM and ground-based observational data, *Ann. Geophys.*, 9, 797– 803, 1991.

Encrenaz, T., *Infrared Spectroscopy of Solar-System Planets*, *Space Science Reviews*, published by Springer Netherlands, Volume 135, Numbers 1-4 / March, 2008

Encrenaz, T., Lellouch, E., Gernicharo, J., Paubert, G., Gulkis, S., and Spilker, T. (1995). The Thermal Profile and Water Abundance in the Venus Mesosphere from H<sub>2</sub>O and HDO Millimetre Observations. *Icarus*, 117:162-172.

Encrenaz, T., Lellouch, E., Paubert, G., and Gulkis, S. (1991). First detection of HDO in the atmosphere of Venus at radio wavelengths: an estimate of the H<sub>2</sub>O vertical distribution. *Astronomy and Astrophysics*, 246:63-66.

Esposito, L. W. Winick, J. R. and Stewart, A. I. (1979). Sulphur dioxide in the Venus atmosphere: Distribution and implications. *Geophys. Res. Lett.*, 6:601-604.

Esposito, L. W., Copley, M., Eckert, R., Gates, L., Stewart, A. I. F., and Worden, H. (1988). Sulphur dioxide at the Venus cloud tops: 1978-1986. *J. Geophys. Res.*, 93:5267-5276.

Esposito, L. W., Knollenberg, R. (I., Marov, M. Y., Toon, O. B., and P., T. R. (1983). The clouds and hazes of Venus, pages 215-279. Space Science Series. University of Arizona Press.

Esposito, L., 1984. Sulphur dioxide: episodic injection shows evidence for active Venus volcanism. *Science* 223, 1072–1074.

Evans, K. F. (1998). The spherical harmonics discrete ordinate method for three-dimensional atmospheric radiative transfer. *J. Atmos. Sci.*, v. 55, p. 429–446. See also F. Evans' web-site: <http://nit.colorado.edu/~evans/>.

Fels, S.B., Schofield, J.T., Crisp, D., 1984. Observations and theory of the solar semidiurnal tide in the mesosphere of Venus. *Nature* 312 (5993), 431–434.

Fink, U., Larson, H. P., Kuiper, G. P., and Poppen, R. F. (1972). Water vapour in the atmosphere of Venus. *Icarus*, 17:617-631.

Fiorenza, C. and Formisano, V., A Solar spectrum for PFS data analysis, *Planetary Space Science*, 2004

Fletcher, R. (1971). A modified Marquardt subroutine for nonlinear least squares fitting. Technical report, Report R6799, A.E.R.E., Harwell.

Formisano, V. et al., The Planetary Fourier Spectrometer (PFS) onboard the European Mars Express Mission, *Planetary Space Science*, 2004a

Formisano, V., Cottini, V., Giuranna, M., Grassi, D., Khatuntsev, I., Ignatiev, N., Maturilli, A., Piccioni, G., Saggin, B., Zasova, L. and the PFS TEAM, FIRST OBSERVATIONS OF THE PLANETARY FOURIER SPECTROMETER AT MARS, *Advanced Space Research, Advances in Space Research, Volume 36, Issue 6, Pages 1074-1083, 2005*

Gamache, R. R., Hawkins, R. L., and Rothman, L. S. (1990). Total internal partition sums in the temperature range 70-3000 K - Atmospheric linear molecules. *J. Molec. Spec.*, 142(2):205-219.

Giuranna, M. et al. Calibration of the Planetary Fourier Spectrometer Short Wavelength Channel, *Planet. Space Sci.*, **53**, issue 10, 975–991, (2005a)

Giuranna, M et al. (2005b) Calibration of the Planetary Fourier Spectrometer Long Wavelength Channel, *Planet. Space Sci.*, **53**, issue 10, 993–1007.

Gmitro, J. I. and Vermeulen, T. (1964). Vapour-liquid equilibria for aqueous Sulphuric Acid. *Am Inst Chem Eng*, 10:740-746.

Goody, R. M. and Yung, Y. L. (1989). *Atmospheric Radiation, Theoretical Basis*. Oxford University Press.

Goody, R. M., West, R., Chen, L., and Crisp, D. (1989). The Correlated-k method for radiation calculations in non-homogeneous atmospheres. *J. Q. S. R. T*, 42:539550.

Grassi, D., Zasova, L.V., Ignatiev, N.I., Maturilli, A., G. A. Bianchini, Formisano, V., Giuranna, M., *Methods for the Analysis of Data from the Planetary Fourier Spectrometer on the Mars Express Mission*, *Planetary Space Science*, in press, 2005

Greene, T. P., A. T. Tokunaga, D. W. Toomey, and J. S. Carr, CSHELL: A high spectral resolution echelle spectrograph for the IRTF, *Proc. SPIE*, 1946, 313– 323, 1993.

Grinspoon, D. H. (1987). Was Venus wet? Deuterium reconsidered. *Science*, 238:1702-1704.

Grinspoon, D. H. (1997). *Venus Revealed; A new look below the clouds of our mysterious twin planet*. Addison-Wesley.

Gull, T. R., O'Dell, C. R., and Parker, R. A. R. (1974). Water vapour in Venus determined by air born observations of the 0.82  $\mu$ m band. *Icarus*, 21:213-218.

Gurnett, D.A., Kurth, W.S., Roux, A., Gendrin, R., Kennel, C.F., Bolton, S.J., 1991. Lightning and plasma wave observations from the Galileo flyby of Venus. *Science* 253, 1522.

Haberle, R. M., J. B. Pollack, J. R. Barnes, R. W. Zureck, C. B. Leovy, J. R. Murthy, H. Lee, and J. Schaeffer, Mars atmospheric dynamics as simulated by the NASA Ames general circulation model, 1, The zonal-mean circulation, *J. Geophys. Res.*, 98, 3093–3123, 1993.

Hanel, R.A., Conrath, B.J., Jennings, D.E., Samuelson, R.E., *Exploration of the Solar System by Infrared Remote Sensing*, edited by Cambridge University Press

Hansen, J. E. and Honevier, J. W. (1974). Interpretation of the polarisation of Venus. *J. Atmos. Sci.*, 31:1137.

Hansen, J. E. and Travis, L. (1974). Light Scattering in Planetary Atmospheres. *Space Sci. Rev.*, 16:527-610.

Hashimoto, G.L., Abe, Y., 2005. Climate control on Venus: comparison of the carbonate and pyrite models. *Planet. Space Sci.* 53, 839–848. Keating, G.M., Taylor, F.W., Nicholson, J.Y., Hinson, E.W., 1979. Short term cyclic variations of the Venus upper atmosphere. *Science* 205, 62–65.

Heathfield, A. E., Newnham, D. A., Ballard, J., Grainger, I., and Lambert, A. (1999). Infrared and visible Fourier-transform spectra of sulphuric acid/water aerosols at 230 and 294 K. *Applied Optics*, 38(30):6408-6420.

Hilsenrath, J. (1960). *Tables of Thermodynamic and Transport Properties of Air, Argon, Carbon Dioxide, Carbon Monoxide, Hydrogen, Nitrogen, Oxygen and Steam*. Pergamon, New York.

Hoffman, J. H., Oyama, V. I., and von Zahn, U. (1983). Measurements of the Venus Lower Atmosphere Composition: A Comparison of Results. *Journal of Geophysical Research*, 85(A13):7871-7881.

Houghton, J. T. and Taylor, F. W. (1975). One remote sounding of the upper atmosphere of Venus. *J. Atmos. Sci.*, 32:620-629.

Houghton, J. T., Taylor, F. W., and Rodgers, C. D. (1984). *Remote Sounding of Atmospheres*. Cambridge University Press.

Hourdin, F., Forget, F., and Talagrand, O. (1995). The sensitivity of the Martian surface pressure and atmospheric mass budget to various parameters: A comparison between numerical simulations and Viking observations. *J. Geophys. Res.*, 100, 5501– 5523, 1995.

Hunilicek, J. (1982). Optimized computation of the Voigt and complex probability functions. *J.Q.S.R.T.*, v. 27, no. 4, p. 437.

Hunilicek, J. (1982). Optimised computation of the Voigt and complex probability functions. *J. Q. S. R. T.*, 27(4):437-44.

Hunten, D. M., CO on Mars: Comment on paper by Rosenqvist et al., *Icarus*, 101, 42–44, 1993.

Hunten, D. M., A. L. Sprague, and L. R. Doose, Correction for dust opacity of Martian atmospheric water vapor abundances, *Icarus*, 147, 42–48, 2000.

Ignatiev, N. I., Grassi, D., Zasova, L. V. (2005). Planetary Fourier spectrometer data analysis: Fast radiative transfer models. *Planet. Space. Sci.*, v. 53, no. 10, p. 1035–1042.

Ignatiev, N., Moroz, V. I., Moshkin, B., and collaborators. (1997). Water vapour in the lower atmosphere of Venus: a new analysis of optical spectra measured by entry probes. *Plan. Space Sci.*, 45:427–138.

Ignatiev, N., Moroz, V. I., Zasova, L., and Khatuntsev, I. (1999). Venera 15: Water vapour in the middle atmosphere of Venus. *Adv. Space Sci.*, 23(9):1549–1558.

Ignatiev, N.I., Grassi, D., Zasova, L.V., Planetary Fourier Spectrometer data analysis: Fast radiative transfer models, *Planetary Space Science*, 2004b

Imamura, T. and Hashimoto, G. L. (1998). Venus cloud formation in the meridional circulation. *J. Geophys. Res.*, 103(E13):31349–31366.

Irwin, P. G. J. (1997). Temporal and Spatial variations in the Venus Mesosphere retrieved from Pioneer Venus OIR. *Adv. Space Res.*, 19:1169–1179.

Irwin, P. G. J., Calcutt, S. B., and Taylor, F. W. (1997). Radiative transfer models for Galileo NIMS studies of the atmosphere of Jupiter. *Adv. Space Sci.*, 19(8):1149–1158.

Isaacs, R. G., *et al.* (1987). Multiple scattering LOWTRAN and FASCODE models. *Applied Optics*, v. 26, no. 7, p. 1272–1281.

Jakosky, B. M., and C. B. Farmer, The seasonal and global behavior of water vapor in the Mars atmosphere: Complete global results of the Viking atmospheric water detector experiment, *J. Geophys. Res.*, 87, 2999–3019, 1982.

James, E. P., Toon, O. B., and Schubert, G. (1997). A Numerical Microphysical Model of the Condensational Venus Cloud. *Icarus*, 129:147–171.

- Janssen, M. A. and Klein, M. J. (1981). Constraints on the composition of the Venus atmosphere from Microwave Measurements near 1.35 cm wavelength. *Icarus*, 46:58-69.
- Jenkins, J. M., Steffes, P. G., Hinson, D. P., Twicken, J. D., and Tyler, G. L. (1994). Radio occultation studies of the Venus atmosphere with the Magellan spacecraft. 2. Results from the October 1991 experiments. *Icarus*, 110:79-94.
- Jones, A. (1976). Optical constants of Sulphuric Acid in the far Infrared. *J. Q. S. R. T.*, 16:1017-1019.
- Kamp, L. W. and Taylor, F. W. (1990). Radiative Transfer models of the night side of Venus. *Icarus*, 86:510-529.
- Kaplan, L. D., J. Connes, and P. Connes, Carbon monoxide in the Martian atmosphere, *Astrophys. J.*, 1457, L187– L192, 1969.
- Kaplan, L.D., et al., Carbon monoxide in the Martian atmosphere, *Astrophysical Journal*, vol. 157, pag. L187-L192, 1969
- Keating, G., Nickolson, J., and Lake, L. (1980). Venus Upper Atmosphere Structure. *J. Geophys. Res.*, 85:7941-7956.
- Kliore, A. J. and Patel, I. R. (1980). Thermal Structure of the Atmosphere of Venus from Pioneer Venus Radio Occultations. *J. Geophys. Res.*, 85:7957-7962.
- Kliore, A. J. and Patel, I. R. (1982). Thermal Structure of the Atmosphere of Venus from Pioneer Venus Radio Occultations. *Icarus*, 52:320-334.
- Knollenberg, R. G. and Hunten, D. M. (1980). The Microphysics of the Clouds of Venus: Results of the Pioneer Venus particle size spectrometer Experiment. *J. Geophys. Res.*, 85(A13):8039-8058.
- Korablev, O. I., V. A. Krasnopolsky, A. V. Rodin, and E. Chassefiere, Vertical structure of Martian dust measured by solar infrared occultations from the Phobos spacecraft, *Icarus*, 102, 76– 87, 1993.
- Koukouli, M. E. (2001). Remote Sensing of Water Vapour in Venus' Middle Atmosphere. Second Year Report, AOPP, Oxford University.

Koukouli, M. E. (2002). Remote sensing of water vapour in Venus' middle atmosphere. PhD thesis, Atmospheric, Oceanic and Planetary Physics, Oxford University.

Krasnopolsky, V. A. (1986). Photochemistry of the atmospheres of Mars and Venus. Physics and Chemistry in Space. Springer-Verlag.

Krasnopolsky, V. A. and Parshev, V. A. (1983). Photochemistry of the Venus atmosphere. In Bougher, S. W., Hunten, D. M., and Phillips, R. J., editors, Venus, Space Science Series, pages 431-458. University of Arizona Press.

Krasnopolsky, V. A. and Pollack, J. B. (1984). H<sub>2</sub>O -H<sub>2</sub>SO<sub>4</sub> system in Venus' clouds and OCS , CO and H<sub>2</sub>SO<sub>4</sub> profiles in Venus' troposphere. Icarus, 109:58-78.

Krasnopolsky, V. A., and G. L. Bjoraker, Mapping of Mars O<sub>2</sub>(1<sub>2</sub>) dayglow, J. Geophys. Res., 105, 20,179– 20,188, 2000.

Krasnopolsky, V. A., and P. D. Feldman, Detection of molecular hydrogen in the atmosphere of Mars, Science, 294, 914–917, 2001.

Krasnopolsky, V. A., Photochemistry of the Atmospheres of Mars and Venus, Springer-Verlag, New York, 1986.

Krasnopolsky, V. A., Photochemistry of the Martian atmosphere (mean conditions), Icarus, 101, 313– 332, 1993a.

Krasnopolsky, V. A., Solar cycle variations of the hydrogen escape rate and the CO mixing ratio on Mars, Icarus, 101, 33– 41, 1993b.

Krasnopolsky, V. A., Uniqueness of a solution of a steady state photochemical problem: Applications to Mars, J. Geophys. Res., 100, 3263–3276, 1995.

Kuiper, G. P. and Forbes, F. F. (1967). High altitude spectra from NASA CV 990 Jet. I: Venus, 1 - 2.5  $\mu$ m, resolution 20 cm<sup>-1</sup>. Comm. Lunar Planet. Lab., 6:177-189.

Kuiper, G. P., Forbes, F. F., Steinmetz, D. L., and Mitchell, R. I. (1969). High altitude spectra from NASA CV 990 Jet. II: Water vapour on Venus. Comm. Lunar Planet. Lab., 6:209-228.

Kuntz, M. (1997). A new implementation of the Humlicek algorithm for the calculation of the Voigt profile function. *J. Q. S. R. T.* v. 57, no 6, p. 819–824.

Kurucz, R. L. (1991). *The Solar Spectrum, in the Solar Interior and Atmosphere*, eds. A.N. Cox, W.C Livingston, and M. Matthews. Tucson, University of Arizona Press.

Kylling, A., K. Stamnes and S.-C. Tsay (1995). A reliable and efficient two-stream algorithm for radiative transfer; Documentation of accuracy in realistic layered media, in print, *J. Atmos. Chem.*, v. 21, no.2, p.115–150.

Lacis, A. A. and Oinas, V. (1991). A description of the Correlated-K Distribution Method for Modelling Non Gray gaseous Absorption, Thermal Emission and Multiple Scattering in Vertically Inhomogeneous Atmospheres. *J. Geophys. Res.*, 19:9027-9063.

Lammer, H., Lichtenegger, H.I.M., Biernat, H.K., Erkaev, N.V., Arshukova, I., Kolb, C., Gunell, H., Lukyanov, A., Holmstrom, M., Barabash, S., Zhang, T.L., Baumjohann, W., 2006. Loss of hydrogen and oxygen from the upper atmosphere of Venus. *Space Sci. Rev.*

Le Doucen, R., Cousin, C, Boulet, C, and Henry, A. (1985). Temperature dependence of the absorption in the region beyond the 4.3 jirn band head of CO<sub>2</sub>. 2: Pure CO<sub>2</sub> case. *Applied Optics*, 24(6):897-906.

Lellouch, E., Clancy, T., Crisp, D., Kliore, A. J., Titov, D., and Bougher, S. W. (1997). Monitoring of Mesospheric Structure and Dynamics. In Bougher, S. W., Hunten, D. M., and Phillips, R. J., editors, *Venus II, Space Science Series*, pages 295-324. University of Arizona Press.

Lellouch, E., G. Paubert, and T. Encrenaz, Mapping of CO millimeter-wave lines in Mars' atmosphere: The spatial variability of carbon monoxide on Mars, *Planet. Space Sci.*, 39, 219– 224, 1991.

Leu, M. T., J. E. Blamont, A. D. Anbar, L. F. Keyser, and S. P. Sander, Adsorption of CO on oxide and water surfaces: Implications for the Martian atmosphere, *J. Geophys. Res.*, 97, 2621– 2627, 1992.

Levenberg, K. (1944). A method for the solution of certain nonlinear problems in least squares. *Quart. Appl. Math.*, 2:164.

Lewis, J. S. (1997). *Physics and Chemistry of the Solar System*. Academic Press.

Lewis, J. S. and Grinspoon, D. H. (1990). Vertical Distribution of Water in the Atmosphere of Venus: A Simple Thermochemical Explanation. *Science*, 249:1273-1275.

Limaye, S. S. and Suomi, V. E. (1981). Cloud motions on Venus: Global structure and organisation. *J. Atmos. Sci.*, 38:1220-1235.

Livingston, W., and L. Wallace, An atlas of the solar spectrum in the infrared from 1850 to 9000  $\text{cm}^{-1}$  (1.1 to 5.4 mm), Tech. Rep. 91401, Nat. Sol. Obs., Kitt Peak, Ariz., 1991.

Luhmann, J.G., Russell, C.T., 1997. Venus: magnetic field and magnetosphere. In: Shirley, J.H., Fainbridge, R.W. (Eds.), *Encyclopaedia of Planetary Sciences*. Chapman and Hall, London, pp. 905–907.

Ma, Q. and Tipping, R. H. (1992). A far wing line shape theory and its application to the water vibrational bands. *J. Chem. Phys.*, 96(12) :8655-8663.

Ma, Q., Tipping, R. EL, Boulet, C, and Bouanich, J.-P. (1999). Theoretical far-wing line shape and absorption for high-temperature CO<sub>2</sub>- *Applied Optics*, 38:599-604.

Maguire, W.C., Martian isotopic ratios and upper limits for possible minor constituents as derived from Mariner 9 infrared spectrometer data, *Icarus*, vol.32, pag. 85-97, 1977

Manatt, S. L. and Lane, A. L. (1993). A compilation of the absorption cross-sections of SO<sub>2</sub> from 106 to 403 nm. *J. Q. S. R. T.*, 50:267-276.

Marov, M. Y., Lystev, V. E., Lebedev, V. N., Lukashovich, N. L., and Shari, V. P. (1980). The structure and microphysical properties of the Venus Clouds: Venera 9, 10, and 11 data. *Icarus*, 44:608-638.

Marquardt, D. W. (1963). An algorithm for least-squares estimation of nonlinear parameters. *SI AM J. Appl. Math.*, 11:431.

*Mars*, 1993, edited by Hugh H. Kieffer, Bruce M. Jakowsky, Conway W. Snyder, Mildred Matthews, Space Science Series, University of Arizona Press.

Matveev, V. S. (1972). Approximate presentation of the absorption coefficient and equivalent width of spectral lines with Voigt contour. *Zhurnal prikladnoi spektroskopii* (*Applied spectroscopy journal*), v. 16, no. 2, p. 228–233 (in Russian).

McElroy, M. B., and T. M. Donahue, Stability of the Martian atmosphere, *Science*, 177, 986– 988, 1972.

Meadows & Crisp 1996, Ground-based near-infrared observations of the Venus nightside: The thermal structure and water abundance near the surface, *Journal of Geophysical Research* 101 E2 [1996] 4595-4622.

Meadows, V. and Crisp, D. (1996). Ground-based near-infrared observations of the Venus nightside: The thermal structure and water abundance near the surface. *J. Geophys. Res.*, 60:4595-4622.

Mie, G. (1908). Belgrade zur optik trueber medienspeziell kolloidaler nietaloesun-gen. *Ann. Physik.*, pages 377-445.

Moroz, V. I. (2002). Studies of the atmosphere of Venus by means of spacecraft: solved and unsolved problems. *Adv. Space Res.*, 29(2):215-225.

Moroz, V. I., Monshkin, B. E., Ekonomov, A. P., Golovin, Y. M., Gnedykh, V., and Grigor'ev, A. V. (1982). The Venera 13 and Venera 14 spectrophotometry experiments. *Soviet Astronomy Letters*, 8:404-410.

Moroz, V. I., Monshkin, B. E., Ekonomov, A. P., San'ko, N. F., Parfent'ev, N. A., and Golovin, Y. M. (1979a). Venera 11 and 12 descent-probe spectrophotometry: The Venus day side sky spectrum. *Soviet Astronomy Letters*, 5:118-121.

Moroz, V. I., Parfent'ev, N. A., and San'ko, N. F. (1979b). Spectrophotometric experiment on the Venera 11 and Venera 12 descent modules. 2. Analysis of Venera 11 spectra data by layer-addition method. *Cosmic Res.*, 17:601-614.

Moroz, V. I., Spankunch, D., Linkin, V. M., and collaborators. (1986). Venus spacecraft infrared radiance spectra and some aspects of their interpretation. *Applied Optics*, 25(10):171(bI719).

Moroz, V. I., Spankunch, D., Titov, D. V., Schafer, K., Dyachkov, A. V., Dohler, W., Zasova, L. V., Oertel, D., Linkin, V. M., and Nopirakowski, J. (1990). Water vapour and sulphur dioxide abundances at the Venus cloud tops from the Venera-15 infrared spectrometry data. *Adv. Space Res.*, 10:(5)77-(5)81.

- Moroz, V.I., Ekonomov, A.P., Golovin, Yu.M., Moshkin, B.E., San'ko, N.F., 1983. Solar radiation scattered in the Venus atmosphere—The Venera 11, 12 data. *Icarus* 53, 509–537.
- Mukhin, L., Gel'man, B. (I., Lamonov, N. I., Mel'nikov, V. V., Nenarokov, D. F., Okhotnikov, B. P., and Khokhlov, V. N. (1982). Venera 13 and Venera 14 gas-chromatography analysis of the Venus atmosphere composition. *Soviet Astronomy Letters*, 8:399-403.
- Na, C. Y. and Esposito, L. W. (1997). Is disulphur monoxide a second absorber on Venus? *Icarus*, 125:364-368.
- Na, C. Y., Esposito, L. W., and Skinner, T. E. (1990). International ultraviolet explorer observation of Venus SO<sub>2</sub> and SO. *J. Geophys. Res.*, 95(D6):7485-7491.
- Nair, H., M. Allen, A. D. Anbar, Y. L. Yung, and R. T. Clancy, A photochemical model of the Martian atmosphere, *Icarus*, 111, 124 – 150, 1994.
- Newman, M., Schubert, G., Kliore, A. J., and Patel, I. R. (1984). Zonal winds in the Middle Atmosphere of Venus from Pioneer Venus Radio Occultation Data. *J. Atmos. Sci.*, 41(12):1901-1913.
- Nicolet, M. (1989). Solar spectral irradiances with their diversity between 120 and 900 nm. *Plan. Space Sci.*, 37(10): 1249-1289.
- Nier and McElroy, Composition and Structure of Mars' Upper Atmosphere: Results from the Neutral Mass Spectrometers on Viking 1 and 2, *Journal of Geophysical Research* 82, p.4341-49, 1977
- Owen, T. (1967). Water vapour on Venus - A Dissent and Clarification. *Astrophys. J.*, 150:121-123.
- Owen, T., Composition and early history of the atmosphere of Mars, in *Mars, a cura di Kieffer, H.H., et al., The University of Arizona Press, 1992*
- Oyania, V. I., Carle, G. C, Woeller, F., B., P. J., Reynolds, R. T., and Graig, R. A. (1980). Pioneer Venus Chromatography of the Lower Atmosphere of Venus. *J. Geophys. Res.*, 82(A13):7891-7902.

- Palmer, K. F. and Williams, D. (1975). Optical constants of sulphuric acid: application to the clouds of Venus? *Applied Optics*, 14:208-219.
- Parkinson, T. D., and D. M. Hunten, Spectroscopy and aeronomy of O<sub>2</sub> on Mars, *J. Atmos. Sci.*, 29, 1380–1390, 1972.
- Phillips, R., Bullock, M. A., and Hauck, S. (2001). Climate and Interior Coupled Evolution on Venus. *Geophys. Res. Let.*, 28(9):1779-1782.
- Phillips, R.J. (Eds.), *Venus 2*. University of Arizona Press, Tucson, pp. 325–351.
- Piccioni, G., Drossart, P., Zasova, L., Migliorini, A., Gérard, J.-C., Mills, F. P., Shakun, A., García Muñoz, A., Ignatiev, N., Grassi, D., Cottini, V., Taylor, F. W., Erard, S., The *Virtis-Venus Express* Technical Team, First detection of hydroxyl in the atmosphere of Venus, *A&A*, Volume 483, pp.L29-L33, 2008
- Pollack J. B., Dalton J. B., Grinspoon D. H., Wattson R. B., Freedman R., Crisp D., Allen D. A., Bezaud B., de Bergh C., Giver L. P., Ma Q., and Tipping R. Near infrared light from Venus nightside: a spectroscopic analysis. *Icarus*, v. 103, no. 1, pp. 1-42, 1993.
- Pollack, J. B., R. M. Haberle, J. R. Murthy, J. Schaeffer, and H. Lee, Simulations of the general circulation of the Martian atmosphere, 2, Seasonal pressure variations, *J. Geophys. Res.*, 98, 3149–3181, 1993.
- Pollack, J. B., Toon, O. B., Whitten, R. C, Boese, R., Tomasko, M., Esposito, L., Travis, L., and Wiedman, D. (1980). Distribution and source of the UV absorption in Venus' atmosphere. *J. G. R.*, 85(A13):8141-8150.
- Pollack, J., Dalton, J. B., Grinspoon, D., Wattson, R., Freedman, R., Crisp, D., Allen, D., Bezaud, B., de Bergh, C, Giver, L., Ma, Q., and Tipping, R. (1993). Near Infrared Light from Venus' Night side: A spectroscopic analysis. *Icarus*, 103:1-42.
- Polyakov, A. V., Timofeev, Y. M., Tonkov, M. V., and Filippov, N. N. (1998). Effect of spectral line mixing on atmospheric transmission functions in CO<sub>2</sub> absorption bands. *Atmospheric and Oceanic Physics*, 3 i(3):318-327.
- R. T. Clancy, D. O. Muhleman and B. M. Jakosky, Variability of carbon monoxide in the Mars atmosphere, *Icarus*, Volume 55, Issue 2, Pages 282-301, 1983

- Revercomb, H. E., Sromovsky, L. A., Suomi, V. E., and Boese, R. W. (1985). Net thermal radiation in the atmosphere of Venus. *Icarus*, 61:521-538.
- Rodgers, C. D. (1976). Retrieval of atmospheric temperature and composition from remote measurements of thermal radiation. *Rev. Geophys. Space Phys.*, 14:609624.
- Rodgers, C. D. (1996). Optical Spectroscopic Techniques and Instrumentation for Atmospheric and Space Research II. In Hays, P. B. and Wang, J., editors, SPIE, volume 2830, pages 136-147.
- Rodgers, C. D. (1998). Information content and optimisation of high spectral resolution remote measurements. *Adv. Space Res.*, 21(3):361-367.
- Rodgers, C. D. (2000). *Inverse Methods for Atmospheric Sounding. Theory and Practise.* Word Scientific.
- Roldan et al (2000) Non-LTE Infrared Emissions of CO<sub>2</sub> in the Atmosphere of Venus, *Icarus*, 147, 11.
- Roos et al (1993). The upper clouds of Venus: determination of the scale height from NIMS-Galileo infrared data, *Planet. Space Sci.* 41, 505.
- Roos-Serote, M., Drossart, P., Encrenaz, T., Lellouch, E., Carlson, R., Baines, K., Taylor, F. W., and Calcutt, S. (1995). The thermal structure and dynamics of the atmosphere of Venus between 70 and 90 km from the Galileo-NIMS spectra. *Icarus*, 114:300-309.
- Rosenqvist, J., P. Drossart, M. Combes, T. Encrenaz, E. Lellouch, J. P. Bibring, S. Erard, Y. Langevin, and E. Chassefiere, Minor constituents in the Martian atmosphere from the ISM/Phobos experiment, *Icarus*, 98, 254– 270, 1992.
- Rossow, W. B., Del Genio, A. D., Limaye, S. S., Travis, L. D., and Stone, P. H. (1980). Cloud morphology and motions from Pioneer Venus images. *J. Geophys. Res.*, 85:8107-8128.
- Rothman, L. S. (1981). AFGL atmospheric absorption line parameters compilation: 1980 version. *Applied Optics*, 20:791-795.
- Rothman, L. S., *et al.* (1992). The HITRAN molecular database: Editions of 1991 and 1992. *J.Q.S.R.T.*, v. 48, p. 469–507.

Rothman, L. S., *et al.* (1996). The HITRAN molecular spectroscopic database and HAWKS (HITRAN atmospheric workstation): 1996 edition. (PDF document supplied with HITRAN).

Rothman, L. S., *et al.* A number of papers in *J.Q.S.R.T.* – see for the latest version

Rothman, L. S., Gamache, R. R., Tipping, R. EL, and collaborators (1992). The Hitran molecular database: Editions of 1991 and 1992. *J. Q. S. R. T.*, 48:469-507.

Rothman, L. S., Rinsland, C. P., Goldman, A., Massie, S. T., and collaborators. (1998). The Hitran molecular spectroscopic database and HAWKS (Hitran Atmospheric Workstation): 1996 edition. *J. Q. S. R. T.*, 60.

Rothman, L.S., *et al.*, The HITRAN molecular spectroscopic database and HAWKS (HITRAN atmospheric workstation): 2004 edition, distributed in [www.hitran.com](http://www.hitran.com)., 2004

Ruyten, W. (2004). Comment on “A new implementation of the Humlicek algorithm for the calculation of the Voigt profile function” by M.Kuntz [*JQSRT* 57(6) (1997) 819–824]. *J.Q.S.R.T.*, v. 86, p. 231–233.

Salby, M. L. (1996). *Fundamentals of Atmospheric Physics*. Academic Press.

Schaefer, L., Fegley, B., 2004. Heavy metal frost on Venus. *Icarus* 168 (1), 215–219.

Schofield, J. and Taylor, F. W. (1982). Measurements of the mean, solar-fixed temperature and cloud structure of the middle atmosphere of Venus. *Q. J. R. M. S.*, 109:57-80.

Schofield, J., Taylor, F. W., and McCleese, D. (1983). The global distribution of water vapour in the middle atmosphere of Venus. *Icarus*, 52:263-278.

Schofield, J.T., Taylor, F.W., 1982. Net global thermal emission from the Venus atmosphere. *Icarus* 52, 245–262.

Schorn, R. A., Barker, E. S., Gray, L. D., and Moore, R. C. (1969). High-precision spectroscopic studies of Venus II. The water vapour variations. *Icarus*, 10:98-104.

Schubert, G. (1980). General circulation and the dynamical state of the Venus atmosphere. In Bougher, S. W., Hunten, D. M., and Phillips, R. J., editors, Venus, Space Science Series, pages 681-765. University of Arizona Press.

Seiff, A. (1983). Thermal Structure of the Atmosphere of Venus. In Bougher, S. W., Hunten, D. M., and Phillips, R. J., editors, Venus, Space Science Series, pages 215-279. University of Arizona Press.

Seiff, A., Kirk, D. B., Young, R. E., Blanchard, R. C, Findlay, J. T., Kelly, G. M., and Sommer, S. C. (1980). Measurements of thermal structure and thermal contrasts in the atmosphere of Venus and related dynamical observations: Results from the four Pioneer Venus probes. J. Geophys. Res., 85:7903-7933.

Smith, M. D., The annual cycle of water vapor on Mars as observed by the thermal emission spectrometer, J. Geophys. Res., 107(E11), 5115, doi:10.1029/2001JE001522, 2002.

Smith, W. L. (1970). Iterative solution of the radiative transfer equation for temperature and absorbing gas profile of an atmosphere. Applied Optics, 9:1939-1999.

Staley, D. O. (1970). The Adiabatic Lapse Rate in the Venus Atmosphere. J. Atmos. Sci, 27:219-223.

Stamnes, K., *et al.* (1988). Numerically stable algorithm for discrete-ordinate-method radiative transfer in multiple scattering end emitting layered media. Appl. Optics, v. 27, p. 2502-2509.

Stamnes, K., *et al.* (2000). DISORT, a general purpose fortran program for discrete-ordinate-method radiative transfer in scattering end emitting layered media: Documentation of methodology, version 1.1, Mar 2000. (PDF document supplied with DISORT).

Steele, H. M. and Hamill, P. (1981). Effects of temperature and humidity on the growth and optical properties of sulphuric acid-water droplets in the stratosphere. J Aerosol Sci, 12:517-528.

Strow, L. L. and Reuter, D. (1988). Effect of line mixing on atmospheric brightness temperatures near 15 jirn. Applied Optics, 27.

Surkov, Y., Ivanova, V., Pudov, A., Pavlenko, V. A., Davydov, N. A., and Sheinin, D. (1982). Venera 13 and Venera 14 measurements of the water vapour content in the Venus atmosphere. *Soviet Astronomy Letters*, 8:411-413.

Surkov, Y., Shcheglov, O., Ryvkin, M., Davydov, N. A., Sheinin, D., and Zhitnikov, D. E. (1986). Vega 1, 2 humidity profiles for the Venus atmosphere. *Soviet Astronomy Letters*, 12:73-77.

Taylor, F. W. (1974). Remote Temperature Sounding in the Presence of Cloud by Zenith Scanning. *Applied Optics*, 13(7):1559-1566.

Taylor, F. W. (1975). Interpretation of Mariner 10 Infrared Observations of Venus. *J. Atmos. Sci*, 32:1005-1017.

Taylor, F. W. (1988). *The Physics of the Planets*, chapter : The Dynamics of the Atmosphere of Venus, pages 143-159. John Wiley & Sons.

Taylor, F. W. (1997). *Encyclopedia of Planetary Sciences*, chapter Venus: Atmosphere, pages 890-895. Chapman and Hall.

Taylor, F. W. (2002). Some fundamental questions concerning the circulation of the atmosphere of Venus. *Adv. Space Res.*, 29(2):227-231.

Taylor, F. W. Venus before Venus Express. *Planetary and Space Science* 54, 1249–1262 (2006 )

Taylor, F. W., Beer, R., Chahine, M., Diner, D. J., Elson, L. S., Haskins, R., McCleese, D. J., Martonchik, J. V., Reichley, P., Bradley, S. E., Delderfield, J., Schofield, J. T., Farmer, C. B., Froidevaux, L., Leung, J., Gille, J. C, and Coffrey, M. T. (1980). Structure and meteorology of the middle atmosphere of Venus: Infrared remote sensing from the Pioneer Orbiter. *J. Geophys. Res.*, 85:79368006.

Taylor, F. W., Diner, D. J., Elson, L. S., Hanner, M. S., McCleese, D. J., Martonchik, J. V., Reichley, P., Houghton, J. T., Delderfield, J., Schofield, J. T., Bradley, S. E., and Ingersoll, A. P. (1979a). Infrared remote sounding of the middle atmosphere of Venus from the Pioneer Orbiter. *Science*, 203:779-781.

Taylor, F. W., Diner, D. J., Elson, L. S., McCleese, D. J., Martonchik, J. V., Delderfield, J., Bradley, S. E., Schofield, J. T., Gille, J. C, and Coffrey, M. T. (1979b). Temperature,

cloud structure and dynamics of Venus middle atmosphere by infrared remote sensing from Pioneer Orbiter. *Science*, 205:65-67.

Taylor, F. W., Hunten, D. M., and Ksanfomality, L. V. (1983). The thermal balance of the middle and upper atmosphere of Venus. In Bougher, S. W., Hunten, D. M., and Phillips, R. J., editors, *Venus, Space Science Series*, pages 650-680. University of Arizona Press.

Taylor, F. W., Vesceles, F. E., Locke, J. R., Foster, P. B., Beer, R., Houghton, J. T., Delderfield, J., and Schofield, J. T. (1979c). Infrared radiometer for the Pioneer Venus Orbiter. 1. Instrument Description. *Applied Optics*, 18:3893-3900.

Taylor, F.W., 1981. Equatorial cloud properties on Venus from Pioneer Orbiter infrared observations. *Adv. Space Res.* 1, 151–154.

Taylor, F.W., 1995. Carbon monoxide in the deep atmosphere of Venus. *Adv. Space Res.* 16 (6), 81–88.

Taylor, F.W., 2006a. *Climate Variability On Venus And Titan, Space Science Series of ISSI, vol. 19, Solar Variability and Planetary Climates, Springer*

Taylor, F.W., 2006b. On the distribution and variability of water vapour in the middle atmosphere of Venus. *Adv. Space Res.*

Taylor, F.W., Beer, R., Chahine, M.T., Diner, D.J., Elson, L.S., Haskins, R.D., McCleese, D.J., Martonchik, J.V., Reichley, P.E., Bradley, S.P., Delderfield, J., Schofield, J.T., Farmer, C.B., Froidevaux, L., Leung, J., Coffey, M.T., Gille, J.C., 1980. Structure and meteorology of the middle atmosphere of Venus: infrared remote sounding from the Pioneer Orbiter. *J. Geophys. Res.* 85, 7963–8006.

Taylor, F.W., Crisp, D., Berzard, B., 1997. Near-Infrared sounding of the lower atmosphere of Venus. In: Bougher, S.W., Hunten, D.M.,

Theodore, B., E. Lellouch, E. Chassefiere, and A. Hauchecorne, Solstitial temperature inversions in the Martian middle atmosphere: Observational clues and 2-D modeling, *Icarus*, 105, 512– 528, 1993.

Tikhonov, A. N. (1963). On the solution of incorrectly stated problems and a method of regularisation. *Dokl. Acad. Nauk. SSSR*, 122:2530.

- Tillman, J. E., Mars global atmospheric oscillations: Annually synchronized, transient normal-mode oscillations and the triggering of global dust storms, *J. Geophys. Res.*, 93, 9433– 9451, 1988.
- Tisdale, R. T., Glandorf, D. L., Toldert, M. A., and Toon, O. B. (1998). Infrared optical constants of low temperature H<sub>2</sub>SO<sub>4</sub> solutions representative of stratospheric sulfate aerosols. *J. Geophys. Res.*, 103(D19):25353-25370.
- Titov et al., *The Atmosphere of Venus: Current Knowledge and Future Investigations*, in *Solar System Update*, a cura di Blondel e Mason, Springer, Berlino, 2006
- Titov, D. V. (1995). Radiative Balance in the Mesosphere of Venus from the Venera 15 Infrared Spectrometer Results. *Adv. Space Res.*, 15( i):173 177.
- Titov, D. V. and Haus, R. (1997). A fast and accurate method of calculation of gaseous transmission functions in planetary atmospheres. *Planet. Space Sci.*, 45(3):369-377.
- Tobiska, W. K., Woods, T., Eparvier, F., Viereck, R., Floyd, L., Bouwer, D., Rottman, G., and White, O. R. (2000). The Solar2000 empirical solar irradiance model and forecast tool. *J. Atm. Solar Terr. Phys.*, 62:1233-1250.
- Tomasko, M., 1983. The thermal balance of the lower atmosphere of Venus. In: Hunten, D.M., Colin, L., Donahue, T.M., Moroz, V.I. (Eds.), *Venus*. University of Arizona Press, Tucson, pp. 604–631.
- Traub, W. A. and Carleton, N. P. (1975). Observations of O<sub>2</sub>, H<sub>2</sub>O and HD in planetary atmospheres. In Woszczyk, A. and Iwaniszewska, C., editors, *Exploration of the Planetary System*, pages 223-228. Dordrecht: Reidel.
- Travis, L. D. (1978). Nature of the atmospheric dynamics on Venus from power spectrum analysis of Mariner 10 images. *J. Atmos. Sci.*, 35:1584-1595.
- Twomey, S. (1963). On the numerical solution of Fredholm integral equation of the first kind by the inversion of the linear system produced by quadrature. *J. Ass. Comput. Mach.*, 10:97.
- Twomey, S., Herman, B., and Rabinoff, R. (1977). An extension to the Chahine method of inverting the radiative transfer equation. *J. Atmos. Sci.*, 34:1085.

Ustinov, E. A. (1991). Inverse problem of thermal sensing: 3. Reconstructing the vertical profile of the mixing ratio of a minor gaseous component. *Kosmicheskie Issledovaniya*, 29(2):289-297.

Valdes, P. J. (1984). Large scale waves in the atmosphere of Venus. PhD thesis, Atmospheric Physics Department, Oxford University.

Varanasi, P., Measurements of line widths of CO of planetary interest at low temperatures, *J. Quant. Spectrosc. Radiat. Transfer*, 15, 191– 196, 1975.

*Venus, 1983, and Venus II, 1997*, edited by S. W. Bougher, Hunten, D. M. and Phillips, R. J., Space Science Series, University of Arizona Press.

von Zahn, U., Kumar, S., Niemann, H., and Prinn, R. (1983). Composition of the Venus Atmosphere. In Bougher, S. W., Hunten, D. M., and Phillips, R. J., editors, *Venus*, Space Science Series, pages 299-430. University of Arizona Press.

Walterscheid, R. L., Schubert, G., Newmann, M., and Kliore, A. J. (1985). Zonal winds and the angular-momentum balance of Venus' Atmosphere within and above the clouds. *J. Atmos. Sci.*, 42(19):1982-1990.

Winick, J. R. and Stewart, I. F. (1980). Photochemistry of SO<sub>2</sub> in Venus' upper cloud layers. *J. Geophys. Res.*, 85:7849-7860.

Wiscombe, W. J. (1980). Improved Mie scattering algorithms. *Applied Optics*, v. 19, no. 9, p.1505–1509.

Woo, R., Armstrong, W. J., and Kliore, A. J. (1982). Small-scale turbulence in the atmosphere of Venus. *Icarus*, 52:335-345.

Yamamoto, G., Tanaka, M., and Aoki, T. (1969). Rotational Line Widths of Carbon Dioxide Bands. *J.Q.R.S.T*, 9:371-382.

Yamamoto, M. and Tanaka, K. (1997). Formation and maintenance of the 4-day circulation in the Venus middle atmosphere. *J. Atmos. Sci.*, 54.

Young, L., Young, A., and Zasova, L. V. (1984). A new interpretation of the Venera 11 Spectra of Venus. The 0.94  $\mu\text{m}$  water band. *Icarus*, 60:138-151.

Yung, Y. L. and DeMore, W. B. (1982). Photochemistry of the Stratosphere of Venus; Implications for Atmospheric Evolution. *Icarus*, 51:199-247.

Zasova, L. V., Khatountsev, I. A., Moroz, V. I., and Ignatiev, N. I. (1999), Structure of the Venus middle atmosphere: Venera 15 Fourier Spectrometry data revisited. *Adv. Space Res.*, 23(9):1559-1568.

Zasova, L. V., Krasnopolsky, V. A., and Moroz, V. I. (1981), Vertical distribution of SO<sub>2</sub> in upper cloud layer of Venus and origin of UV absorption. *Adv. Space. Res.*, 1:31.

Zasova, L. V., Moroz, V. I., and Linkin, V. M. (1996). Venera-15,16 and VEGA mission results as sources for improvements of the Venus reference atmosphere. *Adv. Space Sci*, 17:(11)171-(11)180.

Zasova, L. V., Moroz, V. I., Esposito, L. W., and Na, C. Y. (1993). SO<sub>2</sub> in the middle atmosphere of Venus: IR measurements from Venera 15 and comparison to UV data. *Icarus*, 105:92-109.

